Compression Failure Of Fibrous Laminated Composites In The Presence Of Stress Gradients: Experiment and Analysis

Thesis by

Anthony M. Waas

In Partial Fulfillment of the Requirements
for the Degree of
Doctor of Philosophy

Research supported by Grant NSG 1483
from the NASA Langley Research Center

California Institute of Technology
Pasadena, California

1988

(submitted October 2, 1987)

To:

- *My parents, brothers and sister, uncle Anton and Jane.*
- *The memory of my grandparents, Austin and Florence de Mel, and to the memory of a great teacher, Charles Babcock Jr.*

for all they have done.

Acknowledgements

It gives me pleasure to acknowledge those who have been concerned with my education. Firstly, I am extremely grateful to the late Prof. Charles Babcock Jr., my 'guru' for five years. I have benifited immensely from my association with him. His expertise in structural mechanics combined with fine teaching skills and above all, his display of qualities as a good human being, made my stay at Caltech memorable.

The advice and helpful suggestions, particularly concerning the experiment, given by Prof. Wolfgang Knauss are greatly appreciated. I thank him for his patience and assistance in the preparation of this thesis.

Towards the latter part of this investigation I had the opportunity of interacting with Profs. J.K. Knowles and J. Singer. I have learned alot from this association.

The help of Louis Johnson, from Central Engineering Services, Jean Anderson and Pat Gladson, from the Aero Library, Richard Gomez, from the Graphics Arts facillity, and Betty Wood, from the Aero Department, is acknowledged. I would like to thank Bill Glass, of Sonics Engineering, and Gabor Faludi, from the Chemistry Glass Shop, for the use of their facillities.

The interest of Dr. J. Starnes Jr., of NASA Langley Research Center, and Dr. Herzl Chai, of the University of Dayton Research Institute, is much appreciated.

Thanks are due to my friends in the solid mechanics group at GALCIT, including Mrs. Marta Goodman, for their friendship throughout these years. In particular, I thank Pete Washabaugh and Raghu Madhavan, and especially Richard Pfaff, friend and colleague, for his generosity and participation in an endless number of valuable discussions, too numerous to mention. Thanks are due to Dr. Howard Stone for numerous cups of coffee during the preparation of this thesis.

Finally, I thank my loving parents, brothers and sister for their continuous support throughout my education.

Abstract

A series of experiments were performed to determine the mechanism of failure in compressively loaded laminated plates in the presence of stress gradients generated by a circular cutout. Real time holographic interferometry and in-situ photomicrography of the hole surface, were used to observe the progression of failure.

The test specimens are multi-layered composite flat plates, which are loaded in compression. The plates are made of two material systems, T300/BP907 and IM7/8551-7. Two different lay-ups of T300/BP907 and four different lay-ups of IM7/8551-7 are investigated.

The load on the specimen is slowly increased and a series of interferograms are produced during the load cycle. These interferograms are video-recorded. The results obtained from the interferograms and photo-micrographs are substantiated by sectioning studies and ultrasonic C-scanning of some specimens which are unloaded prior to catastrophic failure, but beyond failure initiation. This is made possible by the servo-controlled loading mechanism that regulates the load application and offers the flexibility of unloading a specimen at any given instance in the load-time history.

An underlying objective of the present investigation is the identification of the physics of the failure initiation process. This required testing specimens with different stacking sequences, for a fixed hole diameter, so that consistent trends in the failure process could be identified.

It is revealed that the failure is initiated as a localized instability in the 0^0 plies at the hole surface, approximately at right angles to the loading direction. This instability emanating at the hole edge and propagating into the interior of the specimen within the 0^0 plies is found to be fiber microbuckling. The microbuckling is found to occur at a local strain level of $\simeq 8600$ μstrain at the hole edge for the IM material system. This initial failure renders a narrow zone of fibers within the 0^0 plies to loose structural integrity. Subsequent to the 0^o-ply failure, extensive delamination cracking is observed with increasing load. The through thickness location of these delaminations is found to depend on the position of the 0^o plies.

The delaminated portions spread to the undamaged areas of the laminate by a combination of delamination buckling and growth, the buckling further enhancing the growth. When the delaminated area reaches a critical size, about 75-100% of the hole radius in extent, an accelerated growth rate of the delaminated portions is observed. The culmination of this last event is the complete loss of flexural stiffness of each of the delaminated portions leading to catastrophic failure of the plate. The levels of applied load and the rate at which these events occur depend on the plate stacking sequence.

A simple mechanical model is presented for the microbuckling problem. This model addresses the buckling instability of a semi-infinte layered half-plane alternatingly stacked with fibers and matrix, loaded parallel to the surface of the half-plane. The fibers are modelled using Bernoulli-Navier beam theory, and the matrix is assumed to be a linearly elastic foundation. The predicted buckling strains are found to overestimate the experimental result. However, the dependence of the buckling strain on parameters such as the fiber volume fraction, ratio of Youngs moduli of the constituents and Poisson's ratio of the matrix are obtained from the analysis. It is seen that a high fiber volume fraction, increased matrix stiffness, and perfect bonding between fiber and matrix are desirable properties for increasing the compressive strength.

Contents

Tables

Figures

List of Figures

List of Tables

CHAPTER 1.

INTRODUCTION

1.1 Composites

The use of composite materials for structural applications is not new. This is best summarized by the quote below.

> *‘ Then the officers of the children of Israel came and cried unto Pharaoh, saying, “ Wherefore dealest thou thus with thy servants ? There is no straw given unto thy servants and they say to us,‘ Make brick ’ ; and, behold, thy servants are beaten ; but the fault is in thine own people.”*
>
> *‘ But he said, “ Ye are idle, ye are idle ; therefore ye say, ‘ Let us go and do sacrifice to the Lord’.*
>
> *Go therefore now, and work ; for there shall no straw be given you, yet shall ye deliver the tale of bricks.”*
>
> *Exodus, 5:15-18*

Thus, as far back as several centuries ago, man’s use of straw bricks demonstrates his awareness of the usefulness of a composite. The straw was used in the clay to prevent it from cracking when rapidly dried in the sun. The word ‘composite’ implies consisting of at least two different phases or constituent materials. Several examples from nature, such as human teeth, bone and muscle display the character of a composite structure. These structures appearing in nature are optimally designed in the sense that they are rather efficient for their intended use.

Wood is a classic example of a natural composite. Wood displays a complicated cell like structure, but rather efficiently designed. The cell walls are made of cellulose fibrallae, which are wound in threaded form around the cells in the shape of a spiral or helix. It also posseses a characteristic property of a composite in that its mechanical properties display a directional dependence.

More recently there has been renewed interest in the use of composites and an increasing proportion of fiber laminated composites are finding application particularly in the aerospace and automobile industry. In these fields it is desirable to maximize the stiffness/weight ratio while still maintaining the necessary strength requirements in selecting a material for a particular application. The reason for this is that much of the structure of an aircraft, for instance, is in compression, and compression carrying members are usually beams and plates, which are thin in comparison with their length. These structures fail by elastic buckling, not by direct crushing, and the cause of such failures is lack of stiffness, not lack of strength. This type of failure is referred to as " Euler collapse ", in honor of Leonhard Euler, the discoverer of buckling.

The requirements of high strength and stiffness/weight ratio are seldom compatible in many materials, and it is this facet of design that composites are able to exploit. There are several types of modern composites at our disposal. An excellent article describing the availability and uses of many of these can be found in Chou et. al [1.1].

The investigation reported in this thesis is concerned with continuous fiber laminated composites. These composites contain two distinct constituents, fiber and matrix, that are combined together to form a laminate. Each lamina (or ply) of the laminate contains fibers (reinforcement of high stiffness) pre-impregnated in a soft matrix(low stiffness,tough), which are available in tape form. These tapes are typically 0.15mm thick and contain within them about 20-30 layers of densely packed fiber and matrix (see Figure 1.1). Fiber volume fractions of 0.5-0.6 are typical of the material used in the industry. The tape material is laid up in different directions to yield desirable mechanical properties to suit a particular application. The freedom to tailor the directional dependence of stiffness, and possessing a high stiffness/weight ratio are clear advantages composites have over traditional materials like metals. These facts are evident from the comparison presented in Table 1.1, taken from Gordon [1.2].

1.2 Analysis Methods

There are two levels of abstraction adopted when studying composites. These are referd to as *micromechanics* and *macromechanics*. In micromechanics, one seeks to characterize the mechanical behavior of each *lamina* by recognizing its heterogeneous fine structure; fiber,matrix etc. Thus, the fiber diameter (or equivalently the fiber spacing) emerges as a natural length scale. It must be emphasized that the term micromechanics does not imply analysis carried out on an atomic scale; instead, one seeks to obtain effective moduli, which reflect the fine detail of each lamina. There are several ways to obtain effective moduli that incorporate various levels of sophistication. Some of these are best described in Hashin [1.3], Chamis and Sendeckyj [1.4] and Pagano [1.5]. The main product of the micromechanical formulation is the evaluation of the effective modulli of a uni-directional lamina (parallel fibers) which are stacked up to form a laminate.

The *mechanics of materials* approach, first introduced by Ekvall [1.6] has found wide use due to the generally accepted good agreement with experimental data [1.7]. The key assumption here is that the strains in the fiber direction of a uni-directional fibrous composite are the same in the fibers as in the matrix. This method, refered to as the *rule of mixtures*, yields the following results for a uni-directional lamina;

$$\begin{aligned} E_{11} &= E_f V_f + E_m V_m \\ \nu_{12} &= \nu_f V_f + \nu_m V_m \\ E_{22} &= \frac{E_m E_f}{V_m E_f + V_f E_m} \\ G_{12} &= \frac{G_m G_f}{V_m G_f + V_f G_m} \end{aligned} \tag{1.1}$$

In general the first two estimates have been found to yield good agreement with experiment , but the same cannot be said about the latter two. Using (1.1), the lamina is characterized as being a single layer of equivalent homogeneous material.

The next level of abstraction in composites is refered to as *macromechanics*, which attempts to characterize the laminate in terms of the lamina constitutive behavior. Since laminates are frequently much smaller in one dimension compared to the other two, beam, plate, and shell theories are frequently used in analysis, with the kinematic assumption of linear variation in the in-plane displacement components through the thickness. This is a good assumption as long as the aspect ratio S (ratio of characteristic in-plane dimension to thickness of laminate) is greater than $\approx$10. This is illustrated in Figure 1.2, taken from Pagano and Hatfield [1.8], for the static bending of a nine-layer Graphite/Epoxy laminate. A natural length scale in macromechanics is the lamina thickness.

The main body of analysis in macromechanics is encompassed in *Classical Laminated Plate theory*, popularly referred to as CLT. This theory serves two main purposes. Firstly, it gives the approximate field equations in the solution of specific boundary value problems and secondly a constitutive description of the laminate can be directly obtained. For the latter task, one considers an infinetesimal element of the laminate and derives relations between the in-plane forces and moments per unit length and the mid-plane strains and curvatures as in classical plate theory, invoking the Kirchoff hypothesis. Following this procedure the *laminate constitutive relation* is obtained (see, for example Jones [1.25], chap.4).

1.3 Literature Review

Much of the work performed in the past to study the compressive behavior of plates containing holes has been aimed at studying the stress concentration effect and the influence of hole size on the global buckling behavior of the plate. Kirch [1.9] was the first to determine the stress concentration factor (**SCF**) in an infinite isotropic plate containing a hole. Howland [1.10] studied the effect of finite plate width and showed that the **SCF** increased as the diameter(**d**) of the hole attained smaller values in relation to the plate width(**w**), significant corrections being attained for $\frac{\mathbf{w}}{\mathbf{d}} \leq 2$. With regard to orthotropic materials, the work of Green and Zerna [1.11], Lekhnitskii [1.12] and Savin [1.13] have to be mentioned. Greszczuk [1.14] presents results for the **SCF** for different laminate configurations by using CLT to obtain the laminate constitutive relation. He then extends his earlier work, [1.15] on failure criteria for three-dimensional orthotropic solids based on the Hencky-Von Mises criterion, to laminates with cut-outs.

Many other researchers have recently employed boundary layer theory [1.16] in the manner for isotropic plates developed by Reiss [1.17] and numerical techniques such as the finite element method to study the laminate behavior in the presence of a cut-out. This work is reviewed in Chapter 3.

Another group of workers, Waddoups, Eisenmann and Kaminitskii [1.18], approach this problem from a fracture mechanics viewpoint. The regions of high stress concentration near the hole is modelled as a "crack-like region of intense energy". This enables expressing the failure of the plate in terms of a critical stress intensity factor. While this may prove successful for plates loaded in tension, neither its usefulness nor its physical basis has been established for the compressive case. This work was extended by Nuismer, Whitney and co-workers [1.19-1.20]. An excellent literature survey related to this topic is available in Crews [1.21].

Unfortunately, the effort to study the underlying problem *experimentally* has been lacking. Apart from the work of researchers at NASA-Langley Research Center (references are listed at the end of Chapter 3.), which will be spelled out in the next chapter, mention must be made of the experimental efforts of Daniel, Rowlands and Whiteside [1.22-1.23], who studied the effects of geometry, material properties and stacking sequence on the behavior of laminates with holes and Knauss, Starnes and Henneke [1.24], who investigated the buckling behavior of laminates containing holes.

1.4 Motivation for Present Work

The objective of the present study was to examine experimentally the mechanisms associated with the failure of a compressively loaded laminated plate in the presence of stress gradients, generated by a circular cutout. It was imperative that such a task be undertaken so that the usefulness of the analytical and numerical work aimed at addressing this problem could be established. The geometry used in the present experiment was influenced by two considerations. Firstly, the elasticity solution, based on the generalized plane stress approximation, for an orthotropic plate containing a cutout and loaded parallel to an axis of orthotropy was established (see Chapter 3.). Secondly, it was necessary to control the area of failure so that a thorough and detailed examination of this area could be caried out. In addition, a detection technique was required that was capable of isolating failure mechanisms that occured on the *micro* length scale of the material; the fiber diameter. This requirement was met by choosing an optical technique such as inteferometry. As to the particular type of interferometry, it was decided that *Holographic interferometry* would best be suited since it required a *diffusely refelective* surface. The laminates contain a protective mat on the outer surface, and thus, these surfaces were ideally suited for producing the diffuse reflectance.

The interferometric information alone would not suffice for a complete understanding of this problem. It was necessary to relate the interferometric results to the damage development on the hole surface, as well as damage to the interior of the laminate. This was accomplished by following the damage development on the hole surface through an optical microscope, with the interferometeric information serving as a guide. In addition, sectioning studies of partly damaged plates loaded upto various load levels, as well as C-scanned maps of integrated through-thickness damage and surface strain gage measurements at critical locations on the specimen, provided information that was critical in following the progressive nature of failure. A detailed and extensive study in addressing compressive failure of laminates in the presence of cutouts, such as described in this thesis, has not been undertaken before, to the knowledge of this author.

The experimental results, that are obtained as described above, are used in formulating mechanical models that have an underlying physical basis. These models enhance our knowledge about the various stages of failure in a laminate. In addition, the parameters that influence the compressive strength of the laminate can be identified from these models. The results thus obtained serve towards improving the compressive strength of composite laminates.

1.5 Organization of Thesis

The thesis is divided into two sections. In the first section consisting of Chapter 2, the experiment and associated methodology is presented first. This chapter concludes with a presentation and discussion of results of each type of laminate. The next section consists of chapters 3 and 4. In Chapter 3, the stress analysis problem for an orthotropic plate containing a circular cutout and loaded along an axis of orthotropy is computed in the manner described in Lekhnitskii [1.12]. In Chapter 4, a mechanical model for fiber microbuckling is presented.

The thesis concludes with Chapter 5, which is a summary of the main findings of this investigation and suggestions for future research.

1.6 References

1.1 Chou,T.W, McCullough, R.L and Pipes, B. (1986),"Composites", *Sci.American Journal*, Vol. 255, pp192-203.

1.2 Gordon, J.E. (1984),"*The new science of strong materials*", Princeton University Press.

1.3 Hashin, Z. (1964),"Theory of mechanical behavior of heterogeneous media", *Appl.Mech.Rev.*, Vol. 17, pp1-9.

1.4 Chamis, C. and Sendeckyj, G.P. (1968),"Critique on theories predicting thermoelastic properties of fibrous composites", *J.Comp.Matls*, Vol. 2, pp332-358.

1.5 Pagano, N.J. (1974),"The role of effective modulii in the elastic analysis of composite laminates", *Mechanics of composite materials*, 2nd ed., G.P. Sendeckyj, Academic press.

1.6 Ekvall, J.C. (1961),"Elastic properties of orthotropic monofilament laminates," *Am.Soc.Mech.Eng.*, Paper 61-Av-5.

1.7 Bert, C.W. and Francis, P.H. (1974),"Composite material mechanics; thermoelastic micromechanics",*Trans.New York Acad.Sci.*,series ii, Vol. 36, pp663-674.

1.8 Pagano, N.J. and Hatfield, S.J. (1972),"Elastic behavior of multi-layered bidirectional composites", *AIAA J.*, Vol. 10, pp931-933.

1.9 Kirch, G. (1898),"Die theories der elastizitat und die bedurfuisse der festigkeitslehre", *Z.Ver.deut.Ing.*, Vol. 32, pp797-807.

1.10 Howland, R.C.J. (1929),"On the stresses in the neighbourhood of a circular hole in a strip under tension", *Phil.Trans.Roy.Soc.(Lon)*, series A, Vol. 229, pp49.

1.11 Green, A.E. and Zerna, W. (1960),"*Theoretical Elasticity*", Clarendon at Oxford press.

1.12 Lekhnitskii, S. (1963),"*Theory of elasticity of an anisotropic body*", Holden-Day Inc., San Fransisco.

1.13 Savin, G. (1968),"Stress distribution around holes", NASA report TTF-607.

1.14 Greszczuk, L.B. (1972),"Stress and failure criteria for orthotropic and anisotropic plates with circular openings, ASTM STP 497, pp363-381.

1.15 Greszczuk, L.B. (1967),"Failure criteria for three dimensional orthotropic solids", Douglas missile and space systems, division report No.60869.

1.16 Tang, S. (1977),"Interlaminar stresses around circular cutouts in composite plates under tension", *AIAA J.*, Vol.15, pp1631-1637.

1.17 Reiss, E.L. (1961),"extension of a thick infinite plate with a circular hole", NYU report IMM-NYU-281.

1.18 Waddoups, M., Eisenmann, J.R. and Kaminski, B. (1971),"Macroscopic fracture mechanics of advanced composite materials", *J.Comp.Matls*, Vol. 5, pp446-454.

1.19 Nuismer, R.J. and Whitney, J. (1975),"Uniaxial failure of composite laminates containing stress concentrations", ASTM STP 593, pp117-142.

1.20 Whitney, J. and Nuismer, R.J. (1974)," Stress fracture criteria for laminated composites containing stress concentrations", *J.Comp.Matls.*, Vol. 8, pp253.

1.21 Crews, J. (1984)," A survey of strength analysis methods for laminates with holes", *Aero.Soc. of India J.*, Vol. 36, pp287-303.

1.22 Daniels, I., Rowlands, R.E. and Whiteside, J. (1974),"Effects of material and stacking sequence on behavior of composite plates with holes", *Exp.Mech.*, Vol. 14, pp1-9.

1.23 Rowlands, R.E., Daniel, I. and Whiteside, J. (1973),"Stress and failure analysis of a glass/epoxy composite plate with a circular hole", *Exp.Mech* ., Vol. 13, pp31-37.

1.24 Knauss, J., Starnes, J. and Henneke, E. (1978),"The compressive failure of graphite/epoxy plates with circular holes", NASA CR 157115, N78-24295.

CHAPTER 2.

EXPERIMENTAL DETAILS

2.1 Introduction

The use of graphite/epoxy laminates in various fields of engineering has posed a new challenge to engineering design. In many instances, it is necessary to look for new techniques to characterize these materials which differ from isotropic, homogeneous materials in their response to mechanical load.

One situation where these laminates exhibit a different type of behavior is when they are subjected to compressive loads. One or several competing modes of failure are present, and the researcher is left with the task of identifying the most important aspect of the failure process from a design standpoint. When structural components are made out of these laminates, it is seldom that they will persist in an environment free of stress concentrations. Stress raisers can be lethal and are potential sites where damage can initiate in a structure.

The open hole strengths of these laminates has been the subject of numerous investigations [2.1-2.4]. Figure 2.1 depicts ultimate load carrying capacity of these laminates as a function of the normalized hole diameter. Mikulas [2.5], has shown that these results could be bounded by simple criteria based on notch sensitivity. If the material is notch insensitive, the failure strains are directly proportional to the reduction in cross-sectional area; while if the material is notch sensitive, then it is postulated that the material fails when the strain concentration at the hole edge equals the failure strain of the material. It is seen that the latter assumption is too-conservative in that the failure strain is underestimated for (a/w) ratios less than 0.4. This situation indicates the possibility that the strain concentration effect alone cannot possibly account for the failure process and that a localized failure mechanism may be present. Based on this premise, Starnes et al [2.1] carried out open hole strength testing of these laminates and reported a *shear crippling* type of failure to be prevalent in the vicinity of the hole prior to catastrophic failure. This conclusion was based on post-mortem examination of damaged specimen.

In these and other similar investigations, no attempt has been made to follow the progression of failure. The progressive nature of failure, in many cases, by various stages is a characteristic property of laminated composites. Several different failure processes are prevalent when these laminates are stressed, and what is required is to identify the key aspects of failure in a particular situation.

Motivated from such an understanding, the present chapter describes a detailed experimental investigation to identify the initiation and propagation of failure in laminates in the presence of a stress raiser. The stress concentration effect is produced by choosing a flat plate with a centered circular hole and subjecting it to an inplane compressive load. The hole is carefully cut in order to insure that excessive local damage does not occur during the machining process. The damage initiation and propagation throughout the entire load history is studied via real time *holographic Interferometry* and *photomicrography* of the hole surface. The results thus obtained are substantiated by post experiment examination of the damaged specimen *ultrasonically* and under an *optical Microscope.*

In the sections to follow, the experiment and associated methodology is presented first. Pertinent details are given where necessary but no attempt is made to go into extensive detail. The interested reader is referred to relevant texts on holography, ultrasonic scanning etc. for a detailed treatment of the subject. It must be emphasized that the main goal of this project is not a systematic investigation of the stress gradient effect on the failure of the laminates, but rather, having chosen a geometry that produces stress gradients, to identify the mechanisms of failure.

2.2 The Experiment

2.2.1 Assembly

Figure 2.2 is a photograph showing the arrangement of the various devices used in the experiment. On a pneumatically vibration isolated table, optical components are arranged to produce a hologram and generate interferograms of the test specimen which is loaded using a table top compression device. An optical microscope is mounted on a tripod which is situated adjacent to the optical table by the testing machine. A 35 *mm* motor driven SLR camera attached to the microscope is used to take photographs of the test specimen hole surface during the testing sequence. Recording and developing of the hologram is done on a thermoplastic plate which is housed in the body of the instant recording device(IRD) as marked in Figure 2.2. This device, which is electronically controlled, replaces the conventional wet chemical processes which would be used had the recording being done on a photographic plate. A video camera placed behind the thermoplastic plate views the test specimen through the hologram. A VCR records the interferometric pattern generated during the loading sequence. A TV monitor is used to view the interferograms during a typical test, therby enabling the testing to be done interactively. In the following sections, the main components of the experiment are described.

2.2.2 Specimen

The multi-layered laminated plates used in the tests were supplied by NASA-Langley Research Center. The composition of the laminae in the specimen consisted of Thornel-300 graphite fibers preimpregnated with American Cyanamide BP 907 epoxy resin, and IM7 graphite fibers pre-impregnated in 8551-7 epoxy resin. The

IM7 fibers have a smaller diameter ($5\mu m$) than the T300 fibers ($7\mu m$). The fiber volume fraction in both these systems is 0.5-0.6. These laminates are typical of those used in the aerospace industry. Four types of lamina stacking sequence were used in the tests. The first, designated type A, is 48 ply $[+45/\text{-}45/0/0/+45/\text{-}45/0/0/+45/\text{-}45/0/90]_{2s}$, while the other, type B, is obtained by rotating the first sequence by ninety degrees, the angles being measured with respect to the loading direction counterclockwise. type C is 48 ply $[+45_6/-45_6/0_6/90_6]_s$, while type D is obtained by rotating type C in the same manner decribed for types A and B. Table 3.3 summarizes the laminate types. Diamond impregnated core drills and saws are used for machining the specimen. Two sizes of specimen are used. The first, S" is 7.62 *cm* × 10.2 *cm* and the other, "L", is 12.7 *cm* × 15.3 *cm*.

2.2.3 Specimen Supports

The laminated plates need to be supported in a manner that allows a smooth load transfer from the testing machine on to the plates. To facilitate this, specimen holders made of mild steel are used in these tests. The diameters of the holders are chosen to be the widths of the specimen. The holders contain grooves of 1.27 cm depth and widths large enough to accomodate the specimen and the thin layers of bonding agent. The test specimens are inserted into the grooves and bonded to the support holders with DEVCON bonding agent. Edge stiffeners are attached to the sides of the specimen to avoid plate buckling. These stiffeners increase the flexural stiffness of the plate but carry no load. A typical set of edge stiffeners is shown in Figure 2.3.

2.2.4 Testing Machine

The use of real time holographic interferometry requires vibration isolation of test specimen and testing device. As such, a special purpose testing device was designed and constructed for this purpose. Both tension and compression load can be applied using this device. At the commencement of a test one end of the specimen support holders is inserted into an adapter which threads onto the actuator arm of the loading device. A ball joint is attached to the other end. The mating part of the ball joint is positioned at the center of a 445 kN(100,000 lbf) load cell. The load cell is mounted on one of the flanged box beams of the testing machine. A photograph of the testing machine and accessories positioned on the optical table is shown in Figure 2.4a. A photograph of a specimen mounted as described earlier with the balljoint arrangement is shown in Figure 2.5.

The load-time history is regulated through a servo controlled loading mechanism. The servo valve and associated accessories are mounted on a plate which fits on the cylinder of the loading device. A function generator is used to program the loading path. A picture of the servo valve and accessories is shown in Figure 2.4b.

2.2.5 Holographic Interferometry

Real time holographic interferometry is used in this study to record the out of plane displacement changes Δw of the specimen during the loading sequence. The revelant details of the technique as applicable to the present experiment are given in section **2.2.7** . One novelty in the present experiment is the use of an electronically controlled process in the recording and development of a hologram. In conventional holography, a wet chemical process is used in the development of the photographic glass plates. The time consumed during this process, which is of the order of 7-9 minutes, is a significant portion of the total duration of a test, which is of the order of 2 hours. During a continuous loading sequence, the information on the displacement history is lost during this development time. The electronic process referred to above and explained in the next section overcomes this drawback.

2.2.6 The Instant Recording Device

In the reconstruction process of a hologram, the conventional silver halide photographic plates cause diffraction via an *amplitude grating* which is representative of the spatial distribution of light(amplitude and phase) that is emitted from the diffusely reflective surface of the object. However, the same task could be accomplished with a *phase grating* i.e. , a surface contour variation which is representative of the light off of the object. This is the basic idea behind the success of the thermoplastic recording device. The device has several stages of operation as shown in Figure 2.6. Steps (a) through (d) require less than one minute - a considerable saving of time. Furthermore, with real time holographic interferometry, a complete deformation history of the object up to failure can be recorded. This is important in the study of composites which exhibit several stages of failure. There are four basic steps in the creation of a hologram with this device.

Step 1.

A uniform charge is deposited on the thermoplastic plate as shown in Figure 2.6a. A movable coronatron deposits this charge. A corresponding negative charge forms on the transparent electrical conductor which is connected to ground.

Step 2.

The plate is exposed. Charge passes through the photoconductor only in the illuminated areas (Figure 2.6b.).

Step 3.

Another charge is provided to the plate. Because the plate is now not exposed to the light the charge does not move across the photoconductor. Thus, the areas of the thermoplastic that were illuminated experience a greater electric field; the charge density is greater in the illuminated areas.

Step 4.

The development of the hologram is carried out by heating the thermoplastic plate. In areas where the electric field is greater, the heat softened thermoplastic becomes thinner(Figure 2.6d). This creates the surface contour variation which causes the diffraction of light in the reconstruction stage.

The *coronatron* is a device that consists of a wire anode running down the center of a slotted cylinder. The slot is oriented to face the thermoplastic plate. The slotted cylinder and plate are grounded and the anode is raised to a potential of several kilovolts. The resulting electric fields ionize the surrounding air, producing electrons and positive ions. The electrons are collected on the wire which results in a positive charge on the slotted cylinder and the thermoplastic plate (Figure 2.7).

The detailed structure of the thermoplastic plate is shown in Figure 2.8. On a quartz substrate, an optically transparent electrode of indium-tin oxide is deposited on top of which a 1 μm thick layer of trinitro-fluorenone doped photoconductive organic polymer is placed and finally a 0.7 μm thermoplastic layer is added. Metal electrodes are attached to each side of the transparent electrode which provides a ground plane for the coronatron. A current passed through the transparent electrode produces resistive heating sufficient to soften the thermoplastic.

The cycle of events explained above is sequenced by a control unit supplied with the recording device. Dry nitrogen is used as the coolant for the thermoplastic plate in the erase process. This consists of reheating the thermoplastic to releive it of the surface contour variation and to produce a ripple free surface. Upon cooling, the plate is ready to be used again in the formation of a hologram.

2.2.7 Experimental Procedure

A schematic of the holographic interferometer used in this study is shown in Figure 2.9. It is a standard off axis holographic system. Proper choice of reference to object beam intensity ratio is important for producing the best holograms. With the use of the instant recording device, the quality of the hologram is insensitive to the exposure time. In the real time mode, the test specimen is illuminated in a state S_1 (say) with coherent light transmitted from the laser via the object wave path (this consists of the beam splitter, a beam expander-spatial filter, collimating lens). The corresponding load is $\mathbf{P}_1$ (refer to Figure 2.10). A hologram is then recorded by exposing the thermoplastic plate positioned at the junction of the reflected light and reference beam. Upon completion of the first exposure, the specimen, which is continuously loaded, is viewed through a camera attached to a VHS recording system (a VCR and a monitor). The resulting image consists of fringes which are dynamical in nature representing contour maps of the changes, with respect to the state S_1, of the out of plane displacement component w of the stressed specimen. These fringes, together with the load cell reading are recorded. The load cell reading is obtained by focussing the display of the voltmeter, exhibiting the load cell reading, at the position of the circular hole in the plane of the test specimen. With increasing load on the specimen, the fringe density becomes high, so that the resolution of the interferogram becomes poor. At this stage, a new hologram of the test specimen is made, and the above cycle of events is repeated. Thus, finally at the end of each experiment, an interferometric recording of the complete load-out of plane displacement history of the specimen is obtained. This sequence of events just described is shown graphically in Figure 2.10.

Each of the holographic interference fringe fields is related to the change in surface displacement of the specimen under load, by the vector expression

$$n\lambda = \tilde{k}.\tilde{d} \tag{2.1}$$

where,

n fringe number

λ wavelength of the coherent laser light

$\tilde{k}$ sensitivity vector $(\tilde{\imath}_2 - \tilde{\imath}_1)$

$\tilde{d}$ surface displacement vector at point of observation.

$\tilde{\imath}_1$ and $\tilde{\imath}_2$ are the unit vectors in the illumination and observation directions, respectively. In the present experimental setup the diffusely reflective surface of the specimen is oriented normal to the bisector of the angle 2α, between $\tilde{\imath}_1$ and $\tilde{\imath}_2$ (Figure 2.11). Thus, since the sensitivity vector, $\tilde{k}$, also points along this bisector, the interferometer senses only the out of plane displacement component w. Equation (2.1) then becomes

$$n\lambda = 2w cos\alpha$$

$$w = \frac{n\lambda}{2cos\alpha} \tag{2.2}$$

In the present experimental setup, the surface normal is 10^0 off the observation direction. With $\lambda = 0.633\ \mu m$, this shows that each fringe represents an out of plane displacement change of $0.321\ \mu m$.

A schematic of the present experimental set up is shown in Figure 2.12. During the entire loading program, the surface of the hole is viewed through a microscope at an oblique angle, and photographs are taken at various times. Due to the oblique viewing angle, the hole surface appears curved on the photo-micrographs, which will be discussed in the next section. A fiber optic cable attached to a high-intensity lamp is used to illuminate the hole surface. The interferograms displayed on the TV monitor is helpful in taking these photomicrographs interactively in an efficient manner.

The interferometric data reveal the changes in the w displacement component. These changes may be the manifestations of internal damage. Thus, some specimens were loaded to a post initiation level but were unloaded prior to catastrophic failure. The unloaded specimens were sectioned in the region of stress concentration and were examined under an optical microscope. In the following section, the results obtained from *interferometry*, *photomicrography* and *interior damage studies* are presented.

2.3 Results and Discussion

Tables 2.1 and 2.2 summarize the test conditions, and the results obtained. In these tables, "AS" for example, refers to type "A", small. P_i is the load at which failure initiates, as detected by the inteferometer. P_f is the failure load of the specimen. The interferometric data are presented only in the immediate neighborhood of the hole. The photomicrographs are only captured on one side of the hole surface as indicated in Figure 2.13. The horizontal shiny stripes appearing on the photomicrographs are 0^0 plies, while vertical lines are pencil marks for purposes of reference. The top edge of the hole surface appearing in the photomicrographs, marked 'AB' for example in the first frame of Figure 2.21a, corresponds to the intersection of the hole surface edge with the plate surface on which side the w component is measured interferometrically.

Consider now the different stages of failure as exhibited by the interferometric results and substantiated by the photomicrographs. In the pre-damaged situation, an increase in the load on the specimen results in a uniform pattern of fringes as shown in the first three frames of Figure 2.19a. These fringes are a few in number and correspond to the thickness changes due to the Poisson's ratio effect, coupled with some rigid body motion and/or slight bending. The rigid body motion and the bending cannot be totally avoided in a compression test. The slight bending may be the result of any initial imperfection in the specimen. Added to this, one must realize the high sensitivity of the measurement technique which is a function of the wave length of the laser light. (Displacement changes as small as 0.316 μm can be detected). In the discussion to follow, the responses of types A, B, C, and D specimen are considered separately. Then, the features of the failure process, that are common to all the laminate types, are summarized at the end. For ease of presentation, the T300/BP907 material system will be refered to as 'TB', while the IM7/8551-7 will be refered to as 'IM'.

2.3.1 Type B specimen

This type of specimen is one in which there are a fewer number of 0^0 plies (8.3%). Figure 2.14 shows a series of interferometric patterns, which correspond to the first instance at which internal damage was detected. The numbers below each picture represent the load in KN $\left((4.448\ x\ 10^3)^{-1} lbf\right)$ corresponding to each frame, while P_h indicates the load at which the hologram was made for that particular set of frames(*Reference load*). Notice the highly localized fringe cluster adjacent to the hole edge at approximately 90^0 to the loading direction. When any form of internal damage occurs that manifests itself as a localized perturbation in the normal displacement component w, the resulting interferometric patterns display this event as shown in Figure 2.14. A view of the hole surface corresponding to this fringe pattern is shown in frame 2 of Figure 2.15a. Notice the damage to the midplane 0^0 plies which appear as a black spot. Adjacent to this spot is a delamination crack. Inspection of the photomicrographs prior to this event revealed no damage to the hole surface. In *all* experiments conducted, it was revealed that a *perturbation* in the *interferometric data always corresponded to* 0^0 *ply damage at the hole surface.* This interferometric pattern is interpreted as a localized bulging of the surface just above the damage site. This localized damage to the 0^0 plies is found to be the triggering of extensive delamination cracking and localized buckling of the delaminated portions, that follows subsequently. The above sequence of events is consistently observed in all of the type B specimen. At this stage, it is pointed out that the word damage is used to describe any form of destruction to the specimen caused by the application of mechanical load as picked up on the interferograms. The interferograms corresponding to the initiation event reveal the displacements within the damage zone to be increasing with increasing load. This is clear by noting a sharp increase in the fringe density within the damage zone as loading proceeds. Subsequent to the initiation, the remaining 0^0 plies undergo failure while delaminations are seen to appear between various ply interfaces. An inspection of the sequence of photomicrographs in Figure 2.15a shows this. The delaminations undergo a stage of slow growth as shown in the next set of interferometric patterns (Figure 2.16a). Here the reference state corresponds to a load $P_h = 159$ kN, while the three frames span a load increase, ΔP of 1.73 kN. The displacement patterns extracted from the interferograms in Figure 2.16a, are shown in Figure 2.17. Here the displacements are measured with respect to displacements in areas remote from the hole edge. The origin of the axes is placed at the edge of the hole as indicated. The X- and Y-axes are scaled while the vertical Z-axes representing Δw is 1:1. The fringe patterns in Figure 2.16a reveal the displacements to be growing faster within the damage zone than the rest of the specimen. Further, the damage area is also seen to grow indicating that the delaminated portions are spreading outward approximately at right angles to the direction of applied load. The corresponding photomicrographs (Figure 2.15a) show the extent to which delamination cracking occurs. Notice the zero fiber breaks as well as the large (on the order of a ply thickness) mode I type displacements. These observations lead us to conclude that *delamination buckling* is the mechanism chiefly responsible for spreading of the damage to the undamaged areas of the plate. Once the delaminated portions reach a sizeable extent, an increase in the growth rate is noticed. This is shown in the last series of interferograms (Figure 2.18). In these the fringe density within the damage zone is very high, so much so, that the resolution of the interferogram within this area is poor. However, the manner in which these delaminations grow and respond can be deduced by follwing the fringe development within the damage area. This will be discussed later in the context of type A specimen. It must be pointed out that playback of the recorded video information displays a continuous transition in the fringe data which enables following the damage progression un-interrupted as opposed to the limited number of frames displayed here. The present discussion is influenced from such a knowledge. The culmination of the last growth event is the complete loss of flexural stiffness of each of the delaminated portions, leading to catastrophic failure. These findings and conclusions are drawn from the consistency with which these failure events occur in all type B specimen. Figures 2.19a through 2.20d depict the same information obtained interferometrically of events leading to failure as described for specimens of the IM series. The corresponding photomicrographs are shown in Figures 2.21a and 2.21b.

The interferometric patterns displayed in this thesis can be categorized into three typical patterns. These patterns are typical of the vast amounts of frames accumulated on video-tape for each test. The first type was displayed in Figure 2.16a and the corresponding displacements summarized in Figure 2.17. The next type of fringe patterns are shown in Figure 2.19c. Here, it is noted that Δw displayes more than one half wave in the radial direction, characteristic of plate buckle mode shapes. The third type of fringe pattern is as shown in Figure 2.20a, set (ii) and Figure 2.41c (lower half of the frames displayed). These patterns and corresponding normalized displacement profiles are schematically illustrated in Figure 2.21c. There is some difficulty with extracting Δw from the fringe patterns just referred to, due to a loss of resolution in the optical train that transfers the data from the hologram to the data displayed here. This situation was somewhat remedied and will be discussed in the context of type A specimen.

It was felt that the 0^0 ply damage observed in the preceeding section warranted further examination. As such, some specimens were loaded into the post initiation level but unloaded prior to catastrophic failure. In particular, the specimen, whose interferometric results were discussed earlier, was unloaded near its ultimate failure load and sectioned for further study. An enlarged view of the black spot appearing in the photomicrographs is shown in "A" of Figure 2.22a. Notice that a part of the picture is out of focus. This is because the fibers in that region have jutted out of the plane of the hole surface (plane of the picture). Examination of similar damage to other 0^0 layers revealed the same type of jutout failure. In Figure 2.22b, a similar result, obtained from a scanning electron microscope is shown for a IM series specimen. Notice clearly, that all the 0^0 plies have undergone failure. Also, a matrix crack is seen to run across the 90^0 ply, originating from the mid-plane 0^0 ply failure.

It was also of interest to determine the extent to which the hole surface damage propagated into the interior of the specimen. The laminate was sectioned at different locations as indicated in Figure 2.23. Magnified views of the 0^0 layers at sections

"E" and "D" are shown in Figures 2.22a and 2.24. Notice the dark regions showing broken fiber segments scattered at different angles. In "D" an undamaged portion of the midplane 0^0 layer is shown contrasted against a damaged portion which clearly indicates a characteristic pattern. Here, a V-shaped matrix rich area, within which the fibers have undergone rotations, is clearly visible. The maximum width of the V-shaped zone measures to be approximately 0.3 *mm*. The matrix rich portion in the bottom right hand picture is seen inclined at an angle of 65^0 to the 0^0 fiber direction. These characteristic patterns of failure have collectively been referred to as *fiber kinking* in the literature. This type of kinking failure has also been observed in other studies dealing with compressive strengths of laminates (see for example ref.[2.9]-[2.11]).

Sectioning beyond cross-section "D" and inspection under the microscope revealed no further damage. Similar inspection to other specimen loaded to levels just prior to catastrophic failure revealed that the damage zone was contained within about one hole radius distance from the edge of the hole. Similar sectioning studies and results for an IM series specimen are shown in Figures 2.25a and 2.25b. Notice again, the delaminated crack adjacent to the 0^0 ply failure in (B) of Figure 2.25b.

Planform views of the damaged midplane 0^0 layer as obtained by mechanical polishing are shown in (a) of Figure 2.26. Here we note the matrix rich damage zone which measures in width to approximately 70 fiber diameters (0.5 *mm*). Closer examination of the edge of the damage zone, near the hole, revealed that the fibers had undergone rotation in the plane of the picture. Thus, in this zone, the fibers have not only undergone rotations in the XY-plane, but also in the XZ-plane as indicated by the sectioning studies earlier. Similar results were obtained from the deplying study, which consists of heating the damaged samples to about 600^0 F and removing ply by ply to observe internal damage. Shown in Figure 2.27a and 2.28b are C-scan maps of specimens loaded up to about 65% and 80% of their failure loads, respectively. These scans are planform views of the integrated through thickness damage. Here a clear resemblence between the shape of the damaged area and the portion of the interferometric patterns that contain a very high fringe density is noticed.

2.3.2 Type A specimen

These specimen have a higher number of 0^0 layers (42%) than type B. Figures 2.29 and 2.30 show a series of interferograms corresponding to the failure initiation event and immediately thereafter. A sharp localized cluster of fringes is seen to form at the edge of the hole which spreads very rapidly with a small increase in load. It is seen that the area in which the fringes are unresolvable extends out to about 80% of the hole radius, from the hole edge. The corresponding photomicrograph is shown in frame 2 of Figure 2.31 (corresponds P=129 kN). Here a single 0^0 ply failure remote from the front surface of the specimen is visible. The interferometer detects this internal damage. A fringe count of frame 5 in Figure 2.29 reveals a w displacement change of approximately 6-10 μm at the hole edge, perpendicular to the direction of applied load. This displacement is on the order of a fiber diameter (7 μm). In the last frame of this sequence, the fringe density at the hole edge is too high, precluding any possibility of a fringe count. With increasing load, surface buckle formation on the other edge of the hole, approximately at 90^0 to the loading direction, is found to occur. This event is shown in the series of interferograms that are displayed in Figure 2.32. The buckle formation occurs very rapidly and, as indicated in the figure the duration between the last two frames is 0.1 seconds. Inspection of the photomicrographs shown in Figure 2.31 reveals the manner in which progressively the remaining zero layers fail with increasing load. Adjacent to some of the damaged 0^0 plies, delamination cracking is found to occur. A picture of the damaged, unloaded specimen is shown in the last frame of Figure 2.31. A similar pattern of failure is displayed by several other specimen, and a sequence of such photomicrographs is shown in Figures 2.33,2.34a and 2.34b. In Figure 2.33, the first 0^0 fiber failure occurs at 124 kN, close to the front edge of the specimen, and is shown in the third frame of the montage of pictures. The fourth frame, corresponding to several zero ply failure and the formation of a *surface buckle,* is designated the time T=0 seconds. The subsequent progression of failure leading to catastrophic failure is shown in the next series of frames, with the final disintegration of the specimen occurring within about one minute subsequent to frame 4. Notice the damage to all 0^0 plies, and the formation of surface buckles on both surfaces of the specimen.

In many of the interferometric sequences discussed so far, it was found that fringe resolvability was poor close to the hole surface. This is because the displayed pictures are shot off of a TV monitor screen, after being recorded on standard video-tape and re-played. The thermoplastic plate has a resolution at maximum diffraction efficiency of 800 lines/mm (or 800 x 30 full screen, assuming no spatial variation [2.16]) but the resolution of the optical system is controlled by the component with the poorest resolving capability. In this case, it is the VCR, which is capable of only retaining 240 lines per frame at best. At maximum fringe density this is a reduction by a factor of 100. However, in practice, speckle size and other limitations have to be accounted for in order to assess an accurate measure for this reduction factor [2.14,2.15]. Thus, for high fringe densities, some picture quality is lost in this process. To check the regions of high fringe density, the recording procedure was modified by placing a beam splitter behind the thermoplastic plate and taking pictures of the interferograms using a 35 *mm* SLR camera, while still recording on the VCR. A sequence of such interferograms showing the final stages of failure of a type A specimen is shown in Figure 2.35. The fringes on the top half of the pictures display a continuous variation in w. Further, the fringe gradient is seen to rapidly decrease away from the hole edge. A fringe count of frame 3 reveals a w displacement change at the hole edge of 10 μm. These pictures display a superior resolution to those taken off of the TV monitor. However, to adopt this method for the entire duration of a test would not be cost effective. What is important here is to compare the fringe patterns to those taken off of the TV screen. It is seen that the areas in which the fringes were unresolvable earlier could be smoothly extrapolated from the areas in which the fringes are resolvable. In this figure, it is also seen that a surface buckle is already formed on the bottom half of the specimen. This damage is contained within a distance of approximately half a hole radius. The sequence 1-4 depicts the formation of the buckle on the top half of the specimen which is found to be the last event prior to catastrophic failure. These pictures were taken with an exposure time of approximately 1 second with the duration between frames approximately 2-3 seconds.

Bearing in mind the information obtained from the surfaces of the specimen, we now turn to a discussion of post experiment sectioning studies. Shown in Figure 2.27b and 2.28a are C-scan maps of damaged specimen. In Figure 2.27b, the extent of the damage area is contained within about a hole radius. The damaged area in these figures depends on the load at which the specimen was unloaded. This information is given in Tables 2.1 and 2.2. In Figure 2.36(a) a typical section through this damaged area is shown. Here the interior 0^0 layers show several inclined narrow zones of fiber breaks, identified as *fiber kink bands*. A typical complimentary kink band is shown in Figure 2.36(b). We note here a kink band inclination of 65^0 to the load carrying direction. The lengths of the fibers in the inclined zone measures to 50-84 μm. More importantly it is pointed out that the region between the inclined zone appears undamaged and oriented parallel to the fiber direction. The geometry of the kink band is summarized in Figure 2.37. In this figure, the notation used to describe a typical kink band from Evans et al. [2.10] is also included. In that study, carbon fiber bundles of width $\approx 400\ \mu m$ oriented in three orthogonal directions were set in a graphite matrix and subjected to localized impact. Post-experimental examination revealed typical *kink orientation* angles α of 45^0 - 60^0 and kink boundary orientation β obeying $\beta \approx \frac{\alpha}{2}$ for broad$(\frac{l}{d} \geq 0.1)$ kinks. Here β is measured from the ***perpendicular*** to the fiber direction. For narrow kinks, β was found to increase and α was found to be random. Corresponding results in our study which fall into the category $\frac{l}{d} \geq 0.1$ indicate $\beta \approx 25^0 - 30^0$ and $\alpha \approx 15^0 - 30^0$. However, no definite trend between α and β can be established.

From the photomicrographs presented earlier (type A), it was observed that the outermost plies of the laminate underwent large displacements in the buckling process leading to fiber breaks. A magnified view of such a fiber break is shown in Figure 2.36c. It was of interest to examine the propagation of the initial fiber kinking failure into the interior of the specimen. This was done by sectioning at several positions and following the damage of a typical 0^0 ply. The results thus obtained are shown in Figure 2.38. Notice that the appearance of the kink is unaltered at several different cross sections. Further, the same type of geometry as found before is seen to prevail with an area of undamaged fibers between two inclined bands of damaged fibers which have undergone rotation in the XZ-plane. The lengths of the fibers in the damage zone are comparable to those seen before. Similar results for a typical IM series specimen is shown in Figure 2.39. A planform view of such a damaged 0^0 layer is shown in Figure 2.36(b) and (c). The damage zone width is approximately 0.27 *mm* (38 fiber diameters). Here we note the fiber jutout failure at the edge of the hole. The damage zone appears dark as the fibers in this area which are broken and kinked out of plane were polished off during preparation of the specimen for microscopic examination. Results from an IM series type A specimen is shown in Figure 2.39. Finally in Figure 2.40, the outer layer delamination crack at two different cross sections is shown. Note here that the root of the delamination crack originated from the buckled 0^0 ply.

2.3.3 Summary of Common Features of Failure for Types A and B.

In this section, we summarize the results presented so far and try to identify features that are common to types A and B laminates.

In both, types A and B, the failure is initiated by a 0^0 fiber failure at the hole edge approximately at right angles to the loading direction. In type A, with increasing load more 0^0 fiber failure is seen to occur with simultaneous surface delamination buckling. These events occur very close to the catastrophic failure load. In type B, subsequent to 0^0 fiber failure, which occurs at around 75% of the ultimate failure load, gradual development of delamination cracking is observed, with the outermost delaminated sections undergoing buckling. In both types, the delaminations are seen to grow with increasing load. *delamination buckling* is found to be the mechanism responsible for the spreading of the damage. When the delaminated portions grow to a critical size, approximately on the order of 75-100% of the hole radius, an accelerated growth of the delaminations is observed. At this time, the specimen fails catastrophically.

The mechanics of the 0^0 fiber failure, which shows up at the hole edge and is captured by the interferometer, is found to be a localized microbuckling/fiber kinking. Information regarding fiber kinking published elsewhere and here, have been obtained once the damage has taken place and the structure loaded into a post-damaged state. Qualitative information regarding the pre damaged state, from the interior of the structure, is difficult to obtain as these systems are opaque. Furthermore, the development of delaminations which underwent delamination buckling warranted further examination. To address these questions, it was decided to experiment with a laminate that had a simpler stacking sequence but still exhibited similar ply orientation to types A and B. The idea was to reduce the number of different interfaces (ie., an interface between two dissimilar plies) but to still maintain the overall laminate thickness. Thus, each ply group was clustered into groups of six, leading to types C and D. Therefore, type D for example, had a group of twelve 0^0 plies sandwiched in between the outer angle plies of [+45/-45] (see Table 2.3).

2.3.4 Type C specimen

This type of specimen has 25% of 0^0 plies. Shown in Figure 2.41a is the first instance at which a perturbation in the fringe pattern was detected. These patterns contain a gradually increasing fringe density as the edge of the hole is approached from the far field. A fringe count for frame 2 reveals a Δw greater than $4 \mu m$. The corresponding photomicrograph is shown in frame 4 (at a load of 82.1KN) of Figure 2.42. Notice the black spot appearing on one of the clustered 0^0 ply groups. The frame prior to this, however, at 78.1 KN, reveals some damage occurring within the 0^0 plies which did not give rise to any anomaly in the fringe distribution. Thus, in this case, the appearence of a black spot on the photomicrograph did not correspond to localized bulging as before. To investigate this further, a similar specimen was loaded (IM22) up to 135.7 KN and then unloaded prior to any detectable damage on the interferometer. Next, a careful examination of the hole surface was carried out. A magnified view of the isolated 0^0ply cluster is shown in (ii) of Figure 2.51. This figuire reveals the typical jutout failure as noticed before for types A and B, apart from the fact that the 0^0plies remain aligned regularly implying a smooth separation as opposed to signs of an abrupt occurrence. Next, the specimen was sectioned at 0.5 *mm* away from the hole edge and inspected under an optical microscope. This inspection revealed no damage to the 0^0 ply cluster. Thus, it is seen that the fiber jutout failure in these specimens develops gradually with a few layers of surface fibers participating. Next, when the external load reaches a critical value, 0^0 *fiber microbuckling* is seen to occur; this damage propagates away from the hole edge. This introduces a zone of damaged fibers within the 0^0 plies, which in turn causes the (+45/-45) plies immediately above this zone to bulge out of the plane. This event is picked up on the interferometer. As the loading proceeds, the damaged area spreads in the form of planar (x-y plane) delamination cracks and causes local buckling of delaminated ply groups. These events are displayed interferometrically in Figures 2.41b and 2.41c. The corresponding photomicrographs are shown in Figure 2.42. In Figure 2.41c, the damage development on the bottom half of the specimen is shown. Notice clearly, that the initiation of damage leads immediately to localized buckling. The fringe patterns are as discussed before (see Figure 2.21c). A circumferential wave form characteristic of buckle mode shapes in plate buckling problems is indicated. Photomicrographs showing the events just described for a different specimen are shown in Figure 2.43.

Specimen IM15 was unloaded prior to catastrophic failure and was C-scanned. The C-scan map is shown in Figure 2.28 (c). Notice the planar delaminated area which resembles the area of high fringe density in Figure 2.41c. Next, this specimen was polished mechanically and inspected under an optical microscope. The resulting damage in the x-y plane of the specimen is indicated in Figure 2.44. Notice the damage zone within the 0^0 plies that originated at the hole edge and propagated into the interior of the specimen.

2.3.5 Type D specimen

The 0^0 ply percentage of type D is the same as for type C (25%). The sequence of events leading to failure is similar to that described for the type C specimen, except for two of the specimens (IM12 and IM14-see Table 2.2). These specimens failed abruptly without prior indication of fiber microbuckling. Inspection of the photomicrographs for these specimens indicated that the fiber jutout failure on the hole surface developed gradually. Thus, the value of P_i, quoted in Table 2.4 for these specimens correspond to the first occurrence of the jut-out failure, as obtained from the photo-micrographs. However, since the photo-micrographs are taken discretely, the actual value of load at this occurrence lies between 65.6 KN and 74.3 KN for IM12 and 68.1 KN and 75.4 KN for the IM14. Shown in Figure 2.45 are a series of interferograms indicating the localized buckling of a delaminated portion subsequent to initial failure for this type of specimen.

Figures 2.46,2.47 and 2.48 show a series of photo-micrographs that show the gradual development of failure. Notice that subsequent to the 0^0 ply failure, delamination cracking within the the 0^0 ply cluster is observed. To investigate the spreading of these delaminations and the extent of the propagating microbuckling failure, specimen IM23 whose photo-micrographs are shown in Figure 2.48 was unloaded at an applied load of 150.1 KN. Next, this specimen was C-scanned and the damaged area is as indicated in (d) of Figure 2.28. As before, the delaminated planform area extends out to about 75% radius of the hole.

This specimen was then mechanically polished, sectioned and inspected under an optical microscope. The findings are shown in Figure 2.44. The narrow zone of local fiber failure in the XY-plane extends outward from the hole edge. Notice the large fiber rotations in the XY-plane. In (c) of Figure 2.49, the jutout failure of the hole surface is presented in two pictures. These pictures complement each other in that the areas which appear unfocussed in one picture, appear focussed in the other. This is because a part of the 0^0 plies have lifted off the surface of the hole (surface of the figure).

Shown in Figure 2.50 are the results of the sectioning study. Some of the pictures presented here were obtained through a scanning electron microscope. Notice a narrow zone of damaged fibers that runs across the entire thickness of the clustered mid-plane 0^0-plies (12 of them) at section A-A. This zone measures approximately $59.5\mu m$ (or 12 fiber diameters). The SEM photos at different sections also show that the fibers have undergone undulations that form as inclined bands of broken fiber segments. Following the notation introduced in Evans et al. [2.10] , which is indicated in Figure 2.37, it is found that for the kink band shown in Figure 2.50, $\frac{l}{d} \approx 12$, while $\alpha = 84^0$ near the lower end marked 'E' and $\beta = 9^0$. Near the end 'D', $\alpha = 72^0$, while $\beta = 12^0$. From the SEM photos, it is seen that the damage zone extent is $\approx 32\mu m$ at section G-G, $\approx 35\mu m$ at B-B and $\approx 32\mu m$ at section F. With a fiber diameter of $5\mu m$, the damage zone width (synonymous with 'l' marked in Figure 2.37) is found to be approximately $\frac{l}{d} \approx 7$, implying a *short wave-length instability.*

2.3.6 Summary of Experimental Findings

Damage patterns typical of those observed in the XZ-plane are summarized in Figure 2.52. A 3-d view of the damage to a 0^0 ply is summarized in Figure 2.53. The 0^0 ply microbuckling/kinking which occurs, both in plane (XY) as well as out of plane (XZ), is found to originate at the hole surface and persist well into the interior of the specimen. This causes a narrow zone ($\frac{l}{d} \approx 7-12$) within the 0^0 plies to lose structural integrity. *Continuous viewing* of the recorded videotapes shows the surface manifestation of this event as a well defined cluster of fringes originating at the hole edge and propagating rapidly away from the hole.

Some of the IM series of specimens were mounted with surface strain gages. This work is described in Appendix 2A at the end of this chapter. From the strain gage measurements, it was found that the microbuckling failure for the IM series of material originated at a localized strain level of $\approx$ 8600 μstrain measured at the hole edge (see Figure 2.54 for strain gage locations). The origination of fiber kinking at a free edge and its subsequent propagation into the interior of the structure has been reported before in a different context. We cite here the of work of Chaplin [2.9] and Hahn et al. [2.11].

The initiated damage leads to the formation of delamination cracks. The through thickness locations of these are found to depend on the position of the 0^0 plies as shown on the photo-micrographs. In type A, for example, the initiation event leads immediately to delamination buckling/growth resulting in complete failure. In type B, the delaminated portions undergo an initial phase of slow growth until reaching a critical delaminated area. Then, delamination buckling is found to occur. This leads to further growth/buckling, which culminates in catastrophic failure. In types C and D, the failure is similar to that of type B.

From the table of results presented for the IM series (see Table 2.2), where the results for the 'small' specimen have been grouped according to type, the average initiation and failure loads can be calculated. These are presented in Table 2.3. Since some specimens were unloaded prior to final failure, the number of data points used to compute P_f is lesser than the same for P_i. A similar procedure was not followed for the larger specimens, as data for the type 'AL' is lacking. This is because, this laminate demands high load values at failure (the table top compression device has a maximium load capacity of 222 KN) which are in excess of the loading device's capacity. From the results in Table 2.3, it is seen that the load carrying capacity of a laminate, beyond initiation, is dictated by the 0^0 ply percentage within the laminate. Indeed, a larger percentage of 0^0 plies leads to a 'stiffer' laminate which fails in a 'brittle' fashion (initiation and final failure loads are close to each other). As the percentage of 0^0 plies are reduced, the laminate is seen to fail in a 'ductile fashion' (initiation and final failure are not close, this being dictated by the percentage of 0^0 plies). Thus, it is seen that beyond failure initiation by microbuckling, the delamination buckling/growth phase is influenced by the overall laminate stiffness.

However, *common* to *all* the laminates tested in this investigation is the level of *localized strain* at which initiation occurs. This initiation strain can be used as a useful design guide, since for all practical purposes, once 0^0 ply failure has occured, it is reasonable to deem the laminate as being unsafe. A mechanical model for the initiation problem is formulated in chapter 4.

2.4 References

2.1 Starnes, J. and Williams, J.G. (1982)," Failure characteristics of Gr/Epoxy struc tural components loaded in compression ", NASA TM 84552.

2.2 Rhodes, M., Mikulas, M. and McGowan, P. (1982),"Effect of orthotropic properties and panel width on the compression strength of Gr/Epoxy laminates with holes", AIAA Paper No. 82-0749.

2.3 Shuart, M.J and Williams, J.G. (1986), "Compression behaviour of [+45/-45] dominated laminates with a circular hole or impact damage", *AIAA J.*, Vol. 24, pp115

2.4 Knauss J., Starnes, J. and Henneke, E. (1978), "The compressive failure of Gr/Epoxy plates with circular holes", NASA CR 157115, N78-24295.

2.5 Mikulas, M. (1980), "Failure prediction techniques for compression loaded composite laminates", NASA CP 2142.

2.6 Babcock, C.D. and Waas, A.M. (1985), "Effect of stress concentrations in composite structures", GALCIT SM Report 85-12.

2.7 Rosen, B.W. (1965), "Mechanics of composite strengthening", *Fiber Composite Materials*, Am.Soc. for Metals Seminar

2.8 Schuerch, H. (1966), "Prediction of compressive strength in uniaxial Boron fiber metal matrix composite materials", *AIAA J.*, Vol. 4, pp102-106

2.9 Chaplin, C.R. (1977), "Compressive fracture in uni-directional glass reinforced plastics", *J. of Mat.Science*, Vol. 12, pp347-352

2.10 Evans, A. and Adler, A. (1977), "Kinking as a mode of structural degradation in carbon fiber composites", *Acta Metallurgica*, Vol. 26, pp725-738

2.11 Hahn, H. and Williams, J.G. (1984), "Compression failure mechanisms in unidirectional composites", NASA TM 85834.

2.12 Budiansky, B. (1983), "Micromechanics", *Computers & Structures*, Vol. 16, pp3-12

2.13 Chai, H. (1982), "Growth of impact damage in compressively loaded laminates", P.hD thesis, California Institute of Technology.

2.14 Vest, C.M. (1979), *Holographic Interferometry*, Wiley

2.15 Pfaff, R.D. (1987), private communication, California Institute of Technology.

2.16 Owners Manual-HC300,301 (1985), Newport Research Corporation, Ca., USA

Appendix 2A

Strain Gage Results

It was desirable to obtain the local value of strain at which microbuckling occurred. To do so, some IM series specimen were mounted with standard foil strain gages as indicated in Figure 2.54. The strain gages were connected to a Wheatstone bridge in a single active gage configuration, and at each location back to back gages were placed to obtain both the in-plane axial strain in the direction of applied load as well as the bending strain. Initially, the data was acquired manually for specimen IM18 through IM22. This procedure was somewhat cumbersome in that the loading had to be temporarally held constant for the data aquisition. Therefore, an in-house computer was programmed to do this task. The gage outputs from the Wheatstone bridge were sent through an amplification stage and fed into the 'North Star' system [2.17]. The data was then transfered to VAX 11/750 for manipulation.

Figures 2.55 through 2.69 show the Load (KN) vs Compressive μ-strain ($\frac{cm}{cm}$ x 10^6) plots for specimen IM18 through IM32. Consider Figure 2.62, corresponding to specimen IM28. In this figure, the response of the strain gages, near the hole edge (Figure 2.62 (a)), and at far field loactions A and B (Figure 2.62 (b)), are shown. An example of a poorly bonded strain gage is shown here (gage 3). Consider Figure 2.62(a). Here, as the far-field load increases, the strains are seen to increase linearly. When the load reaches P_i (corresponding to microbuckling of the 0^0 plies), the load vs strain behaviour shows a kink (marked 'A'), implying a localized softening. With failure of other 0^0 plies, the softening continues (marked 'B'), until reaching 'C', when strain reversal is detected on one gage. This reversal occurs because the delaminated portions closest to the surface on which the gage is attached undergo *buckling.* The buckling which causes large bending strains results in tensile strains on the outer surface, causing a net reduction in the compressive strain.

One drawback in the present work is the lack of data aquisition channels to record several gages simultaneously. This could have been overcome by using a multiplexer and analog to digital converters for each gage, but, time constraints have thwarted aquiring a complete data base. This investigation is, therefore, preliminary, and it is hoped to be continued in the near future.

Accurate readings for the failure initiation could only be obtained when initiation occured on that side of the specimen which contained strain gages. This is because, strain gages were mounted only on the positive quadrant as indicated in Figure 2.54. Test results at failure initiation are shown in Table 2.4. Each pair of columns in this table, starting from column 2, report averaged values of the back to back surface gages and the corresponding bending strain at failure initiation. Some specimens were not mounted with strain gages at every location. This is indicated as a 'blank' in Table 2.4. A '*' idicates a non-inclusion of a reading due to a poorly bonded strain gage response such as shown earlier.

Shown in Figure 2.59 is the strain vs load response at the hole edge for a specimen when initiation occured at a load of 60 KN. Notice the gradual strain reversal that occurs with continued loading due to buckling of the delaminated portions. A similar behaviour is observed in other specimens. In Figure 2.68, for example, (spec. IM23, whose photomicrographs are presented in Figure 2.48) the initiation of damage is clearly indicated at the point marked 'A', with strain reversal occurring subsequent to this. The detection of the softening behavior from the strain gages entirely rests on the local reduction in axial stiffness due to the 0^0 ply microbuckling failure. This reduction is dictated by the number of 0^0 plies that undergo damage.

From table 2.4, the critical values of strain at which microbuckling occurs can be extracted for each specimen type. In each case, only those specimen that had strain gages mounted on the side in which microbuckling occurred will be considered. Thus, specimen IM20 and IM21 from type A, IM28 from type B, IM31 from type C and IM30,27 and 23 from type D will be considered. The results for the average microbuckling strain for each specimen type are listed in Table 2.5. Notice that specimen type D has a much lower initiation strain than types A,B and C. An explanation follows.

The microbuckling failure in type B (see Figures 2.21a and 2.21b) occurs in the mid-plane (z=0). Thus, the bending strain at the hole edge does not influence the computed average axial strain. In type A (see Figures 2.34a and 2.34b) one or several 0^0 plies fail simultaneously, and there is no trend as to the through thickness location of the failed 0^0 plies. However, in type C (see Figures 2.42 and 2.43), there are two discrete locations corresponding to the through thickness position of the clustered six 0^0 ply groups at which microbuckling can occur. Thus, the bending strain has to be taken into account when considering the failure initiation strain for these specimens. With this consideration, and assuming a linear variation in strain through the thickness, the value of 9020 μstrain quoted in Table 2.7 for type C is corrected as 9020±351. In type D (see Figure 2.46 through 2.48), most of the centered twelve 0^0 plies participate in the failure process. The reason for the lower failure strain can be understood by inspecting Figure 2.50. There one sees the appearence of a relatively thick matrix interlayer between each individual ply in the mid-plane 0^0 ply cluster which is seen in supported by the cross-sectional photograph marked section A-A. The effect of this matrix rich layer is to lower the effective fiber volume fraction of the ply group considered as one unit. As will be seen later, in chapter 4, this reduction is detrimental to its compressive strength, leading to a lowering of the buckling strain.

In summary, it is seen that the local value of the averaged axial-strain at the hole edge at which microbuckling occurs is given by $8555 \leq \epsilon_{x_{cr}} \leq 8789$ for the types A,B and C specimens. A plausible explanation has been forwarded for the low strain value recorded for the type D specimen.

Mounting of gages on both sides of the cutout, as well as attainment of a large data base, are needed before a stronger conclusion can be made. This work is to be completed in the immediate future.

CHAPTER 3.

GENERALIZED PLANE STRESS ANALYSIS FOR LAMINATE

3.1 Introduction

In the introductory chapter of this thesis, it was shown (by starting from the basic building block (a uni-directional lamina)) how a useful structural laminate (the end product) can be achieved. In following this path of presentation, the reader was made aware of available analysis capabilities that have attached themselves to each stage of the development process. It was pointed out that apart from a few shortcomings, such as our collective ignorance of the interlaminar stress components (a direct manifestation of the assumption of a plane stress state within each lamina), *Classical Laminated Plate Theory*, hereafter referred to as CLT, plays an essential role in obtaining solutions to the *macroscopic* (or average) behavior of the laminate. By macroscopic, it is meant a level of discretization that ignores the detailed structure of a single uni-directional lamina but still, one which retains the non-homogeneous nature of the composite in the thickness direction. Thus, CLT treats each layer of the composite laminate as being a single layer of homogeneous and anisotropic material whose equivalent properties in terms of the constituents (fibers and matrix) are found by the rule of mixtures. Following CLT, the relations between the inplane stress resultants and inplane strains can be conveniently derived along with the moment-curvature relations . These are presented in Appendix 3A for each type of laminate used in this work. Once these relations are obtained the entire laminate can be characterized as being a single anisotropic and homogeneous structural element. While a complete account of

CLT is beyond the scope of this thesis, it is pertinent to point out that an important assumption in CLT is that each *lamina* of the laminate is in a *planar state of stress.*

The chief violators of this assumption, the stress components σ_{xz}, σ_{yz} σ_{zz}, (z being the coordinate in the thickness direction) are found to persist in a singular fashion at a narrow boundary layer on the order of a *lamina thickness* close to any free edge of the laminate. This result known as the free edge effect has been the topic considered by many a researcher. This effect was first exemplified by Pipes and Pagano [3.6] who considered a particular boundary value problem and used the finite difference method to obtain a numerical solution (see [3.5]). This problem was re-considered recently by Wang[3.5], who used linear elasticity theory to analyse each layer of the lamina and obtained a formal solution. In the period in between, other researchers [3.8-3.19] have introduced various levels of sophistication in an attempt to establish the usefulness of knowing the detailed three dimensional stress field within the boundary layer.

The presence of a singular stress field at a free edge is not surprising as it is well known that a stress singularity exists at the intersection of an interface (ie., the common boundary between two distinct materials along which continuity of tractions and displacements hold) with a free boundary (Bogy [3.7]). However, to obtain the complete solution to a boundary value problem, using anisotropic elasticity theory to analyse each lamina, for a laminate containing several lamina is a lengthy and cumbersome process. Indeed, it is fair to say that such analytical solutions exist only for very special cases of simple loading and geometry. In the present day, the use of numerical techniques such as finite elements and finite differences play a major role in characterising the free edge effect in composites. What must be kept in mind, however, is that in modelling the composite as consisting of alternative layers of different materials, an artificially abrupt change of properties across an interface is introduced. In a real laminate used in the structural laboratory, such an abrupt change is not present. One is likely to find a continuous but rapidly varying function of the material properties through the thickness. However, an exact description of such a variation would have to incorporate information on a microscale, ie., on the fiber-matrix level within each lamina, and this is not easily amenable to analytical description. Thus, due to a lack of better modelling capability, it is assumed that the layers are perfectly bonded along a common interface, entailing an abrupt change in mechanical properties across an interface. This produces a singular state of stress at the free edge/interface intersection deduced from a *linear elasticity* analysis. Away from the free edge, ie., on the order of a lamina thickness, the CLT results are found to prevail. The reader is referred to articles by Salomon[3.22], Wang[3.5] and Raju[3.13], for an exhaustive description of anlytical and numerical work on the free edge effect as related to lamina reinforced composites.

In this chapter, the 48-ply laminate containing a circular hole is modelled along the lines of CLT as an equivalent and homogeneous anisotropic plate. Then, by dimensional considerations where the width and length of the plates are several times the hole diameter, the two-dimensional stress state of an infinite, homogeneous and anisotropic plate containing a circular cutout and subjected to a remotely applied planar state of compressive stress is developed (Figure 3.1). The solution will proceed within the framework of linear elasticity theory with the approximation of *generalized plane stress*, where it is sought to characterize the thickness averaged stress components, $\sigma_x, \sigma_y, \sigma_{xy}$, and the inplane displacement components, u and v, which are functions of only the inplane coordinates x and y. An outline of the method will be given along the lines of Lekhnitskii [3.1] who treated the analgous problem for an elliptical cutout. The solution presented in Lekhnitskii[3.1] will be used and specialized to the case of a circular hole.

3.2 Solution Outline

Defining the problem cordinates as in Figure 3.1, the equlibrium equations are, in the absence of body forces,

$$\begin{aligned} \frac{\partial \sigma_x}{\partial x} + \frac{\partial \sigma_{xy}}{\partial y} = 0 \\ \frac{\partial \sigma_{xy}}{\partial x} + \frac{\partial \sigma_y}{\partial y} = 0. \end{aligned} \tag{3.1}$$

With the assumption of small deformations, the strain-displacement relations are,

$$\begin{aligned} \epsilon_x = \frac{\partial u}{\partial x}, \qquad \epsilon_y = \frac{\partial v}{\partial y} \\ \epsilon_{xy} = \frac{\partial v}{\partial x} + \frac{\partial u}{\partial y}. \end{aligned} \tag{3.2}$$

Then the single equation describing the compatibility between the three strain components ϵ_x, ϵ_y, ϵ_{xy}, is given by,

$$\frac{\partial^2 \epsilon_x}{\partial x^2} + \frac{\partial \epsilon_y}{\partial y} = \frac{\partial^2 \epsilon_{xy}}{\partial x \partial y}. \tag{3.3}$$

The coordinate axes are chosen conveniently to coincide with the axes of orthotropy of the laminate. With this choice, the ***strain-stress*** relation is

$$\begin{aligned}\epsilon_x &= \frac{\sigma_x}{E_x} - \frac{\nu_{yx}\sigma_y}{E_y}\\ \epsilon_y &= \frac{\sigma_y}{E_y} - \frac{\nu_{xy}\sigma_x}{E_x}\\ \epsilon_{xy} &= \frac{1}{G_{xy}}\sigma_{xy}\end{aligned} \tag{3.4}$$

with,

$$\frac{\nu_{xy}}{E_x} = \frac{\nu_{yx}}{E_y}.$$

A stress function $F(x, y)$ defined in the manner described below is chosen such that (3.1) is satisfied identically.

$$\begin{aligned}\sigma_x &= \frac{\partial^2 F}{\partial y^2}\\ \sigma_y &= \frac{\partial^2 F}{\partial x^2}\\ \sigma_{xy} &= -\frac{\partial^2 F}{\partial x \partial y}.\end{aligned} \tag{3.5}$$

Using (3.5) and (3.4) to express the strains in terms of F and then substituting for the strains in (3.3) the following equation is obtained.

$$C_2 \frac{\partial^4 F}{\partial x^4} + C_1 \frac{\partial^4 F}{\partial^2 x \partial^2 y} + \frac{\partial^4 F}{\partial y^4} = 0, \tag{3.6}$$

where the constants C_1 and C_2 are given by,

$$\begin{aligned}C_1 &= \frac{E_x}{G_{xy}} - 2\nu_{xy}\\ C_2 &= \frac{E_x}{E_y}.\end{aligned} \tag{3.7}$$

In the isotropic case, $C_1 = C_2 = 1$ and (3.6) reduces to the well known bi-harmonic equation for the Airy stress function-F. (3.6) is expressed symbolically with the use of four linear differential operators of the first order,

$$D_i = \frac{\partial}{\partial y} - \mu_i \frac{\partial}{\partial x}, \qquad i = 1, 2, 3, 4$$

as,

$$D_1 D_2 D_3 D_4 F = 0, \tag{3.8}$$

where, μ_i are the roots of the characteristic equation associated with (3.6), namely

$$\mu^4 + (\frac{E_x}{G_{xy}} - 2\nu_{xy})\mu^2 + \frac{E_x}{E_y} = 0. \tag{3.9}$$

The quantities μ_i are called *complex parameters*. These can be considered as numbers which characterize the degree of anisotropy in the case of plane problems. Their values give a measure of departure from the isotropic case, for which always $\mu_1 = \mu_2 = i$, and $|\mu_1| = |\mu_2| = 1$. For an orthotropic material, there are three different cases of interest:

I: $\mu_1 = ai, \mu_2 = bi$ (purely imaginary and un-equal)

II: $\mu_1 = \mu_2 = ai$ (equal and imaginary)

III: $\mu_1 = a + bi,\ \mu_2 = -a + bi$ (complex)

The above designations of cases follows from the fact that the roots of (3.9) can be categorised as $\mu_1, \mu_2, \bar{\mu}_1, \bar{\mu}_2$, where an overbar denotes a complex conjugate. Apart from four exceptional cases as noted in Lekhnitskii [3.1-3.2], the roots of

(3.9) are *always* complex. For materials considered in the present investigation, cases (I) & (III) are of interest. In these cases, the solution to (3.9) can be written as

$$F = \sum_{i=1}^{4} F_i(x + \mu_i y), \tag{3.10}$$

where $F_i(x+\mu_i y)$ are functions of argument $(x+\mu_i y)$. Let $z_1 = x + \mu_1 y$ and $z_2 = x + \mu_2 y$ denote two complex quantities. Then the solution of (3.8) can be expressed as,

$$F = \Re[F_1(z_1) + F_2(z_2)]. \tag{3.11}$$

Here $\Re$ denotes the real part of a complex quantity.

Introduce

$$\begin{aligned} \phi_1(z_1) &= \frac{dF_1}{dz_1} \\ \phi_2(z_2) &= \frac{dF_2}{dz_2}. \end{aligned} \tag{3.12}$$

Then using (3.5) together with (3.4) and (3.2), one obtains

$$\begin{aligned} \sigma_x &= 2\Re[\mu_1^2\phi_1'(z_1) + \mu_2^2\phi_2'(z_2)] \\ \sigma_y &= 2\Re[\phi_1'(z_1) + \phi_2'(z_2)] \\ \sigma_{xy} &= -2\Re[\mu_1\phi_1'(z_1) + \mu_2\phi_2'(z_2)] \end{aligned} \tag{3.13}$$

$$\begin{aligned} u &= 2\Re[p_1\phi_1(z_1) + p_2\phi_2(z_2)] - \omega y + u_0 \\ v &= 2\Re[q_1\phi_1(z_1) + q_2\phi_2(z_2)] + \omega x + v_0, \end{aligned}$$

where ω characterizes a rigid body rotation, and u_0, v_0 denote rigid body displacements in the x, y plane. The quantities p_1, p_2, q_1, q_2 are given by

$$\begin{aligned} p_1 &= \frac{1}{E_x}\mu_1^2 - \frac{\nu_{xy}}{E_x} \\ p_2 &= \frac{1}{E_x}\mu_2^2 - \frac{\nu_{xy}}{E_x} \\ q_1 &= -\frac{\nu_{xy}}{E_x}\mu_1 + \frac{1}{E_y}\frac{1}{\mu_1} \\ q_2 &= -\frac{\nu_{xy}}{E_x}\mu_2 + \frac{1}{E_y}\frac{1}{\mu_2}. \end{aligned} \tag{3.14}$$

Thus, the stress function F has been expressed in terms of two unknown functions $F_1(z_1)$, $F_2(z_2)$. These functions are to be determined such that they satisfy the appropriate boundary conditions of the particular problem. Once this is achieved, a complete solution to the particular boundary value problem is obtained by using (3.12) and (3.13). Using the method described above, a collection of solved problems can be found in Lekhnitskii [3.1,3.2] and Savin [3.3], where the complete generalized plane stress solution of an infinite plate containing an ellipitical hole and loaded as shown in Figure 3.1 is also given. This solution is obtained as the superposition of two problems. First, a plate without a cutout under uniform far field compression is considered. This is designated the 'zero' problem. Then, a second problem is considered where a plate with the elliptical cutout is considered, loaded on the cutout boundary by tractions which are equal and opposite to those found on a similar but *fictitious* elliptical boundary of the zero problem. This is designated the 'first' problem. The zero problem is straightforward and the solution is,

$$\begin{aligned}
\sigma_x^0 &= -P\cos^2\phi \\
\sigma_y^0 &= -P\sin^2\phi \\
\sigma_{xy}^0 &= -P\sin\phi\cos\phi \\
u^0 &= P(\frac{\cos^2\phi}{E_x} - \nu_{yx}\frac{\sin^2\phi}{E_y})x \\
v^0 &= P(\frac{\sin^2\phi}{E_y} - \nu_{xy}\frac{\cos^2\phi}{E_x})y.
\end{aligned} \tag{3.15}$$

The 'first' problem is more involved and requires obtaining $F_1(z_1)$ and $F_2(z_2)$ such that the stresses decay to zero at large distances form the cutout. The solution as obtained by Lekhnitskii [3.1], is given below.

$$\begin{aligned}
\phi_j(z_j) &= (-1)^{(j+1)}\frac{1}{(\mu_1-\mu_2)}\sum_{m=1}^{\infty}(\bar{b}_m - \mu_j\bar{a}_m)\zeta_j^{-m} \\
\zeta_j &= \frac{z_j + \sqrt[2]{z_j^2 - a^2 - \mu_j^2 b^2}}{(a - i\mu_j b)} \\
z_j &= x + \mu_j y, \qquad j = 1,2
\end{aligned} \tag{3.16a}$$

with,

$$\begin{aligned}
\bar{b}_1 &= \frac{P}{2}\cos\phi\ (a\sin\phi - ib\cos\phi) \\
\bar{a}_1 &= -\frac{P}{2}\sin\phi\ (a\sin\phi - ib\cos\phi) \\
\bar{a}_m &= \bar{b}_m = 0 \quad \text{for} \quad m \geq 2.
\end{aligned} \tag{3.16b}$$

Substituting (3.16a and b) in (3.13) the stresses and displacements associated with the first problem are obtained. Thus, the complete solution to the original boundary value problem is

$$\begin{aligned}\sigma_x &= \sigma_x^0 + \sigma_x^1 \\ \sigma_y &= \sigma_y^0 + \sigma_y^1 \\ \sigma_{xy} &= \sigma_{xy}^0 + \sigma_{xy}^1 \\ u &= u^0 + u^1 \\ v &= v^0 + v^1 .\end{aligned} \tag{3.17}$$

This solution can now be specialized to the case simulating the present experimental situation by setting

$$\phi = 0 \quad \text{and} \quad a = b = \text{radius of circular hole.}$$

Let a denote the radius of the circular hole. Then,

$$\begin{aligned}&\sigma_x^0 = -P, \quad \sigma_y^0 = 0, \quad \sigma_{xy}^0 = 0 \\ &u^0 = -P\left(\frac{1}{E_x}\right)x \quad , v^0 = -P\left(-\frac{\nu_{xy}}{E_x}\right)y\end{aligned} \tag{3.18a}$$

$$\bar{b}_1 = i\frac{P}{2}a, \qquad \bar{a}_1 = 0 \tag{3.18b}$$

$$\begin{aligned}\phi_j(z_j) &= (-1)^{(j+1)}\frac{iPa^2}{2(\mu_1 - \mu_2)}\left(\frac{(1 - i\mu_j)}{z_j + \sqrt[2]{z_j^2 - a^2(1 - \mu_j^2)}}\right) \\ \phi_j'(z_j) &= (-1)^{(j+1)}\frac{iP}{2(\mu_1 - \mu_2)(1 + i\mu_j)}\left(1 - \frac{z_j}{\sqrt[2]{z_j^2 - a^2(1 + \mu_j^2)}}\right) .\end{aligned} \tag{3.18c}$$

Here i is defined as $i^2 = -1$.

It is convenient to use the following non-dimensionalizations in computing the results for various load cases.

$$\begin{aligned}
\bar{\sigma}_x &= \frac{\sigma_x}{P}, \quad \bar{\sigma}_y = \frac{\sigma_y}{P} \text{ etc.} \\
\bar{z} &= \frac{z}{a} \equiv \frac{x}{a} + \mu_j \frac{y}{a}, \qquad j = 1,2 \\
u^* &= \frac{u}{a}\left(\frac{E_x}{P}\right), \quad v^* = \frac{v}{a}\left(\frac{E_x}{P}\right).
\end{aligned}$$

For the corresponding isotropic case, the solution simplifies to

$$\begin{aligned}
\sigma_r &= -\frac{P}{2}\left(1 - \frac{a^2}{r^2}\right) - \frac{P}{2}\left(1 + 3\frac{a^4}{r^4} - 4\frac{a^2}{r^2}\right)\cos 2\theta \\
\sigma_\theta &= -\frac{P}{2}\left(1 + \frac{a^2}{r^2}\right) + \frac{P}{2}\left(1 + 3\frac{a^4}{r^4}\right)\cos 2\theta \\
\sigma_{r\theta} &= \frac{P}{2}\left(1 - 3\frac{a^4}{r^4} + 2\frac{a^2}{r^2}\right)\sin 2\theta \\
u_r^* &= \frac{u_r E}{Pa} \equiv -\frac{1}{2}\left(\bar{r} + \frac{1}{\bar{r}}\right) - \frac{1}{2}\left(\bar{r} - \frac{1}{\bar{r}^3} + \frac{4}{\bar{r}}\right)\cos 2\theta \\
&\quad + \frac{\nu}{2}\left(\bar{r} - \frac{1}{\bar{r}}\right) - \frac{\nu}{2}\left(\bar{r} - \frac{1}{\bar{r}^3}\right)\cos 2\theta \\
v_\theta^* &= \frac{v_\theta E}{Pa} \equiv \frac{1}{2}\left(\bar{r} + \frac{1}{\bar{r}^3} + \frac{2}{\bar{r}}\right)\sin 2\theta + \frac{\nu}{2}\left(\bar{r} + \frac{1}{\bar{r}^3} - \frac{2}{\bar{r}}\right)\sin 2\theta.
\end{aligned} \tag{3.19}$$

From these, one obtains in cartesian coordinates

$$\begin{aligned}
\sigma_x &= \sigma_r \cos^2\theta + \sigma_\theta \sin^2\theta - \sigma_{r\theta}\sin 2\theta \\
\sigma_y &= \sigma_r \sin^2\theta + \sigma_\theta \cos^2\theta + \sigma_{r\theta}\sin 2\theta \\
\sigma_{xy} &= \frac{1}{2}(\sigma_r - \sigma_\theta)\sin 2\theta + \sigma_{r\theta}\cos 2\theta
\end{aligned}$$

and

$$u_x^* = u_r^*\cos\theta - v_\theta^*\sin\theta$$

$$v_y^* = u_r^*\sin\theta + v_\theta^*\cos\theta$$

with,

$$\bar{r} = \frac{r}{a}, \quad r^2 = x^2 + y^2, \quad \theta = \arctan\left(\frac{y}{x}\right).$$

3.3 Results

Example results are computed for laminates whose constitutive behaviour, derived using CLT, is shown in Appendix 3A. From these results, the two Youngs moduli, $E_x$andE_y , the in-plane shear modulus, G_{xy}, and the major Poisson's ratio, ν_{xy}, are derived. These are shown for each laminate type in Table 3.1. The 0^0 ply properties used for each laminate , T300/BP907 and IM7/8551-7, are shown in Table 3.2. Using these properties, the solution (3.18) is used to compute the stresses and displacements for each laminate for the configuration shown in Figure 3.1. Then, using the *laminate* constitutive relations, the in-plane strains ϵ_x, ϵ_y and ϵ_{xy} are computed. Next, using the constitutive relation for a 0^0 ply, the stresses within the 0^0 ply are computed for each loading case.

Hereafter, the laminate designations indicated in Table 3.3 are used (for simplicity). Figure 3.2 displays the stress distributions for the laminate type A. Figure 3.2a. shows $\bar{\sigma}_x$ and $\bar{\sigma}_y$ distributions along the $\bar{y}$-axis ($\theta = 90^0$). Figure 3.2b shows $\bar{\sigma}_y$ and $\bar{\sigma}_{xy}$ distributions along the $\bar{x}$-direction at $\bar{y} = 1$. Using symmetry, only the positive $\bar{x}$ direction is considered. From expressions (3.13) and (3.18), it can be shown that

$$\begin{aligned} \sigma_x(\bar{x},\bar{y}) &= \sigma_x(-\bar{x},\bar{y}) \\ \sigma_y(\bar{x},\bar{y}) &= \sigma_y(-\bar{x},\bar{y}) \\ \sigma_{xy}(\bar{x},\bar{y}) &= -\sigma_{xy}(\bar{x},\bar{y}). \end{aligned} \tag{3.20}$$

Figure 3.2c shows the $\bar{\sigma}_x$ distribution along the $\bar{x}$ direction at $\bar{y} = 1$. Recall that the stress components have been normalised by the applied compression P, and

$$\bar{x} = \frac{x}{a},\ \bar{y} = \frac{y}{a}$$

are normalised distances.

Indicated in these figures with a solid line are the corresponding stress distributions for the isotropic case. From Figure 3.2a, the stress concentration factors for $\bar{\sigma}_x$ at (0,1) can be deduced for each laminate. These factors are given in Table 3.4. Figures 3.3a through 3.3c display similar findings for type B laminates. Notice that both laminate types A and B are weakly orthotropic in the sense that the stress distribution for these laminates can be closely approximated by the isotropic result. Laminate types C and D pertain only to material IM7/8551-7. These types of laminates exhibit material properties that are usually referred to as quasi-isotropic in the literature. The term quasi-isotropic is used to describe a laminate which has essentially isotropic in-plane stiffnesses as derived from CLT. It is seen from Table 3.1 that laminate types C and D fall into this category. Their stacking sequence is such that when the in-plane modulii E_x, E_y, G_{xy} and ν_{xy} are calculated, the following relations are satisfied:

$$\begin{aligned} E_x = E_y = E; \qquad \nu_{xy} = \nu_{yx} = \nu \\ G_{xy} = \frac{E}{2(1+\nu)}. \end{aligned}$$

Thus, the stress distributions for these laminates (types D and C of IM7) correspond to the isotropic solution (solid line in Figures 3.2 through 3.3). From Figures 3.2a and 3.2b, it is seen that $\bar{\sigma}_x$ is localized near the cut-out and rapidly approaches its far field value of -1. At $\bar{y} = 3$, $|\bar{\sigma}_x|$ for laminate type A is within $\approx 2.5\%$ of unity, while the corresponding result for type B is $\approx$4.5%. The $\bar{\sigma}_y$ and $\bar{\sigma}_{xy}$ distributions at $\bar{y} = 1$ and along $\bar{x}$ are shown in Figures 3.2b and 3.3b. Notice that $\bar{\sigma}_y$ exhibits an oscillatory type of behaviour. Both $\bar{\sigma}_y$ and $\bar{\sigma}_{xy}$ are seen to die out quite rapidly, and for $\bar{x} = 4$ they can be regarded as negligible compared to $\bar{\sigma}_x$. Their peak values are an order of magnitude smaller than the component $\bar{\sigma}_x$ (Figures 3.2b and 3.2c and similarly for 3.3). The $\bar{\sigma}_x$ component is highly localized in the vicinity of the cut-out. It decays from its maximum compressive value, (=**SCF** x (-1) where **SCF** stands for stress concentration factor), to zero at $\bar{x} = 1.35$ and is less than -1 for $\bar{x} \geq 1.35$. At $\bar{x} = 4$, its value is ≈ -0.09 (Figures 3.2c and 3.3c) and approaches -1 as $\bar{x} \rightarrow \infty$.

3.3.1 Zero Ply Stresses

The stress distribution in a 0^0 ply contained within each of the above laminate types is presented next. These stresses are calculated from a knowledge of the strains ϵ_x, ϵ_y and ϵ_{xy} in the laminate and the lamina constitutive relations for the 0^0 ply as explained earlier. The results are presented in the same format as for the *laminate* stress distributions (Figures 3.4-3.5). One immediately notices that the stress concentration factors for $\bar{\sigma}_x$ within the 0^0 ply at the hole edge (at $\bar{x} = 0, \bar{y} = 1$) are quite high compared with the value averaged over the laminate. This is to be expected because the 0^0 plies 'absorb' a larger fraction of the total load owing to the large Young's modulus of the these plies in the load direction as compared with the other lamina. Thus, while the strains ϵ_x, ϵ_y and ϵ_{xy} are equal within every ply, the $\bar{\sigma}_x$ stresses attain a maximum within the 0^0 ply at the hole edge (0,1). The stress concentration factors for the 0^0 plies are summarized in Table 3.4. Inspection of Figures 3.4b and 3.5b reveals one drawback of CLT. In these Figures results are presented for $\bar{\sigma}_y$ and σ_{xy} along $\bar{x}$ at $\bar{y} = 1$. Notice that $\bar{\sigma}_y \neq 0$ at (0,1) violating a traction free condition. The reason for this apparent violation of the boundary condition is that CLT is able to satisfy the traction free condition at a free edge only in an averaged sense. Thus, while $\bar{\sigma}_y$ within a 0^0 ply is non-zero at (0,1), the stress resultant in the y-direction is too, i.e.,

$$N_y = \int_{\frac{-h}{2}}^{\frac{h}{2}} \sigma_y dz = 0.$$

However, the value of $\bar{\sigma}_y(0,1)$ is found to be small compared to the corresponding $\bar{\sigma}_x$(Figures 3.4a and 3.5a). Furthermore, both $\bar{\sigma}_y$ and $\bar{\sigma}_{xy}$ are found to be much smaller than $\bar{\sigma}_x$ for all values of $\bar{x}$ at $\bar{y} = 1$, as well as, the corresponding laminate values (Figures 3.4b and 3.5b).

Similar results for the types C and D (IM7) laminates are shown in Figure 3.6. In each figure, the laminate stresses are presented as a solid line, the corresponding 0^0 ply stresses with a dashed line. Note that since both types C and D are quasi-isotropic with equal modulii, the computed 0^0 ply stresses are the same for *both* laminates.

Finally, in Figure 3.7, the normalized v-displacement of lines parallel to the $\bar{x}$ direction at different values of $\bar{y}$ in the undeformed state is shown for each laminate type. Recall that

$$v^* = \frac{v}{a}\left(\frac{E_x}{P}\right).$$

Notice that the distribution of $v^*(\bar{x}, 1)$ bears a resemblence to the corresponding $\bar{\sigma}_x(\bar{x}, 1)$ distribution presented earlier. In regions of high compressive gradients of $\bar{\sigma}_x$ (ie.$0 \leq \bar{x} \leq 2$) , where $\bar{\sigma}_x$ decreases rapidly in magnitude from its maximum value to its far-field value of -1, the v^* displacements also exhibit a sharp drop in magnitude before increasing gradually to their far-field value.

Summarizing, the results presented so far have given an insight into the stress distribution when an orthotropic laminate containing a circular cut-out is subjected to a uniform compression parallel to an axis of orthotropy. Useful information such as stress concentration factors and stress distributions at various locations have been obtained. In particular, attention was focused on the stress and displacement distribution on a line adjacent to the hole edge parallel to the $\bar{x}$-axis at $\bar{y} = 1$. This was done in the hope of leading towards a local micro-buckling model, whose geometry contains this line, $\bar{y} = 1$, as one of its boundaries. This topic will be discussed next.

3.3.2 Strain Concentration Field

In the previous chapter, it was shown that the localized micro-buckling failure of the 0^0 plies was the failure initiation mechanism for the laminate types used in this investigation. Therefore, a portion of the 0^0 ply adjacent to the hole and in the vicinity of the observed failure is isolated and shown in Figure 3.8a. The thickness of this portion is marked as $9d_f$ and is shown only for illustrative purposes (Figure 3.8b). The ply thickness of the laminates used is $\approx 20d_f$. The stress distribution in this portion prior to buckling is obtained from the results presented earlier in this discussion, where a *plane stress* condition is assumed in the x, y plane. The isolated 0^0-ply portion is conceptualized as consisting of several stacked layers in the x, y plane. A typical layer is shown in Figure 3.9a. The fiber cross section is assumed to be square. The normalized distances $\bar{x}$ and $\bar{y}$ are re-written in the following form:

$$\breve{x} = \frac{x}{d_f} = \bar{x}\left(\frac{a}{d_f}\right)$$
$$\breve{y} = \frac{y}{d_f} = \bar{y}\left(\frac{a}{d_f}\right)$$

where,

$$d_f = \text{fiber diameter} \; .$$

The new quantities $\breve{x}$ and $\breve{y}$, represent a "stretching" of the x and y coordinates so that the pre-buckling stress distribution can be viewed on a length scale compatible with the small-scale physics of the isolated portion. A natural length scale for this portion is the fiber diameter (or the fiber spacing). Both of these are conveniently combined to yield a non-dimensional quantity $V_f = \frac{d_f}{d_f+2c}$, the fiber volume fraction, which gives a measure of the packing density of the fibers.

For the T300 fibers, the fiber diameter is approximately $7\mu m$, while it is $5\mu m$ for the IM7 fibers. The hole radii used in the experiments vary from 1.27cm to 0.635cm, although much of the data was obtained for a hole radius of 1.27cm. For this hole radius, $\left(\frac{a}{d_f}\right) \approx 1814$.

The isolated 0^0 ply portion is to be analyzed along the lines of Bernoulli-Navier beam theory for the fibers and classical elasticity theory for the matrix. The question arises as to the dimensions of the isolated portion to be chosen and to the approximations one could make that enables one to capture the experimental observations. From the discussion in the previous chapters, it was seen that the *initial* fiber damage was contained *within* a zone of about 100 in the $\breve{x}$ direction and approximately 180 in the $\breve{y}$ direction (for a 1.27cm hole radius). Furthermore, it was revealed that failure by microbuckling consisted of buckling displacements in both the y and z directions. It was also shown that all the fibers within the 0^0-ply deformed in a similar fashion as viewed in the x, z plane. In the x, y plane, the fiber displacement in the y-direction showed a gradual decay from the edge of the hole. Thus, the micro-buckling failure is essentially three-dimensional involving buckling displacements in the x, y and z directions.

Let us focus attention on the buckling instability in the x, y plane. On the one hand, it seems reasonable to study the buckling instability of a typical idealized layer that constitutes a 0^0-ply with an approximation of *plane strain* for the *perturbation* problem. This is supported by the observation that the buckling displacements are the same for all the idealized layers constituting the 0^0-ply. On the other hand, if separation does occur at the fiber/matrix interface, then it leads to a decoupling between the layers that constitute a 0^0-ply. In this case a *plane stress* analysis is more suitable for the perturbation problem. This latter assumption is used in the analysis presented in the next chapter. However, due to the correspondence between the *plane strain* and *plane stress* approximations, the results obtained in either case are qualitatively the same. A quantitative inference regarding the *plane strain* approximation can be made, if in the *plane stress* formulation the following substitutions are made.

$$E \rightarrow \frac{E}{1-\nu^2}$$
$$\nu \rightarrow \frac{\nu}{1-\nu}$$

This inference will be discussed further in the next chapter. The overall dimensions of the isolated portion are as marked in Figure 3.9b.

Next, consider the tractions acting on the isolated portion's free edges. These can be obtained from the stress distributions presented in the preceeding discussion. However, it is evident from those results, that the important traction quantity, in the sense of being dominant, is the $\bar{\sigma}_x$ component acting on the faces $\bar{x} = \pm 0.02$ of the isolated portion (infered from the stress distributions presented for the 0^0 plies within the laminate). It is seen that, along the faces $\bar{x} = \pm 0.02, 0 \leq \bar{y} \leq 0.1$, this component varies approximately in the manner shown in Figures 3.*a (* denotes 2-6) for the various types of laminates. In Figure 3.5a, for example, $\bar{\sigma}_x$ is seen to drop from its maximum value at $\bar{y} = 0$ to a value which is 75% of this peak at $\bar{y} = 0.1$ (on the *micro* length scale $\bar{y}$=0.1 corresponds to 181 fiber diameters). Thus, the variation of $\bar{\sigma}_x$ at $\bar{x} = \pm 0.2$, as a function of $\breve{y}$ (the micro length scale), is seen to be quite gradual. In view of these considerations, only the component $\bar{\sigma}_x$ is retained as a first step in addressing the stability of the isolated portion. Further, it is assumed that this component acts uniformly along the faces $\bar{x} = \pm 0.02$ of the isolated portion, the configuration of which is shown in Figure 3.10. The problem formulation and its detailed solution are addressed in the next chapter.

3.4 References

3.1 Lekhnitskii, S.G (1963),"*Theory of Elasticity of an Anisotropic Elastic Body*", Holden-Day publishers.

3.2 Lekhnitskii, S.G (1968),"*Anisotropic Elastic Plates*", Gordon and Breach publishers.

3.3 Savin, G.N (1970),"Stress distributions around holes",NASA TT F-607.

3.4 Biot, M.A (1965),"*Mechanics of Incremental deformation*", Wiley & Sons publishers.

3.5 Wang, S.S and Choi I.(1982),"Boundary layer effects in composite laminates: Parts 1 and 2", *J.App.Mech.*, Vol. 49, pp541-560

3.6 Pipes, R.B and Pagano, N.J (1970),"Interlaminar stresses in composite laminates under uniform axial extension", *J.Comp.Matls.*, Vol. 4, pp538-548

3.7 Bogy, D.B (1969),"Edge bonded disimilar orthogonal elastic wedges under normal and shear loading", *J.App.Mech.*, Vol. 40, pp460-466

3.8 Pagano, N.J and Pipes, R.B (1973),"Some observations on the interlaminar strength of composite laminates", *Int.J.Mech.Sci.*, Vol. 15, pp679-698

3.9 Pipes, R.B and Pagano, N.J (1974),"Interlaminar stresses in composite laminates-An approximate Elasticity solution", *J.App.Mech.*, Vol. 41, pp668-672

3.10 Tang, S. (1975),"A boundary layer theory-Part 1: laminated composites in plane stress", *J.Comp.Matls.*, Vol.9, pp33-41

3.11 Tang, S. and Levy, A. (1975),"A boundary layer theory-Part 2: Extension of laminated finite strip", *J.Comp.Matls.*, Vol. 9, pp42-52

3.12 Rybicki, E.F (1976),"Three dimensional stress analysis of a laminated plate containing an elliptical cavity", AFML-TR-76-32

3.13 Raju, I.S and Crews,J.H., *Jr.* (1982),"Three dimensional analysis of $(0/90)_s$ and $(90/0)_s$ laminates with a central circular hole", *Comp.Tech.Review*, Vol. 4, pp116-125

3.14 Wang, S.S and Yuan F.G (1983),"A singular hybrid FEM analysis of boundary layer stresses in composite laminates", *Int.J.Solids & Struct.*, Vol. 19, pp825-837

3.15 Wang, S.S (1983)"Fracture mechanics of delamination problems in composite laminates", *J.Comp.Matls.*, Vol. 17, pp210-223

3.16 Ericsson K., Persson L., Carlsson L. and Gustavsson A. (1984),"On the prediction of the initiation of delamination in a $(0/90)_s$ laminate with a circular hole", *J.Comp.Matls.*, Vol. 18, pp496-505

3.17 Delale, F. (1984),"Stress analysis of multi-layered plates around circular cutouts", *Int.J.Eng.Sci.*, Vol. 22, pp57-75

3.18 Murthy, P. and Chamis, C. (1985),"A study of inter-ply layer effects on the free-edge field of angle plied laminates", *Computers & Struct.*, Vol. 20, pp431-441

3.19 Bar-Yoseph P. and Arrashi, J (1985),"Interlaminar stress analysis for laminated plates containing a curvilinear hole", *Computers & Struct.*, Vol. 21, pp917-932

3.20 Salamon, N.J (1980),"An assessment of the interlaminar stress problem in laminated composites", *J.Comp.Matls.supplement*, Vol. 14, pp177-194

CHAPTER 4

A MECHANICAL MODEL FOR FIBER MICROBUCKLING

4.1 Introduction

Qualitative and quantitative results related to a micromechanical instability were presented in the previous chapters. It was observed that *microbuckling* of the 0^0 plies initiated the failure process that developed into catastrophic failure of the entire plate. These observations and results can be elucidated by a mechanical model, capable of predicting the levels of strain at which microbuckling occurs.

4.2 Previous Work Related to Microbuckling

A problem that has received much attention but moderate success is the prediction of compressive strength. Dow and Gruntfest [4.1] were apparently the first to identify fiber buckling as a viable mode of compressive failure in composites. Their work was followed by that of Fried et al.[4.2] and Leventz[4.3], who addressed experimentally and theoretically the question of compressive strength. In these investigations, an empirical factor was used to obtain a correlation between the experimentally and theoretically predicted values of compressive strength. In 1965, Rosen[4.4] presented an analysis addressing the question of microbuckling which was devoid of any empiricism and laid the foundation for much of the work that was to follow. With a few exceptions, noted later, the analytical research work carried out in the past twenty years is based on the model by Rosen [4.4]. Due to lack of space and because an excellent literature survey on fiber microbuckling exists[4.5], a discussion of the various contributions that have enhanced the understanding of microbuckling will be omitted here. Instead, the discussion will be limited to those aspects that are fundamental in clarifying the state of the art of the subject.

The interested reader is referred to the references at the end of this chapter and the review by Shuart[4.5], in particular, for a complete and up to date account.

The work of Rosen[4.4] will be discussed next. This work addresses the problem of fiber buckling in glass fiber/epoxy laminates under compressive loading. The model presented, which is two-dimensional, treats the fiber layers as plates supported by an elastic matrix (offering lateral support to the fibers at buckling). When the unidirectional composite of infinite extent undergoes failure, Rosen envisages two possible modes of failure which he calls the extension and shear modes. In the extension mode, the matrix material is predominantly in extension and adjacent fibers deform 180^0 out of phase with each other as shown in Figure 4.1. In the shear mode, adjacent fibers deform in phase, and the matrix material is predominantly in shear. Using an energy method to obtain the buckling load, Rosen approximated the buckled mode shape of the fibers to be

$$v = \sum_{n=1}^{\infty} a_n \sin\left(\frac{n\pi x}{L}\right).$$

In evaluating the contribution to the potential energy from the matrix at buckling, he assumed the *strains* in the matrix to be independent of y (Figure 4.1) .This amounts to approximating the displacements in the matrix to vary linearly in y. Next, considering the bending energy contribution of the fiber and the work done by the in-plane compressive loads on the fiber, he obtains the following critical values for the extensional and shear modes:

Extensional mode

$$\sigma_{cr} \;=\; 2V_f\left[\frac{V_f E_m E_f}{3(1-V_f)}\right]^{\frac{1}{2}} \tag{4.1}$$

$$\left(\frac{\lambda}{h}\right)_{cr} = \pi \sqrt[4]{\frac{(1-V_f)}{3V_f}\frac{E_f}{E_m}} \tag{4.2}$$

Shear mode

$$\sigma_{cr} = \frac{G_m}{1-V_f} + O\left((\frac{h}{\lambda})^2\right) \tag{4.3}$$

$$\left(\frac{\lambda}{h}\right)_{cr} \gg 1. \tag{4.4}$$

Here,

σ_{cr} = Critical compressive stress at buckling.

E_m = Youngs modulus of the matrix.

E_f = Youngs modulus of the fiber.

V_f = Volume fraction of fibers.

h = Thickness of a fiber plate.

λ = Wave length of the buckled fiber.

Notice that in the shear mode, the critical value of σ occurs for $\lambda \gg h$. Thus, unlike the extension mode in which a critical buckle wavelength can be evaluated, no such value λ_{cr} exists in the shear mode. The buckling 'load' is continuously dependent on the wave length λ.

A second viewpoint regarding the mode of failure in compression is referred to as *fiber kinking.* Observations on kinking failure go back as far as 1949 when Orowan[4.6] observed that single crystal rods of Cadmium collapse under uniaxial compression into peculiar kinks if the **(0001)** glide plane is nearly parallel to the axis of compression. It is frequently useful to use four axes (thus four Miller indices), three of them co-planar, to describe the crystal planes for hexagonally close packed (HCP) crystals. The **(0001)** for HCP Cadmium is the basal plane. The advent of fibrous materials has rekindled interest in the subject, and in recent years, fiber kinking as a viable mode of failure has been observed by, among others, Weaver and Williams[4.7], as well as, other researchers [4.8-4.11]. Judging from the experimental evidence available, it appears that the formation of compression induced kink bands is closely associated with the existence of a preferable glide plane in the direction of compression. Budiansky[4.12] analyzed kinking by introducing inelastic behavior in the matrix and explained the large scatter in kinking strengths in terms of the composite's sensitivity to initial fiber misalignment. He presents in [4.12] a result for the compressive strength of the composite which depends on the matrix yield stress in shear and on the initial fiber misalignment. However, the experimental evidence available [4.2,4.3,4.22,4.23] does not suggest that kinking failures occur necessarily at levels of strain that permit inelastic matrix behavior.

More recently, Hahn and Williams[4.13] and Sohi et al.[4.14] have reported experimental results related to compression failure in straight fiber laminated test specimens. In these studies, it was repeatedly observed that failure of the fibers in plies aligned along the loading direction (0^0 plies) originated at a *free edge* and subsequently propagated into the interior of the specimen, precipitating a global failure of the test specimen. This observation is consistent with the findings reported here in the previous chapters as regards the origins of the failure process.

The purpose of this chapter is to put forward a simple mechanical model that is able to demonstrate the origins of compressive failure at a free edge. To do so, the problem of a laminated half plane subjected to a uniform far field compression parallel to the surface of the half plane is considered. Despite the fact that experimental observations strongly suggest that fiber-microbuckling originates at a free edge, a model configuration that allows incorporating a free edge has not been examined with the view to understanding microbuckling.

In developing the analysis, a simple example is considered first in which a single fiber perfectly bonded to a half plane is subjected to compression. This is done for two reasons. Firstly, to understand the effects of boundary conditions that are applied at the interface of the different materials, particularly from a buckling standpoint, and secondly, to assist in developing the more elaborate analysis that follows, where a more realistic configuration for the composite is chosen in which the entire half plane is a unidirectionally laminated medium.

4.3 Problem Formulation

4.3.1 An Example Problem

Consider the idealized single fiber composite of unit thickness in the $\hat{z}$ direction, shown in Figure 4.2. For clarity of presentation, upper case letters have been used in the figures for coordinate axes corresponding to their lower case counterparts in the text. The composite is subjected to a uniform compression (P/h) per unit thickness normal to the $\hat{x}, \hat{y}$ plane of the figure. The relatively 'soft' supporting medium (matrix) acts as an *elastic* foundation offering lateral support to the fiber. For convenience, a composite of infinite extent in the $\hat{x}$ direction occupying the space $0 \leq y \leq \infty$ is considered. Standard notation, such as 'E' for Young's modulus and ν for Poisson's ratio is used with the subscripts 'f' and 'm' to denote properties of the fiber and matrix, respectively. The analysis is carried out for composites typical of those used in the aerospace industry where $E_f \gg E_m$. Consequently, the prebuckling deformation of the composite is one of uniform contraction with the compressive load borne essentially by the fiber. Bernoulli-Navier beam theory is used to describe the fiber, while the matrix is modelled as a linearly elastic, homogeneous and isotropic body. The pre-buckled state for the fiber (a positive sign associated with compression) is described by

$$\epsilon_0 = \frac{P}{E_f h}, \quad v = 0. \tag{4.5}$$

Next, the governing equations for the fiber in the buckled state are developed. With reference to Figure 4.3, consider an element of the fiber infinitesimally removed from the straight configuration. It is cut by planes that were parallel to the $\hat{y}, \hat{z}$ plane at $\hat{x}$ and $\hat{x} + d\hat{x}$ in the undeformed state. These sections remain plane and normal to the deformed middle surface. With the assumption that rotations are small compared to unity, force equilibrium and moment equilibrium in the $\hat{x}, \hat{y}$ plane results in

$$\frac{dQ}{d\hat{x}} + \sigma - P\frac{d^2 v}{d\hat{x}^2} = 0 \tag{4.6a}$$

$$\frac{dp'}{d\hat{x}} + q = 0 \tag{4.6b}$$

$$-\frac{d^2 M}{d\hat{x}^2} - \frac{h}{2}\frac{dq}{d\hat{x}} + \frac{dQ}{d\hat{x}} = 0. \tag{4.6c}$$

Here σ and q are the interface tractions developed at buckling because the fiber and matrix are bonded at their common interface. In writing (4.6a), the product $p'\frac{d^2 v}{d\hat{x}^2}$, which is of second order, has been ommited. The buckling under investigation is infinitesimal. p'(per unit length in the $\hat{z}$ direction) is the change in the axial force P at buckling. M is the bending moment in the fiber and v the deflection of the fiber in the $\hat{y}$ direction. Equation (4.6b) can be further simplified by noting that

$$p' = hE_f \frac{du_0}{d\hat{x}}, \tag{4.7}$$

where u_0 is the axial displacement of the fiber due to buckling. Also,

$$M = -EI\frac{d^2v}{d\hat{x}^2}. \tag{4.8}$$

Combining (4.6) through (4.8) the following is deduced

$$\begin{aligned} E_f I\frac{d^4v}{d\hat{x}^4} + P\frac{d^2v}{d\hat{x}^2} - \frac{h}{2}\frac{dq}{d\hat{x}} - \sigma = 0 \\ q + hE_f\frac{d^2u_0}{d\hat{x}^2} = 0. \end{aligned} \tag{4.9}$$

Continuity of displacements at the common interface (Figure 4.4) requires

$$\begin{aligned} u_0 - \frac{h}{2}\frac{dv}{d\hat{x}}\Big|_{\hat{y}=\frac{h}{2}} = u_m\big|_{y=0} \\ v\big|_{\hat{y}=\frac{h}{2}} = v_m\big|_{y=0}. \end{aligned} \tag{4.10}$$

To solve (4.9), periodic perturbations in $u(\hat{x})$ and $v(\hat{x})$ of sinusoidal form about the trivial solution (4.5) with an arbitrary wave length λ are investigated. Then, one seeks the critical value of P required to maintain this disturbance; q and σ are then obtained in terms of the fiber displacements v and u_0. This requires the solution of the elastic displacement equations of equilibrium in the matrix.

4.3.2 The Matrix Problem

With reference to Figure 4.4, it is necessary to solve,

$$\begin{aligned} 2\frac{\partial^2 u_m}{\partial x^2} + (1-\nu_m)\frac{\partial^2 u_m}{\partial y^2} + (1+\nu_m)\frac{\partial^2 v_m}{\partial x \partial y} &= 0 \\ 2\frac{\partial^2 v_m}{\partial y^2} + (1-\nu_m)\frac{\partial^2 v_m}{\partial x^2} + (1+\nu_m)\frac{\partial^2 u_m}{\partial x \partial y} &= 0, \end{aligned} \tag{4.11}$$

which are the elastic displacement equations of equilibrium with the approximation of *plane stress* in the x, y plane, subject to the following boundary conditions:

$$\begin{aligned} at\ y = 0, \qquad u_m &= U\text{cos}\alpha x \\ v_m &= V\text{sin}\alpha x \end{aligned} \tag{4.12a}$$

$$\begin{aligned} as\ y \to \infty, \qquad u_m &\to 0 \\ v_m &\to 0. \end{aligned} \tag{4.12b}$$

Here $\alpha = \frac{2\pi}{\lambda}$ and U, V are arbitrary constants. In writing (4.12), the form of the buckled displacements of the fiber is assumed as

$$\begin{aligned} u_{0f} &= B\text{cos}\alpha\hat{x} \\ v_f &= A\text{sin}\alpha\hat{x}. \end{aligned} \tag{4.13}$$

The solution of (4.11) proceeds in the following manner.

Let

$$\begin{aligned} u_m &= \psi(y)\text{cos}\alpha x \\ v_m &= \phi(y)\text{sin}\alpha x. \end{aligned} \tag{4.14}$$

Using (4.14) in (4.11) and elimination of ϕ(or ψ) results in the following ordinary differential equation for $\psi(\phi)$

$$\psi^{IV} - 2\alpha^2\psi^{II} + \alpha^4\psi = 0, \tag{4.15}$$

where $(\ )^I \equiv \frac{d}{dy}$; a similar equation results for ϕ.

The solution of (4.15) subject to the second condition in (4.12) is

$$\psi = (C_3 y + C_4)e^{-\alpha y}$$

and similarly, (4.16)

$$\phi = (D_3 y + D_4)e^{-\alpha y}.$$

Here the $C's$ and $D's$ are related by

$$\begin{aligned} C_4 &= \frac{D_3}{\alpha}\left[\frac{(3-\nu_m)}{(1+\nu_m)}\right] - D_4 \\ C_3 &= \ -D_3. \end{aligned} \tag{4.17}$$

(4.17) is obtained by substituting (4.16) into (4.11). Incorporating the first of (4.12), one arrives at

$$\begin{aligned} u(x,0) &= \ [\frac{D_3}{\alpha}\frac{(3-\nu_m)}{(1+\nu_m)} - D_4]\text{cos}\alpha x \\ v(x,0) &= \ D_4\text{sin}\alpha x \end{aligned} \tag{4.18}$$

with

$$\begin{aligned} D_4 &= \ V \\ D_3 &= \ \alpha\frac{(1+\nu_m)}{(3-\nu_m)}U + \alpha\frac{(1+\nu_m)}{(3-\nu_m)}V. \end{aligned} \tag{4.19}$$

Next the surface tractions q and σ are computed;

$$\begin{aligned} \tau_{xy} &= \ G_m[\frac{\partial u_m}{\partial y} + \frac{\partial v_m}{\partial x}] \\ &= G_m[\psi' + \alpha\phi]\text{cos}\alpha x. \end{aligned}$$

Thus,

$$\tau_{xy}(x,0) \ \equiv \ q(x,0) \ = \ G_m\left[2\alpha\frac{(1-\nu_m)}{(3-\alpha)}V - \frac{4\alpha}{(3-\nu_m)}U\right]\text{cos}\alpha x. \tag{4.20}$$

The normal stress

$$\begin{aligned} \sigma_y &= \frac{E_m}{(1-{\nu_m}^2)}\left[\frac{\partial v_m}{\partial y} + \nu_m\frac{\partial u_m}{\partial x}\right] \\ &= \frac{E_m}{(1-{\nu_m}^2)}\left[\phi' - \nu_m\alpha\psi\right]\text{sin}\alpha x. \end{aligned}$$

Thus,

$$\sigma_y(x,0) \equiv \sigma(x,0) = -\frac{E_m \alpha}{(1+\nu_m)(3-\nu_m)}\left[2V - U(1-\nu_m)\right] \sin\alpha x. \tag{4.21}$$

Using (4.13) and (4.12a), the following is obtained:

$$\begin{aligned} V &= A \\ U &= B - \frac{h\alpha}{2}A. \end{aligned} \tag{4.22}$$

Substituting (4.20) through (4.22) into (4.9), the following system of equations results.

$$\begin{aligned} (a_1 - \epsilon_0)A + b_1 B &= 0 \\ a_2 A + b_2 B &= 0 \end{aligned} \tag{4.23}$$

where,

$$\begin{aligned} a_1 &= \frac{\rho^2}{12} + \frac{2\mu}{\rho(1+\nu_m)(3-\nu_m)} + \frac{\mu(1-\nu_m)}{2(3-\nu_m)(1+\nu_m)} + \frac{\mu\big(\rho + (1-\nu_m)\big)}{2(1+\nu_m)(3-\nu_m)} \\ a_2 &= \frac{\mu\big((1-\nu_m)+\rho\big)}{\rho(1+\nu_m)(3-\nu_m)} \\ b_1 &= \frac{-\mu}{(1+\nu_m)(3-\nu_m)} - \frac{\mu(1-\nu_m)}{\rho(3-\nu_m)(1+\nu_m)} \\ b_2 &= \frac{2\mu}{\rho(1+\nu_m)(3-\nu_m)} + 1, \end{aligned}$$

and the following non-dimensionalizations have been used.

$$\begin{aligned} \rho &= h\alpha = \frac{2\pi h}{\lambda} \\ \mu &= \frac{E_m}{E_f} \end{aligned} \tag{4.24}$$

For non-trivial solutions for A and B, one requires

$$\begin{vmatrix} (a_1 - \epsilon_0) & b_1 \\ a_2 & b_2 \end{vmatrix} = 0. \tag{4.25}$$

The condition (4.25) implies that

$$\epsilon_0 = a_1 + a_2 \left(\frac{b_1}{b_2}\right). \tag{4.26}$$

4.3.3 Results and Discussion

To illustrate the results, the material properties listed in Table 4.1 have been chosen. These correspond to the two fiber/matrix systems, considered in the previous chapters, designated as T300/BP907 and IM7/8551-7. From now on, these shall be referred to as *BP907* and *IM7*, respectively.

Table 4.1

	BP907	**IM7**
$\frac{E_f}{E_m}$	74.2	79.3
ν_m	0.38	0.33

Figure 4.5 shows the variation of ϵ_0, with the non-dimensional half wave length l. In this plot, the present results (solid curve for BP907 and dashed curve for IM7) are compared with those of two other models. The first one, Gough et al.[4.15], is obtained by neglecting the presence of the interface shear traction q. In that calculation, instead of the continuity conditions, equations (4.10) are replaced by the requirement that the surface of the matrix ($y = 0$) is constrained to satisfy

$$\begin{gathered} \epsilon_x = 0 \\ v = v_m. \end{gathered} \tag{4.27a}$$

In the second model, Reissner[4.16], the surface of the matrix is taken to be free from shearing stress. This amounts to satisfying (at $y = 0$)

$$\begin{aligned} v &= v_m \\ \tau_{xy} &= 0. \end{aligned} \tag{4.27b}$$

In computing the critical strain, the models of Gough[4.15] and Reissner[4.16] do not account for the interface shear traction developed at buckling.

First, attention is focused at the nature of the curve shown in Figure 4.5. As the non-dimensional half wave length l increases from 0, the value of ϵ_0 decreases, goes through a minimum at $l \approx 9$, and increases monotonically. This means that the minimum value of ϵ_0 that can maintain the composite in the assumed buckled configuration corresponds to point **A**. Clearly, a calculation that does not take into account the interface shear traction that develops at buckling underestimates the strength of the composite as is seen here (compare (a), (b) and (c) of Figure 4.5)

The manner in which the buckling strain is affected as a function of the ratio of Young's moduli of the constituents $\frac{E_f}{E_m}$ is shown in Figure 4.6. The corresponding critical wave length variation is depicted in Figure 4.7. Notice that a large disparity in Young's moduli between fiber and matrix($E_f \gg E_m$) leads to a gradually decreasing value of critical strain, with the rate of this decrease diminishing as the limit $\frac{E_f}{E_m} \rightarrow \infty$ is approached. Further, as expected, the agreement between the present calculation and those of [4.15,4.16] improves as this limit is approached. Also, as $\frac{E_f}{E_m} \rightarrow \infty$, by holding E_f constant and letting $E_m \rightarrow 0$, which corresponds to a gradual disapperence of the matrix, the Euler formula, $\epsilon_{cr} = \frac{\rho^2}{12}$, is obtained from the present result (4.26). Next, consider the case of $\frac{E_f}{E_m} \rightarrow 1$. Here, there is a noticeable difference in the predicted values of ϵ_0 between the three calculations. However, in the range $\frac{E_f}{E_m} \leq 20$, the predicted critical non dimensional half wave length l is less than 5. Thus in this situation where the critical wave length becomes comparable to the thickness of the fiber, use of a one-dimensional theory, such as technical beam theory in describing the fiber, is inappropriate. The effect of Poisson's ratio on the buckling strain can be inferred from Figure 4.8. Here, it is seen that when ν_m=0 (a condition which constrains the matrix to behave such that $\epsilon_y = \epsilon_z = 0$ at buckling), the buckling strain is higher than for cases $\nu_m \geq 0$. This is to be expected because the constraining condition 'stiffens' the matrix at buckling.

In summary, it is observed that the effect of the interface shear traction occurring at buckling is to introduce small periodic fluctuations in the axial thrust acting on the fiber (denoted by p' in the formulation) . Further, this shear traction also introduces bending moments because of its eccentricity with respect to the centerline of the fiber. These effects have been included in the present formulation.

The stresses in the matrix associated with the sinusoidally buckled form of the fiber contain the multiplier $e^{-\alpha y}$, and thus diminish as y increases. At a sufficiently large value of y, they may be regarded as negligible. Thus the coefficient $'\alpha'_{cr}$ in the exponent characterizes a boundary layer depth into the matrix to which any surface disturbance can be felt. The quantity 'αy' can be re-written as,

$$\alpha y = \frac{2\pi}{\lambda} y = \frac{\pi}{l} \cdot \left(\frac{y}{h}\right) . \tag{4.28}$$

Figure 4.7 shows a plot of l against the ratio $\frac{E_f}{E_m}$. It is seen that for a 'soft' matrix ($\frac{E_f}{E_m}$=500, say), the surface disturbance is felt to a larger depth than for a 'hard' matrix ($\frac{E_f}{E_m}$=50, say). This result can be interpreted in the light of more realistic composites. Suppose a unidirectional laminated composite contains several fibers. Then, so long as the fiber spacing is larger than a certain minimum value, the interaction between adjacent fibers will be negligible, and the one-fiber model presented here can be used as a measure of the compressive strength of the composite. However, in order to maximize the specific stiffness of the composite (the $\frac{E}{\rho}$ ratio), one needs to attain a high volume fraction of fibers. This makes the spacing between fibers (expressed more readily in terms of fiber volume fraction $V_f = \frac{h}{h+2c}$) small compared with h. Typical values of V_f range from 0.5-0.6 for fiber reinforced laminated systems that are currently in use. Thus, it is informative to address the more general problem of a laminated medium containing many fibers under compressive loading (Figure 4.9) .There are several ways to approach this problem. In the spirit of the previous analysis, this can be modeled as a problem of a single fiber resting on an equivalent orthotropic medium (the 'smeared' foundation). However, unlike before, the prebuckling stress state in the 'foundation' is quite different. No longer can it be assumed that the totality of the load is borne by the surface fiber alone. Indeed, one is compelled to consider a problem in which the 'foundation's' initial stressed state on the buckling of the surface fiber has to be accounted for. Such a consideration can pose difficulties in solving for the displacements of the foundation in the presence of the initial stress, since now a two-dimensional stability problem for the foundation itself has to be considered.

Another approach to the problem is to consider individual fibers separately and account for the interaction effects between adjacent fibers by analyzing the deformation of the sandwiched elastic matrix at buckling. It is this approach that is followed in the next investigation.

4.4 Buckling of a Layered Medium

4.4.1 Problem Formulation

The configuration being studied is shown in Figure 4.9. Here, the end compression is indicated as being carried entirely by the fibers. To verify this assumption, let P (per unit length in the $\hat{z}$ direction) be the applied load to a "unit cell" of depth $(h+2c)$ in the pre-buckled state. Then, the axial compressive stresses in the fiber and matrix are

$$\sigma_{x_f} = \frac{P}{h\left(1+\frac{2c}{h}\frac{E_m}{E_f}\right)}$$

$$\sigma_{x_m} = \frac{P}{h\left(\frac{E_f}{E_m}+\frac{2c}{h}\right)}$$

with,

$$\frac{2c}{h} = \left(\frac{1-V_f}{V_f}\right).$$

These reduce to $\sigma_{x_f} = \frac{P}{h}$ and $\sigma_{x_f} \gg \sigma_{x_m}$, so long as $\left(\frac{E_f}{E_m}\right) \gg \left(\frac{1-V_f}{V_f}\right)$ and $E_f \gg E_m$, which is the case in the present investigation. Thus, the pre-buckled state of the composite is as described by (4.5), with the end compression load carried entirely by the fibers. The matrix acts as an elastic foundation. Next, consider the composite in the buckled configuration (Figure 4.10). Then, considering the equilibrium of a typical fiber, the following set of equations result for the surface fiber (N=1) and the n-th fiber (N=n), respectively. (Here an extra subscript n designates quantities associated with the n-th fiber.)

Surface fiber

$$\begin{aligned} E_f I\frac{d^4 v_1}{d\hat{x}^4} + P\frac{d^2 v_1}{d\hat{x}^2} - \sigma_{u_1} - \frac{h}{2}\frac{dq_{u_1}}{d\hat{x}} &= 0 \\ q_{u_1} + hE_f\frac{d^2 u_{0_1}}{d\hat{x}^2} &= 0. \end{aligned} \tag{4.29}$$

n-th fiber

$$
\begin{aligned}
E_f I \frac{d^4 v_n}{d\hat{x}^4} + P \frac{d^2 v_n}{d\hat{x}^2} - [\sigma_{u_1} - \sigma_{L_{n-1}}] - \frac{h}{2}\frac{d}{d\hat{x}}[q_{u_n} + q_{L_{n-1}}] = 0 \\
[q_{u_n} - q_{L_{n-1}}] + hE_f \frac{d^2 u_{0_n}}{d\hat{x}^2} = 0.
\end{aligned}
\tag{4.30}
$$

In order to proceed with the solution of (4.29) and (4.30), the shearing and normal tractions (q, σ) developed at the fiber/matrix interface at buckling have to be determined. This can be done by considering the deformation of a typical matrix layer sandwiched between any two fibers. Thus, isolate the n$^{\text{th}}$ and (n+1)$^{\text{st}}$ fibers and the matrix in between (Figure 4.11). To proceed, solving for the displacements in the matrix layer, some boundary conditions have to be imposed at the fiber/matrix interface. As before, sinusoidal perturbations in $u(\hat{x}), v(\hat{x})$ are investigated about the trivial solution (4.5). Thus, for the n$^{\text{th}}$ fiber it is assumed,

$$
\begin{aligned}
u_{0n} &= U_{0n} \cos\alpha\hat{x} \\
v_n &= V_n \sin\alpha\hat{x}.
\end{aligned}
\tag{4.31}
$$

U_{0n}, V_n are the unknown amplitudes of the perturbations $u_n(\hat{x}), v_n(\hat{x})$, respectively, of the n$^{\text{th}}$ fiber.

Next, the deformation of the matrix strip between the n$^{\text{th}}$ and (n+1)$^{\text{st}}$ fibers is considered. With reference to Figure 4.11, it is required to solve (4.11) in the matrix subject to the following boundary conditions

n$^{\text{th}}$ fiber/matrix interface

$$
\begin{aligned}
u_{0n} - \frac{h}{2}\frac{dv_n}{d\hat{x}}\Big|_{\hat{y}_n = \frac{h}{2}} &= u_m\big|_{y=-c} \\
v_n\big|_{\hat{y}_n = \frac{h}{2}} &= v_m\big|_{y=-c}
\end{aligned}
\tag{4.32a}
$$

$(n+1)^{st}$ fiber/matrix interface,

$$u_{0(n+1)} + \frac{h}{2}\frac{dv_{(n+1)}}{d\hat{x}}\Big|_{\hat{y}_{n+1}=-\frac{h}{2}} = u_m\big|_{y=c} \tag{4.32b}$$
$$v_{(n+1)}\big|_{\hat{y}_{n+1}=-\frac{h}{2}} = v_m\big|_{y=c}.$$

Notice that by confining attention to the n^{th} and $(n+1)^{st}$ fibers and the sandwhiched matrix inbetween, it is possible to generate the governing equations for *any fiber*. The interface continuity conditions for displacements are completely specified by (4.32), in that, at *every* fiber/matrix interface, one of the conditions (4.32) will apply.

The solution of (4.11) subject to (4.32) is,

$$\begin{aligned} u_m(x,y) &= (C_1\cosh\alpha y + C_2\sinh\alpha y + C_3 y\cosh\alpha y + C_4 y\sinh\alpha y)\cos\alpha x \\ v_m(x,y) &= (D_1\cosh\alpha y + D_2\sinh\alpha y + D_3 y\cosh\alpha y D_4 y\sinh\alpha y)\sin\alpha x, \end{aligned} \tag{4.33}$$

with,

$$\begin{aligned} D_1 &= C_2 - \frac{C_3}{\alpha}\left(\frac{3-\nu_m}{1+\nu_m}\right) \\ D_2 &= C_1 - \frac{C_4}{\alpha}\left(\frac{3-\nu_m}{1+\nu_m}\right) \\ D_3 &= C_4 \\ D_4 &= C_3. \end{aligned} \tag{4.34}$$

Here, C_i (i=1,4) is related to the unknown amplitudes of the adjacent fibers U_{0n}, $U_{0(n+1)}$, V_n, $V_{(n+1)}$ through the conditions (4.32) by

$$\begin{aligned} C_1 &= m_{11}[U_{0(n+1)} + U_{0n} + \frac{\rho}{2}(V_{(n+1)} - V_n)] + m_{12}[V_{(n+1)} - V_n] \\ C_2 &= m_{21}[U_{0(n+1)} - U_{0n} + \frac{\rho}{2}(V_{(n+1)} + V_n)] + m_{22}[V_{(n+1)} + V_n] \\ \frac{C_3}{\alpha} &= m_{31}[U_{0(n+1)} - U_{0n} + \frac{\rho}{2}(V_{(n+1)} + V_n)] + m_{32}[V_{(n+1)} + V_n] \\ \frac{C_4}{\alpha} &= m_{41}[U_{0(n+1)} + U_{0n} + \frac{\rho}{2}(V_{(n+1)} - V_n)] + m_{42}[V_{(n+1)} - V_n]. \end{aligned} \tag{4.35}$$

The constants $m_{11},.....m_{14}$ and $m_{21},.....m_{24}$ are given in Appendix 4A

Having obtained the displacement field for the matrix strip (4.32) in terms of the boundary values $U_{0(n+1)}$, U_n, $V_{(n+1)}$, V_n, the surface tractions $\sigma_{u_n}, \sigma_{L_{(n-1)}}$, $q_{u_n}, q_{L_{(n-1)}}$ acting on the n$^{\text{th}}$ fiber can be computed.

Thus,

$$\begin{aligned}
\sigma_{u_n} &= \frac{E_m \alpha}{(1-{\nu_m}^2)}[{U^1}_n P_{u_1} + U_{(n+1)} P_{u_2} + V_n P_{u_3} + V_{(n+1)} P_{u_4}]\sin\alpha x \\
\sigma_{L_{(n-1)}} &= \frac{E_m \alpha}{(1-{\nu_m}^2)}[U_{(n-1)} P_{L_1} + {U^2}_n P_{L_2} + V_{(n-1)} P_{L_3} + V_n P_{L_4}]\sin\alpha x \\
q_{u_n} &= G_m \alpha [{U^1}_n R_{u_1} + U_{(n+1)} R_{u_2} + V_n R_{u_3} + V_{(n+1)} R_{u_4}]\cos\alpha x \\
q_{L_{(n-1)}} &= G_m \alpha [U_{(n-1)} R_{L_1} + {U^2}_n R_{L_2} + V_{(n-1)} R_{L_3} + V_n R_{L_4}]\cos\alpha x,
\end{aligned} \tag{4.36}$$

where,

$$\begin{aligned}
{U^1}_n &= U_{0n} - \frac{\rho}{2} V_n \\
{U^2}_n &= U_{0n} + \frac{\rho}{2} V_n \\
U_{(n+1)} &= U_{0(n+1)} + \frac{\rho}{2} V_{n+1} \\
U_{(n-1)} &= U_{0(n-1)} - \frac{\rho}{2} V_{n-1}.
\end{aligned} \tag{4.37}$$

Expressions for $P_{u_1}, ..., R_{u_1}....$, etc. are given in Appendix 4A. Substituting (4.36) into (4.30), the following system of equations for the n$^{\text{th}}$ fiber are obtained:

$$\begin{aligned}
\frac{\rho^2}{12} V_n - \epsilon_0 V_n - \frac{\mu}{\rho(1-{\nu_m}^2)} F_1(U_{0(n-1)}, U_{0n}, U_{0(n+1)}, V_{n-1} ... V_n) \\
+ \frac{\mu^*}{2} F_2(U_{0(n-1)}, ...) = 0 \\
\frac{\mu^*}{\rho} F_3(U_{0(n-1)}, ...) - U_{0n} = 0.
\end{aligned} \tag{4.38}$$

Here, $\mu^* = \frac{G_m}{E_f}$. The functions $F_1, ..F_3$ are *linear* combinations of the six unknown amplitudes $U_{0(n-1)}, U_{0n}, U_{0(n+1)}, V_{n-1}, V_n, V_{n+1}$. These functions are given in Appendix 4A . Similarly for the surface fiber from (4.29) the following equations are obtained.

$$\frac{\rho^2}{12}V_1 - \epsilon_0 V_1 - \frac{\mu}{\rho(1-{\nu_m}^2)}F_4(U_{01}, U_{02}, V_1, V_2) + \frac{\mu^*}{2}F_5(U_{01}, .., V_2) = 0$$
$$\frac{\mu^*}{\rho}F_6(U_{01}, ...V_2) - U_{01} = 0. \tag{4.39}$$

The functions $F_4, ...F_6$ are also given in Appendix 4A.

The system of equations (4.38) and (4.39) can be conveniently arranged in the following form

$$[\widehat{Q}^*][\vec{u}_1] + [\bar{Q}][\vec{u}_2] = 0 \tag{4.40a}$$

$$[Q][\vec{u}_{n-1}] + [\widehat{Q}][\vec{u}_n] + [\bar{Q}][\vec{u}_{n+1}] = 0, \tag{4.40b}$$

where elements of the (2 x 2) matrices $Q, \widehat{Q}$, etc. are arranged in Appendix 4B and

$$\vec{u}_n = \begin{bmatrix} u_{0n} \\ v_n \end{bmatrix}.$$

The system (4.40b) will be referred to as the "global system" in the ensuing discussion. The next step is to obtain solutions to (4.40) subject to appropriate boundary conditions. It is of interest to seek solutions to the perturbation amplitudes (U_{0n}, V_n) that exhibit a decay into the interior of the half plane under consideration. Thus, one seeks values of ϵ_0 that permit this behavior. Of all possible ϵ_0 that fall into this category, the minimum ϵ_0 is identified as the buckling 'load' of the system. Thus, the following mathematical problem is considered.

Solve (4.40) subject to the condition

$$\begin{aligned} &U_{01}, V_1 \quad finite \\ &U_{0n}, V_n \rightarrow 0 \ \ as \ \ n \rightarrow \infty. \end{aligned} \tag{4.41}$$

Notice that (4.40) subject to (4.41) is a *difference equation eigenvalue problem*. Here ϵ_0 is the eigenvalue sought and the amplitudes U_{on}, V_n are the associated eigen-functions. The boundary conditions (4.41) are physically motivated to conform to the experimental observations discussed in the previous chapters. The solution proceeds in the following manner. First, the global system (4.40b) is solved using the boundary condition for large n. This enables one to find the general solution for U_{0n}, V_n up to two arbitrary constants. Then, using the first of conditions (4.41) and the obtained general solution, substitute for U_{01}, V_1 into (4.40a). This results in a (2 x 2) system of homogeneous equations for the two as yet undetermined constants. Vanishing of the determinant associated with this system gives the required condition to obtain ϵ_0. Unlike in the previous case, it is not possible to obtain an explicit expression for ϵ_0 (see (4.26)) . This is because each member of the matrix associated with the final system of equations is a function of ϵ_0.

Next, the solution of the global system (4.40b) will be discussed. This can be written out as

$$\begin{aligned} &q_{11}\big(U_{0(n-1)} - U_{0(n+1)}\big) + \hat{q}_{12}V_n + q_{12}\big(V_{(n-1)} + V_{(n+1)}\big) = 0 \\ &q_{21}\big(U_{0(n-1)} + U_{0(n+1)}\big) + \hat{q}_{21}U_n + q_{22}\big(V_{(n-1)} + V_{(n+1)}\big) = 0. \end{aligned} \tag{4.42}$$

Let

$$\begin{aligned} U_{0n} &= \gamma r^n \\ V_n &= \delta r^n, \end{aligned} \tag{4.43}$$

where δ andγ are arbitrary constants. Then substituting (4.43) into (4.42), the characteristic polynomial associated with the global system is obtained.

$$r^4 + ar^3 + br^2 + ar + 1 = 0. \tag{4.44}$$

Here,

$$\begin{aligned} a &= \frac{q_{12}\hat{q}_{21} + q_{21}\hat{q}_{12}}{q_{12}q_{21} - q_{22}q_{11}} \\ b &= 2\left(\frac{q_{12}q_{21} + q_{22}q_{11}}{q_{12}q_{21} - q_{22}q_{11}}\right) + \frac{\hat{q}_{12}\hat{q}_{21}}{q_{12}q_{21} - q_{11}q_{22}}. \end{aligned} \tag{4.45}$$

Notice that the roots of (4.44) appear as reciprocal pairs. Thus, if r_1 is a root of (4.44), then so is $(\frac{1}{r_1})$. (4.44) can be conveniently reduced to a quadratic by the substitution

$$r + \frac{1}{r} = \rho. \tag{4.46}$$

Then, (4.44) reduces to

$$\rho^2 + a\rho + (b-2) = 0. \tag{4.47}$$

If ρ_1, ρ_2 denotes the two roots of (4.47) , the roots of (4.44) can be written out as

$$
\begin{aligned}
r_1 &= \frac{\rho_1}{2} + \frac{1}{2}\sqrt[2]{{\rho_1}^2 - 4} \\
r_2 &= \frac{\rho_1}{2} - \frac{1}{2}\sqrt[2]{{\rho_1}^2 - 4} \\
r_3 &= \frac{\rho_2}{2} + \frac{1}{2}\sqrt[2]{{\rho_2}^2 - 4} \\
r_4 &= \frac{\rho_2}{2} - \frac{1}{2}\sqrt[2]{{\rho_2}^2 - 4},
\end{aligned}
\tag{4.48}
$$

where,

$$
\begin{aligned}
\rho_1 &= -\frac{a}{2} + \frac{1}{2}\sqrt[2]{a^2 - 4(b-2)} \\
\rho_2 &= -\frac{a}{2} - \frac{1}{2}\sqrt[2]{a^2 - 4(b-2)}.
\end{aligned}
\tag{4.49}
$$

Therefore, the general solution of the global system is

$$
\begin{aligned}
U_{0n} &= \sum_{i=1}^{4} \gamma_i r_i^n \\
V_n &= \sum_{i=1}^{4} \delta_i r_i^n.
\end{aligned}
\tag{4.50a}
$$

Notice that there are eight constants γ_i, δ_i in (4.50) out of which four are independent. The dependence between the constants can be found by substituting (4.50) into (4.42). This results in

$$
\begin{aligned}
\gamma_j &= (-1)^{j+1}\omega_1\,, \qquad j = 1,2 \\
\gamma_k &= (-1)^{k+1}\omega_2\,, \qquad k = 3,4
\end{aligned}
\tag{4.50b}
$$

with,

$$
\omega_j = \frac{q_{12}(r_j^2 + 1) + \hat{q}_{12} r_j}{q_{11}(r_j^2 - 1)}, \qquad j = 1,2.
$$

The boundary condition for large n necessiates that the roots obey

$$|r| < 1. \tag{4.51}$$

This, together with the reciprocity of the roots, reduces the number of unknowns to two. Then, using (4.29) and the first of (4.41), the condition for determining ϵ_0 is obtained. Unlike the first problem, this condition is implicit in ϵ_0 and can be written as

$$G(\epsilon_0, l) = 0. \tag{4.52}$$

Newton's method is used to solve (4.52) for a specified l. Depending on the geometry and material properties of the composite, several cases will be discussed next.

4.4.2 Results and Discussion

Results are computed for composites whose material properties are listed in Table 4.1. For clarity of presentation , the results are displayed in the(ϵ_0, l) plane. In the discussion to follow, the term "decaying solution" is used to refer to solutions of (4.41). The first step is to demarcate the boundaries on the $(\epsilon_0,\ l)$ plane that denote the nature of the roots $r_1, \ldots. r_4$ (ie. real or complex). This can be done by investigating the behavior of the discriminants associated with the two equations (4.46, 4.47) for pairs of values (ϵ_0, l). The results for a particular geometry and material properties are shown in Figures 4.12a and 4.12b. Notice that in the range of interest ($\epsilon_0 \geq 0$), ρ_1, ρ_2 are real. Hence, from (4.48), it is immediately seen that for all values of (ϵ_0, l) for which *both* $\rho_1 < 2$ and $\rho_2 < 2$, *all* roots $r_1 .. r_4$ are complex. Further, by writing $\rho_{1,2}^2 - 4 = i^2(4 - \rho_{1,2}^2)$, in this case, it follows that $|r| = 1$. Thus, there is no possibility of satisfying the second boundary condition (4.41). Therefore, those values of (ϵ_0, l) for which *both* $\rho_1 \geq 2$ and $\rho_2 \geq 2$ are investigated. When at least one of these conditions is violated , ie. when $\rho_1 \geq 2$ and $\rho_2 < 2$ or vice versa, then one pair of roots (4.48) is complex and conjugate while the other pair is real. The corresponding values of (ϵ_0, l) lie above the curve marked as 'curve 1' in Figures 4.12a and 4.12b. The complex roots have the property that $|r| = 1$ and so are immediately excluded on account of the condition (4.51).Of the real pair of roots, one always has $|r| > 1$, due to its reciprocal property. This leaves us to express both U_{0n}, V_n in terms of just one unknown constant. However, (4.40a) involves two conditions on U_{0n}, V_n, which have to be simultaneously satisfied. Thus, there is one degree of freedom missing. Hence, in these situations, ie.for (ϵ_0, l) values lying above 'curve 1', there are no solutions conforming to the mathematical problem posed (4.41). It is seen that 'curve 1' (Figures 4.12a and 4.12b) separates the (ϵ_0, l) plane into two regions. For values of (ϵ_0, l) lying above 'curve 1', no decaying solutions exist. Values of (ϵ_0, l) lying below this curve (corresponding to *both* $\rho_1 > 2$ and $\rho_2 > 2$) furnish solutions for U_{0n} and V_n that conform to the required boundary condition at large n. Of *all* such (ϵ_0, l), the ones that satisfy the condition (4.52) are identified as the required solutions to the problem considered. In the discussion to follow, it becomes clear that, for a given value $\frac{E_f}{E_m}$ and ν_m, there is a limited range of V_f for which decaying solutions can be found conforming to treating the fibers within the assumption of Euler beam theory. First, however, it is imperative to understand the nature of 'curve 1'.

Recall that 'curve 1', shown in Figures 4.12a and 4.12b, is obtained by examining the discriminants associated with the equations (4.46,4.47). It turns out as shown below that this curve also corresponds to the (ϵ_0, l) values predicted by the Rosen shear mode (also known as Rosen's In-plane Mode), hereafter refered to as RIM. The global system (4.40b) can be specialized to the displacement field assumed in RIM, namely,

$$U_{0n} = 0, \quad ...V_{(n-1)} = V_{(n)} = V_{(n+1)}....... \tag{4.53}$$

Correspondingly, the value of ϵ_0 predicted by such a specialization is obtained by substituting (4.53) into (4.40b). One finds then

$$\epsilon_0 \;=\; \hat{q}_{12}\,. \tag{4.54}$$

Values of (ϵ_0, l) conforming to (4.54) and referred to here as 'curve 1' are indeed the RIM prediction. However, in order that (4.54) be a solution to (4.41) it must in addition satisfy (4.40a) and the required boundary condition for large n. Clearly, this is not the case. The reason is that the Rosen shear mode result holds only for a composite of infinite extent, without recourse to a traction free edge. Furthermore, the Rosen result,

$$\sigma_{cr}\big|_{min} \;=\; \frac{G_m}{(1-V_f)},$$

is obtained in the limit $\left(\frac{l}{h}\right) \to \infty$, implying a mode of buckling with a long wave length. Thus, the Rosen prediction ('curve 1') corresponds to buckling of an *infinite* medium where *all* wave lengths $(l \gg h)$ are admissible solutions. Physically, the RIM prediction furnishes values of ϵ_0 corresponding to the equilibrium of the composite in a non-trivial configuration in which *every fiber buckles in an identical manner*. Where appropriate, the RIM prediction is included in the results presented for comparison purposes.

In Figures 4.13a and 4.13b, a plot of variation of strain with l for a composite with a low fiber volume fraction V_f=0.1 is shown. In this figure, the result obtained from the present analysis has been compared with those of RIM and REM (Rosen extensional mode). Notice that the buckling strain as predicted by the present analysis and marked as point **B** is lower than both the RIM and REM predictions. Similar curves for other values of V_f are shown in Figure 4.13c. Here, the minimum point of the curves marked as 'decay mode' shifts to the right with increasing values of V_f. Beyond a certain value of V_f, the minimum is found to disappear. The non-existence of a true minimum implies a continuous dependence of ϵ_0 on the half wave length l. Thus, for a fixed value of $\frac{E_f}{E_m}$ a critical decay buckling mode of short wave-length exists below a certain V_f. Above this value of V_f a short wave length buckling instability is still present but shows a continuous dependence on l. With increasing V_f, the buckling strain increases, while the corresponding critical half wave length decreases as is shown in Figures 4.14 and 4.15. However, under these conditions the thickness of a fiber is comparable to l. In such cases, treating the fiber via beam theory is inadequate. To properly address this question requires treating the fibers as a two-dimensional continuum. Such a treatment is postponed to the future.

A critical strain (ϵ_{cr}) is defined by points corresponding to such as **B** in Figure 4.13a, and when a true minimum does not exist, the minimum of all admissible (ϵ_0, l). Then, Figure 4.14 shows plots of ϵ_{cr} against the volume fraction V_f. In this figure, curves for a composite of large $\frac{E_f}{E_m}$ (=200) and $\nu_m = 0.3$ have also been included for comparison purposes (Figure 4.14c). The corresponding plots for the corresponding critical wave length are shown in Figure 4.15. In Figure 4.14a, the portion of the curve marked **A**-**A**$'$ is a region of almost constant strain. This region spans a range of V_f that is large for small values of the composite's $\frac{E_f}{E_M}$. This can be inferred from Figure 4.14c. The 'section' **A-A$'$** corresponds to the value of ϵ_0 obtained from the previous analysis for a single fiber composite. Physically, this implies that for values of V_f less than that corresponding to point **A$'$**, the fiber spacing is large enough that there are no interactions between fibers. Thus, the buckling is as predicted for a single fiber composite. Beyond point **A$'$**, one can no longer ignore this interaction effect. That this is so was emphasized in our previous discussion on a single fiber composite. There, the existence of a certain critical depth into the matrix to which any surface effects were felt was discussed. It was noted that for a 'soft' composite ($\frac{E_f}{E_m} \approx 200$, say) this depth was larger than for a 'hard' composite ($\frac{E_f}{E_m} \approx 50$, say). Thus, here, it is not surprising that the region of constant strain **A-A$'$** persists further for the softer composite (4.14c). However, it is seen that in situations where the interaction effect is present, the present decay mode prediction yields a higher value of buckling strain as compared with the RIM prediction for a composite of infinite extent. The RIM prediction as reported in the literature and observed in the present experimental investigation overestimates the strength of the composite by about 40%.

Before discussing possible causes for such a discrepancy, the difference in the results between a *plane stress* and *plane strain* approximation for the perturbation problem needs to be addressed. The plane strain result can be generated by making the appropriate substitutions for the elastic constants as stated in chapter 3. Results are computed for the BP907 composite. For the single fiber case, Figure 4.16 shows the critical strain and critical half wave length variation as a function of $\left(\frac{E_f}{E_m}\right)$. With the plane strain approximation, the computed ϵ_{cr} is slightly larger than the corresponding plane stress result, while l_{cr} is slightly lower. The Poisson's ratio of the fiber is assumed as 0.2. The corresponding results for the uni-directional composite exhibit a similar trend as shown in Figure 4.17.

It was seen that values of ϵ_{cr} calculated for the RIM result and the present investigation overestimated the experimentally observed buckling strains. In addition, the present decay mode result is higher than the RIM result. The reason for this latter discrepancy is that the decay mode, which accounts for interaction between adjacent fibers, yields a critical wave length that is a small multiple of the fiber diameter as compared with the longer wave length RIM result. Further, the decay buckling mode is two-dimensional involving a dependence on both the $\hat{x}$ and $\hat{y}$ directions, while the RIM is essentially one dimensional, showing that *all fibers* buckle in an identical manner. Thus, the RIM model is less constrained than the present model. However, it is phsyically unrealistic as compared with the experimental observations reported here, as well as, by Hahn and Williams[4.13], Sohi et al.[4.14] and Hahn et al.[4.22], which indicate a decay mode type of buckling originating at a free edge. In these investigations [4.13,4.14,4.22], evidence of multiple fracture in the damage area was presented. It was also postulated that microbuckling of fibers originated with the buckling of a single fiber which caused tensile stresses to develop in the matrix in between, thus reducing the buckling load of the adjacent straight fiber. This process progressively involved additional fibers as the damage propagated. Both the RIM and the present model enforce perfect bonding conditions between fibers and matrix. In addition, the fibers are assumed to be perfectly aligned in a regular fashion. Both of these simplifications are unrealistic from a physical view-point in that neither are the fibers perfectly aligned nor are they perfectly bonded to the matrix (Evidence to this effect is presented in Figure 4.18 (taken from [4.22]), that show SEM micrographs of the cross-section of a typical virgin specimen). An attempt was made to characterize the imperfect bonding between fibers and matrix in Kulkarni et al.[4.21]. However, no specific parameter was identified that enables quantifying the imperfect nature of the bonding by a suitable measurement in the laboratory. Although, not entirely conclusive, the reasons stated above are the primary causes for the discrepancy between the predictive microbuckling models (RIM and present) and the experimental results reported here and in [4.13,4.14,4.22,4.23].

Apart from the reasons stated above, a possible improvement to the present model to study the localized fiber microbuckling failure occurring near holes, can be identified from the laminate stress analysis presented in chapter 3. There, the pre-buckling stress distribution in the entire plate based on the assumption of *generalized plane stress* was presented. In that analysis, it was shown that the fiber lying adjacent to the hole along the loading direction had a distribution of non-zero surface traction σ_{xy}, σ_y as shown in Figures 3.*b (* denotes 2-6). This fiber corresponds to the surface fiber of the local model that was considered, which was assumed to be traction free. It is felt that the inclusion of these tractions as well as accounting for the non-homogeneous pre-buckling stress distribution (in particular, the $\bar{\sigma}_x$ component which is assumed to be constant here, displayed a variation along the y-direction, as was seen in chapter 3) in analyzing the buckling failure would better simulate conditions in the vicinity of the hole. The procedure to carry out such an analysis requires developing the general equations of equilibrium for a solid slightly disturbed from a state of initial stress. These equations have been derived before by Biezeno and Hencky[4.24], and by Biot[4.25]. A complete formulation of the present problem in the spirit of Biot[4.25] is beyond the scope of this thesis and is suggested for the future.

4.5 References

4.1 Dow, N.J and Gruntfest, I.J (June 1960), "Determination of most-needed, potentially possible improvements in materials for ballistic and space vehicles", General Electric Company, Air Force Contract AF 04(647)-269

4.2 Fried, N. and Kaminetsky, J. (Feb.1964), "The influence of material variables on the compressive properties of parallel filament reinforced plastics ",Proc. of the 19th Annual Technical and Management Conference, Reinforced Plastics Division, Soc. of the Plastics Industry, Inc., pp.(9-A)1-10.

4.3 Leventz, B. (Feb. 1964), "Compressive applications of large diameter fiber reinforced plastics", Proc. of the 19th Annual Technical and Management Conference, Reinforced Plastics division, Soc. of the plastics industry, Inc., pp.(14-D)1-18

4.4 Rosen, B.W (1965), "Mechanics of composite strengthening", Fiber composite materials, American Society for metals, pp.37-75

4.5 Shuart, M.J (Nov.1985), "Short wave-length buckling and shear failures for compression-loaded composite laminates", NASA TM87640.

4.6 Orowan, E. (June 1942), "A type of plastic deformation new in metals", *Nature*, Vol. 149, pp643-644

4.7 Weaver, C.W and Williams, J. (1975), "Deformation of a carbon-epoxy composite under hydrostatic pressure", *J. of Mat. Sci*, Vol. 10, pp 1323-1333.

4.8 Dale, W.C and Baer, E. (1974), "Fiber buckling in composite systems: A model for the ultra-structure of uncalcified collagen tissues", *J. of Mat. Sci*, Vol. 9, pp369-382.

4.9 Robinson, I.M et. al (1986), "Stress induced twinning of polydiacetylene single crystal fibers in composites", *J. of Mat. Sci*, Vol. 21, pp.3440-3444.

4.10 Evans, A.G and Adler, W.F (1983), "Kinking as a mode of structural degradation in carbon fiber composites", *Acta Metallurgica*, Vol. 26, pp.725-738.

4.11 Chaplin, C.R (1977), "Compressive fracture in unidirectional glass reinforced plastics", *J. of Mat. Sci*, Vol. 12, pp.347-352.

4.12 Budiansky, B. (1983), "Micromechanics", *Computers & Structures*, Vol. 16, pp.3-12.

4.13 Hahn, H.T and Williams, J.G (March 1986), "Compression failure mechanisms in unidirectional composites", NASA TM85834.

4.14 Sohi, M.S ,Hahn, H.T and Williams, J.G (Aug. 1984), "The effect of resin toughness and modulus on compressive failure modes of quasi-isotropic Gr/epoxy laminates", NASA TM87604.

4.15 Gough, G.S et al. (Aug. 1939), "The stabilisation of a thin sheet by a continuous supporting medium", *J. Roy. Aero. Soc.*, pp12-43.

4.16 Reissner, M.E (1937), "On the theory of beams resting on a yielding foundation", *Proc. National Academy Sci.*, Vol. 23, pp328-333

4.17 Goodier, J.N (1946), "Cylindrical buckling of sandwich plates", *J.App.Mech.*, Vol. 13, pp A253-60.

4.18 Hoff, N.J and Mautner, S.E (1945), "Buckling of sandwich type panels", *J.Aero.Sci.*, Vol. 12, pp285-97

4.19 Hoff, N.J and Mautner, S.E (Dec 1948), "Bending and buckling of sandwhich beams", *J.Aero.Sci.*, Vol. 15, pp707-720

4.20 Williams, D., Leggett, D.M ,Hopkins, H.G (1941), "Flat sandwich panels under compressive end loads", A.R.C., R & M N0.1987, pp484-507

4.21 Kulkarni, S.V , Rice, J.S and Rosen, B.W (1973),"An investigation of the compressive strength of PRD 49-3/Epoxy composites", NASA-CR-112334

4.22 Hahn, H.T , Sohi, M. and Moon, S. (1986),"Compression failure mechanisms of composite structures", NASA-CR 3988

4.23 Lager, J. and June, R. (1969),"Compressive strength of Boron/Epoxy composites", *J.Comp.Matls*, Vol. 3, pp48-56

4.24 Biezeno, C.B and Hencky, H. (1928), " On the general theory of elastic stability ", *Koninklijke akademie van wetenschappen te Amsterdam, Proc.*, Vol. 31

4.25 Biot, M. (1939)," (a) Non linear theory of elasticity and the linearized case for a body under initial stress ", *Phil.Mag.*, Vol. 27, p468.

Appendix 4A

$$
\begin{aligned}
m_{11} &= \frac{-Ch + \frac{2\bar{k}}{\rho r} Sh}{\Delta^*} \\
m_{12} &= \frac{Sh}{\Delta^*} \\
m_{21} &= \frac{-Sh + \frac{2\bar{k}}{\rho r} Sh}{\Delta^{**}} \\
m_{22} &= \frac{Ch}{\Delta^{**}} \\
m_{31} &= \frac{2Ch}{\rho r \Delta^{**}} \\
m_{32} &= \frac{2Sh}{\rho r \Delta^{**}} \\
m_{41} &= \frac{2Sh}{\rho r \Delta^*} \\
m_{42} &= \frac{2Ch}{\rho r \Delta^*}
\end{aligned}
\tag{4A.1}
$$

With,

$$
\begin{aligned}
\Delta^* &= \frac{2\bar{k}}{\rho r} \sinh \rho r - 2 \\
\Delta^{**} &= \frac{2\bar{k}}{\rho r} \sinh \rho r + 2 \\
Ch &\equiv \cosh\left(\frac{\rho r}{2}\right) \\
Sh &\equiv \sinh\left(\frac{\rho r}{2}\right) \\
\rho &= \frac{2\pi h}{\lambda} \\
\bar{k} &= \frac{3 - \nu_m}{1 + \nu_m} \\
r &= \frac{2c}{h}
\end{aligned}
\tag{4A.2}
$$

$$
\begin{aligned}
P_{u_1} = {} & (1-\nu_m)Chm_{11} + (1-\nu_m)Shm_{21} + [(1-\bar{k})Sh + \frac{\rho r}{2}(1-\nu_m)Ch]m_{31} \\
& + [(1-\bar{k})Ch + \frac{\rho r}{2}(1-\nu_m)Sh]m_{41} \\
P_{u_2} = {} & (1-\nu_m)Chm_{11} - (1-\nu_m)Shm_{21} - [(1-\bar{k})Sh + \frac{\rho r}{2}(1-\nu_m)Ch]m_{31} \\
& + [(1-\bar{k})Ch + \frac{\rho r}{2}(1-\nu_m)Sh]m_{41} \qquad (4A.3) \\
P_{u_3} = {} & -(1-\nu_m)Chm_{12} - (1-\nu_m)Shm_{22} + [(1-\bar{k})Sh + \frac{\rho r}{2}(1-\nu_m)Ch]m_{32} \\
& + [(1-\bar{k})Ch + \frac{\rho r}{2}(1-\nu_m)Sh]m_{42} \\
P_{u_4} = {} & (1-\nu_m)Chm_{12} - (1-\nu_m)Shm_{22} + [(1-\bar{k})Sh + \frac{\rho r}{2}(1-\nu_m)Ch]m_{32} \\
& - [(1-\bar{k})Ch + \frac{\rho r}{2}(1-\nu_m)Sh]m_{42}
\end{aligned}
$$

$$
\begin{aligned}
R_{u_1} &= -2Shm_{11} - 2Chm_{21} - [(1-\bar{k})Ch + \rho rSh]m_{31} \\
&\quad - [(1-\bar{k})Sh + \rho rCh]m_{41} \\
R_{u_2} &= -2Shm_{11} + 2Chm_{21} + [(1-\bar{k})Ch + \rho rSh]m_{31} \\
&\quad - [(1-\bar{k})Sh + \rho rCh]m_{41} \qquad (4A.4) \\
R_{u_3} &= 2Shm_{12} + 2Chm_{22} - [(1-\bar{k})Ch + \rho rSh]m_{32} \\
&\quad - [(1-\bar{k})Sh + \rho rCh]m_{42} \\
R_{u_4} &= -2Shm_{12} + 2Chm_{22} - [(1-\bar{k})Ch + \rho rSh]m_{32} \\
&\quad + [(1-\bar{k})Sh + \rho rCh]m_{42}
\end{aligned}
$$

The following relations hold between the P's and R's.

$$\begin{aligned} P_{L_1} &= P_{u_2} \\ P_{L_2} &= P_{u_1} \\ P_{L_3} &= P_{u_3} \\ P_{L_4} &= P_{u_3} \end{aligned} \tag{4A.5a}$$

$$\begin{aligned} R_{L_1} &= -R_{u_2} \\ R_{L_2} &= -R_{u_1} \\ R_{L_3} &= \ R_{u_3} \\ R_{L_4} &= \ R_{u_4} \end{aligned} \tag{4A.5b}$$

$$\begin{aligned} F_1 = {} & -P_{L_1} U_{n-1} + P_{u_1} {U_n}^1 - P_{L_2} {U_n}^2 + P_{u_2} U_{n+1} \\ & - V_{n-1} P_{L_3} + V_n (P_{u_3} - P_{L_4}) + V_{n+1} P_{u_4} \\ F_2 = {} & \ R_{L_1} U_{n-1} + R_{u_1} {U_n}^1 + R_{L_2} {U_n}^2 + R_{u_2} U_{n+1} \\ & + V_{n-1} R_{L_3} + V_n (R_{u_3} + R_{L_4}) + V_{n+1} R_{u_4} \\ F_3 = {} & -R_{L_1} U_{n-1} + R_{u_1} {U_n}^1 - R_{L_2} {U_n}^2 + R_{u_2} U_{n+1} \\ & - V_{n-1} R_{L_3} + V_n (R_{u_3} - R_{L_4}) + V_{n+1} R_{u_4} \end{aligned} \tag{4A.6}$$

Appendix 4B

$$Q = \begin{pmatrix} q_{11} & q_{12} \\ q_{21} & q_{22} \end{pmatrix} \tag{4A.7}$$

and similarly for $[\widehat{Q}]$ etc.

$$\begin{aligned} q_{11} &= \frac{\mu}{\rho(1-{\nu_m}^2)}[P_{L_1}] + \frac{\mu^*}{2}[R_{L-1}] \\ q_{12} &= \frac{-\mu}{\rho(1-{\nu_m}^2)}[\frac{\rho}{2}P_{L_1} - P_{L_3}] + \frac{\mu^*}{2}[-\frac{\rho}{2}R_{L_1} + R_{L_3}] \\ q_{21} &= \frac{\mu^*}{\rho}[-R_{L_1}] \\ q_{22} &= \frac{\mu^*}{\rho}[\frac{\rho}{2}R_{L_1} - R_{L_3}] \end{aligned}$$

$$\begin{aligned} \hat{q}_{11} &= 0 \\ \hat{q}_{12} &= \frac{\rho^2}{12} - \epsilon_0 - \frac{\mu}{\rho(1-{\nu_m}^2)}[-\frac{\rho}{2}(P_{u_1} + P_{L_2}) \\ &\qquad + 2P_{u_3}] + \frac{\mu^*}{2}[-\frac{\rho}{2}(R_{u_1} - R_{L_2}) + 2R_{u_3}] \\ \hat{q}_{21} &= \mu^*\rho[2R_{u_1}] - 1 \\ \hat{q}_{22} &= 0 \end{aligned}$$

$$\begin{aligned} \bar{q}_{11} &= -q_{11} \\ \bar{q}_{12} &= q_{12} \\ \bar{q}_{21} &= q_{21} \\ \bar{q}_{22} &= -q_{22} \end{aligned}$$

$$\hat{q_{11}}^* = \frac{-\mu}{\rho(1-{\nu_m}^2)}[P_{u_1}] + \frac{\mu^*}{2}R_{u_1}$$

$$\hat{q_{12}}^* = \frac{\rho^2}{12} - \epsilon_0 - \frac{\mu}{\rho(1-{\nu_m}^2)}[\frac{-\rho}{2}P_{u_1} + P_{u_3}]$$

$$+ \frac{\mu^*}{2}[-\frac{\rho}{2}R_{u_1} + R_{u_3}]$$

$$\hat{q_{21}}^* = \frac{\mu^*}{\rho}[R_{u_1}] - 1$$

$$\hat{q_{22}}^* = \frac{\mu^*}{\rho}[-\frac{\rho}{2}R_{u_1} + R_{u_3}]$$

The above expressions for the matrix elements have been simplified by using relations (4A.5) between the R's and P's.

CHAPTER 5.

CONCLUDING REMARKS

5.1 Summary of Experimental Findings

In an attempt to understand the mechanisms for the initiation and spreading of damage in compressively loaded composite laminates containing a circular cutout, a detailed experimental investigation has been carried out. The investigation was aimed at recognizing the distinction between an unfailed laminate and a failed laminate and providing the transitional information that would serve to develop analysis capabilities with an underlying physical basis. This information is seldom obtained by following a purely theoretical path, and it was necessary that this problem be looked at experimentally. Qualitative and quantitative results have been obtained which have been discusssed in the main body of this thesis. The following conclusions have been derived:

i. The initiation of failure in *all* the laminate types investigated is by fiber microbuckling in the 0^0 plies. This failure gradually develops at the hole surface in the form of a fiber jutout failure. When the far-field load reaches a critical value, the corresponding localized value of strain at the hole edge reaches a critical value of $\approx 8600\mu$strain (deduced from the IM series specimen). At this value of local strain, fiber microbuckling failure within the 0^0 plies is seen to occur, resulting in a propagation of the damage into the interior of the specimen. The damage zone extends out to approximately 75% of the hole radius. The microbuckling process results in the 0^0 fibers undergoing large rotations in-plane (XY) as well as out-of-plane (XZ). This leads to the formation of narrow ($\frac{l}{d} \approx 7 - 11$) bands of broken fiber segments that align themselves at an inclination to the loading direction. The initiation occurs at a far-field applied load which is 75-95% of the ultimate failure load of the specimen, the exact value depending on the laminate type. Thus, for all practical purposes the laminate can be termed "failed" once microbuckling of the 0^0 plies occurs.

ii. The surface manifestation of the initiation process is captured by the interferometer as a well defined perturbation in an otherwise smooth fringe pattern.

iii. The interferometric data is substantiated by ultrasonic C-scanning, hole surface photomicrography and sectioning studies under an optical microscope.

iv. Subsequent to 0^0ply damage, delamination cracks are seen to form at ply interfaces close to the location of the 0^0 plies as shown by the photomicrographs. The extent of the initial delaminated portion, the far field load at which the delamination forms and the thickness of the delaminated portion, govern the occurrence of delamination buckling. The load levels at which this occurs as well as the rate (with respect to load) at which this occurs were discussed in detail in chapter 2.

v. The buckling enhances growth of the delminated portions which spread to the undamaged areas of the laminate approximately at right angles to the direction of applied load.

vi. When the delaminated area extends outward to about 75-100% of the hole radius, the growth process is seen to accelerate rapidly. The culmination of this last event is the catastrophic failure of the plate due to a complete loss of flexural stiffness of each of the delaminated portions. The load carrying capacity beyond initiation, at which stage delamination buckling/growth occurs, is dictated by the overall stiffness of the laminates. This, in turn, is governed by the 0^0 ply percentage as discussed in chapter 2.

vii. These results have been observed consistently for laminates of two different material systems and four different stacking sequences tested in the present investigation.

5.2 Review of Analytical Models

From the foregoing conclusions, two specific mechanics problems have been identified. The first problem was addressed in chapter 4 and relates to the initiation of failure. There, a mechanical model was formulated for fiber microbuckling. In particular, the buckling strain's dependence on parameters such as the fiber volume fraction, ratio of the moduli of the constituents was obtained. However, this model was found to be non-conservative in comparison with the experimental results reported in this thesis. Possible causes for such a discrepancy were discussed in chapter 4. In that chapter possible extensions of the the proposed model were also addressed and discussed.

The second problem relates to the buckling and growth of the delaminated portions. As a first step in addressing this problem, the buckling load of a delaminated portion in the form of a sector-plate lying adjacent to the hole has been calculated for an isotropic material, using an approximate Rayleigh-Ritz approach. The details of this analysis is reported in Waas and Babcock [5.1]. The analysis for the growth of the delaminated portions is an immoderate task. Such a task involves considerations of elastic stability and fracture of a multiple-delaminated anisotropic structure, exhibiting bending-stretching coupling. The continuation of [5.1] to study the growth problem, necessitates employing a suitable fracture criterion that governs the spreading of the damage to the undamaged areas of the plate. In this regard mention must be made of the work by Chai,Knauss and Babcock [5.2], Chai,Babcock and Knauss [5.3] and Chai and Babcock [5.4], who successfully modeled the growth of impact damage in compressively loaded laminates using a delamination buckling process coupled with the Griffith criterion [5.5] in fracture mechanics. Such a process could be used in extending the analysis of Waas and Babcock [5.1], but it was felt that such an extension would merely consist of lengthy and tedious algebra, rather than display any fundamental differences in outcome from the analysis of Chai [5.6].

5.3 Suggestions for Future Work

It would be interesting to extend the experimental procedure so that holographic interferometric measurements could be taken from *both* surfaces of the laminate. This would require extra optical equipment as well as two recording devices. Alternatively, holographic interferometry could be carried out on one surface of the laminate, while *shadow moire* interferometry could be carried out on the other specimen surface (in the manner described by Chai [5.6]), which would facilitate control of the resolution of the measurements to be made. The moire method could help in extracting the buckle displacements more precisely. This can be done by designing the moire grid to reduce the number of fringes per frame. Further, this will help in studying the rapid growth process. On the other hand, one could be more sophisticated and, provided there are no financial constraints, invest in state-of-the-art image processing equipment. As a start, a high resolution solid-state camera could replace the video camera to obtain a sharper image having more information content. Next, storing the image directly on a computer (digitally), would facilitate processing the fringe data in a wide variety of ways. For example, extraneous fringes occurring due to rigid body motion could be removed by taking the Fourier transform, filtering and inverse transforming the stored digital data. Other benefits such as contrast enhancement and pixel-level analysis of the data, would improve the accuracy of the measurements. Unfortunately, more often than not, economical considerations can pose some limitations.

The analytical model for microbuckling can be extended to incorporate time-dependent behavior of the matrix and to study the effect of the bond conditions between fibers and matrix on the buckling strain. In this regard, the present analysis has been used to study the buckling behaviour of a single fiber sandwiched between two half-planes. Several cases, pertaining to different bond conditions between the fiber and half-plane, will be studied. Of particular interest is the case of complete unbonding between the fiber and matrix. This is the extreme case of no shear transfer between fiber and matrix. Preliminary results have been promising, in that, a drastic reduction in the buckling load is obtained [5.7]. This work is to be extended to account for partial bonding at the interfaces, time-dependent behavior of the matrix, as well as treating the fibers within the context of a two-dimensional continuum. This investigation is at its preliminary stages, and the author anticipates its fruitful completion in the near future.

5.4 References

5.1 Waas, A. and Babcock, C.D. (1985), "The failure of composite laminates containing a circular cutout under in-plane compression: 1.Delamination Buckling ", GALCIT SM Report 85-29, Caltech, Pasadena, USA.

5.2 Chai, H., Knauss, W.G. and Babcock, C.D. (1983), "Observation of damage growth in compressively loaded laminates ",*Exp.Mech.*, Vol. 23, pp329

5.3 Chai, H., Babcock, C.D. and Knauss, W.G. (1981), "One dimensional modeling of failure in laminated plates by delamination buckling", *Int.J.Solids Structures*, Vol. 17, pp1069.

5.4 Chai, H. and Babcock, C.D. (1985), " Two-dimensional compressive modeling of compressive failure in delaminated laminates", *J.Comp.Matls*, Vol. 19, pp67-98.

5.5 Sih, G.C. and Liebowitz, H. (1967), " On the Griffith energy criterion for brittle fracture", *Int.J.Solids Structures*, Vol. 3, pp1-22

5.6 Chai, H. (1982), " The growth of impact damage in compressively loaded laminates", P.hD thesis, Caltech, Pasadena, USA.

5.7 Minahen, T. and Knauss, W.G. (1987), unpublished work, Caltech, Pasadena, USA.

Young's moduli of conventional structural materials

Material	S.G	E p.s.i x 10^6	E MN/m^2	$\frac{E}{S.G}$ p.s.i x 10^6	$\frac{E}{S.G}$ MN/m^2
Molybdenum	10.5	40.0	270,000	3.9	25,000
Iron and steel	7.8	30.0	210,000	3.8	25,000
Titanium	4.5	17.0	120,000	3.9	25,000
Aluminium	2.7	10.5	73,000	3.9	25,000
Common glasses	2.5	10.0	70,000	4.0	26,000
Magnesium	1.7	6.0	42,000	3.7	24,000
Wood-spruce parallel to grain	0.5	1.9	13,000	3.8	25,000

Some high specific modulus materials

Material	S.G	E p.s.i x 10^6	E MN/m^2	$\frac{E}{S.G}$ p.s.i x 10^6	$\frac{E}{S.G}$ MN/m^2	T_m
Aluminium nitride	3.3	50	340,000	15	103,000	2,450
Alumina	4.0	55	380,000	14	95,000	2,020
Boron	2.3	60	410,000	26	180,000	2,300
Beryllia	3.0	55	380,000	18	130,000	2,530
Beryllium	1.8	44	300,000	24	170,000	1,350
Carbon whiskers	2.3	110	750,000	48	330,000	3,500
Magnesia	3.6	41	280,000	11	78,000	2,800
Silicon	2.4	23	160,000	10	66,000	1,400
Silicon carbide	3.2	75	510,000	23	160,000	2,600
Silicon nitride	3.2	55	380,000	17	120,000	1,900
Titanium nitride	5.4	50	340,000	9	63,000	2,950

- E - Young's modulus
- S.G - Specific gravity (grams/c.c)
- T_m - Melting point ^{0}C

Table 1.1 - Comparison of Young's moduli and Specific stiffness ($\frac{E}{S.G}$) of conventional materials and typical constituents of composite materials (from Gordon [1.2]).

SPEC./TYPE	HOLE DIA. (cm)	THICKNESS (mm)	P_i(KN)	P_f(KN)
TB1-AS	2.54	7.51	126.0	127.0*
TB2-AS	2.54	7.51	124.0	125.0*
TB10-AS	2.54	7.53	124.0	127.0
TB12-AS	2.54	7.53	125.0	127.0
TB7-BS	2.54	7.51	64.0	91.0
TB13-BS	2.54	7.47	69.0	90.0
TB6-BL	2.54	7.51	127.0	168.0
TB11-BL	2.54	7.53	123.0	165.0**
TB9-BL	2.54	7.51	119.0	169.0
TB14-AS	1.90	7.47	130.0	142.0
TB17-AS	1.90	7.53	128.0	143.0**
TB16-BS	1.90	7.47	70.0	97.0**
TB18-BS	1.90	7.53	79.0	110.0
TB15-AS	1.27	7.47	152.0	161.0**

- * - Load held constant after initiation.
- ** - Maximum load sustained. Specimen unloaded for microscopic examination.

Table 2.1 - Test results for **T300/BP907** laminates.

SPEC./TYPE	HOLE DIA. (cm)	THICKNESS (mm)	P_i(KN)	P_f(KN)
IM2-AS	2.54	7.44	128.5	144.1
IM4-AS	2.54	7.31	135.7	141.9
IM5-AS	2.54	7.33	124.8	129.0
IM7-AS	2.54	7.33	125.0	133.2
IM16-AS[4]	2.54	7.32	119.2	128.3
IM20-AS	2.54	7.36	127.7	132.8
IM21-AS[4]	2.54	7.32	125.0	134.3
IM29-AS	2.54	7.32	125.9	133.2
IM1-BS	2.54	7.38	68.7	97.8
IM3-BS	2.54	7.32	72.0	88.3
IM6-BS	2.54	7.36	70.5	92.1
IM8-BS[4]	2.54	7.36	67.2	89.4
IM9-BS[4]	2.54	7.33	72.1	89.8
IM19-BS[4]	2.54	7.36	68.9	76.3
IM32-BS	2.54	7.30	60.0	90.3
IM24-BL[4]	2.54	7.36	127.0	136.3
IM25-BL[4]	2.54	7.44	123.2	165.5
IM28-BL	2.54	7.33	114.3	164.1
IM11-CS	2.54	7.38	83.0	91.0
IM13-CS	2.54	7.36	87.2	91.6
IM15-CS[4]	2.54	7.31	81.8	91.2
IM18-CS	2.54	7.38	88.5	93.0
IM31-CS	2.54	7.36	85.0	92.7
IM22-CL[2,4]	2.54	7.36	—	135.7
IM26-CL	2.54	7.33	143.0	164.6
IM10-DS	2.54	7.38	72.5	87.6
IM12-DS[1]	2.54	7.25	74.3	95.0
IM14-DS[1]	2.54	7.36	75.4	90.3
IM17-DS[4]	2.54	7.28	75.6	79.4
IM30-DS[3]	2.54	7.28	76.5	82.3
IM23-DL[4]	2.54	7.33	128.8	150.1
IM27-DL	2.54	7.28	136.6	147.0

- [1] Failure initiated at the hole surface with no indication of propagation. Final failure occured abruptly.

- [2] Specimen unloaded prior to indication of failure initiation.

- [3] Transients in the power lines driving the servo-controller led to pre-mature initiation.

- [4] Maximum load sustained. Specimen unloaded for microscopic examination.

Table 2.2 - Test results for **IM7/8551-7** laminates.

		P_i				P_f			
Type	Zero Ply %	No. of Specs. (N)	Mean P_i	σ_x	$\frac{\sigma_x}{\sqrt{N}}$	No. of Specs. (N)	Mean P_f	σ_x	$\frac{\sigma_x}{\sqrt{N}}$
A	42	8	126.5	4.6	1.6	6	135.7	5.9	2.4
B	8	7	68.5	4.2	1.6	4	92.1	4.1	2.0
C	25	5	85.1	2.8	1.2	4	92.1	0.9	0.4
D	25	4	74.4	1.4	0.7	3	91.0	3.7	2.1

- Standarad deviation $\sigma_x = \sqrt[2]{\frac{1}{N-1}\sum_{i=1}^{N}(x_i - \bar{x})^2}$

- Standard deviation of the mean $\equiv \frac{\sigma_x}{\sqrt[2]{N}}$

Table 2.3 - Averaged initiation and final failure loads for IM series specimens.

SPEC./TYPE	P_i	$\epsilon_{x_a}^H$	$\epsilon_{x_b}^H$	$\epsilon_{x_a}^A$	$\epsilon_{x_b}^A$	$\epsilon_{x_a}^B$
IM20-AS	127.7	8763	300	—	—	4128
IM21-AS	125.0	8006	688	3210	94	4123
IM29-AS	125.9	7748	340	2888	158	3712
IM19-BS	68.9	8894	1202	—	—	4922
IM32-BS	60.0	8210	290	3443	18	3928
IM24-BL	127.0	7062	2594	2973	1068	*
IM25-BL	123.2	7584	2332	2493	435	2871
IM28-BL	114.3	8612	213	4032	*	3632
IM18-CS	88.5	9026	1036	—	—	—
IM31-CS	85.0	9020	936	2522	37	3350
IM26-CL	143.0	6958	2494	2016	188	3011
IM22-CL[1]	—	6041	*	2098	6	1923
IM30-DS	76.5	6828	2286	2647	111	3305
IM23-DL	128.8	5896	30	2265	*	2878
IM27-DL	136.6	7366	620	2410	102	2317

- Note–Strain values are in μ-strain (strain x 10^6)
- [1]Specimen unloaded prior to initiation. Strain values quoted are a load of 101.0 KN
- * bending strain unavailable; poorly bonded strain gage. Correspo strain value quoted is from one surface gage (see plots of Load vs
- P_i - Applied load at initiation (KN)
- $\epsilon_{x_a}^H$ - Axial-strain at hole edge
- $\epsilon_{x_b}^H$ - Bending-strain at hole edge
- $\epsilon_{x_a}^A$ - Axial-strain at far-field location 'A'
- $\epsilon_{x_b}^A$ - Bending-strain at far-field location 'A'
- $\epsilon_{x_a}^B$ - Axial-strain at far-field location 'B'
- $\epsilon_{x_b}^B$ - Bending-strain at far-field location 'B'

Table 2.4 - Strain values at failure from strain gage measurements for IM7/8 laminates.

SPEC./TYPE	AVG. STRAIN AT INITIATION (μstrain)
A	8385
B	8612
C	9020
D	6697

Table 2.5 - Averaged local strain values at the hole edge, at initiation-IM series specimens.

Table 3.1 - 0^0-ply material properties.

Material	$E_x(GPa)$	$E_y(GPa)$	G_{xy}	ν_{xy}	Thickness(m)
T300/BP907	111	13.0	6.40	0.38	$1.55\text{x}10^{-4}$
IM7/8551-7	141	6.69	3.17	0.33	$1.50\text{x}10^{-4}$

Table 3.2 -laminate material properties.

Laminate Type	Material	$E_x(GPa)$	$E_y(GPa)$	$G_{xy}(GPa)$	ν_{xy}
A	T300/BP907	60.6	31.1	17.0	0.464
B	T300/BP907	31.1	60.6	17.0	0.238
A	IM7/8551-7	70.0	30.7	19.4	0.529
B	IM7/8551-7	30.7	70.0	19.4	0.232
C	IM7/8551-7	51.5	51.5	19.4	0.320
D	IM7/8551-7	51.5	51.5	19.4	0.320

$$1Psi \equiv 6895Pa$$

Table 3.3 -laminate configurations.

Type	Stacking sequence
A	$(+45/-45/0_2/+45/-45/0_2/+45/-45/0/90)_{2s}$
B	$(-45/+45/90_2/-45/+45/90_2/-45/+45/90/0)_{2s}$
C	$(+45_6/-45_6/0_6/90_6)_s$
D	$(-45_6/+45_6/90_6/0_6)_s$

Table 3.4 -Stress Concentration Factors.

Laminate Type	Material	**SCF** at (0,1)	**SCF** for 0^0-ply at (0,1)
A	T300/BP907	3.33	6.08
B	T300/BP907	2.67	9.59
A	IM7/8551-7	3.36	6.73
B	IM7/8551-7	2.56	11.8
C	IM7/8551-7	3.00	8.20
D	IM7/8551-7	3.00	8.20

Table 3.5a-Laminate constitutive behavior.

Laminate: Type A

Stacking Sequence: *see* **Table III**

Material: T300/BP907

Nominal Ply Properties

Longitudinal Modulus, $E_1 =$ 111 Gpa

Transverse Modulus, $E_2 =$ 13.0 Gpa

Shear Modulus, $G_{12} =$ 6.40 Gpa

Major Poisson's Ratio, $\nu_{12} =$ 0.38

Ply Thickness, $t =$ 1.55 x 10^{-4} m

Laminate Stiffness Parameters

$$\begin{bmatrix} \mathrm{N} \\ \\ \mathrm{M} \end{bmatrix} = \begin{bmatrix} \mathrm{A} & \mathrm{B} \\ \\ \mathrm{B} & \mathrm{D} \end{bmatrix} \begin{bmatrix} \epsilon \\ \\ \epsilon \end{bmatrix}$$

Units:

A_{ij} : GN/m

D_{ij} : x 10^{-8} $GN - m$, $\quad i, j = 1, 2, 6$

$$\begin{bmatrix} \mathrm{N}_x \\ \mathrm{N}_y \\ \mathrm{N}_{xy} \\ \mathrm{M}_x \\ \mathrm{M}_y \\ \mathrm{M}_{xy} \end{bmatrix} = \begin{bmatrix} 0.509 & 0.121 & 0.000 & 0.00 & 0.00 & 0.00 \\ 0.121 & 0.261 & 0.000 & 0.00 & 0.00 & 0.00 \\ 0.000 & 0.000 & 0.127 & 0.00 & 0.00 & 0.00 \\ 0.000 & 0.000 & 0.000 & 236 & 60.7 & 2.88 \\ 0.000 & 0.000 & 0.000 & 60.7 & 110 & 2.88 \\ 0.000 & 0.000 & 0.000 & 2.88 & 2.88 & 65.6 \end{bmatrix} \begin{bmatrix} \epsilon_x \\ \epsilon_y \\ \epsilon_{xy} \\ \kappa_x \\ \kappa_y \\ \kappa_{xy} \end{bmatrix}$$

$$\epsilon_x = \frac{\partial u}{\partial x}, \quad \epsilon_y = \frac{\partial v}{\partial y}, \quad \epsilon_{xy} = \frac{\partial v}{\partial x} + \frac{\partial u}{\partial y}$$

$$\kappa_x = -\frac{\partial^2 w}{\partial x^2}, \quad \kappa_y = -\frac{\partial^2 w}{\partial y^2}, \quad \kappa_{xy} = -\frac{2\partial^2 w}{\partial x \partial y}$$

Table 3.5b

Laminate: Type B

Stacking Sequence: *see* **Table III**

Material: T300/BP907

Nominal Ply Properties

Longitudinal Modulus, $E_1 =$ 111 Gpa

Transverse Modulus, $E_2 =$ 13.0 Gpa

Shear Modulus, $G_{12} =$ 6.40 Gpa

Major Poisson's Ratio, $\nu_{12} =$ 0.38

Ply Thickness, $t =$ 1.55 x 10^{-4} m

Laminate Stiffness Parameters

$$\begin{bmatrix} \mathrm{N} \\ \\ \mathrm{M} \end{bmatrix} = \begin{bmatrix} \mathrm{A} & \mathrm{B} \\ \\ \mathrm{B} & \mathrm{D} \end{bmatrix} \begin{bmatrix} \epsilon \\ \\ \epsilon \end{bmatrix}$$

Units:

A_{ij} : GN/m

D_{ij} : x 10^{-8} $GN-m$, $\quad i,j = 1,2,6$

$$\begin{bmatrix} \mathrm{N}_x \\ \mathrm{N}_y \\ \mathrm{N}_{xy} \\ \mathrm{M}_x \\ \mathrm{M}_y \\ \mathrm{M}_{xy} \end{bmatrix} = \begin{bmatrix} 0.261 & 0.121 & 0.000 & 0.00 & 0.00 & 0.00 \\ 0.121 & 0.509 & 0.000 & 0.00 & 0.00 & 0.00 \\ 0.000 & 0.000 & 0.127 & 0.00 & 0.00 & 0.00 \\ 0.000 & 0.000 & 0.000 & 110 & 60.7 & 2.88 \\ 0.000 & 0.000 & 0.000 & 60.7 & 236 & 2.88 \\ 0.000 & 0.000 & 0.000 & 2.88 & 2.88 & 65.6 \end{bmatrix} \begin{bmatrix} \epsilon_x \\ \epsilon_y \\ \epsilon_{xy} \\ \kappa_x \\ \kappa_y \\ \kappa_{xy} \end{bmatrix}$$

$$\epsilon_x = \frac{\partial u}{\partial x}, \quad \epsilon_y = \frac{\partial v}{\partial y}, \quad \epsilon_{xy} = \frac{\partial v}{\partial x} + \frac{\partial u}{\partial y}$$

$$\kappa_x = -\frac{\partial^2 w}{\partial x^2}, \quad \kappa_y = -\frac{\partial^2 w}{\partial y^2}, \quad \kappa_{xy} = -\frac{2\partial^2 w}{\partial x \partial y}$$

Table 3.5c

Laminate: Type A

Stacking Sequence: *see* **Table III**

Material: IM7/8551-7

Nominal Ply Properties

Longitudinal Modulus, $E_1 =$ 141 Gpa

Transverse Modulus, $E_2 =$ 6.69 Gpa

Shear Modulus, $G_{12} =$ 3.17 Gpa

Major Poisson's Ratio, $\nu_{12} =$ 0.33

Ply Thickness, $t =$ 1.50 x 10^{-4} m

Laminate Stiffness Parameters

$$\begin{bmatrix} \mathrm{N} \\ \mathrm{M} \end{bmatrix} = \begin{bmatrix} \mathrm{A} & \mathrm{B} \\ \mathrm{B} & \mathrm{D} \end{bmatrix} \begin{bmatrix} \epsilon \\ \epsilon \end{bmatrix}$$

Units:

A_{ij} : GN/m

D_{ij} : x 10^{-8} $GN-m$, $\quad i,j = 1,2,6$

$$\begin{bmatrix} \mathrm{N}_x \\ \mathrm{N}_y \\ \mathrm{N}_{xy} \\ \mathrm{M}_x \\ \mathrm{M}_y \\ \mathrm{M}_{xy} \end{bmatrix} = \begin{bmatrix} 0.577 & 0.134 & 0.000 & 0.00 & 0.00 & 0.00 \\ 0.134 & 0.253 & 0.000 & 0.00 & 0.00 & 0.00 \\ 0.000 & 0.000 & 0.140 & 0.00 & 0.00 & 0.00 \\ 0.000 & 0.000 & 0.000 & 250 & 64.1 & 3.50 \\ 0.000 & 0.000 & 0.000 & 64.1 & 95.8 & 3.50 \\ 0.000 & 0.000 & 0.000 & 3.50 & 3.50 & 67.2 \end{bmatrix} \begin{bmatrix} \epsilon_x \\ \epsilon_y \\ \epsilon_{xy} \\ \kappa_x \\ \kappa_y \\ \kappa_{xy} \end{bmatrix}$$

$$\epsilon_x = \frac{\partial u}{\partial x}, \quad \epsilon_y = \frac{\partial v}{\partial y}, \quad \epsilon_{xy} = \frac{\partial v}{\partial x} + \frac{\partial u}{\partial y}$$

$$\kappa_x = -\frac{\partial^2 w}{\partial x^2}, \quad \kappa_y = -\frac{\partial^2 w}{\partial y^2}, \quad \kappa_{xy} = -\frac{2\partial^2 w}{\partial x \partial y}$$

Table 3.5d

Laminate: Type B

Stacking Sequence: *see* **Table III**

Material: IM7/8551-7

Nominal Ply Properties

Longitudinal Modulus, $E_1 =$ 141 Gpa

Transverse Modulus, $E_2 =$ 6.69 Gpa

Shear Modulus, $G_{12} =$ 3.17 Gpa

Major Poisson's Ratio, $\nu_{12} =$ 0.33

Ply Thickness, $t =$ 1.50 x 10^{-4} m

Laminate Stiffness Parameters

$$\begin{bmatrix} \mathrm{N} \\ \mathrm{M} \end{bmatrix} = \begin{bmatrix} \mathrm{A} & \mathrm{B} \\ \mathrm{B} & \mathrm{D} \end{bmatrix} \begin{bmatrix} \epsilon \\ \epsilon \end{bmatrix}$$

Units:

A_{ij} : GN/m

D_{ij} : x 10^{-8} $GN - m$, $\quad i, j = 1, 2, 6$

$$\begin{bmatrix} \mathrm{N}_x \\ \mathrm{N}_y \\ \mathrm{N}_{xy} \\ \mathrm{M}_x \\ \mathrm{M}_y \\ \mathrm{M}_{xy} \end{bmatrix} = \begin{bmatrix} 0.253 & 0.134 & 0.000 & 0.00 & 0.00 & 0.00 \\ 0.134 & 0.577 & 0.000 & 0.00 & 0.00 & 0.00 \\ 0.000 & 0.000 & 0.140 & 0.00 & 0.00 & 0.00 \\ 0.000 & 0.000 & 0.000 & 95.8 & 64.1 & 3.50 \\ 0.000 & 0.000 & 0.000 & 64.1 & 250 & 3.50 \\ 0.000 & 0.000 & 0.000 & 3.50 & 3.50 & 67.2 \end{bmatrix} \begin{bmatrix} \epsilon_x \\ \epsilon_y \\ \epsilon_{xy} \\ \kappa_x \\ \kappa_y \\ \kappa_{xy} \end{bmatrix}$$

$$\epsilon_x = \frac{\partial u}{\partial x}, \quad \epsilon_y = \frac{\partial v}{\partial y}, \quad \epsilon_{xy} = \frac{\partial v}{\partial x} + \frac{\partial u}{\partial y}$$

$$\kappa_x = -\frac{\partial^2 w}{\partial x^2}, \quad \kappa_y = -\frac{\partial^2 w}{\partial y^2}, \quad \kappa_{xy} = -\frac{2\partial^2 w}{\partial x \partial y}$$

Table 3.5e

Laminate: Type C

Stacking Sequence: *see* **Table III**

Material: IM7/8551-7

Nominal Ply Properties

Longitudinal Modulus, $E_1 =$ 141 Gpa

Transverse Modulus, $E_2 =$ 6.69 Gpa

Shear Modulus, $G_{12} =$ 3.17 Gpa

Major Poisson's Ratio, $\nu_{12} =$ 0.33

Ply Thickness, $t =$ 1.50 x 10^{-4} m

Laminate Stiffness Parameters

$$\begin{bmatrix} \mathrm{N} \\ \\ \mathrm{M} \end{bmatrix} = \begin{bmatrix} \mathrm{A} & \mathrm{B} \\ \\ \mathrm{B} & \mathrm{D} \end{bmatrix} \begin{bmatrix} \epsilon \\ \\ \epsilon \end{bmatrix}$$

Units:

A_{ij} : GN/m

D_{ij} : x 10^{-8} $GN-m$, $\quad i,j = 1,2,6$

$$\begin{bmatrix} \mathrm{N}_x \\ \mathrm{N}_y \\ \mathrm{N}_{xy} \\ \mathrm{M}_x \\ \mathrm{M}_y \\ \mathrm{M}_{xy} \end{bmatrix} = \begin{bmatrix} 0.415 & 0.134 & 0.000 & 0.00 & 0.00 & 0.00 \\ 0.134 & 0.415 & 0.000 & 0.00 & 0.00 & 0.00 \\ 0.000 & 0.000 & 0.140 & 0.00 & 0.00 & 0.00 \\ 0.000 & 0.000 & 0.000 & 161 & 96.1 & 29.5 \\ 0.000 & 0.000 & 0.000 & 64.1 & 122 & 29.5 \\ 0.000 & 0.000 & 0.000 & 29.5 & 29.5 & 98.5 \end{bmatrix} \begin{bmatrix} \epsilon_x \\ \epsilon_y \\ \epsilon_{xy} \\ \kappa_x \\ \kappa_y \\ \kappa_{xy} \end{bmatrix}$$

$$\epsilon_x = \frac{\partial u}{\partial x}, \quad \epsilon_y = \frac{\partial v}{\partial y}, \quad \epsilon_{xy} = \frac{\partial v}{\partial x} + \frac{\partial u}{\partial y}$$

$$\kappa_x = -\frac{\partial^2 w}{\partial x^2}, \quad \kappa_y = -\frac{\partial^2 w}{\partial y^2}, \quad \kappa_{xy} = -\frac{2\partial^2 w}{\partial x \partial y}$$

Table 3.5f

Laminate: Type D

Stacking Sequence: *see* **Table III**

Material: IM7/8551-7

Nominal Ply Properties

Longitudinal Modulus, $E_1 =$ 141 Gpa

Transverse Modulus, $E_2 =$ 6.69 Gpa

Shear Modulus, $G_{12} =$ 3.17 Gpa

Major Poisson's Ratio, $\nu_{12} =$ 0.33

Ply Thickness, $t =$ 1.50 x 10^{-4} m

Laminate Stiffness Parameters

$$\begin{bmatrix} \mathrm{N} \\ \\ \mathrm{M} \end{bmatrix} = \begin{bmatrix} \mathrm{A} & \mathrm{B} \\ \\ \mathrm{B} & \mathrm{D} \end{bmatrix} \begin{bmatrix} \epsilon \\ \\ \epsilon \end{bmatrix}$$

Units:

A_{ij} : GN/m

D_{ij} : x 10^{-8} $GN-m, \qquad i,j = 1,2,6$

$$\begin{bmatrix} \mathrm{N}_x \\ \mathrm{N}_y \\ \mathrm{N}_{xy} \\ \mathrm{M}_x \\ \mathrm{M}_y \\ \mathrm{M}_{xy} \end{bmatrix} = \begin{bmatrix} 0.415 & 0.134 & 0.000 & 0.00 & 0.00 & 0.00 \\ 0.134 & 0.415 & 0.000 & 0.00 & 0.00 & 0.00 \\ 0.000 & 0.000 & 0.140 & 0.00 & 0.00 & 0.00 \\ 0.000 & 0.000 & 0.000 & 161 & 96.1 & 29.5 \\ 0.000 & 0.000 & 0.000 & 64.1 & 122 & 29.5 \\ 0.000 & 0.000 & 0.000 & 29.5 & 29.5 & 98.5 \end{bmatrix} \begin{bmatrix} \epsilon_x \\ \epsilon_y \\ \epsilon_{xy} \\ \kappa_x \\ \kappa_y \\ \kappa_{xy} \end{bmatrix}$$

$$\epsilon_x = \frac{\partial u}{\partial x}, \quad \epsilon_y = \frac{\partial v}{\partial y}, \quad \epsilon_{xy} = \frac{\partial v}{\partial x} + \frac{\partial u}{\partial y}$$

$$\kappa_x = -\frac{\partial^2 w}{\partial x^2}, \quad \kappa_y = -\frac{\partial^2 w}{\partial y^2}, \quad \kappa_{xy} = -\frac{2\partial^2 w}{\partial x \partial y}$$

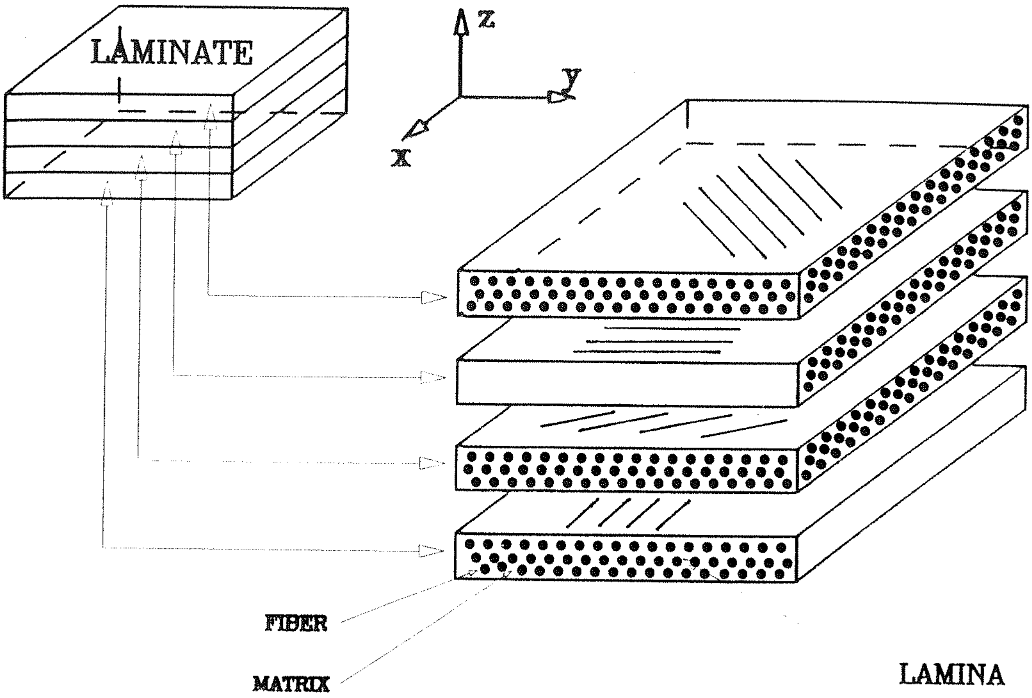

Figure 1.1 Schematic of typical fiber composite laminate showing constituents

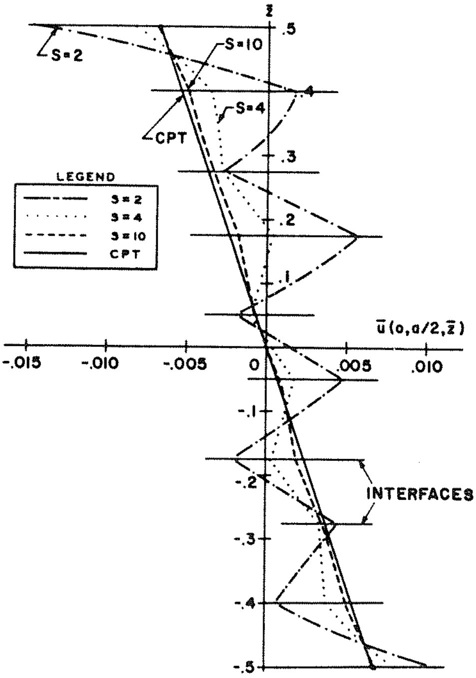

Figure 1.2 Displacement distribution through the thickness, as a function of aspect ratio S ($=\frac{l}{h}$)*, for static bending of nine layer Graphite/Epoxy beam, showing convergence towards CLT (or CPT) solution with increasing S (from [1.8]).*

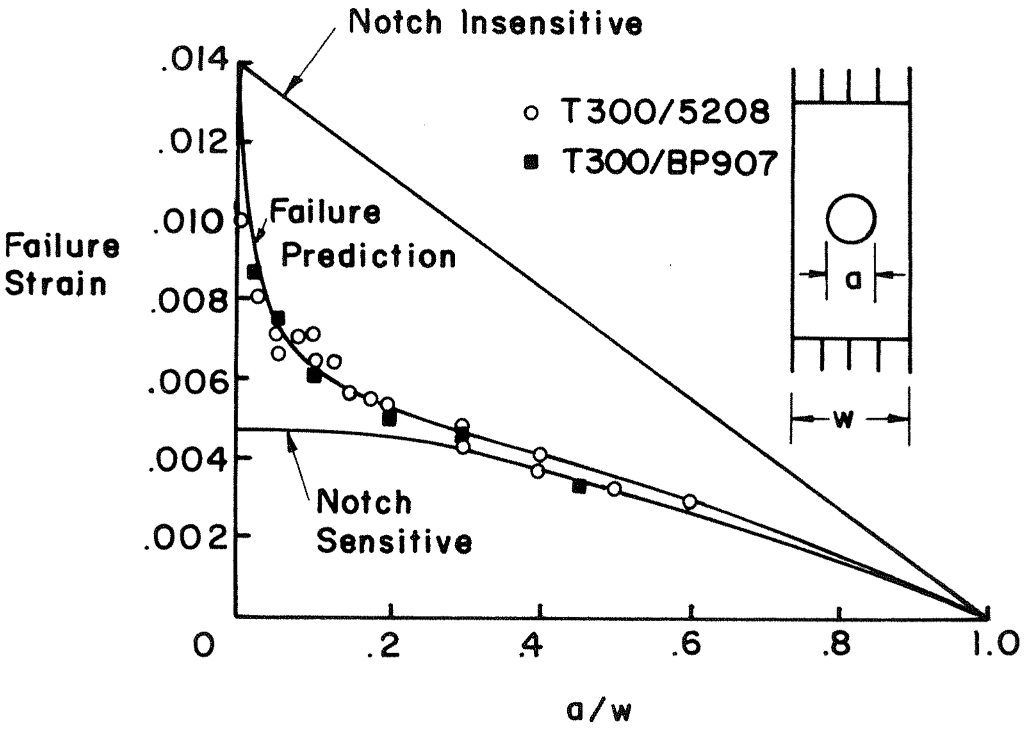

Figure 2.1 Summary of test results for T300/BP907 and T300/5208 Composite laminates. w= 13 cm (from [2.1]).

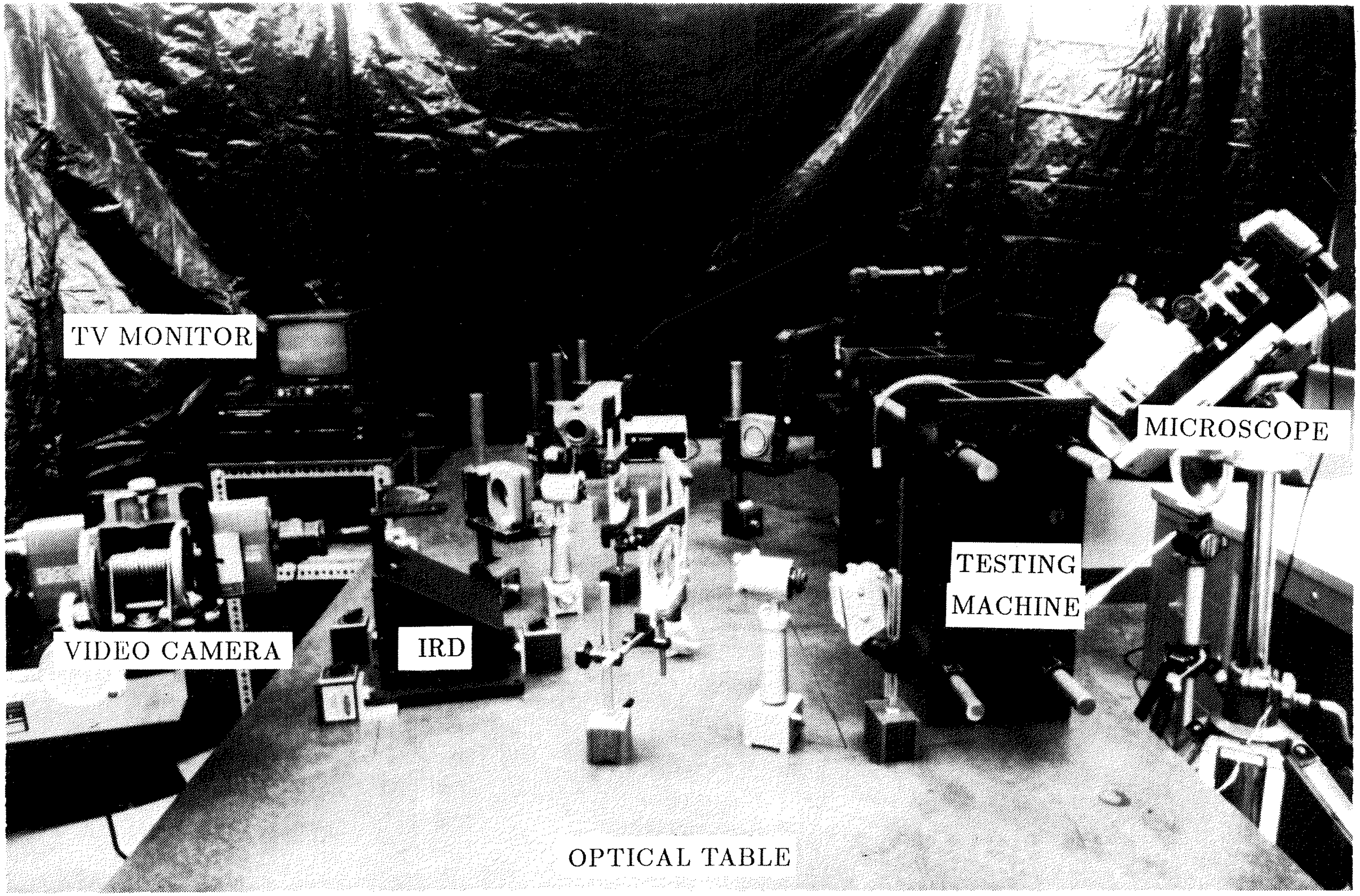

Figure 2.2 Experimental set up.

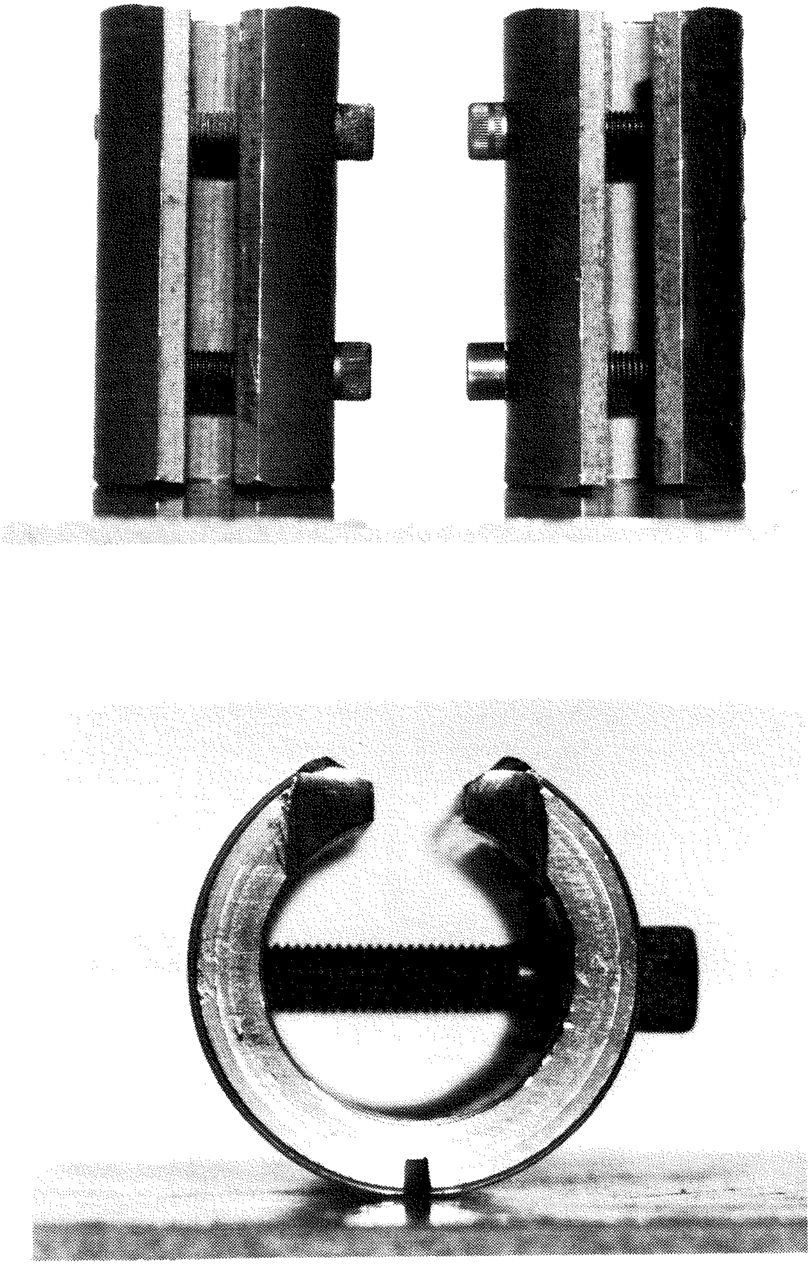

Figure 2.3 *Typical set of edge stiffeners.*

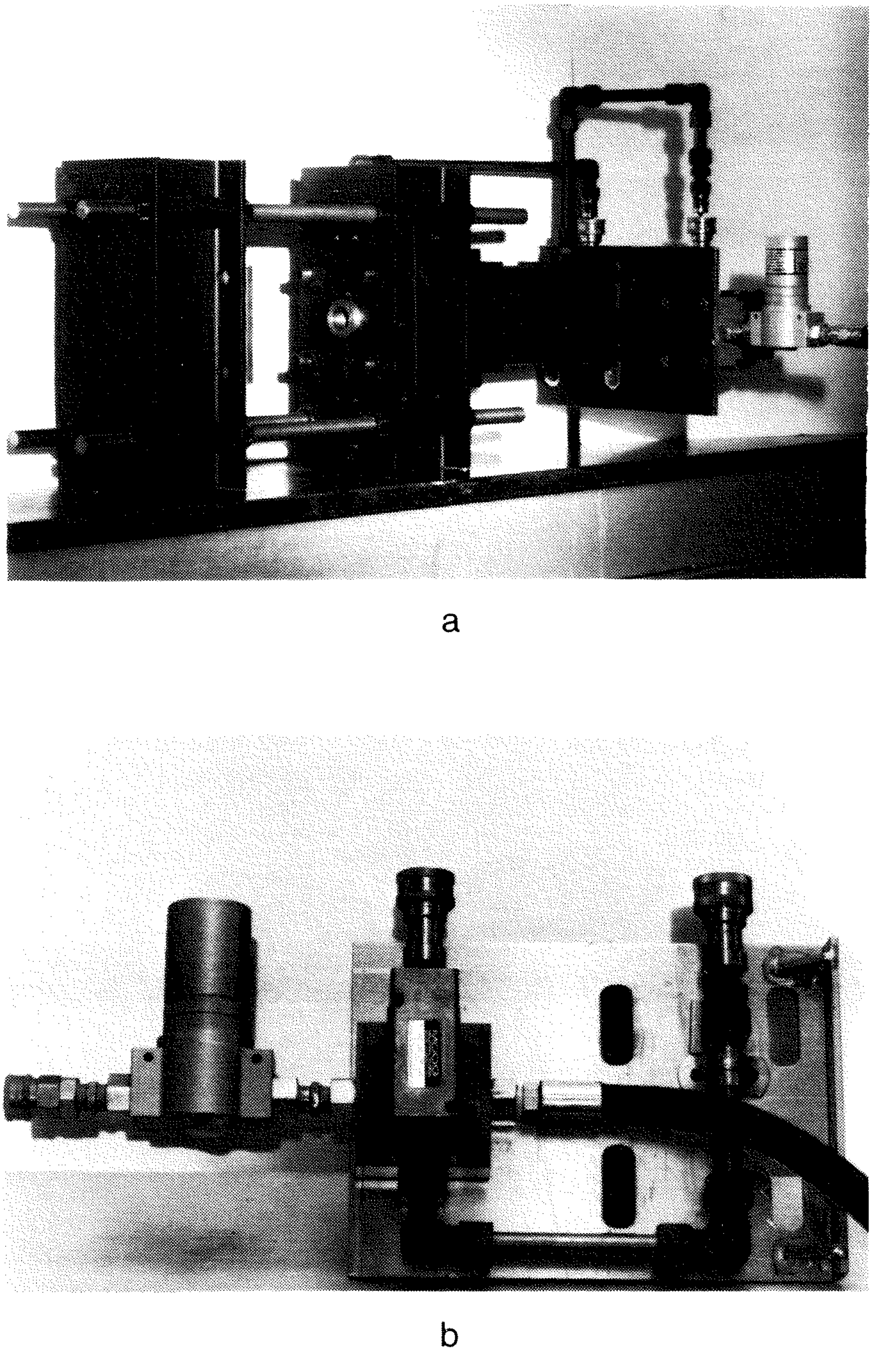

a

b

Figure 2.4 (a) Testing machine on optical table. (b) Servo-valve and accessories.

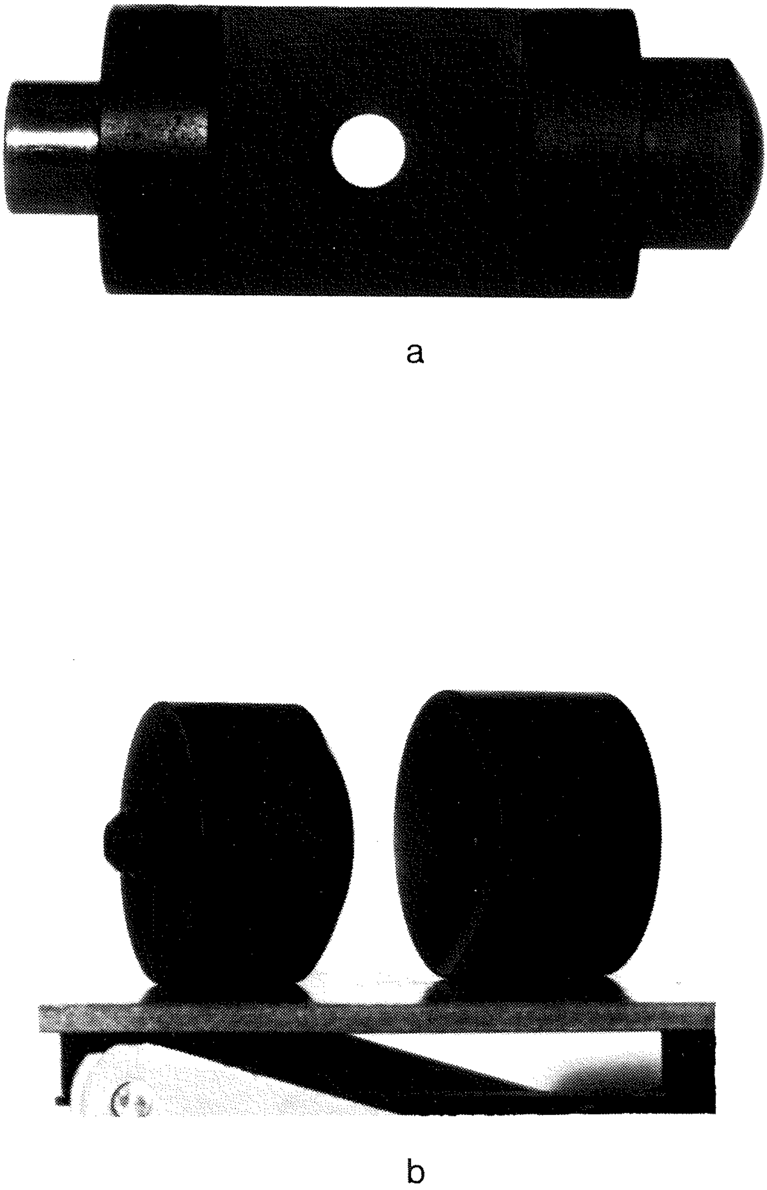

Figure 2.5 (a) Specimen inserted in holders. (b) Ball joint arrangement.

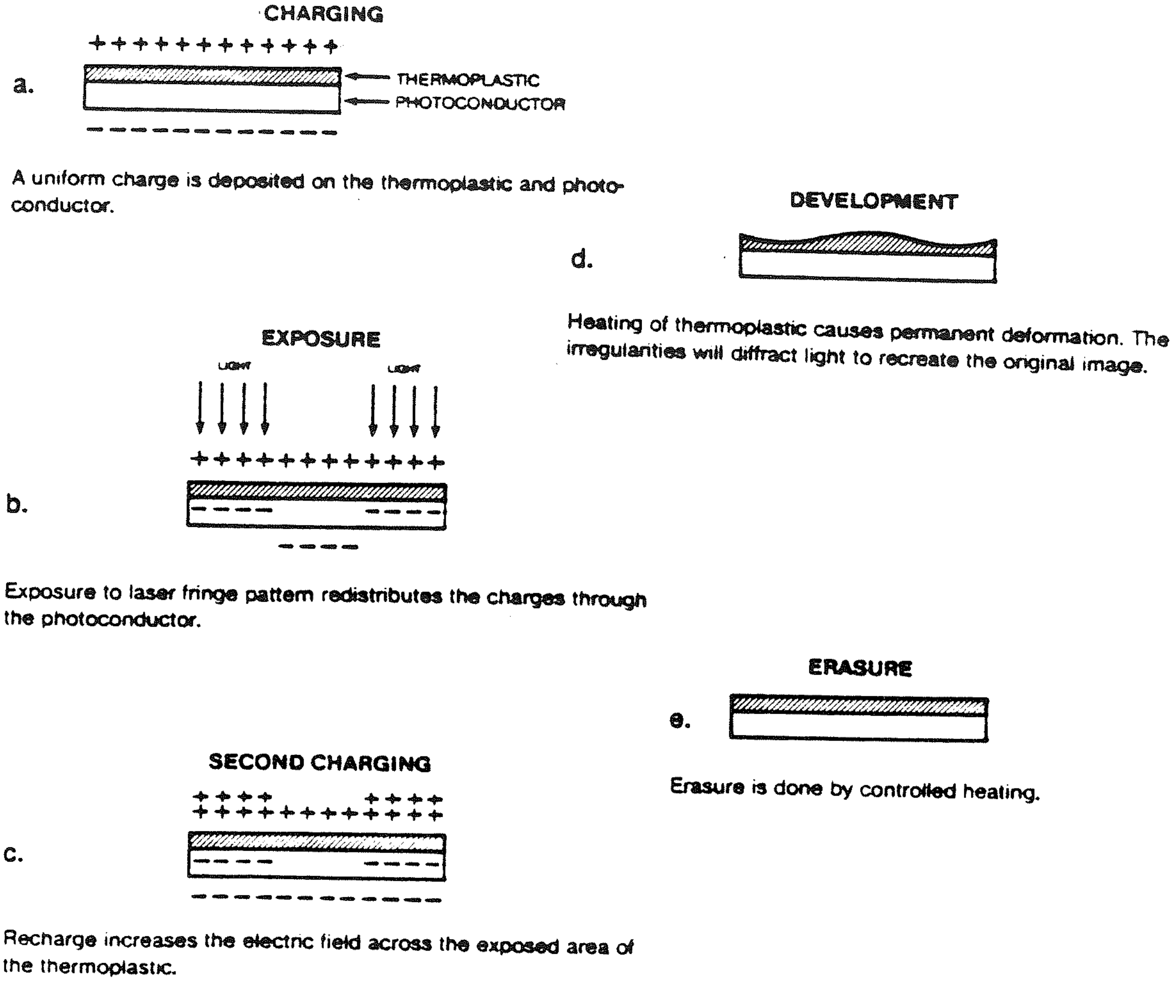

A uniform charge is deposited on the thermoplastic and photoconductor.

Exposure to laser fringe pattern redistributes the charges through the photoconductor.

Recharge increases the electric field across the exposed area of the thermoplastic.

Heating of thermoplastic causes permanent deformation. The irregularities will diffract light to recreate the original image.

Erasure is done by controlled heating.

Figure 2.6 Process of creating a surface-releif hologram on a thermoplastic plate (from ref. 2.2).

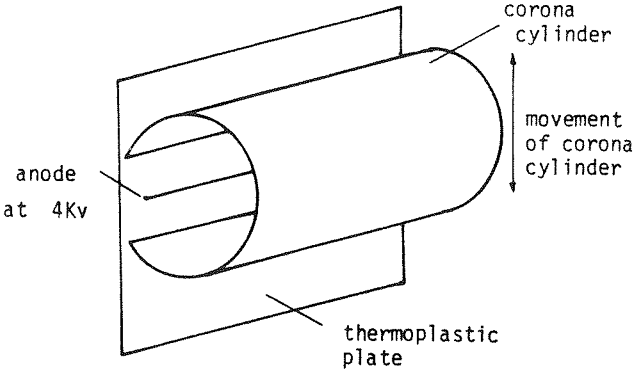

Figure 2.7 The coronatron deposits a uniform charge on the thermoplastic plate.

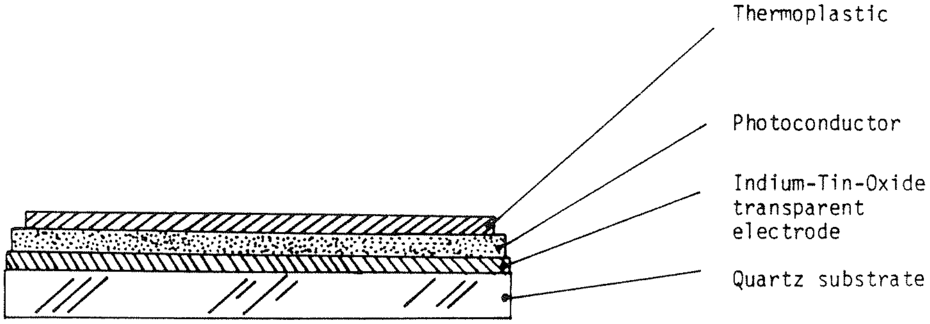

Figure 2.8 Detailed diagram of thermoplastic plate, showing Quartz substrate and transparent electrode.

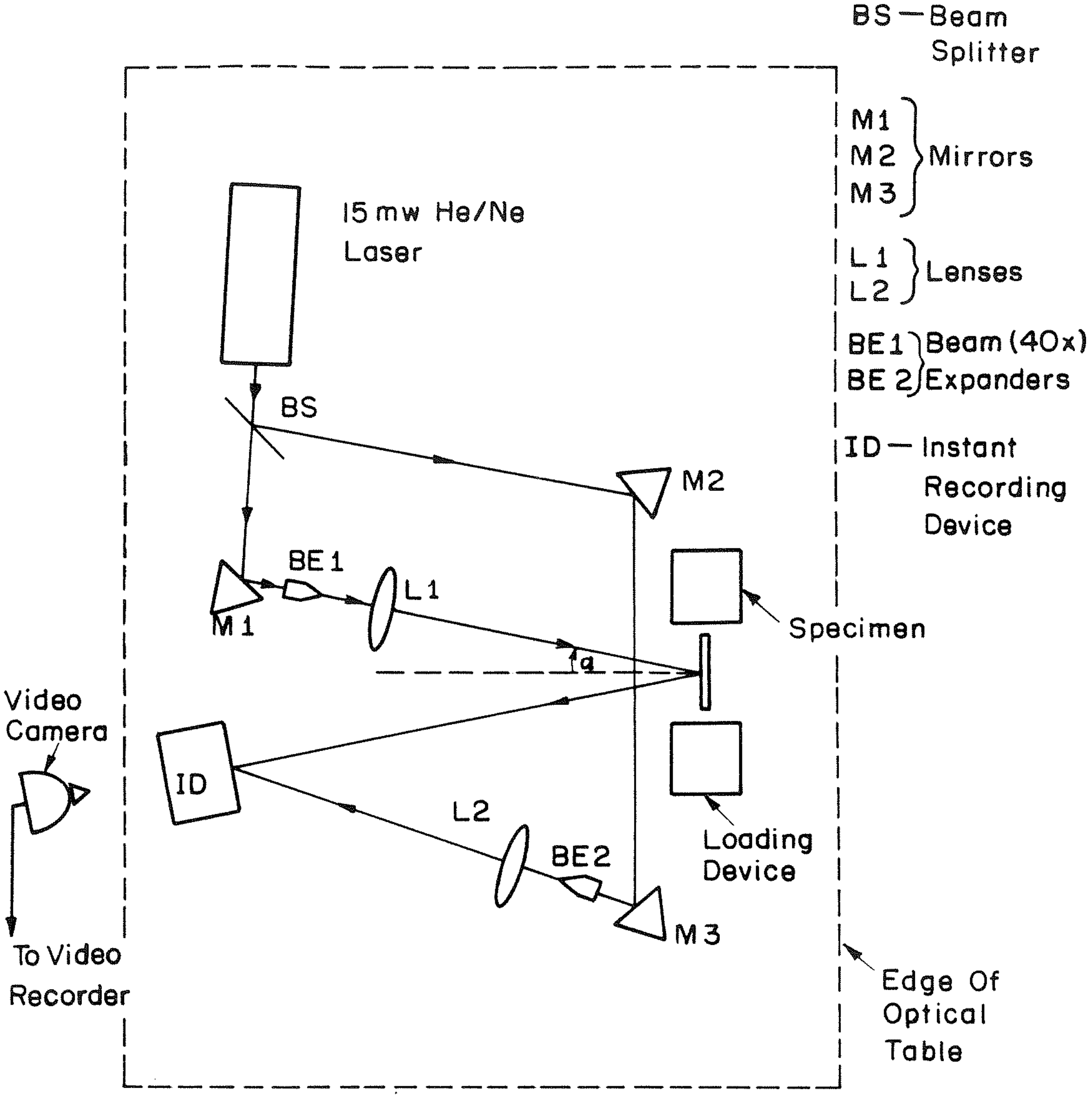

Figure 2.9 Holographic interferometer.

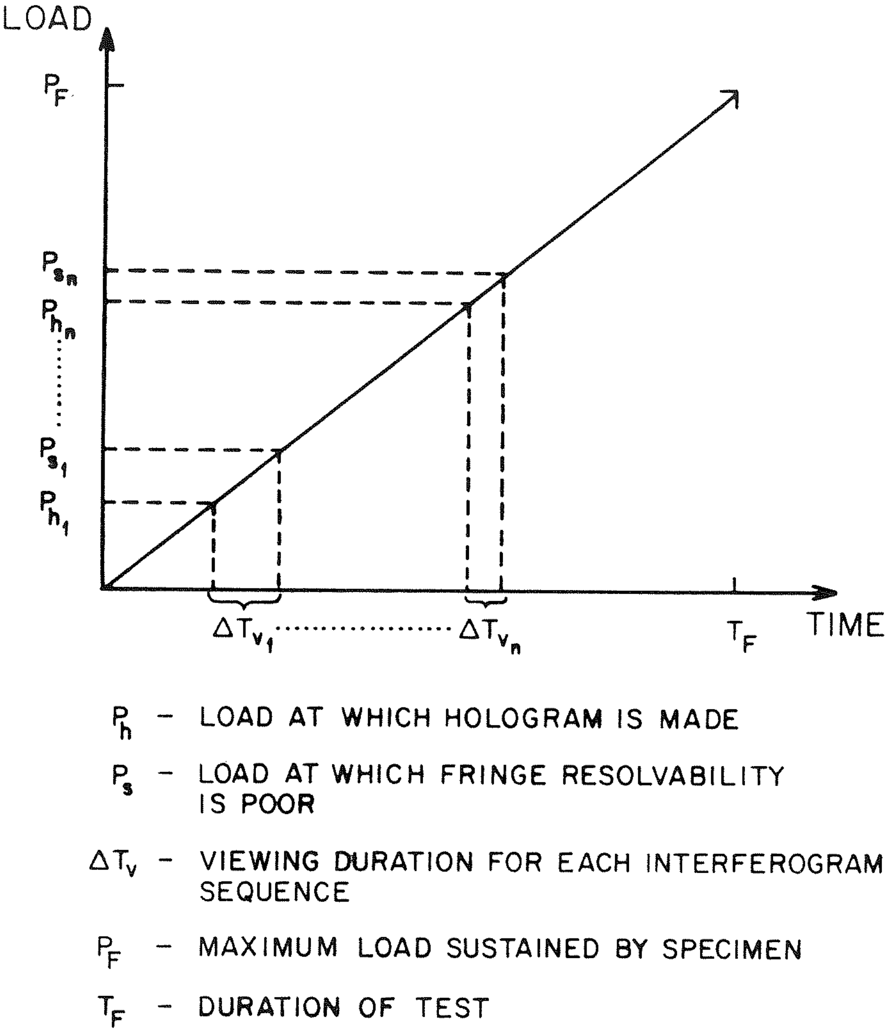

Figure 2.10 Experimental procedure for generating holograms.

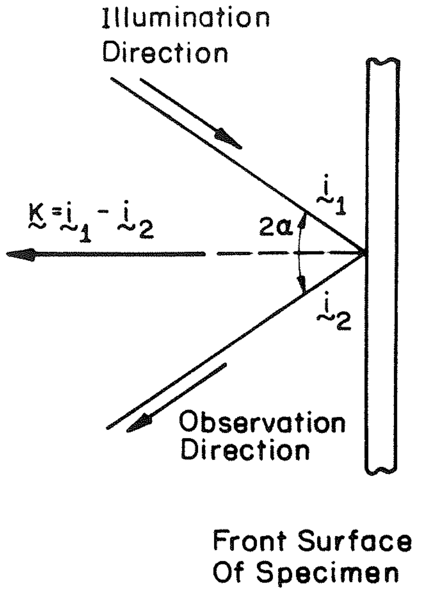

$\underset{\sim}{i}_1$ Unit Vector In Illumination Direction

$\underset{\sim}{i}_2$ Unit Vector In Observation Direction

$\underset{\sim}{K}$ Sensitivity Vector

$\underset{\sim}{d}$ Displacement Vector

w Component Of Displacement Normal To Plane Of Specimen

$$n\lambda = \underset{\sim}{k} \cdot \underline{d}$$

n Fringe Number

λ Wavelength Of The Coherent Laser Light

Figure 2.11 Details of interferometer.

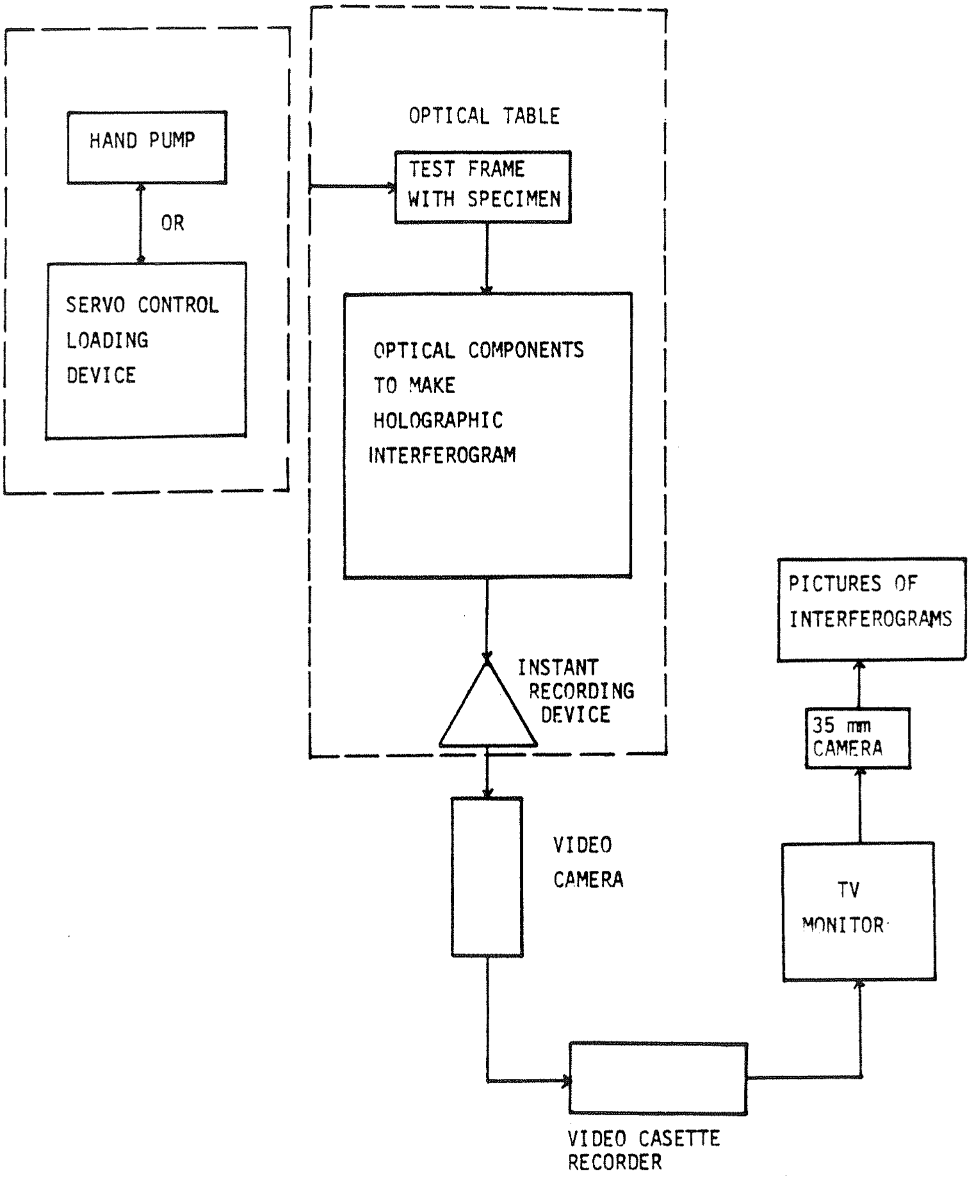

Figure 2.12 Schematic of experimental set up.

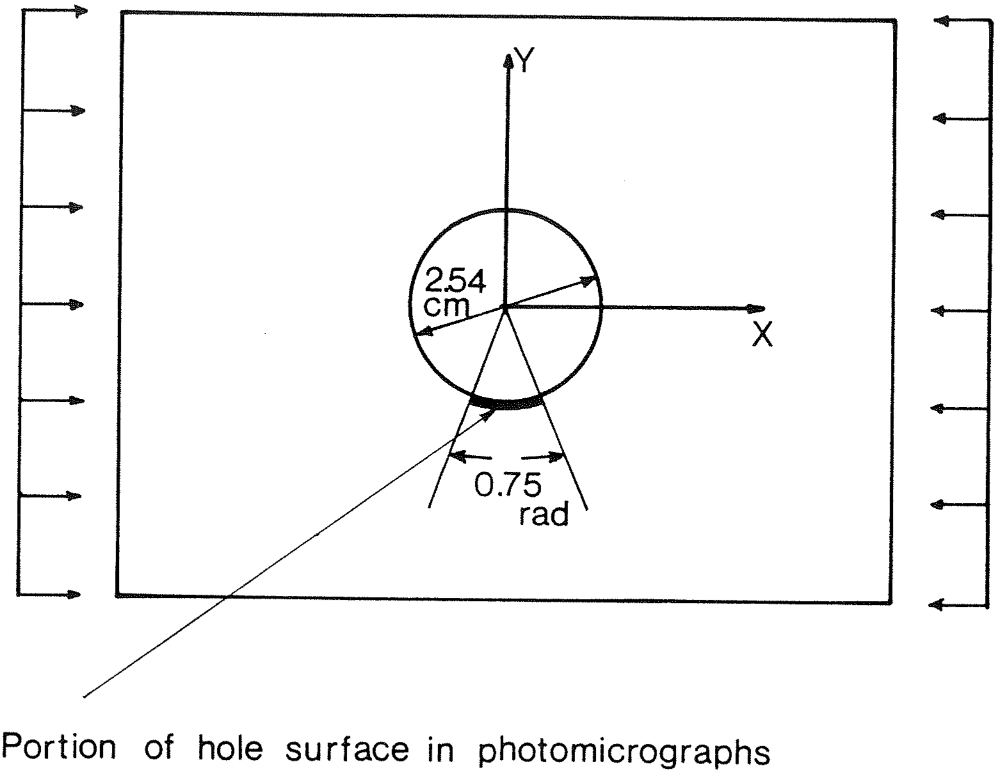

Figure 2.13 Digram showing portion of hole surface that is viewed obliquely through an optical microscope.

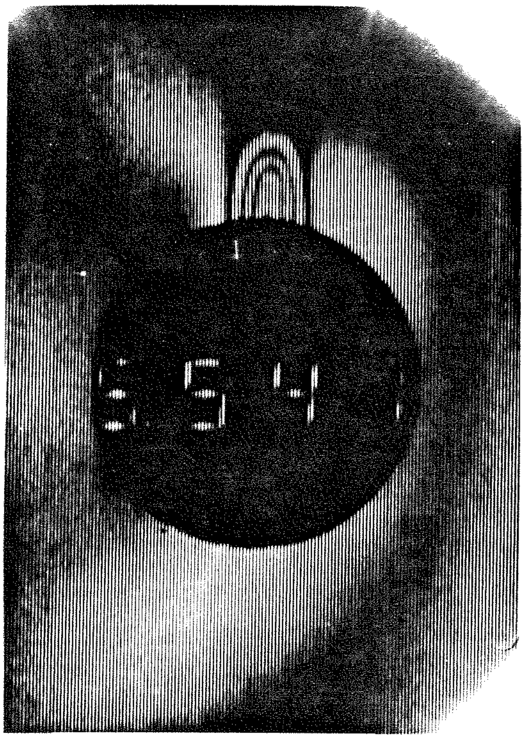

123.2

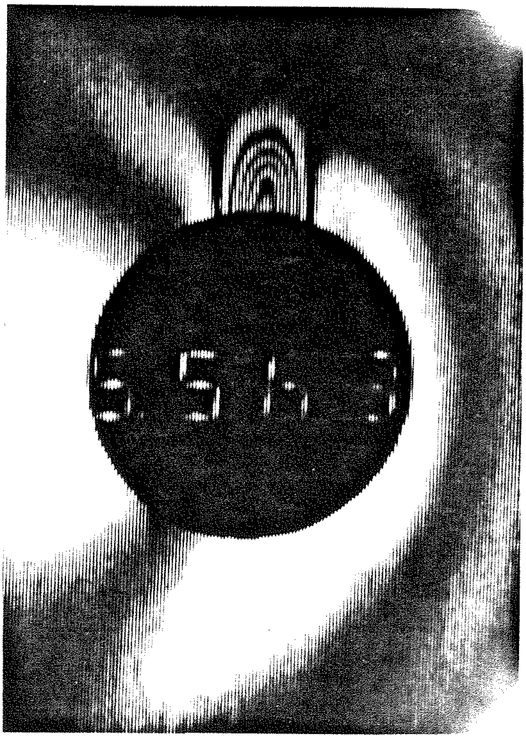

123.7

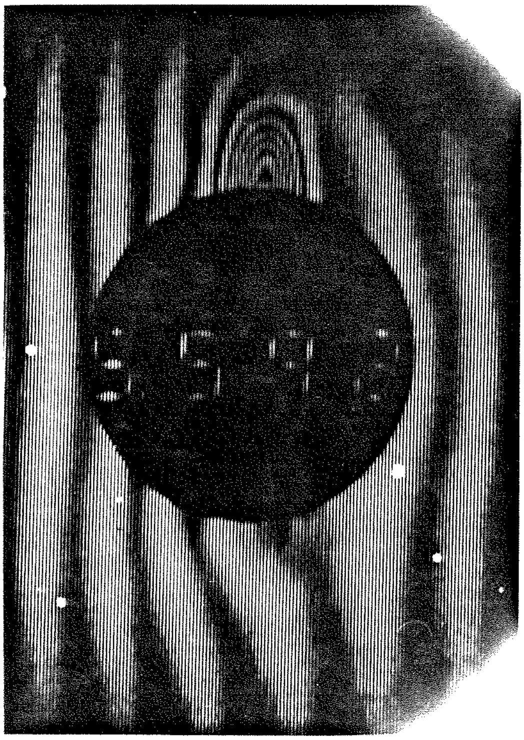

124.4

P$_h$=123.2

Figure 2.14 Initiation of damage (spec. TB11).

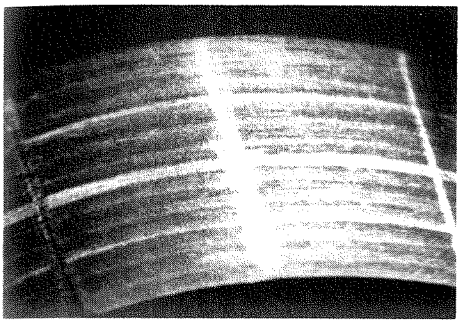

66.7

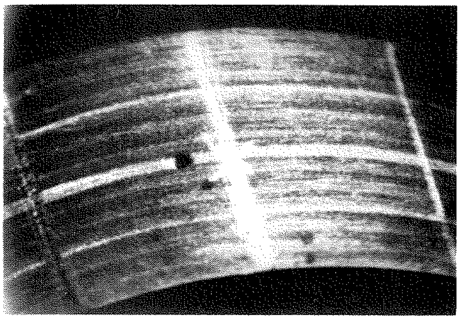

123.2

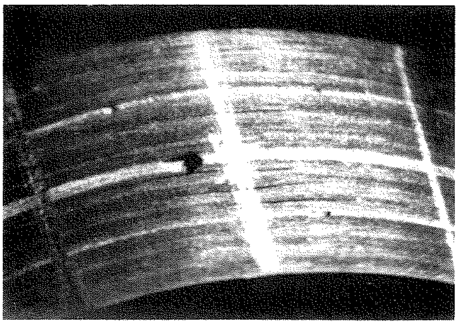

159.1

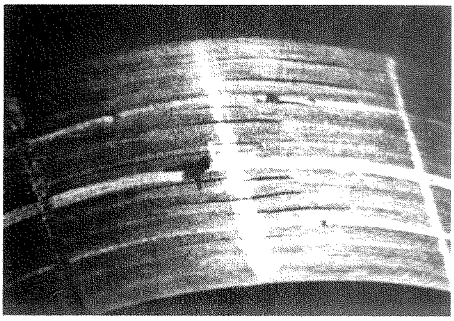

164.5

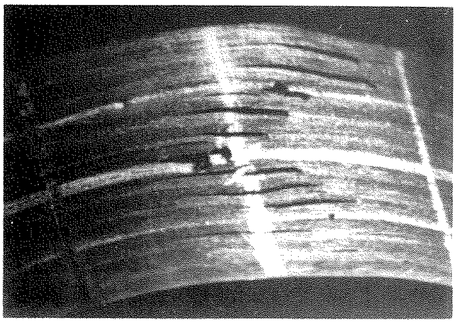

165.0

Figure 2.15a Hole surface photo-micrographs (spec. TB11).

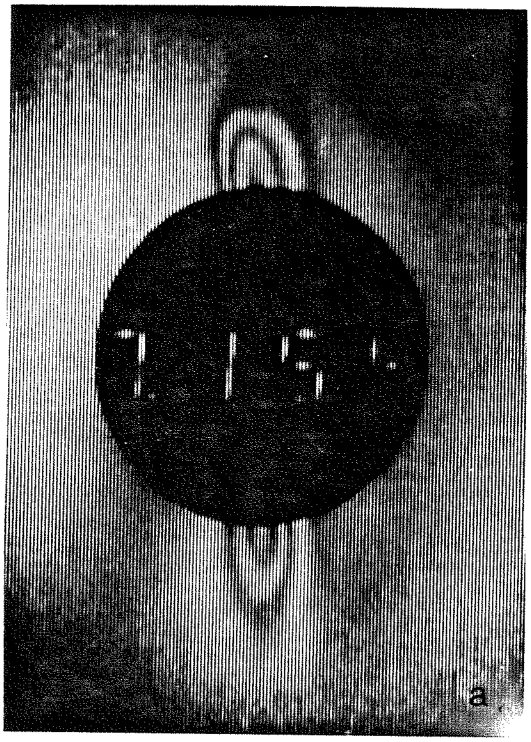

159.1

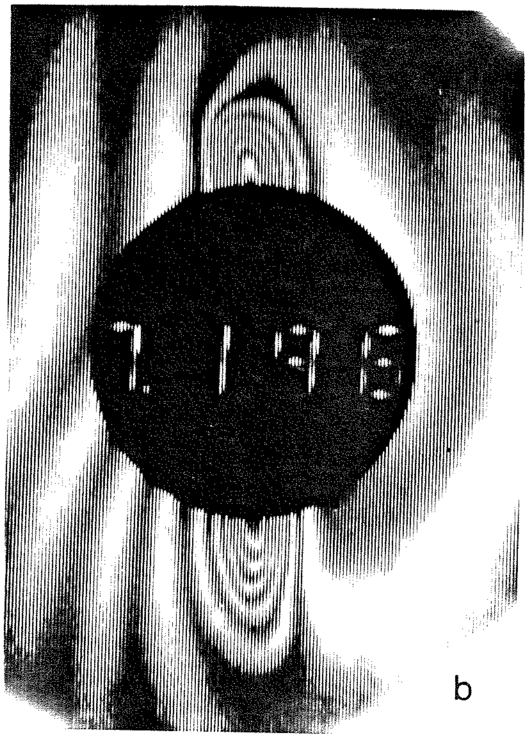

160.0

160.8

P$_h$=159.0

Figure 2.16a Buckling and spreading of delaminated portions (spec. TB11).

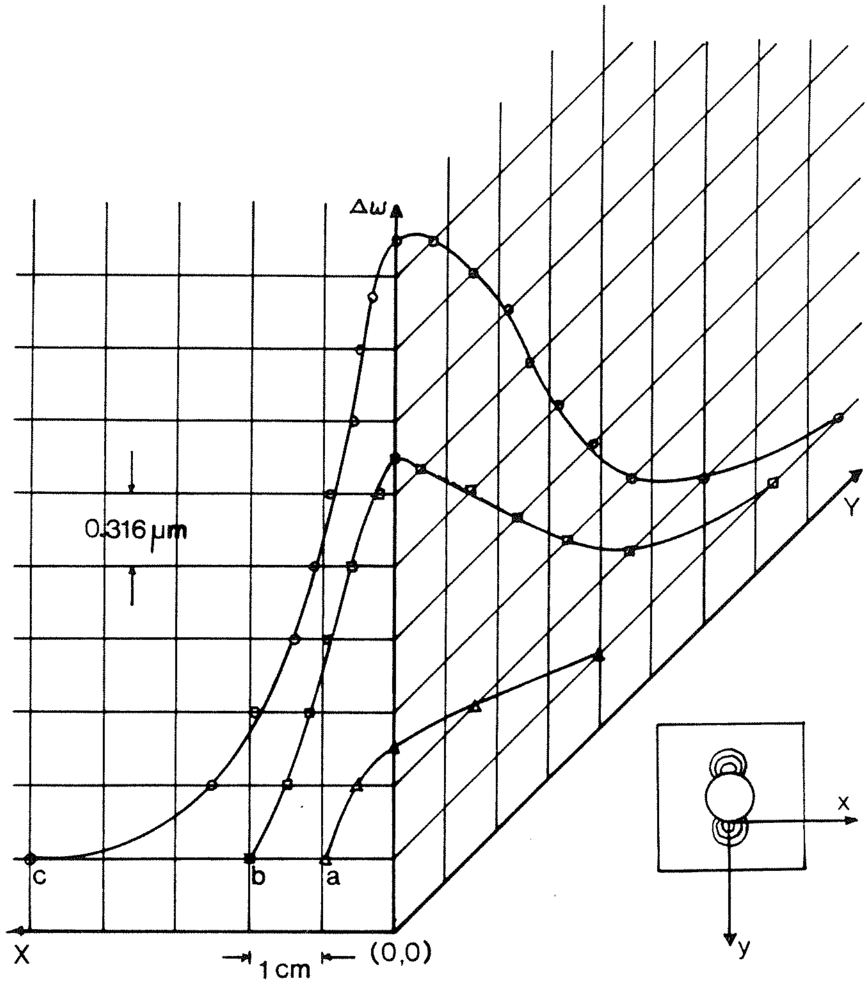

SCALE 1:0.37
(X&Y axes)

Figure 2.17a Summary of displacements corresponding to Figure 2.16a.

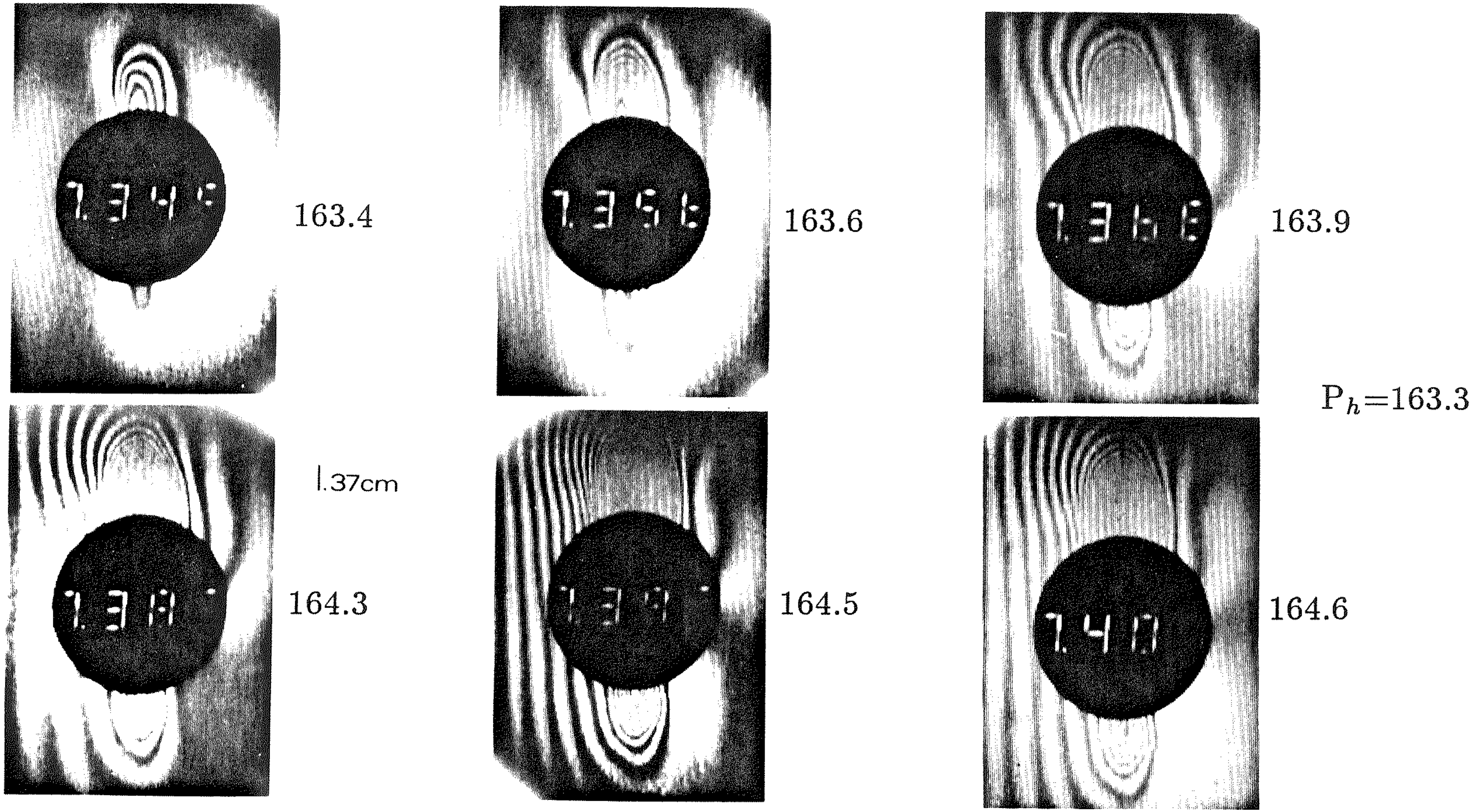

Figure 2.18a Buckling and spreading of delaminated portions just prior to catastrophic failure (spec. TB11).

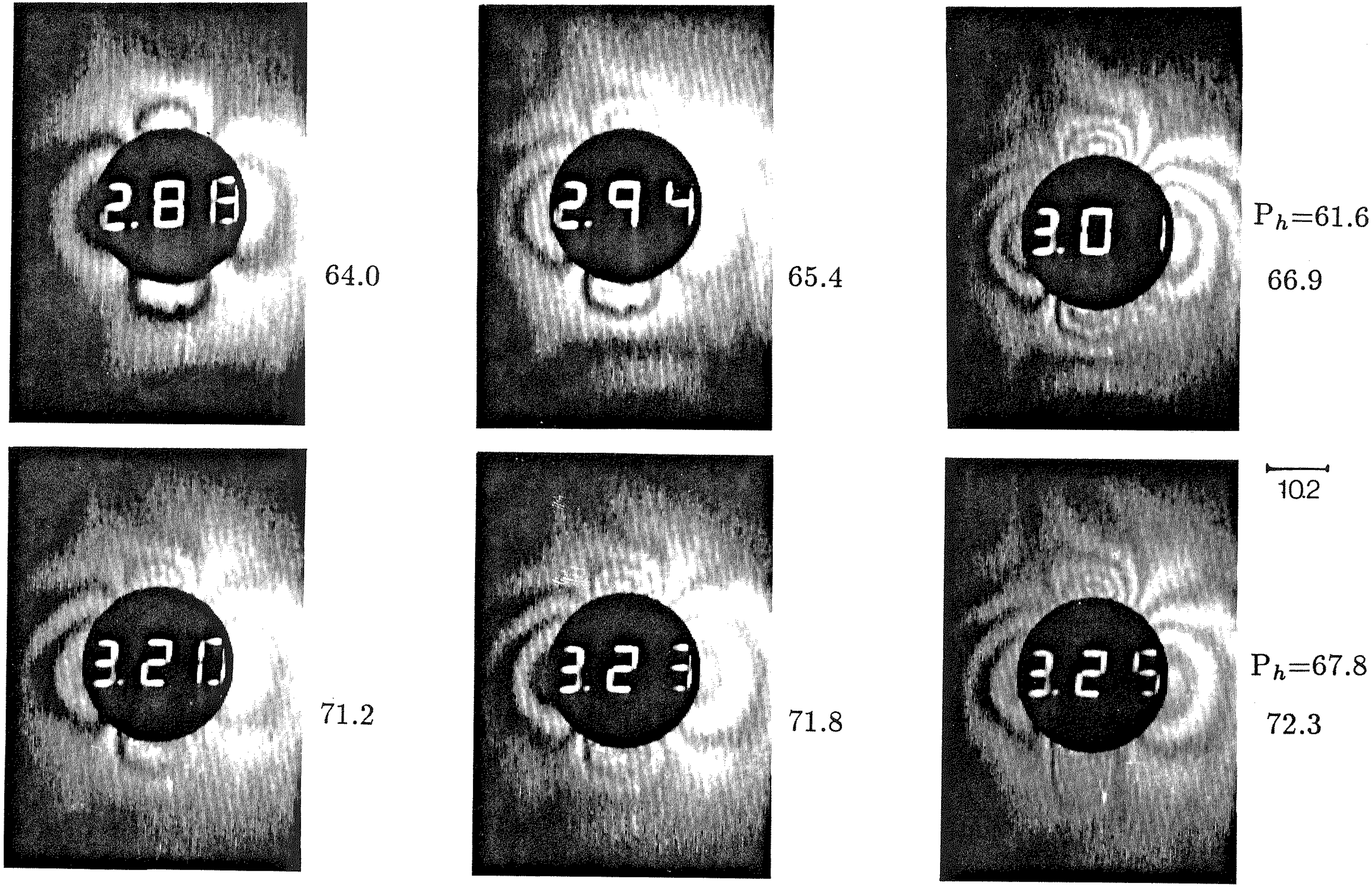

Figure 2.19a (i) Fringe distribution in the pre-damaged state (spec. IM9). (ii) Fringe distribution at failure initiation (spec. IM9).

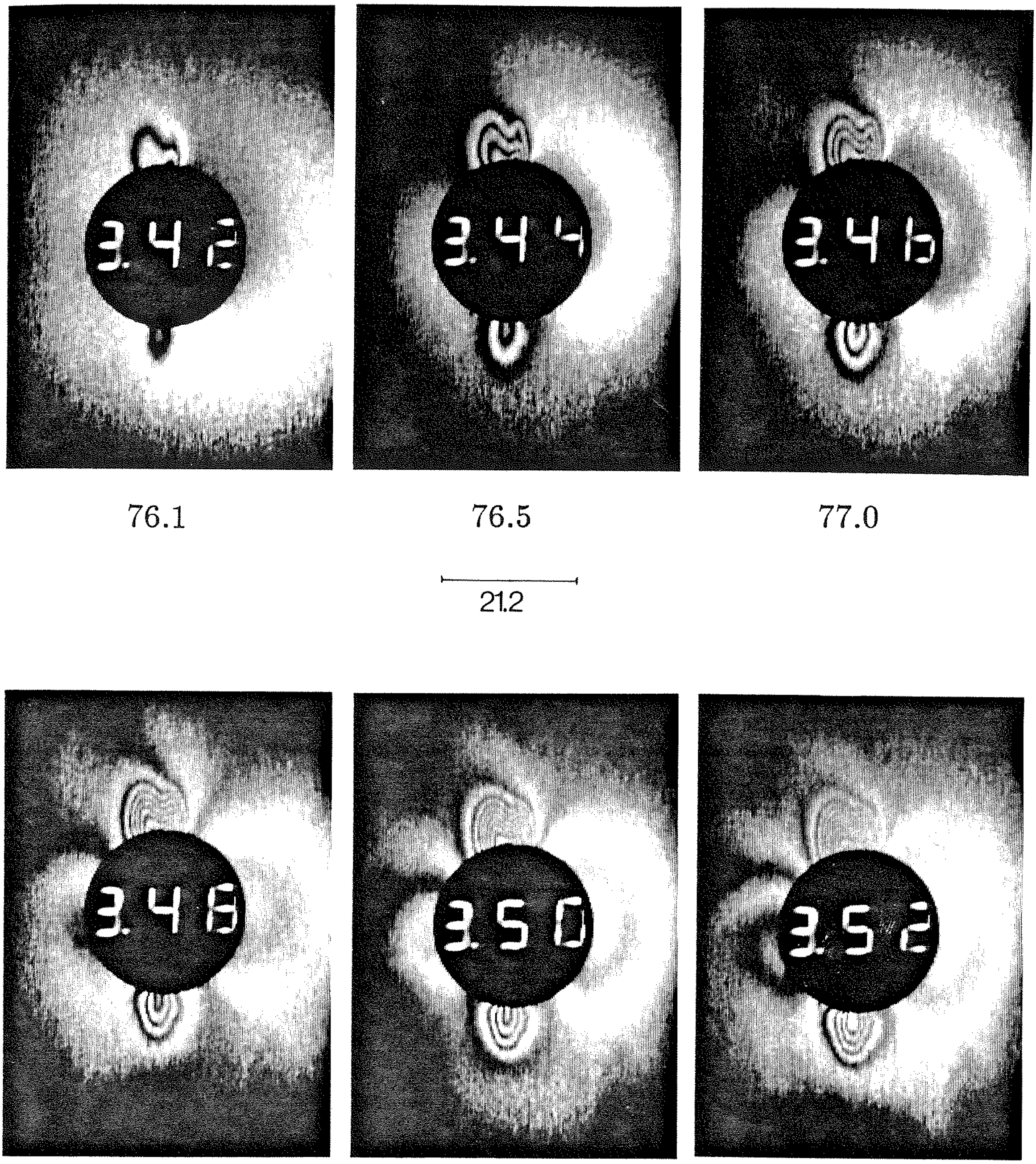

76.1 76.5 77.0

77.4 77.8 78.3

P$_h$=75.6

Figure 2.19b Response of locally delaminated portions (spec. IM9).

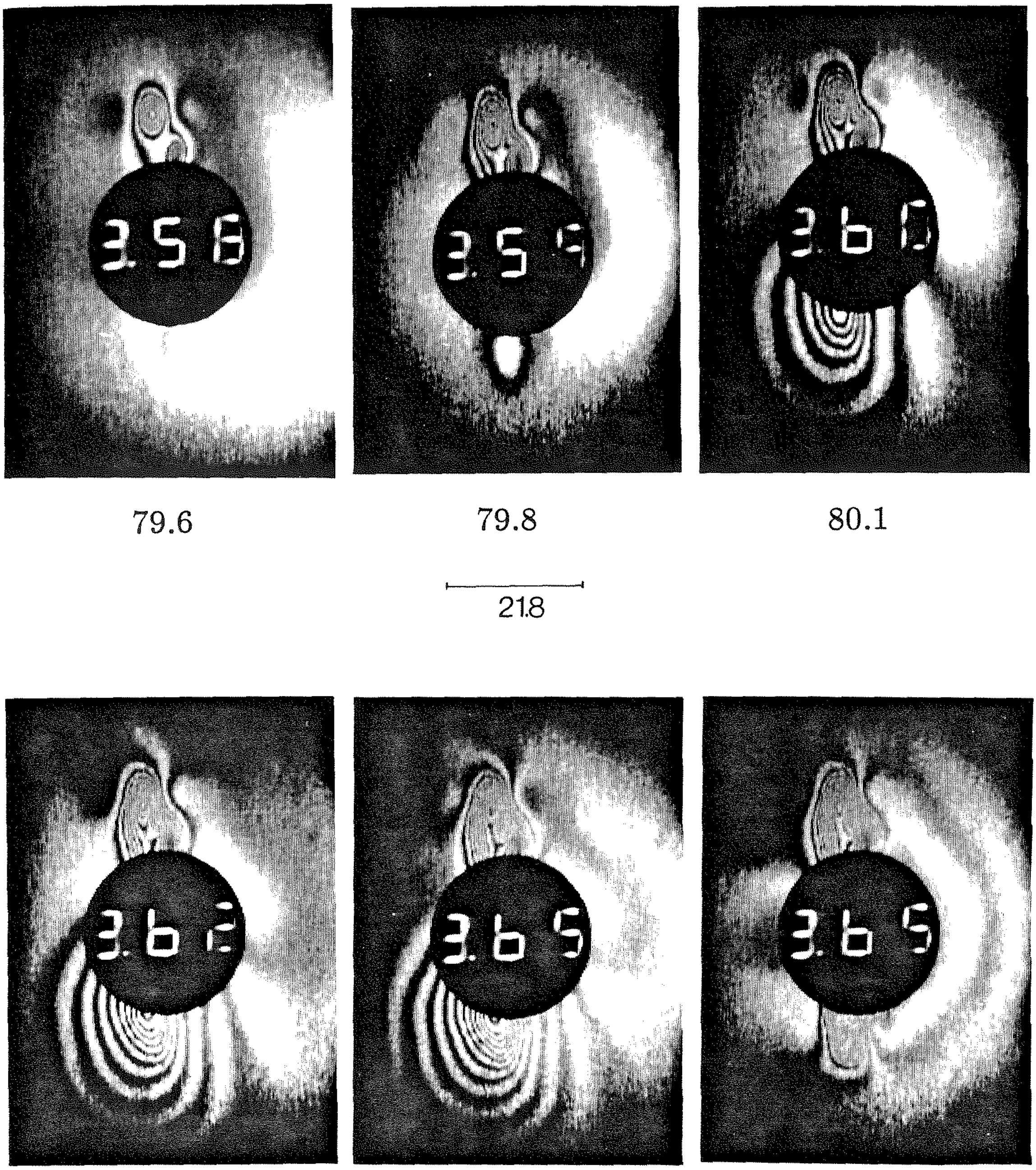

79.6 79.8 80.1

80.5 81.2 81.2 (2 frames later)

P_h=79.4

Figure 2.19c Buckling and spreading of delaminated portions (spec. IM9).

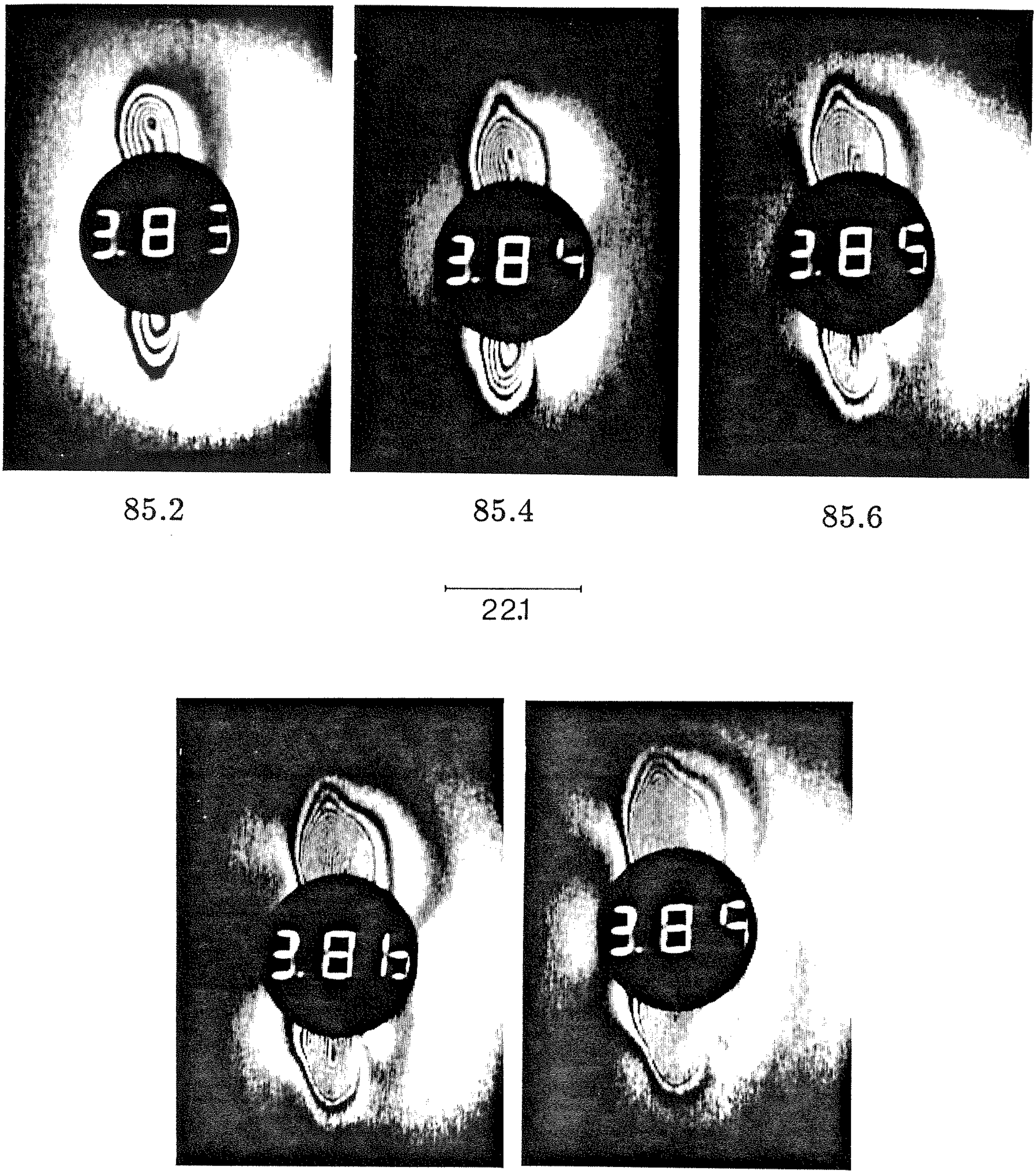

85.2 85.4 85.6

22.1

85.8 86.5

P_h=85.0

Figure 2.19d Buckling and spreading of delaminated portions close to catastrophic failure (spec. IM9).

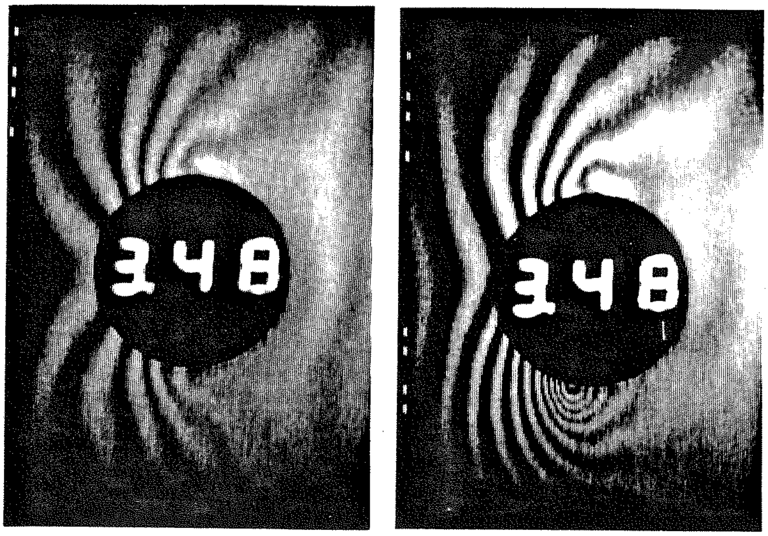

P$_h$=75.2

77.4 77.4 (2 frames later)

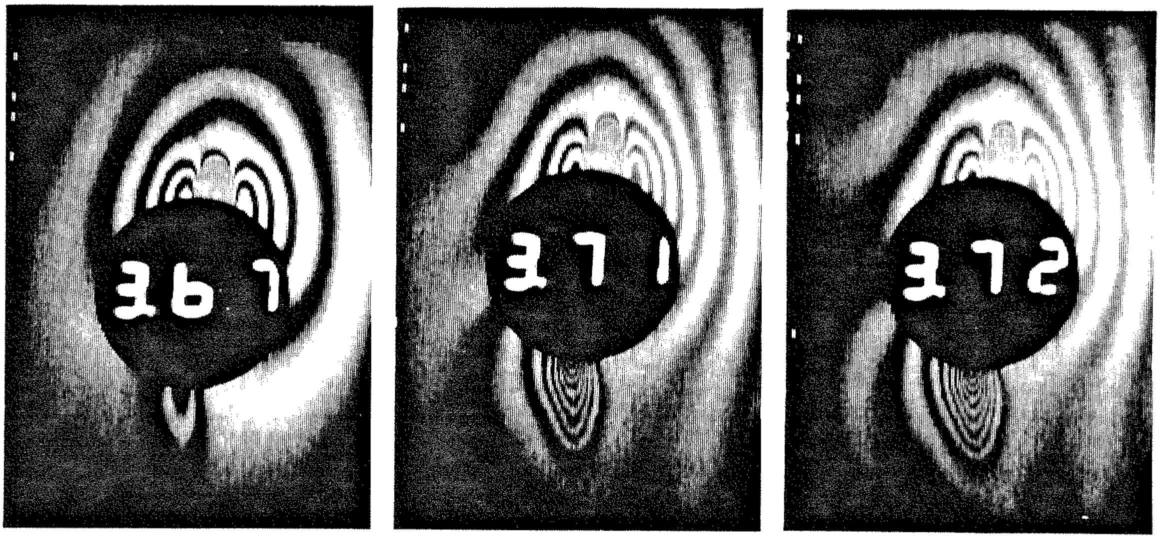

81.6 82.5 82.7

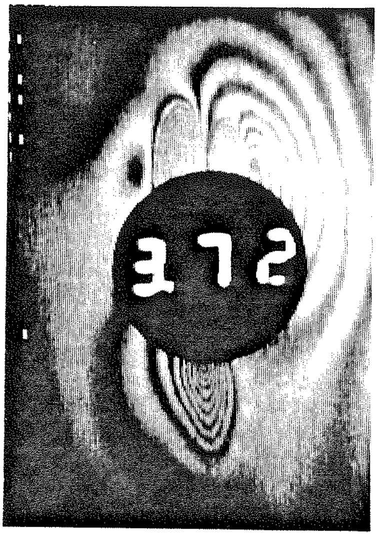

82.7 (2 frames later)

20.0

P$_h$=81.4

Figure 2.20a (i) Initiation of damage (spec. IM6).

(ii) Buckling of locally delaminated portions (spec. IM6).

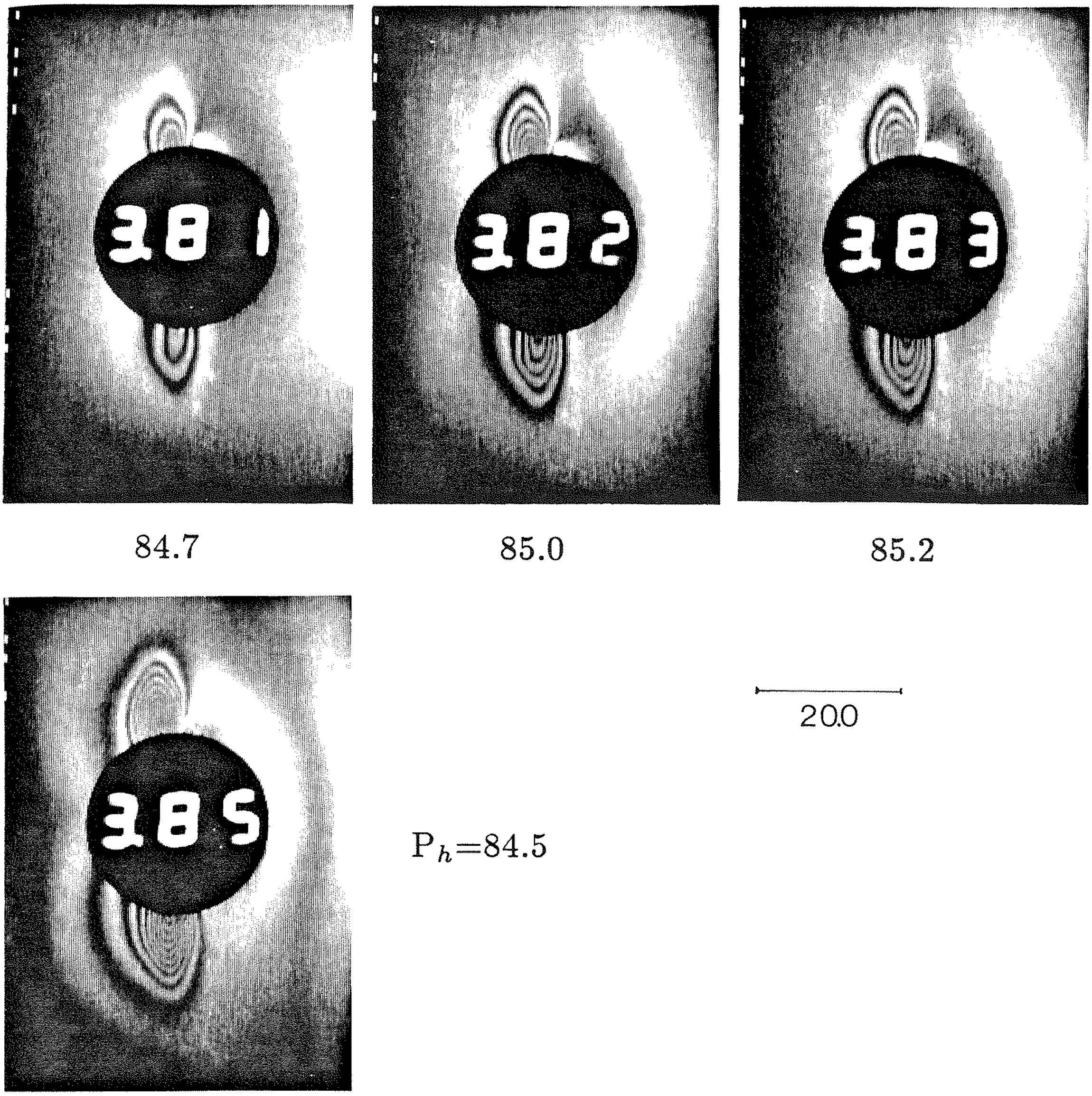

84.7

85.0

85.2

85.6

$P_h = 84.5$

Figure 2.20b Response of buckled delaminated portions (spec. IM6).

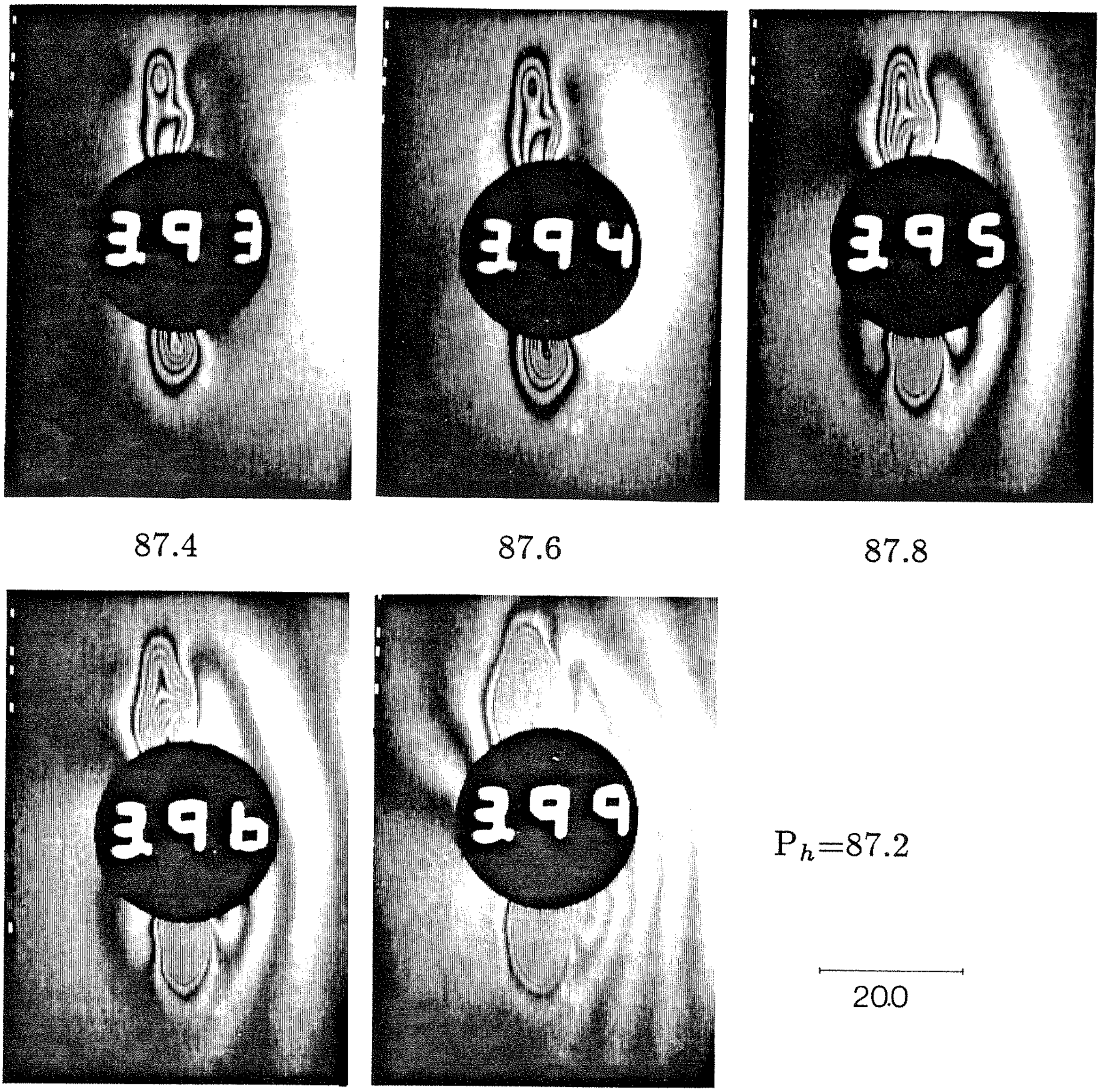

87.4 87.6 87.8

88.1 88.7

P_h=87.2

Figure 2.20c Buckling and spreading of delaminated portions (spec. IM6).

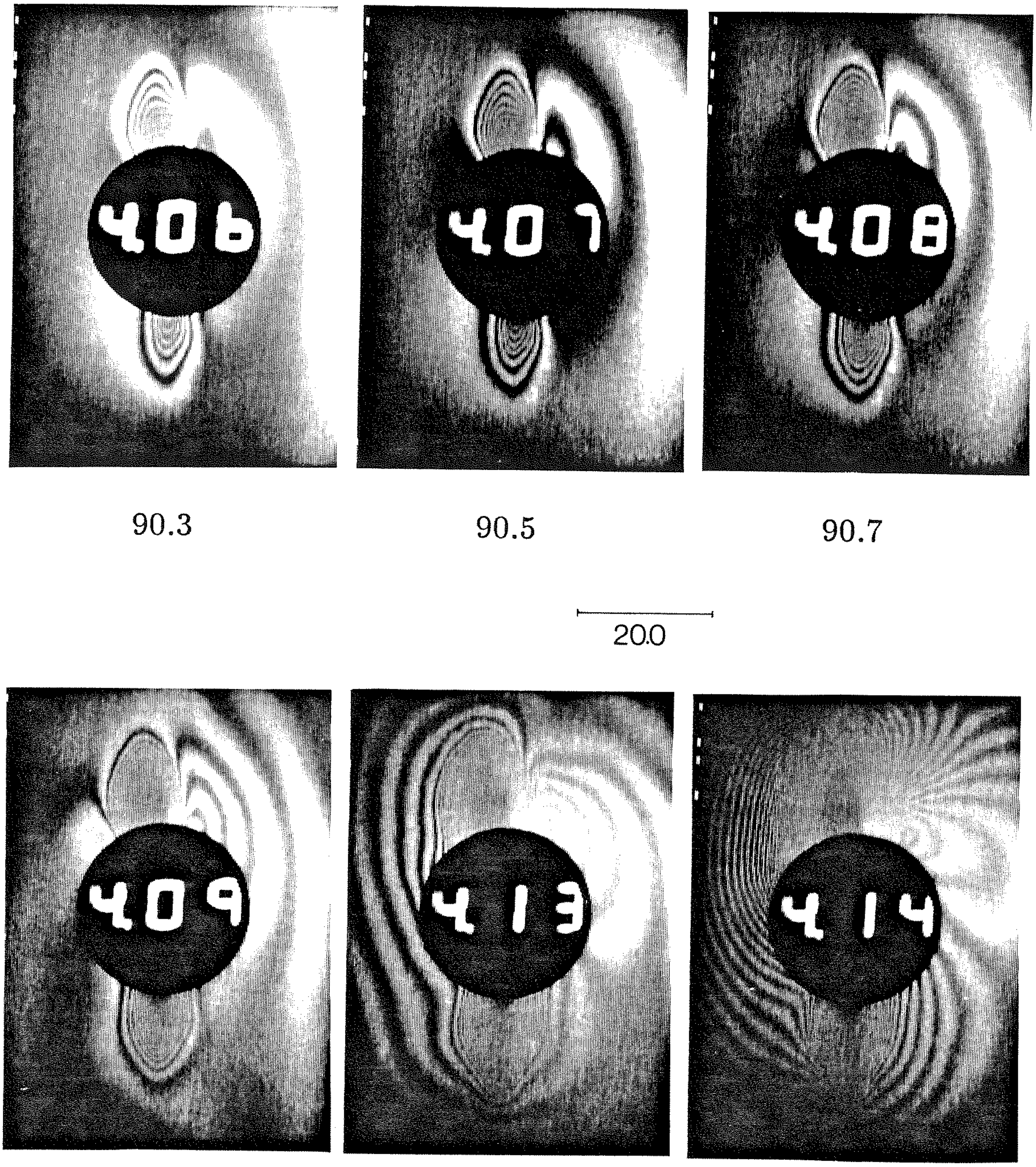

90.3 90.5 90.7

91.0 91.8 92.1

P$_h$=90.1

Figure 2.20d Buckling and spreading of delaminated portions just prior to catastrophic failure (spec. IM6).

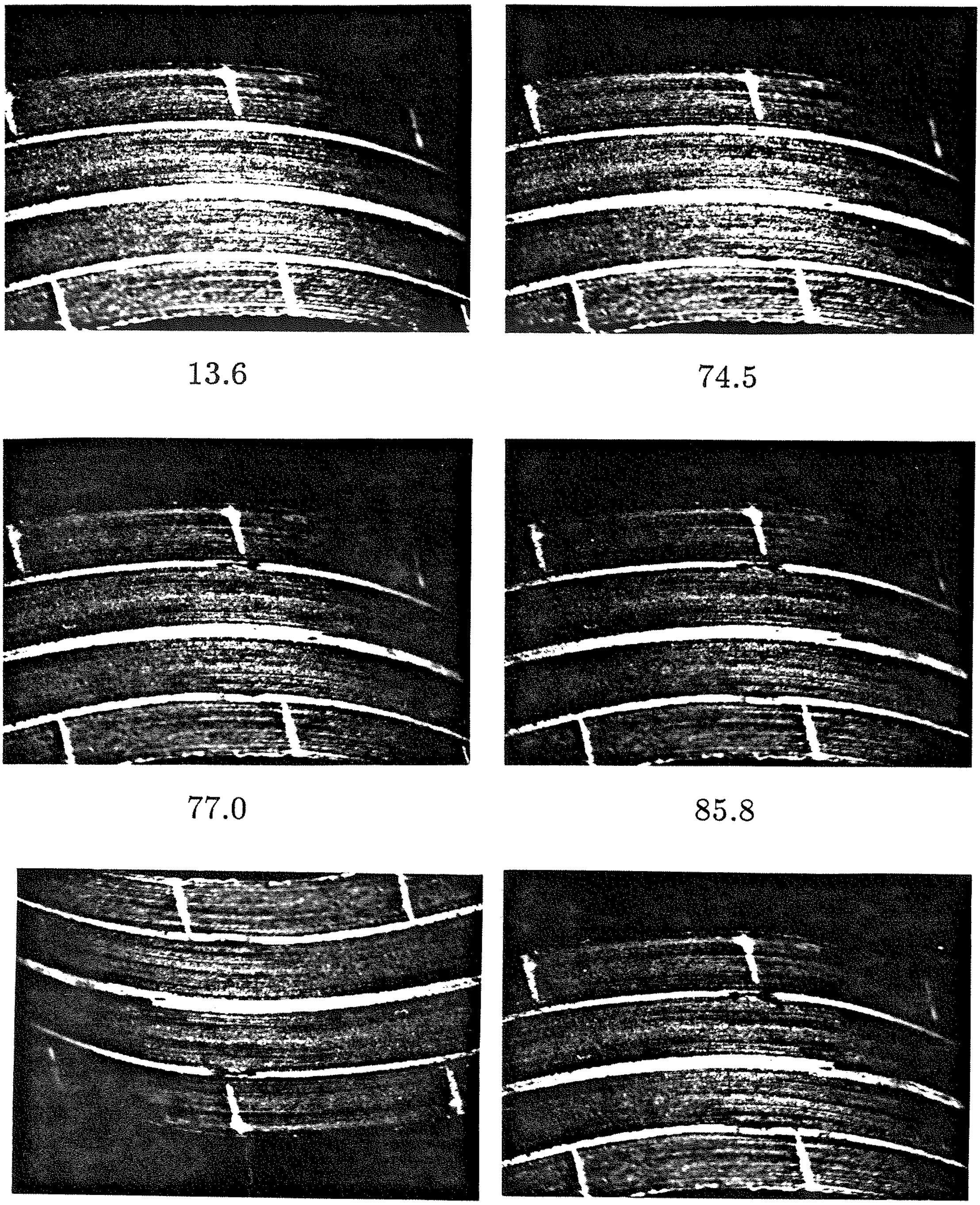

13.6

74.5

77.0

85.8

89.0

89.6

Specimen thickness = 7.33

Figure 2.21a Hole surface photomicrographs (spec. IM9).

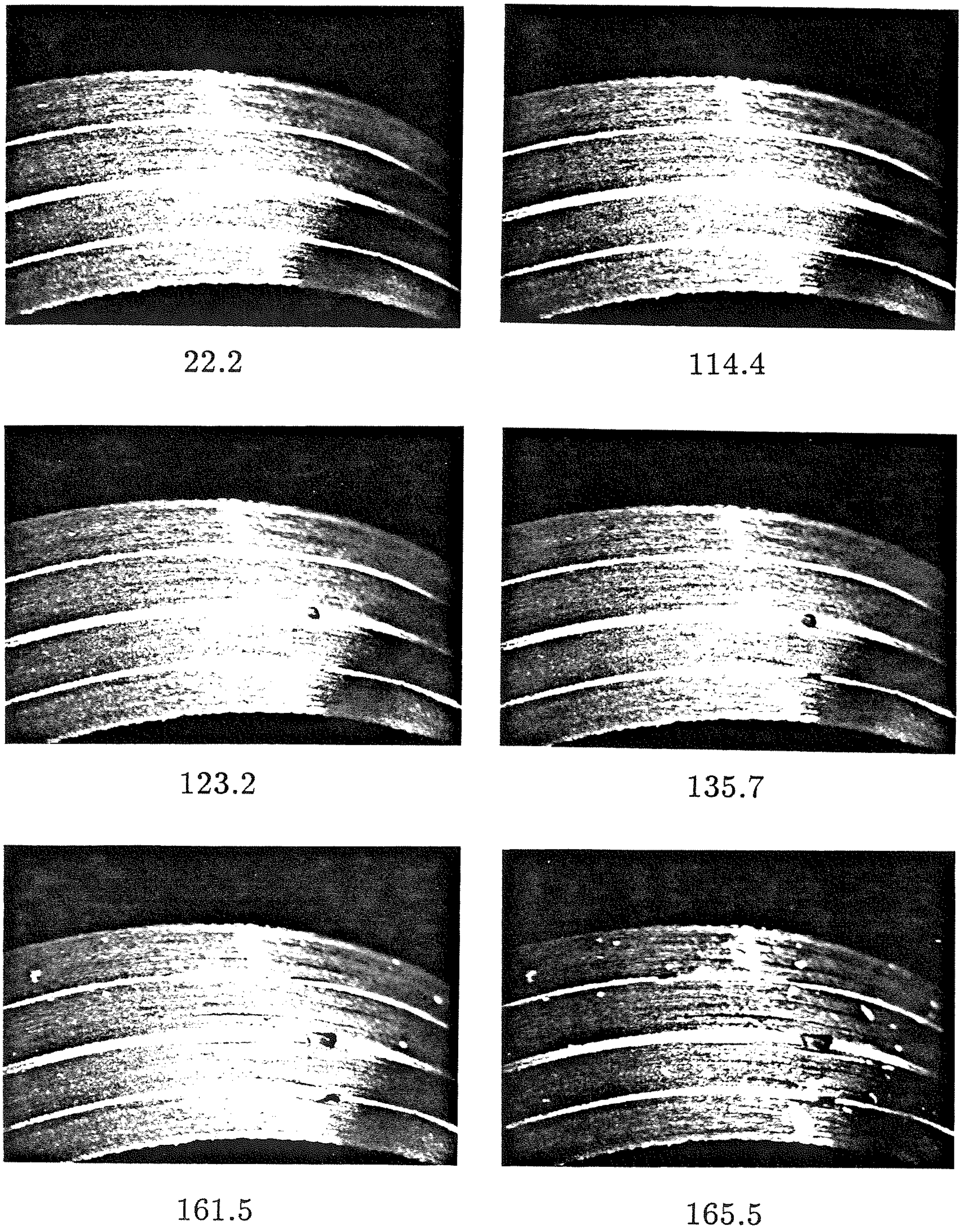

22.2

114.4

123.2

135.7

161.5

165.5

Specimen thickness = 7.44

Figure 2.21b Hole surface photomicrographs (spec. IM25).

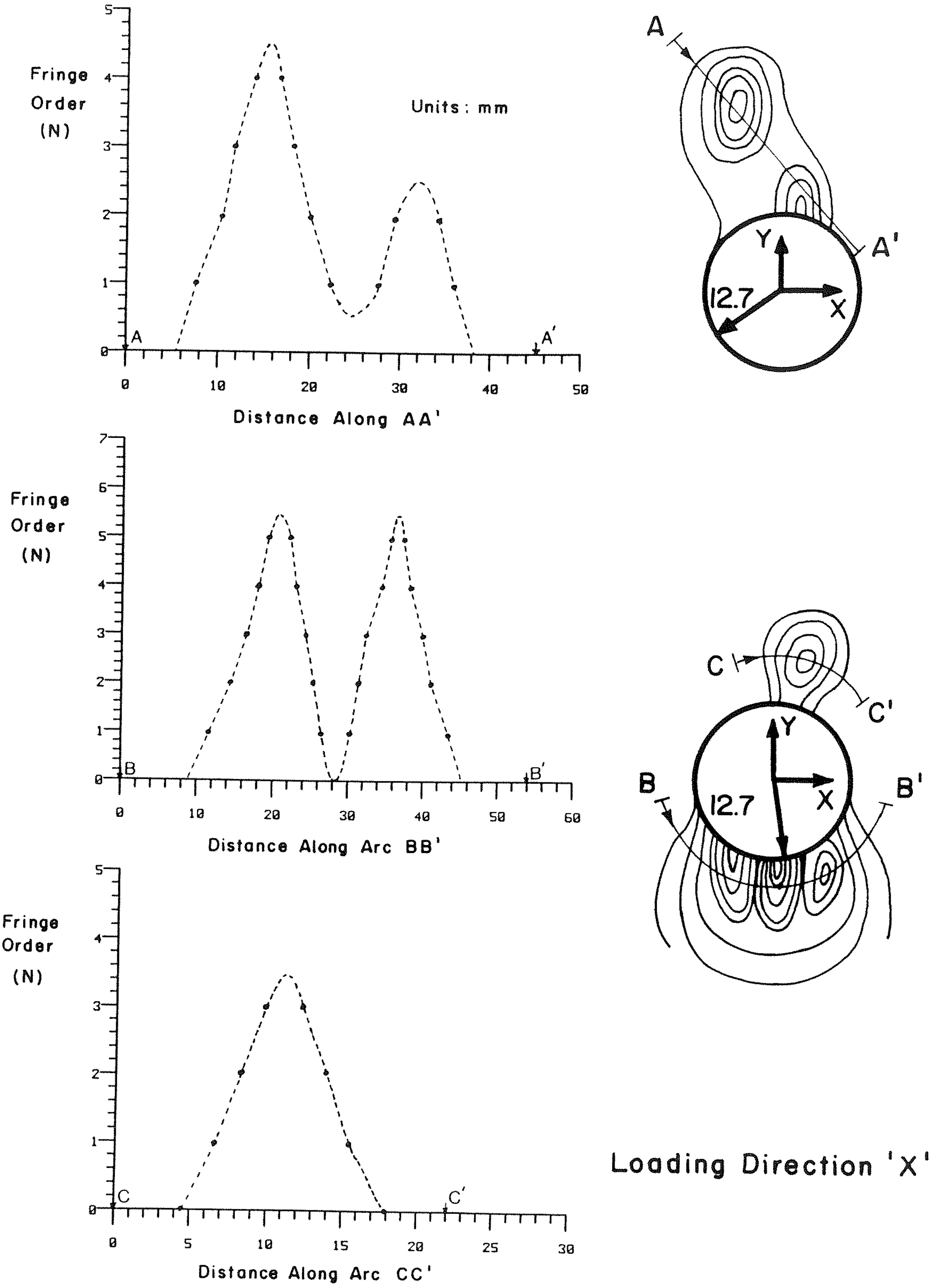

Figure 2.21c Typical interferometric patterns and corresponding displacements (not to scale).

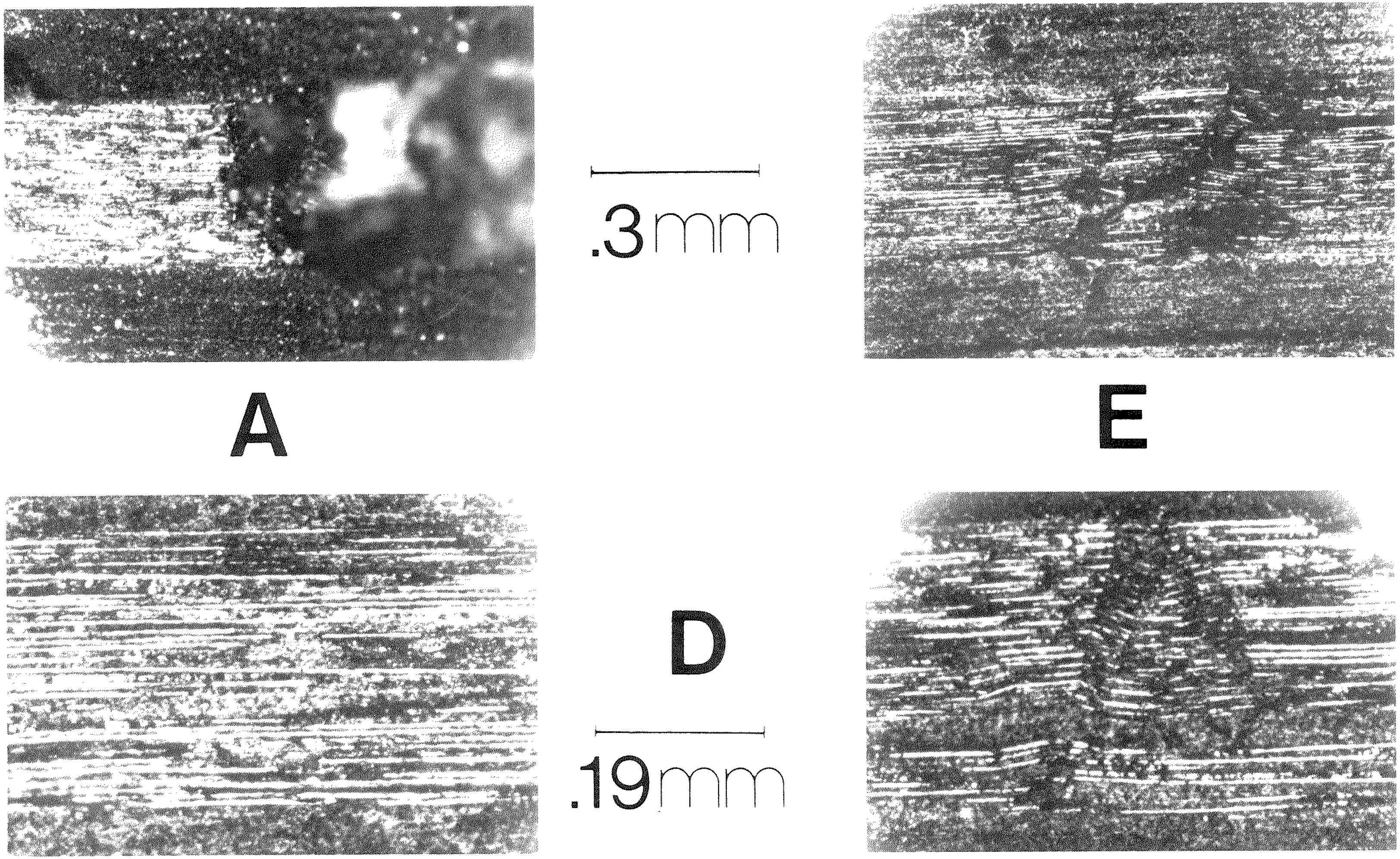

Figure 2.22a Surface/Internal damage to spec. TB11 at different cross-sections.

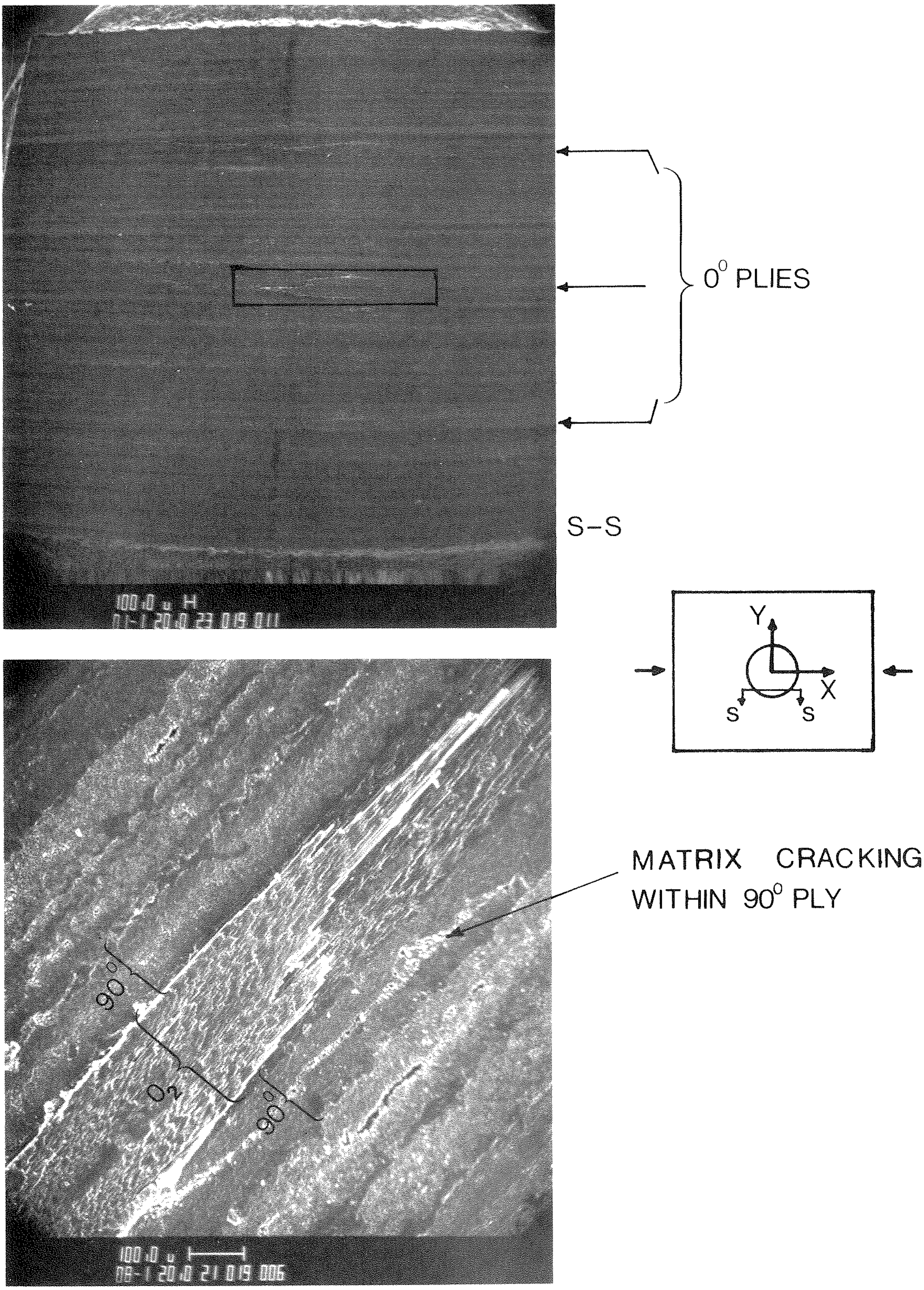

Figure 2.22b Scanning Electron Micrographs of hole surface showing 0^0-ply failure (spec. IM19).

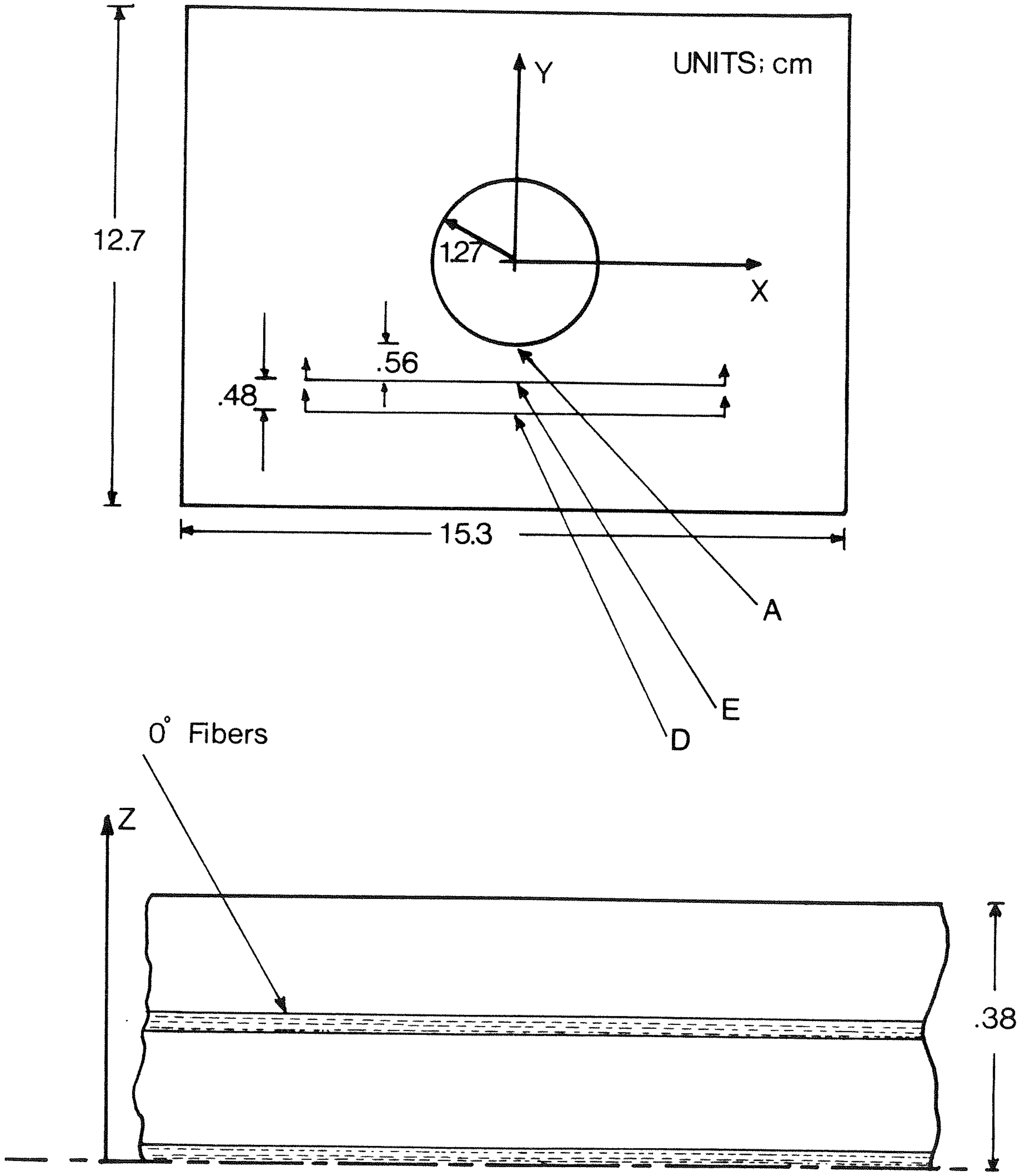

Figure 2.23 Post experiment microscopic examination (spec. TB11).

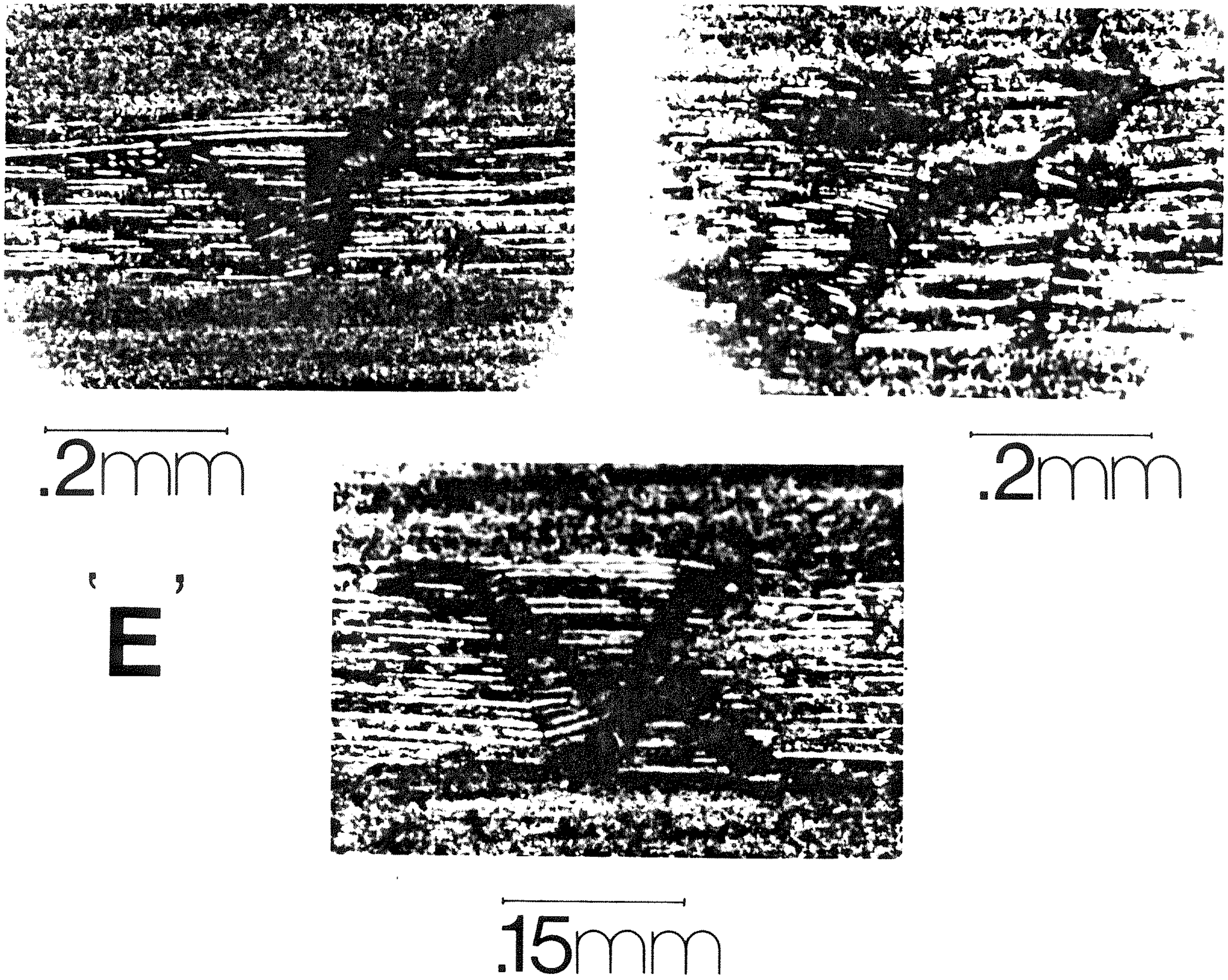

Figure 2.24 Internal damage at Section 'E' in spec. TB11 (see figure 2.23).

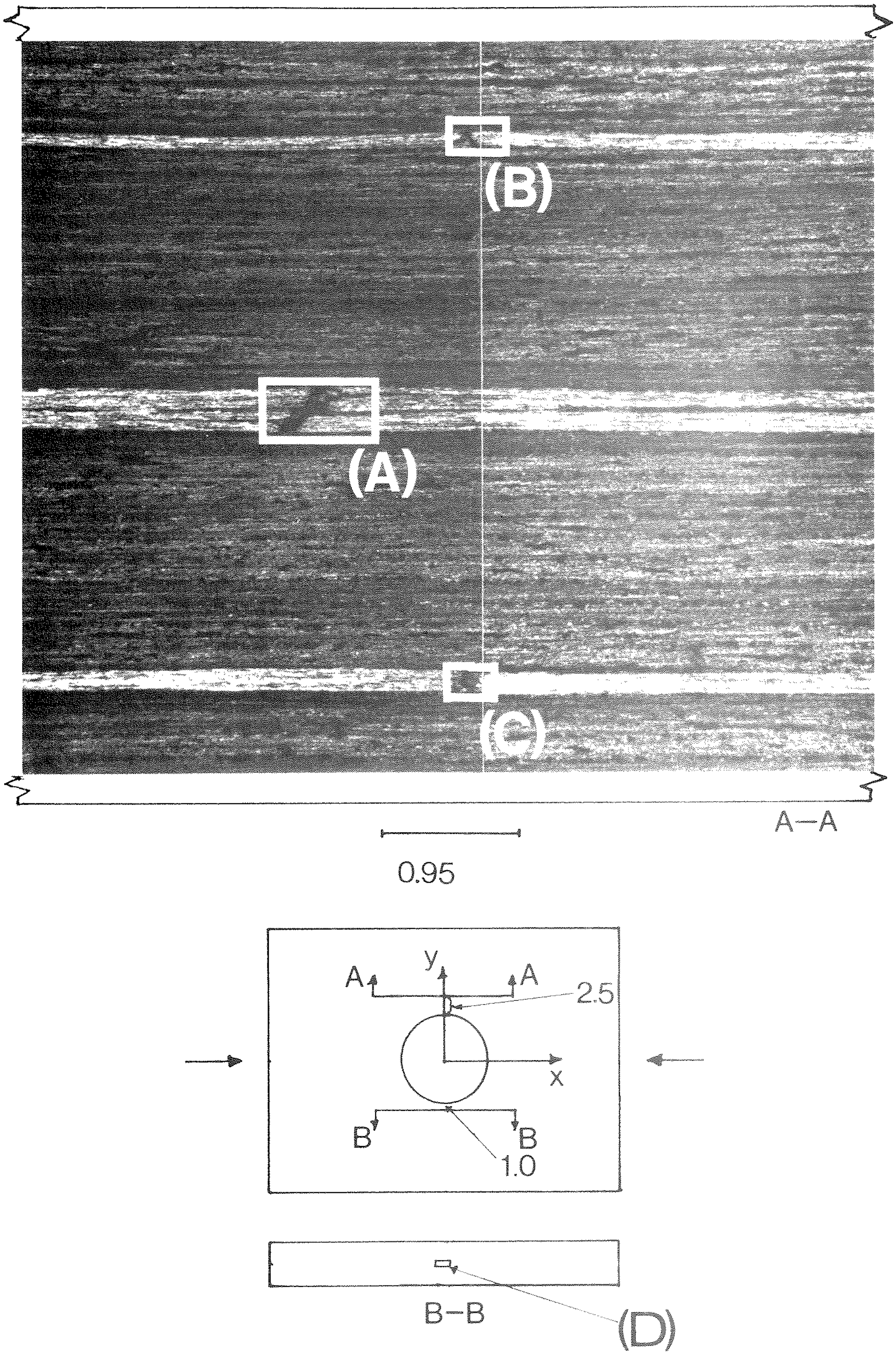

Figure 2.25a Sectional study of spec. IM 9.

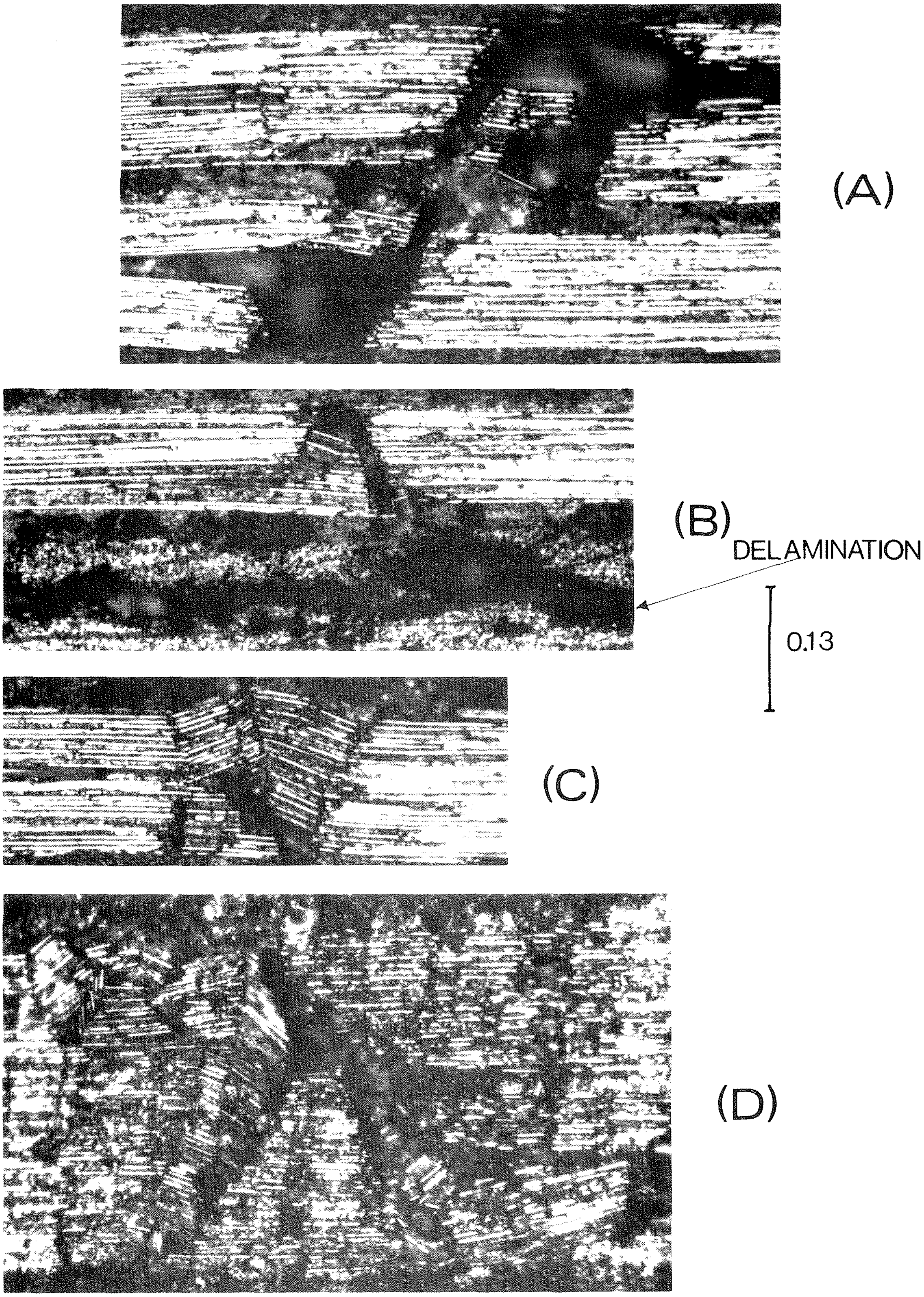

Figure 2.25b Magnified view of 0^0 ply damage in spec. IM 9 (see Figure 2.25a for damage locations).

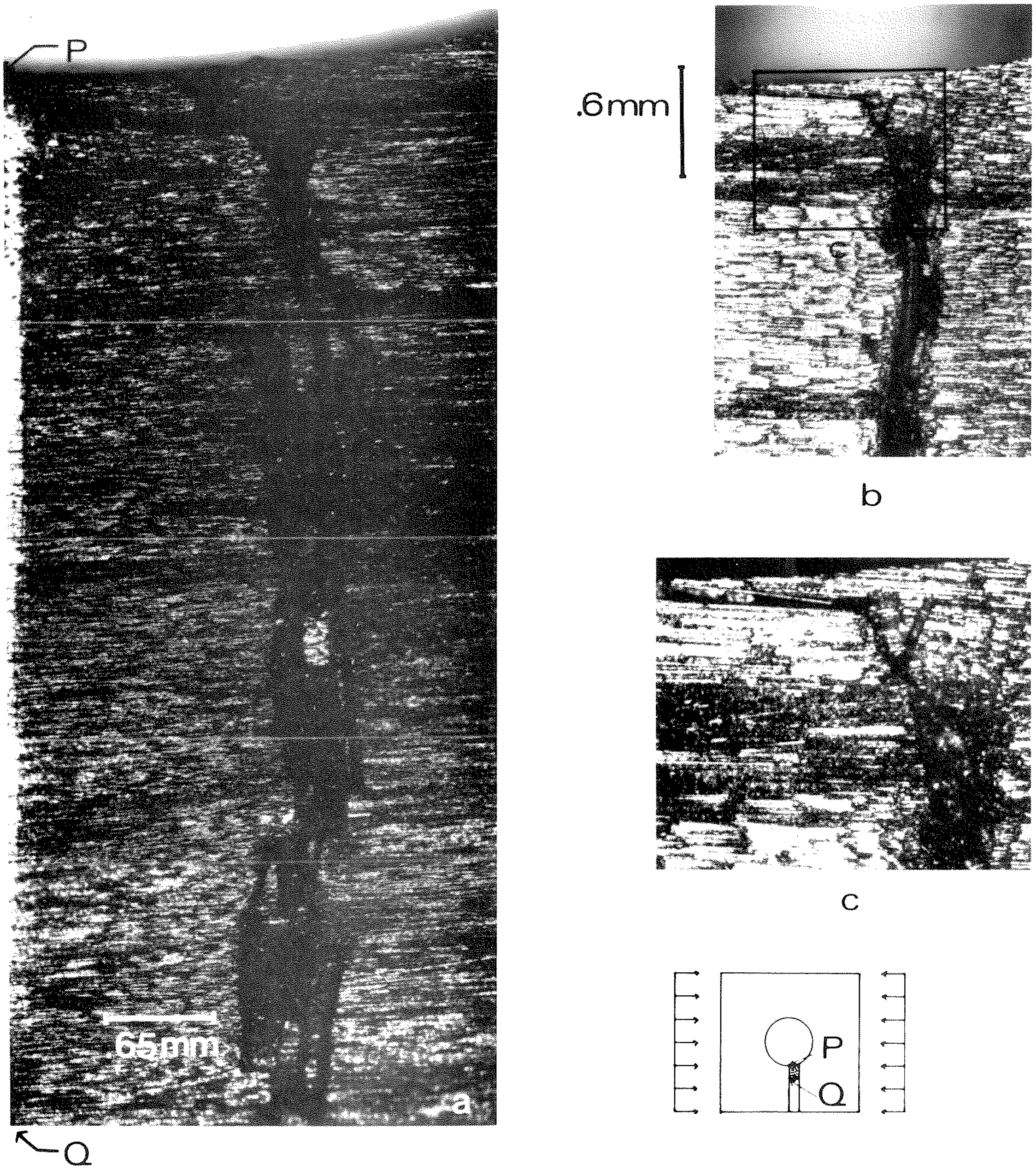

Figure 2.26 Planform view of internal damage to 0^0 plies. a)Mid-plane (z=0) 0^0 layer (spec. TB11). b) 0^0 layer at z=-2.6 mm (spec. TB17). c) Inset of (b).

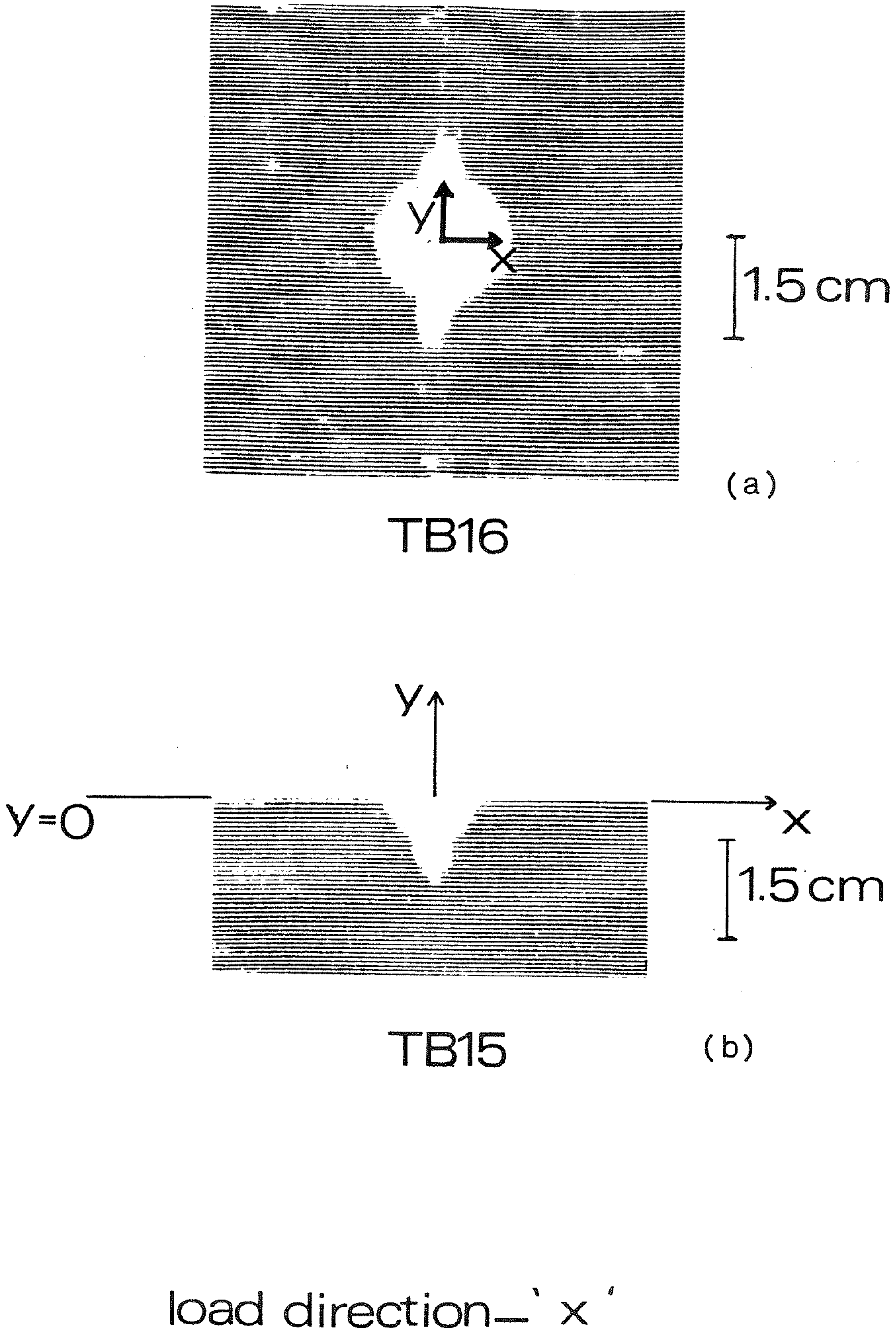

Figure 2.27 C-scan maps of damaged specimens. (a) Spec. TB16. (b) Spec. TB15.

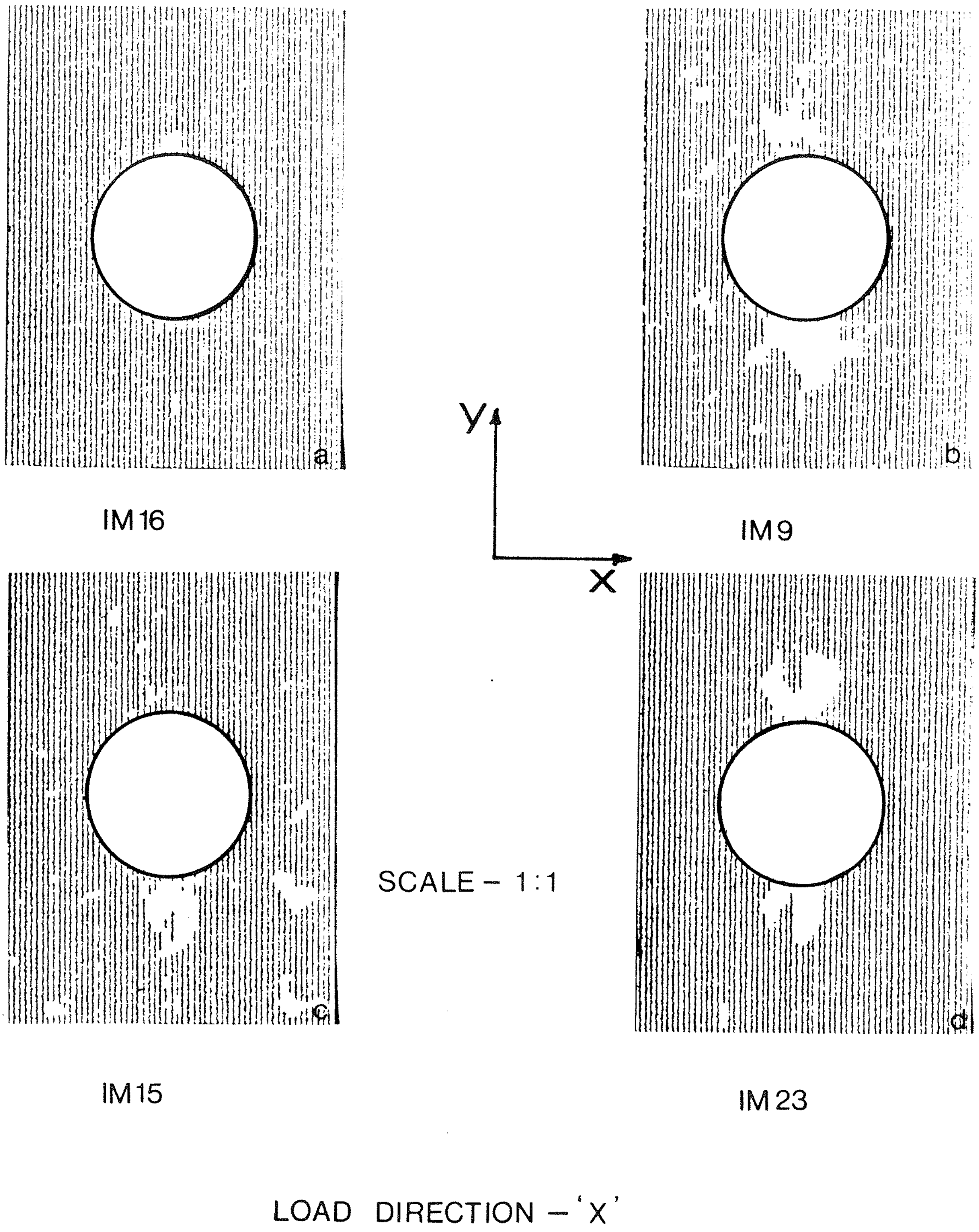

Figure 2.28 C-scan maps of damaged specimens. (a) Spec. IM16. (b) Spec.IM9. (c) Spec. IM15. (d) Spec. IM23.

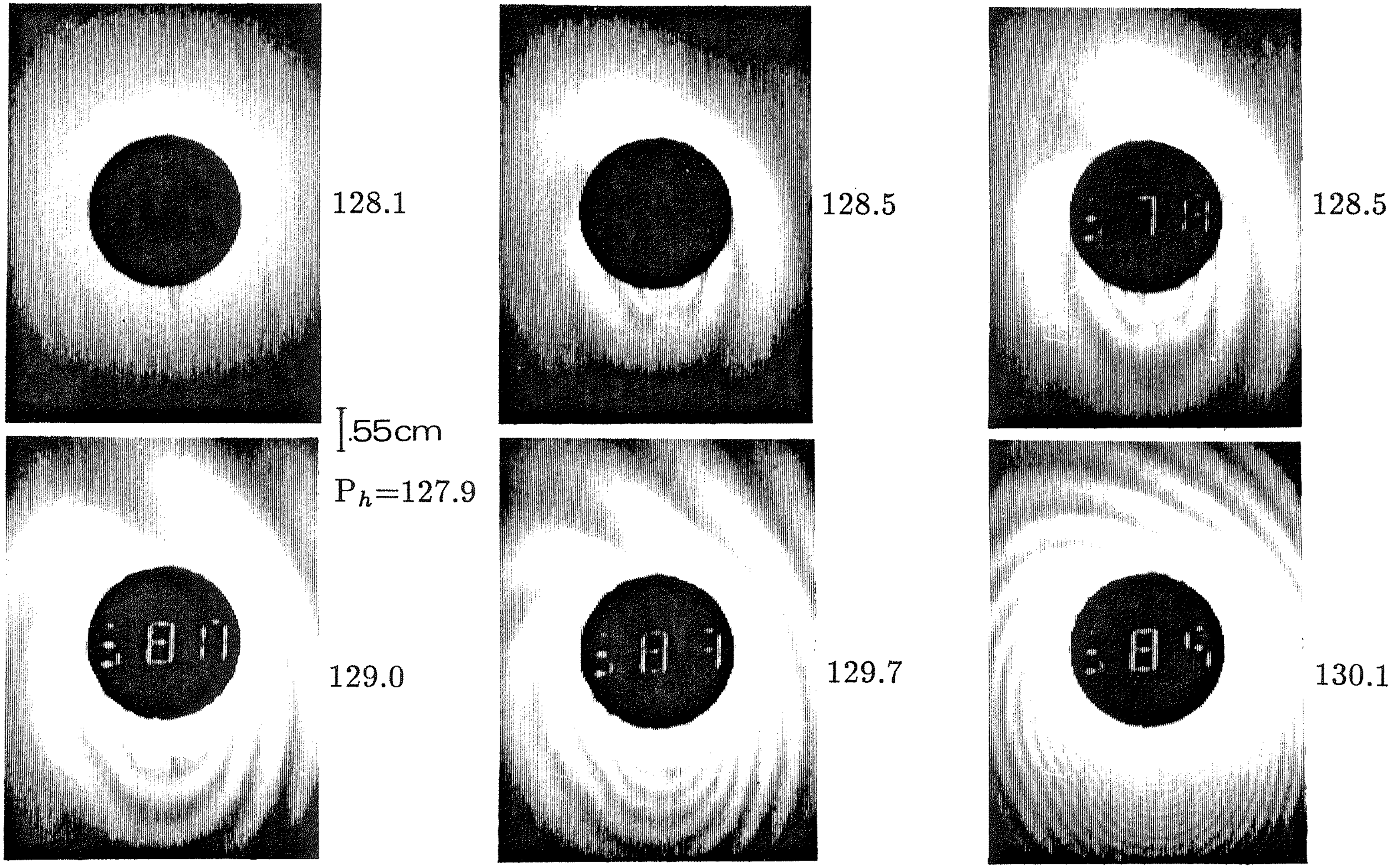

Figure 2.29 Surface buckle formation on lower half of spec. TB17.

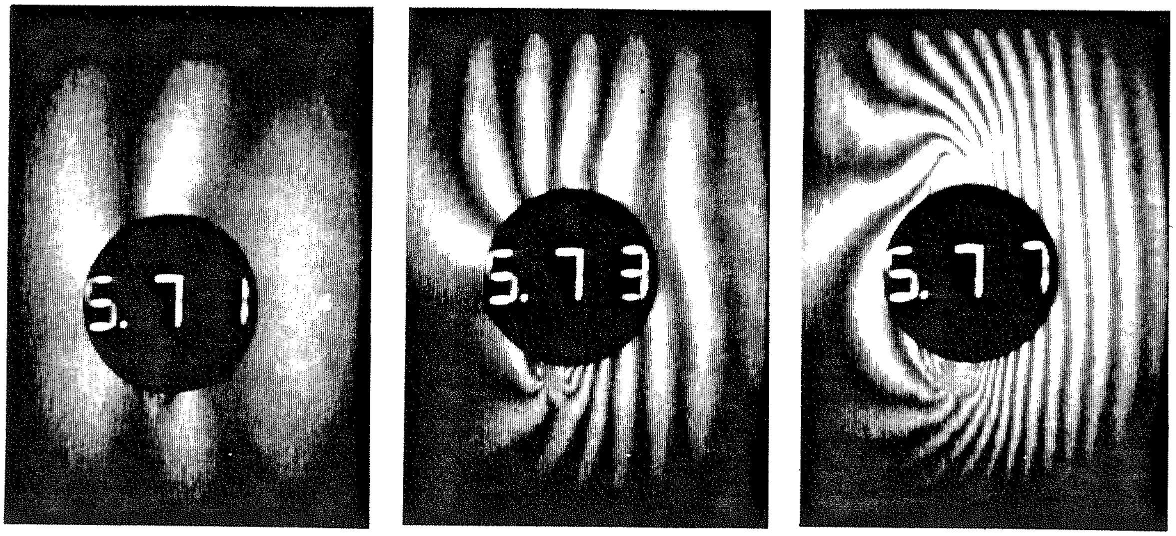

127.0 127.4 128.3

P_h=126.3

(a) IM7

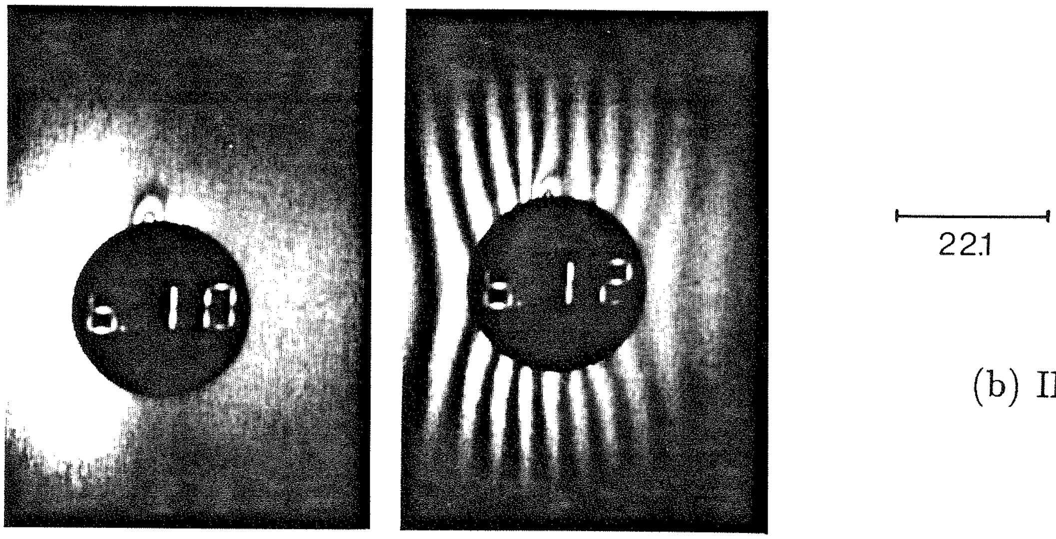

135.7 136.1

P_h=135.7

(b) IM2

Figure 2.30 (a) Initiation of damage in spec. IM7. (b) Localised bulging of surface near hole edge immediately after initiation (spec. IM2).

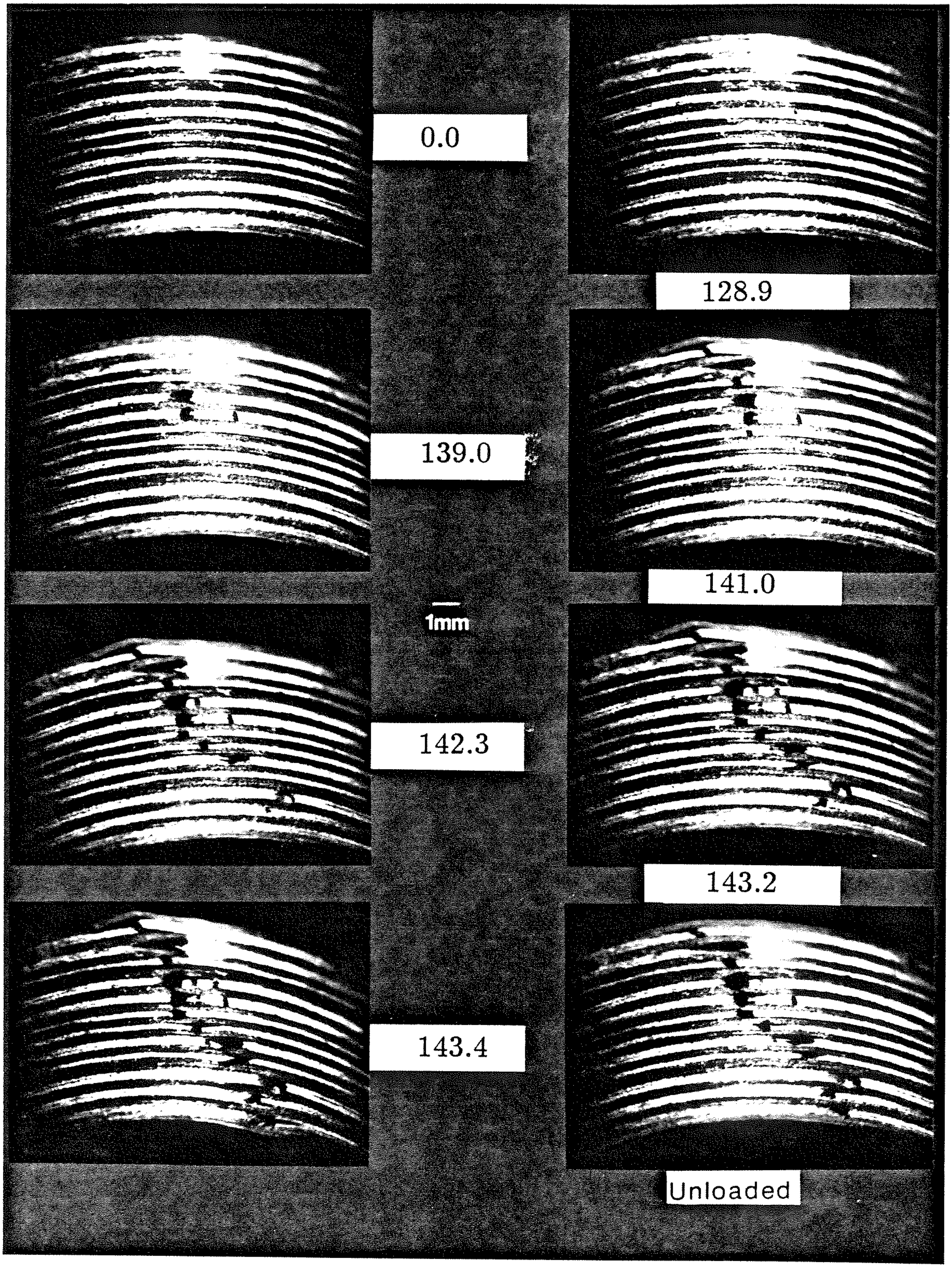

Figure 2.31 Hole surface photomicrographs showing damage progression (spec. TB17).

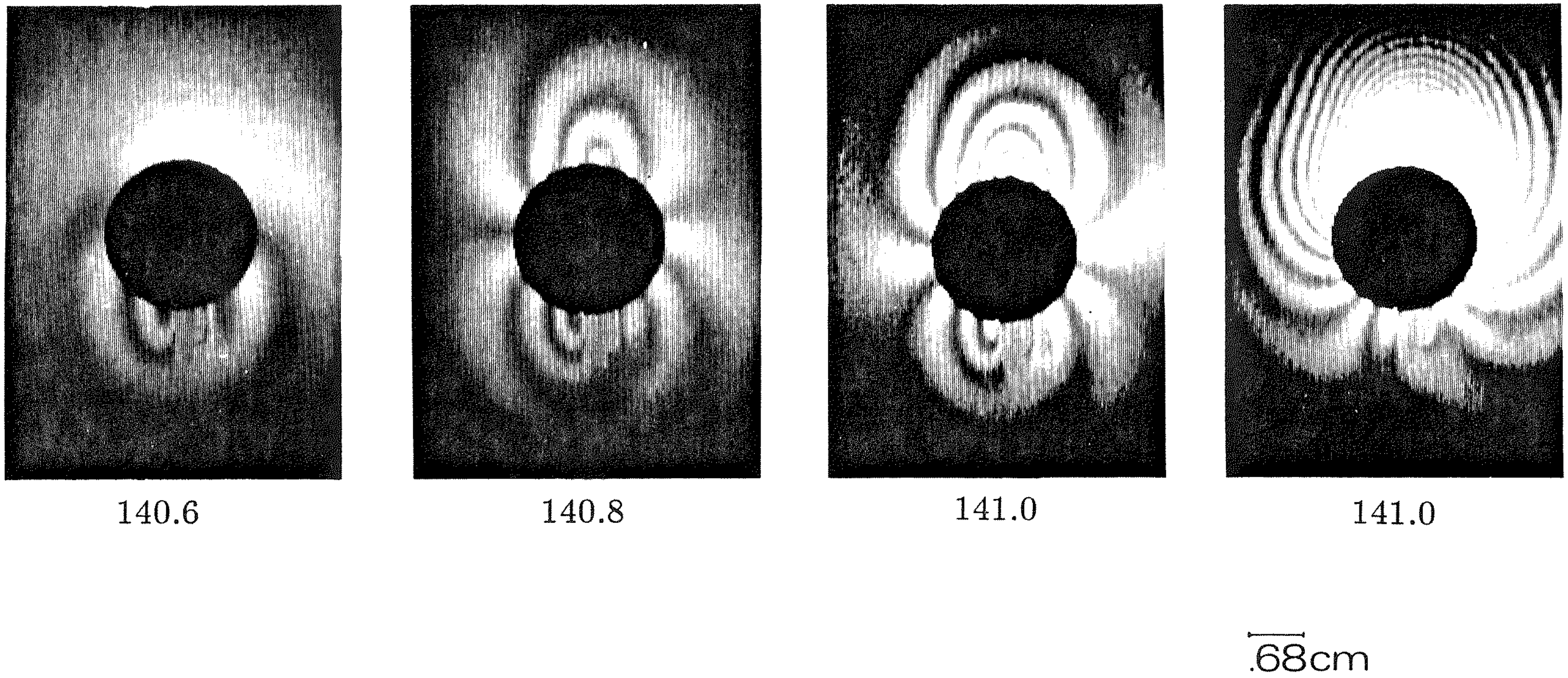

P_h=140.3

Figure 2.32 Initial buckling of surface delamination (spec. TB17). Duration between last two frames is 0.1 secs.

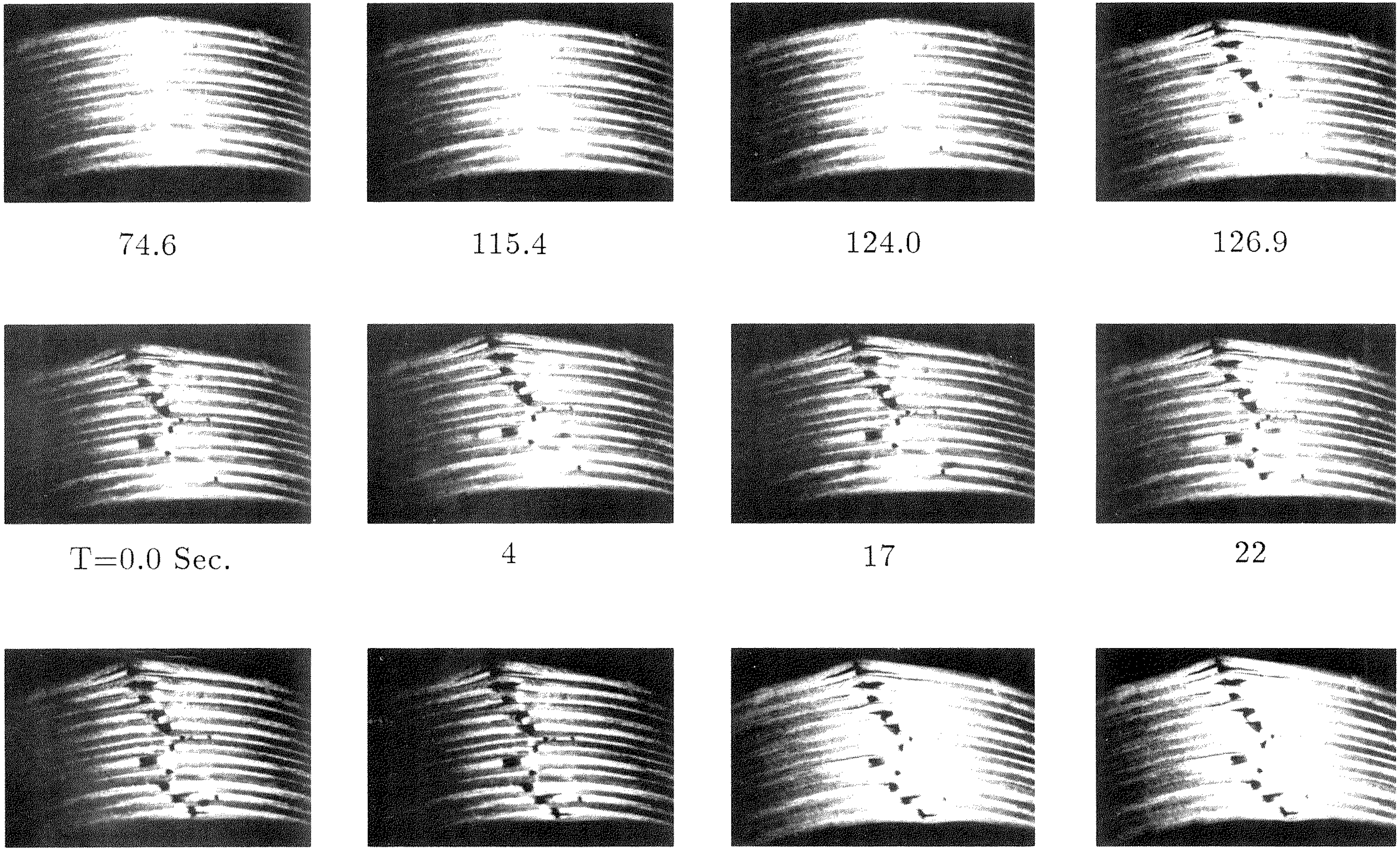

74.6

115.4

124.0

126.9

T=0.0 Sec.

4

17

22

27

32

47

52

Figure 2.33 Hole surface photo-micrographs (spec. TB10).

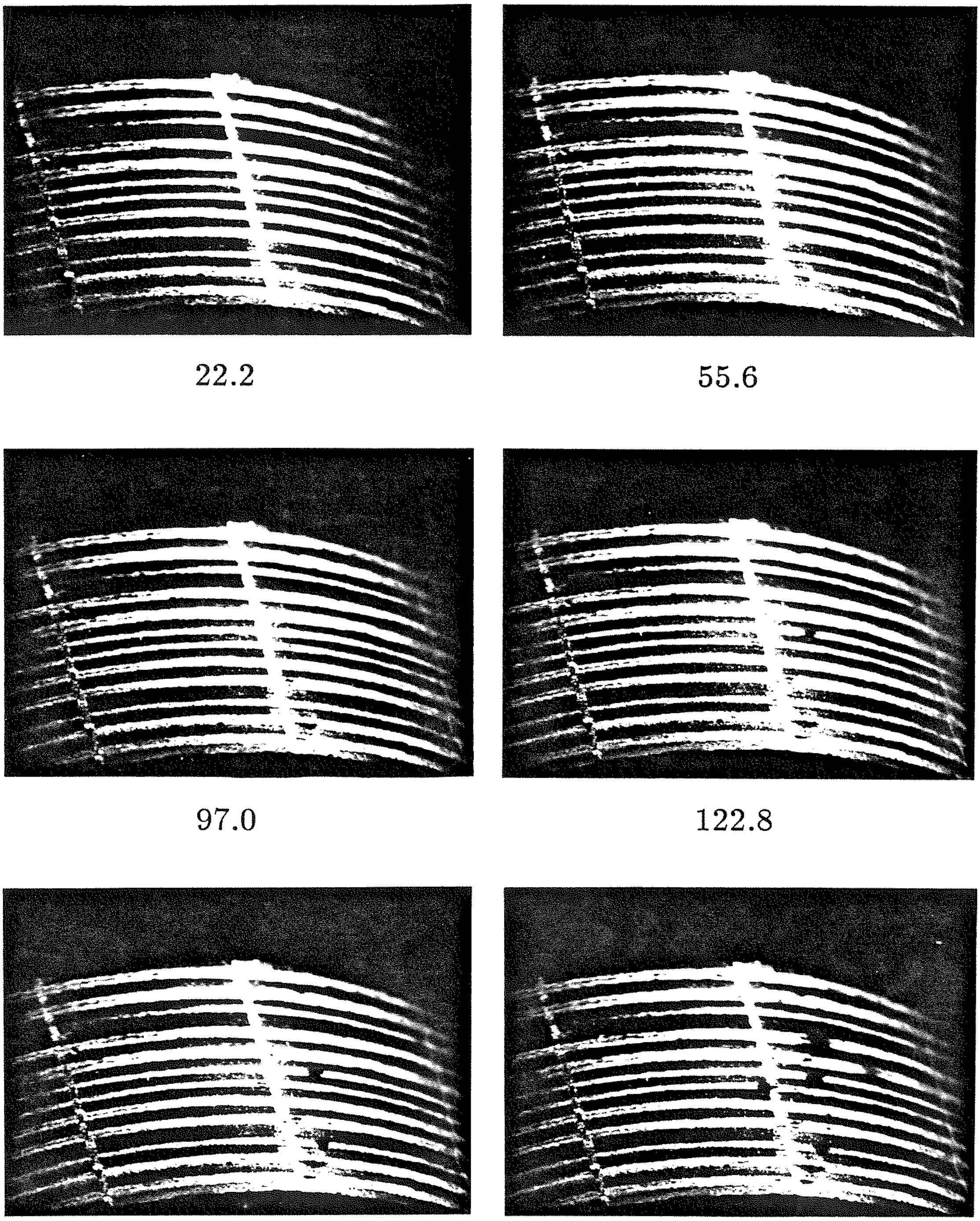

22.2

55.6

97.0

122.8

129.4

141.9

Specimen thickness = 7.44

Figure 2.34a Hole surface photomicrographs (spec. IM2).

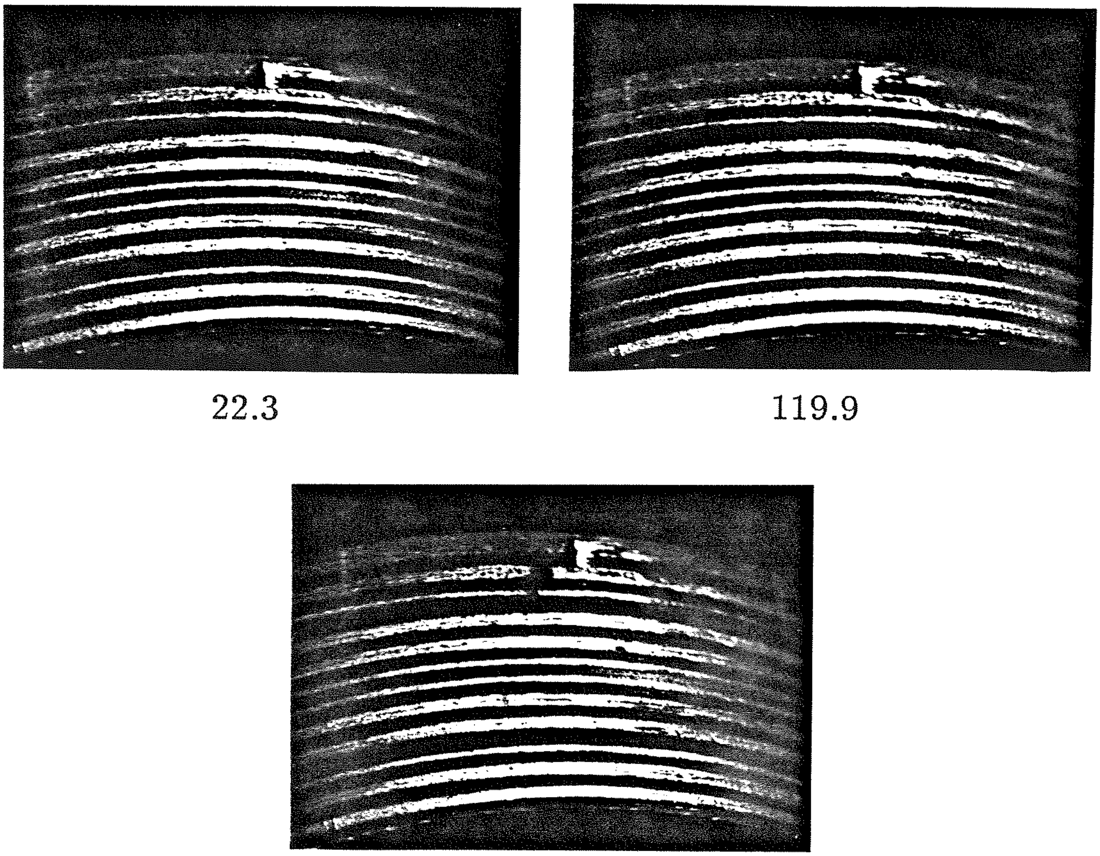

22.3

119.9

122.3

Specimen thickness = 7.32

Figure 2.34b Hole surface photomicrographs (spec. IM16).

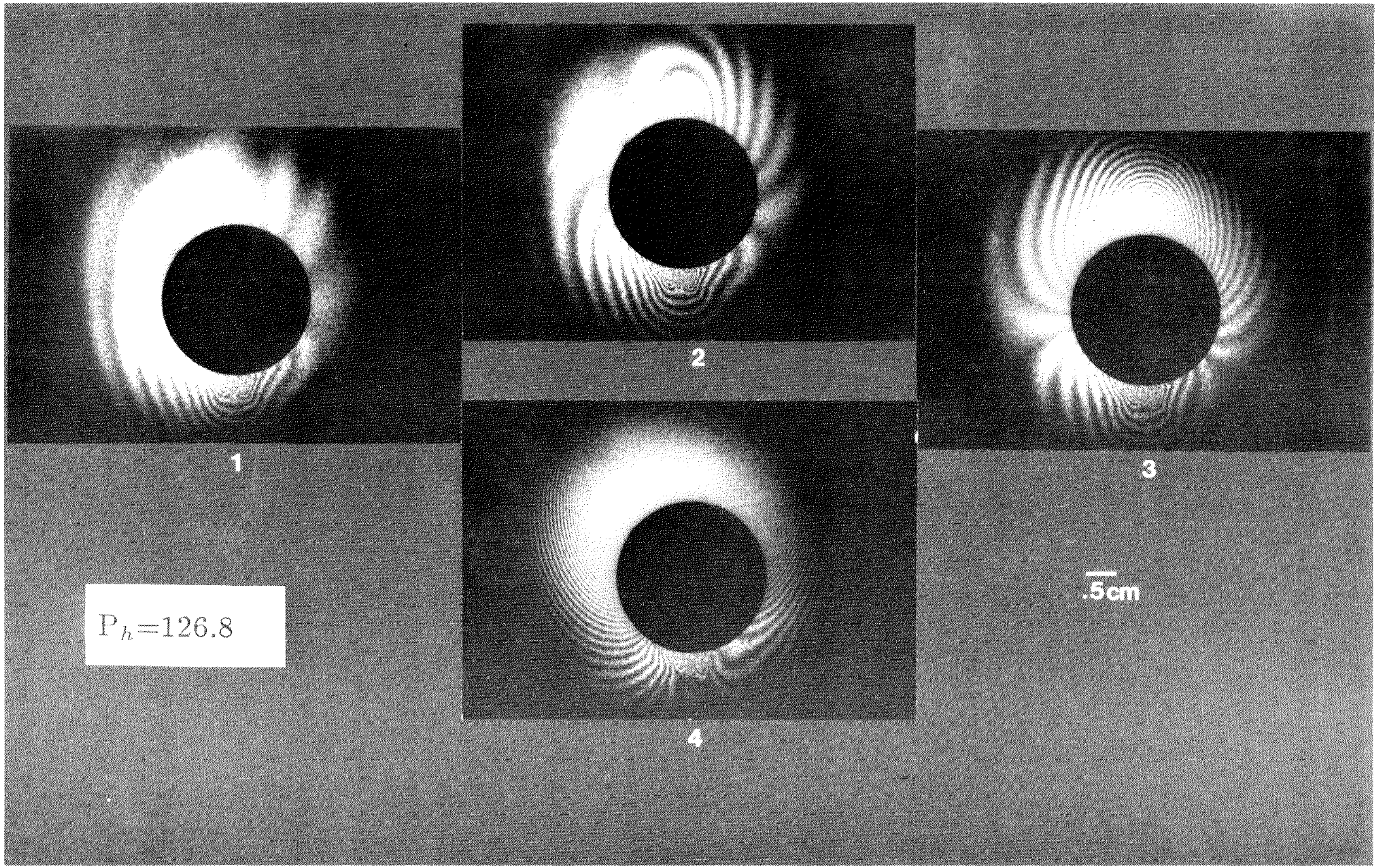

Figure 2.35 Propagation of surface buckle leading to catastrophic failure (spec. TB1).

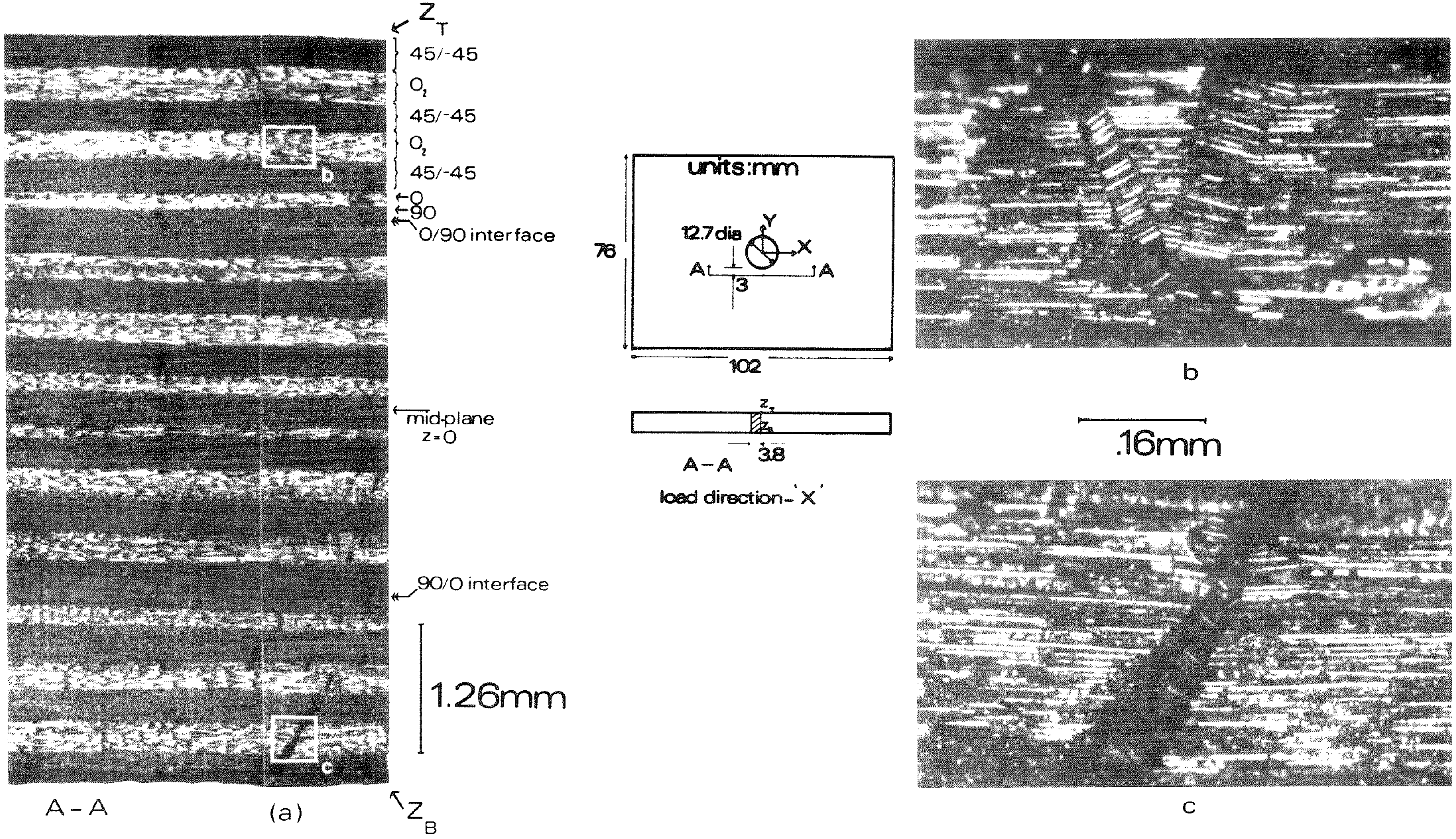

Figure 2.36 Internal damage at the vicinity of the hole (spec. TB15). a) Entire cross-section. b) Complimentary kink in second 0^0 layer from top. c) Magnified view of damage to bottom 0^0 layer.

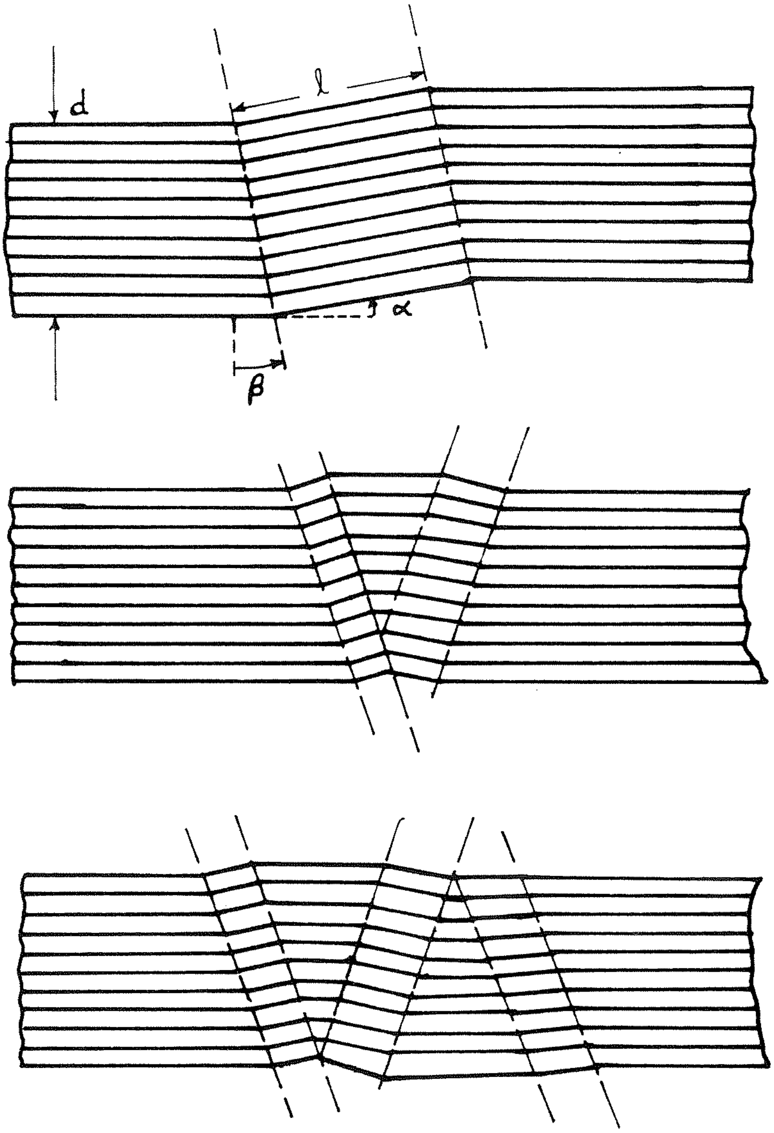

(ref. 10)

Figure 2.37 Geometry of a kink band.

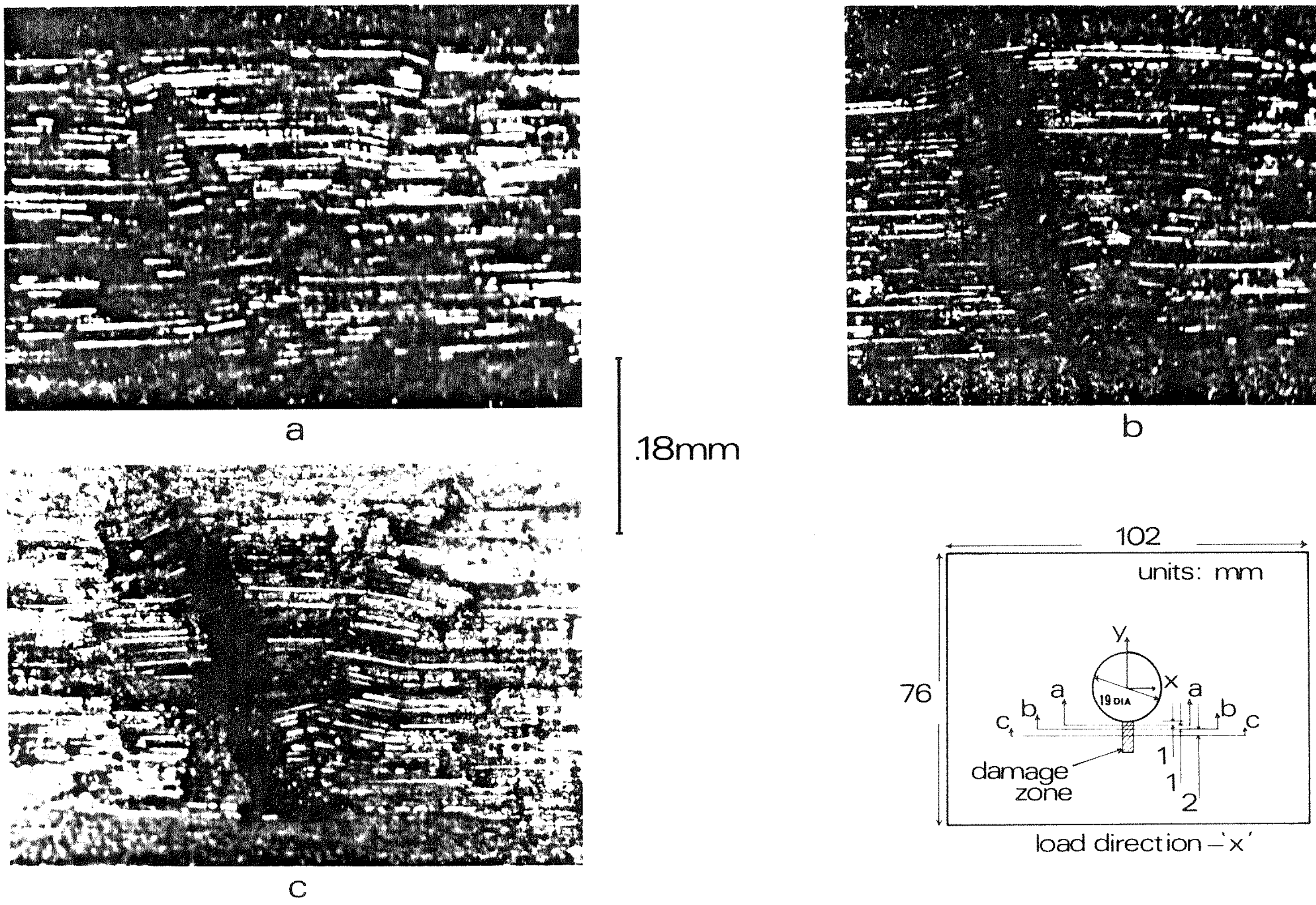

Figure 2.38 Kink band appearence at different cross-sections (spec. TB17).

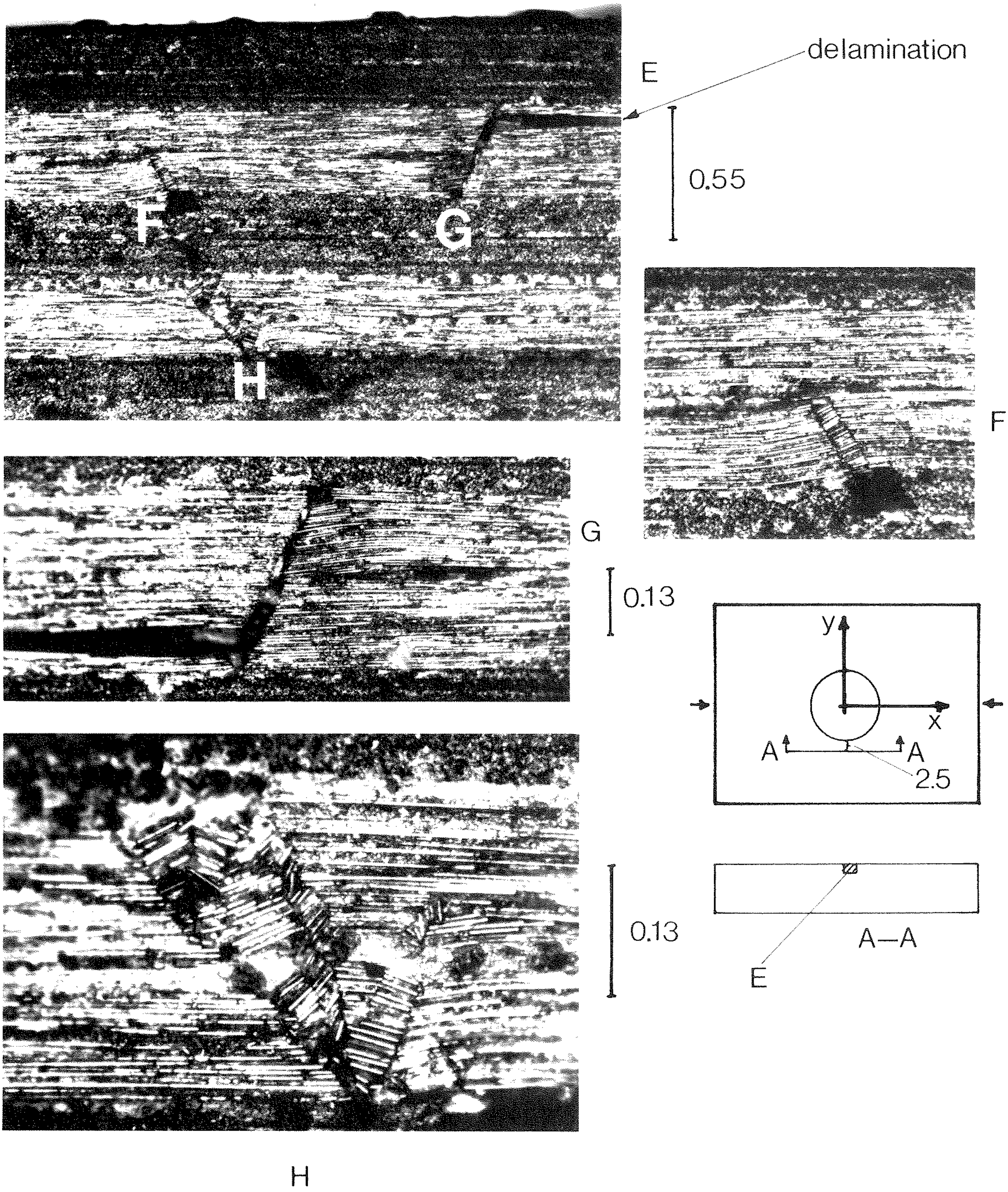

Figure 2.39 Internal damage at section A-A in spec. IM16.

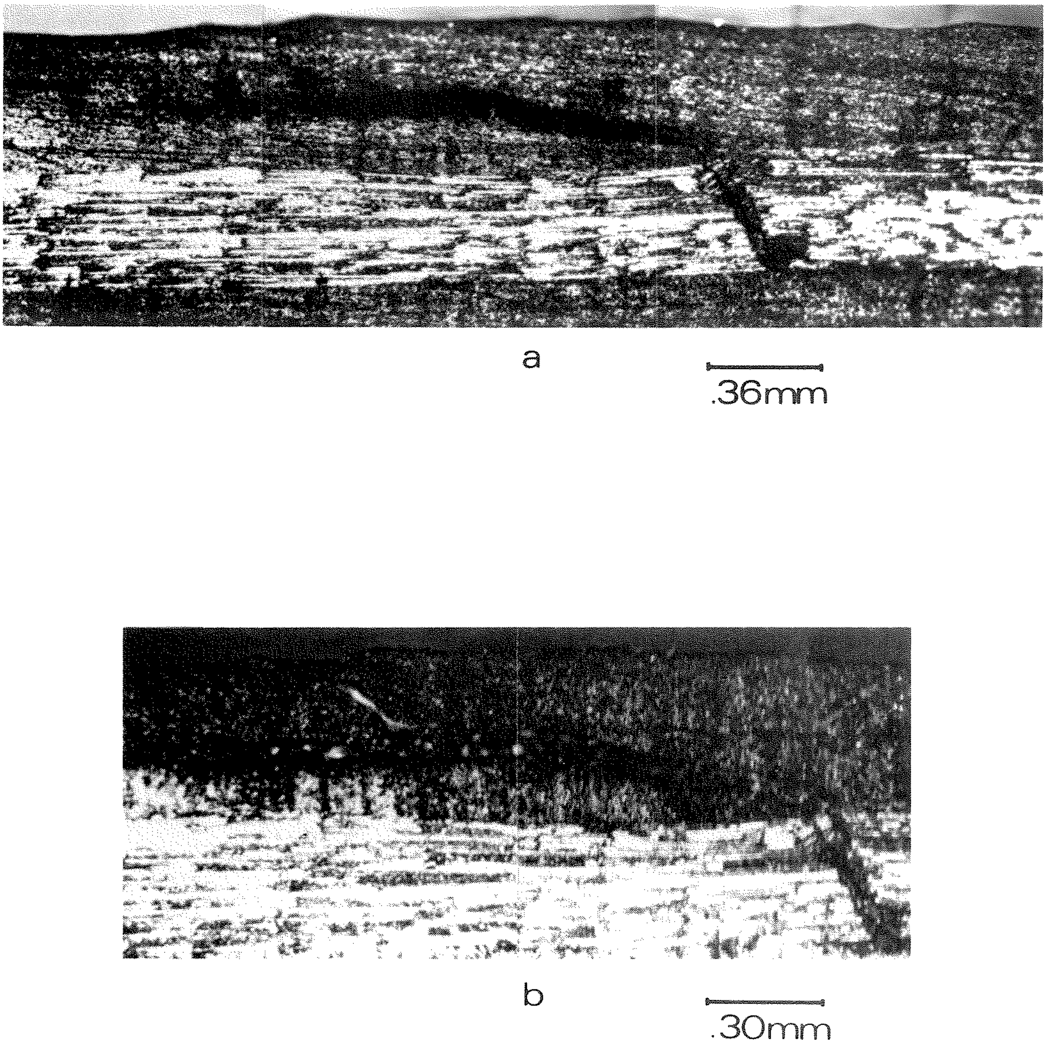

Figure 2.40 Sectional study indicating surface delamination in spec. TB17.

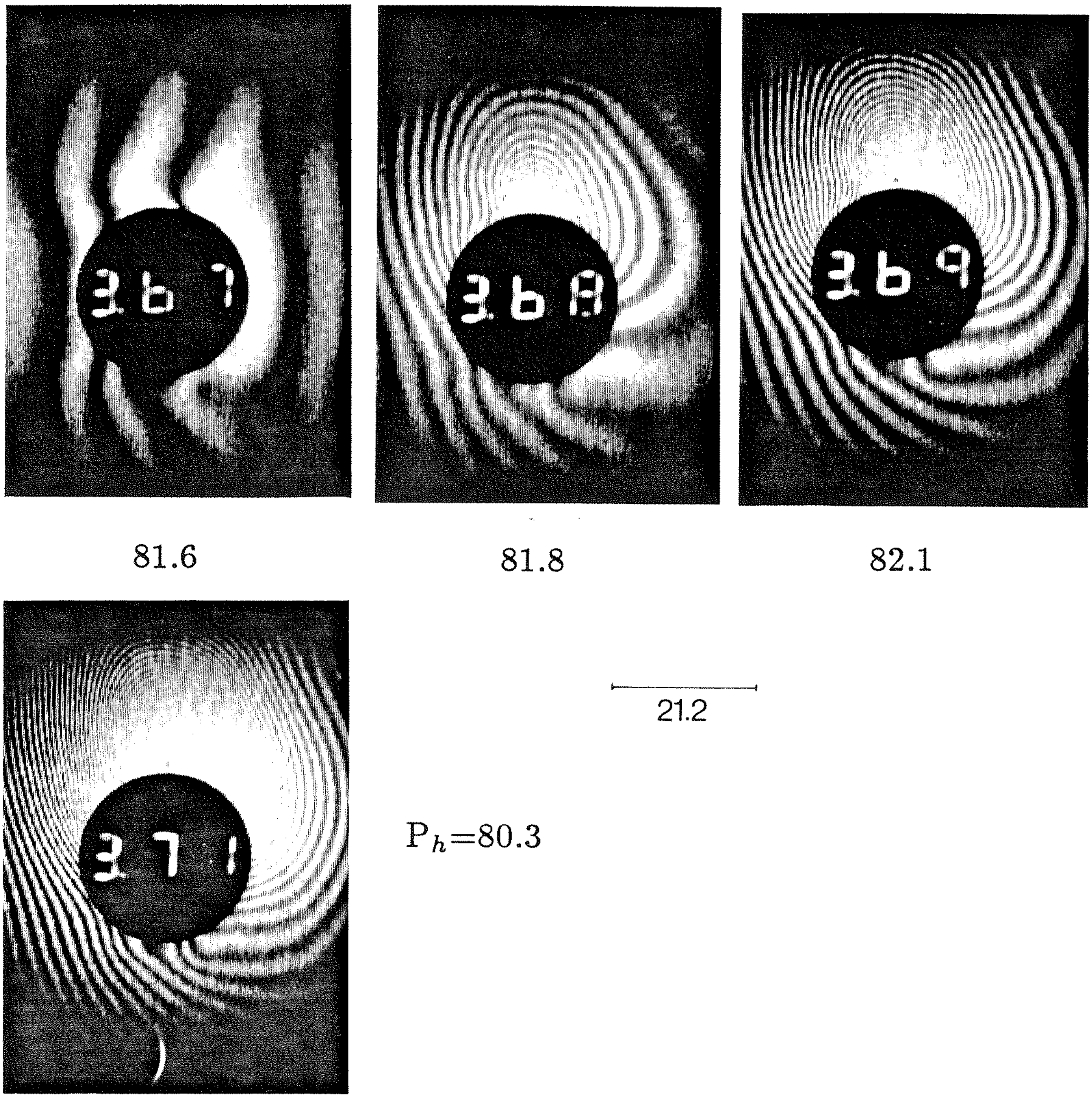

81.6

81.8

82.1

82.5

P_h=80.3

Figure 2.41a Initiation of damage in spec. IM15

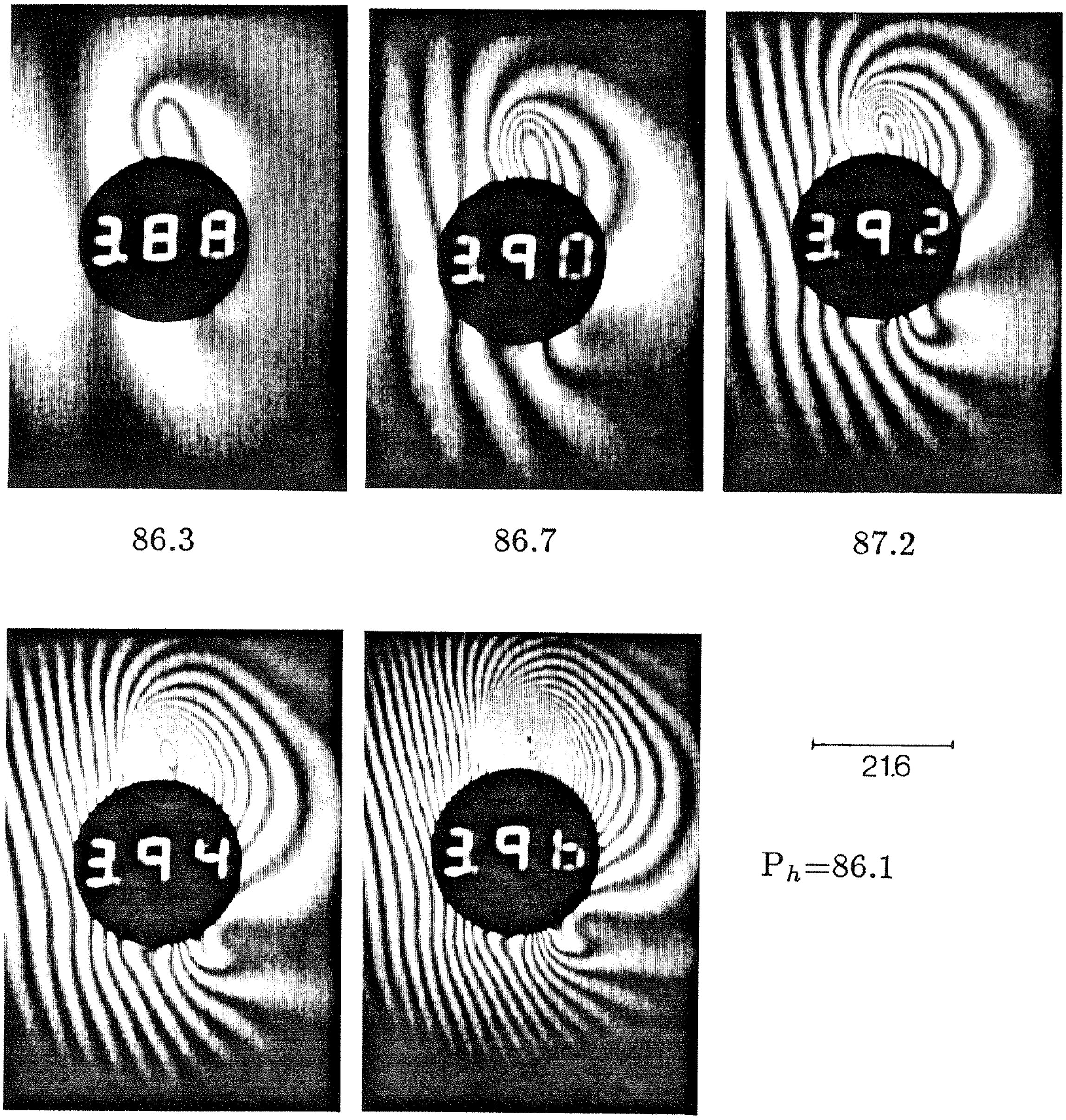

86.3 86.7 87.2

87.6 88.1

P_h=86.1

Figure 2.41b Response of buckled delaminated portions (spec. IM15).

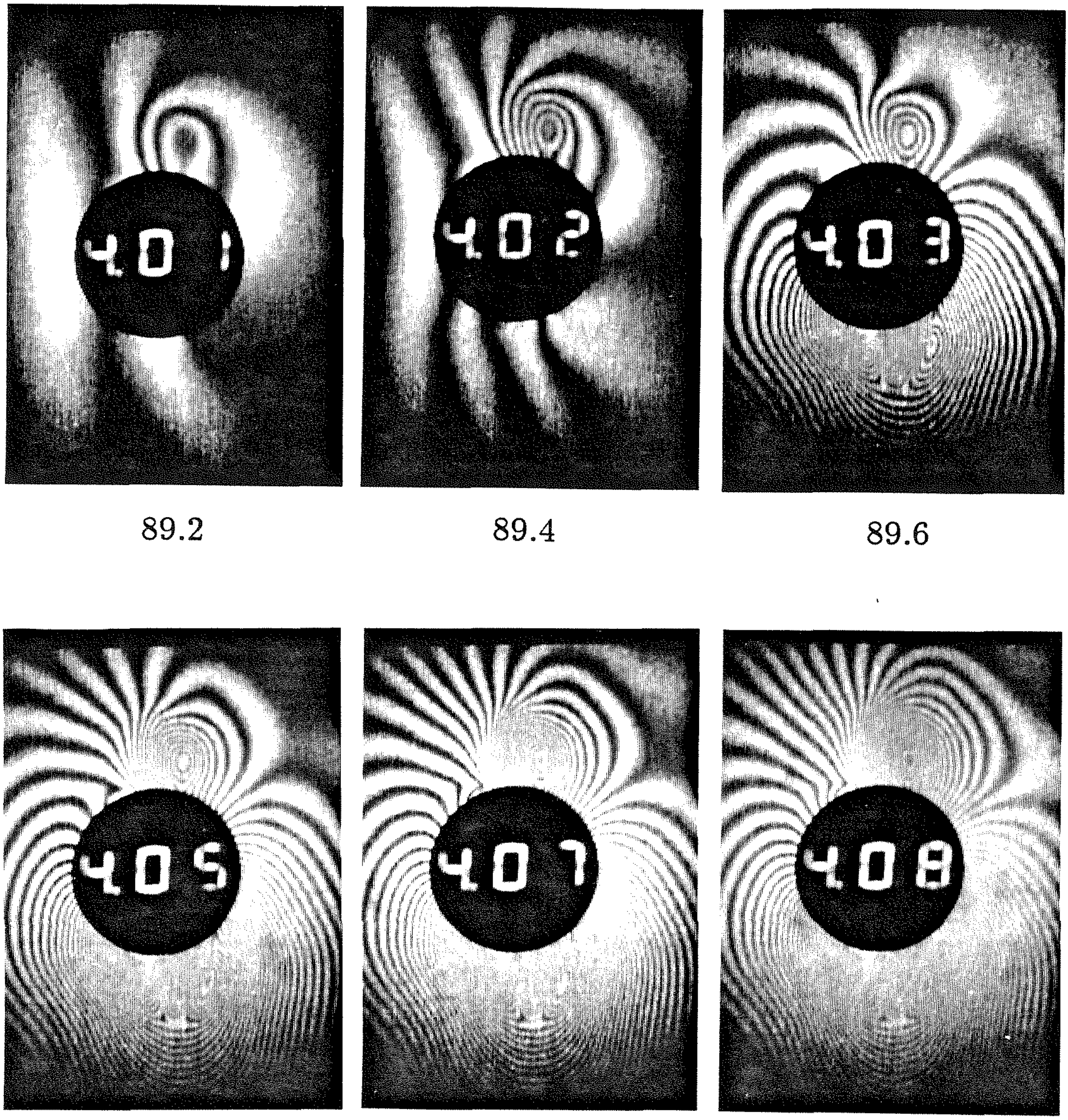

89.2 89.4 89.6

90.1 90.5 90.7

P_h=88.9

21.2

Figure 2.41c Initiation of damage on lower half of specimen (compare frames 2 and 3) leading to buckling of delaminated portions (spec. IM15).

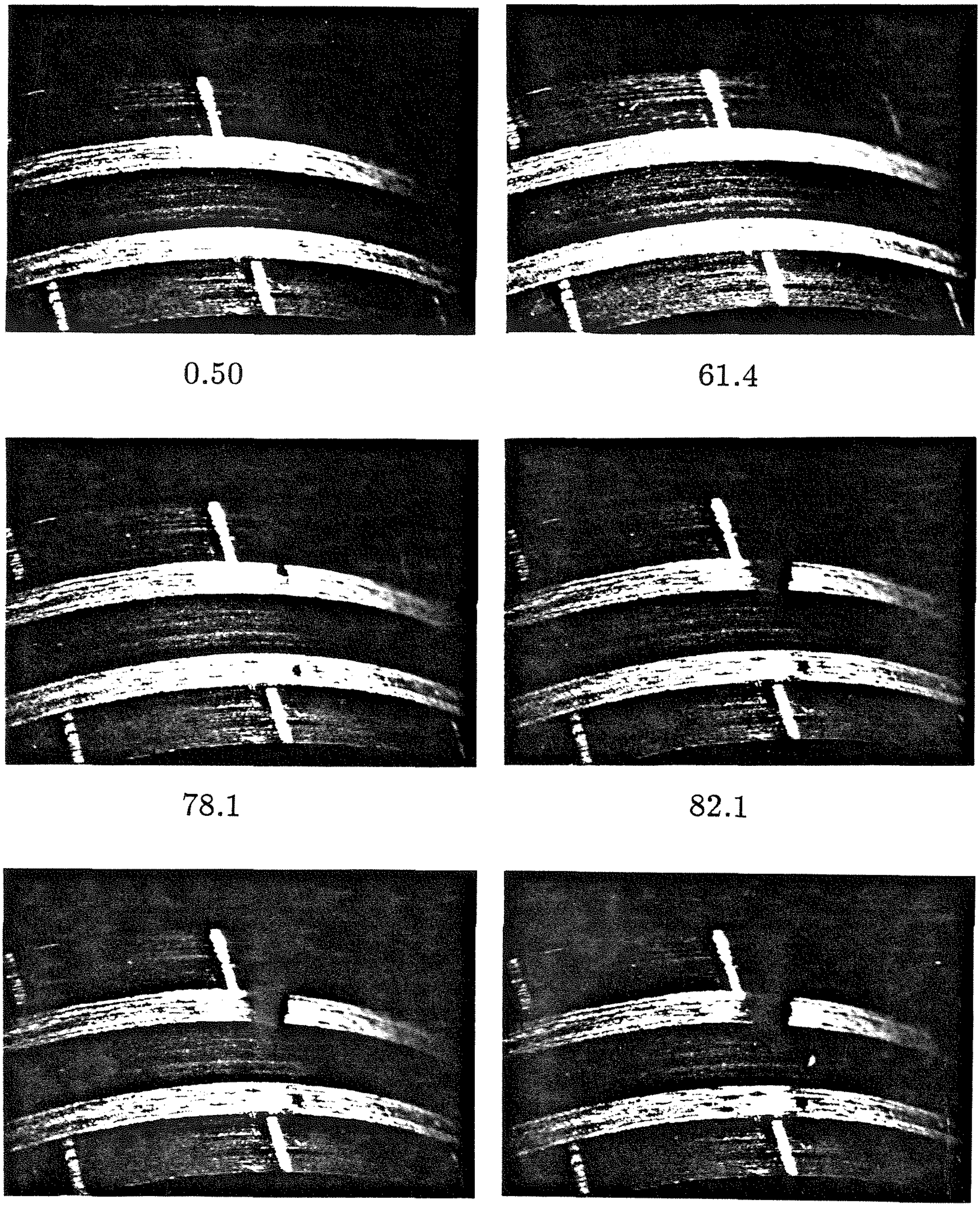

0.50

61.4

78.1

82.1

87.8

91.2

Specimen thickness = 7.31

Figure 2.42 Hole surface photomicrographs (spec. IM15).

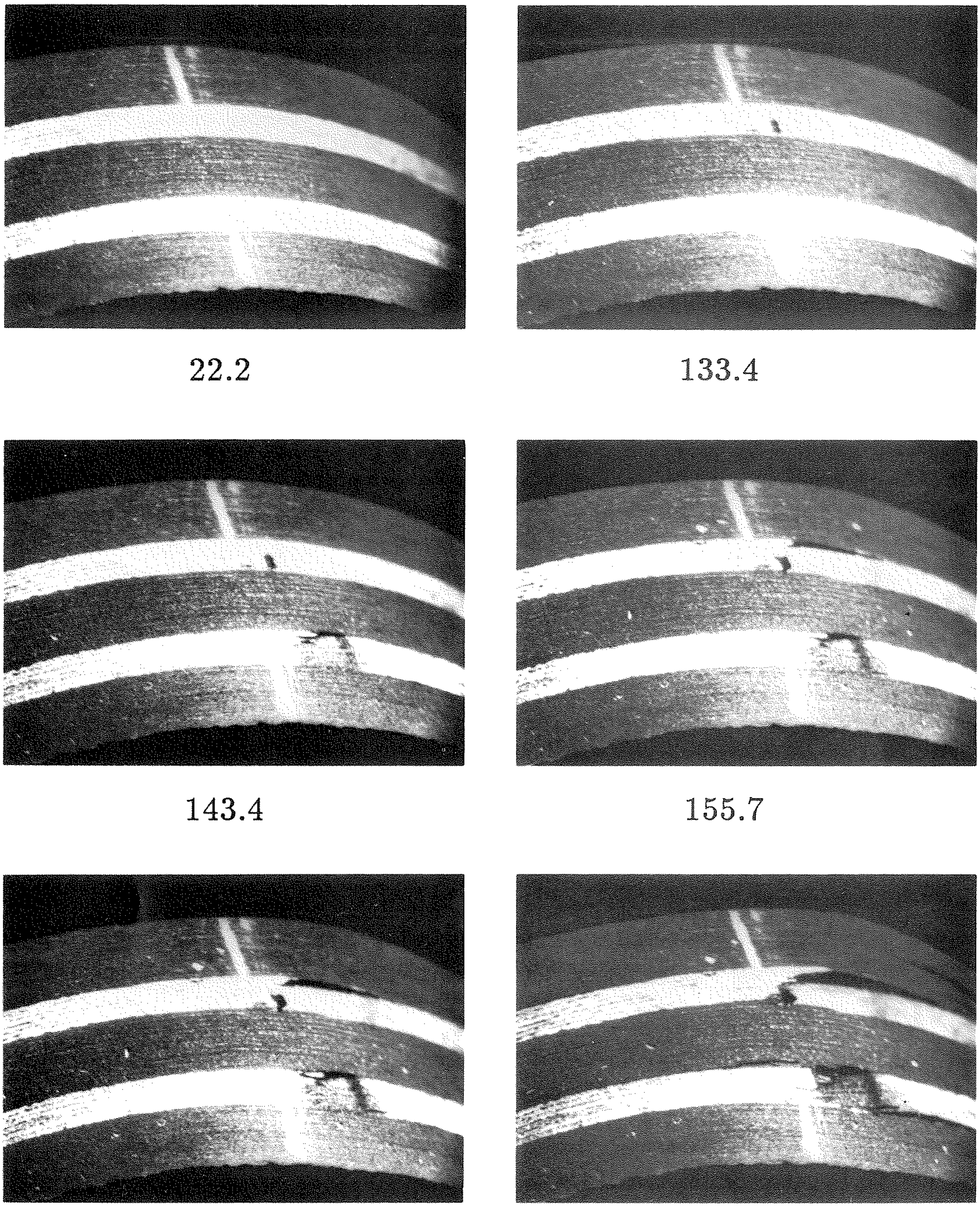

22.2

133.4

143.4

155.7

159.7

164.7

Specimen thickness = 7.33

Figure 2.43 Hole surface photo-micrographs (spec. IM26).

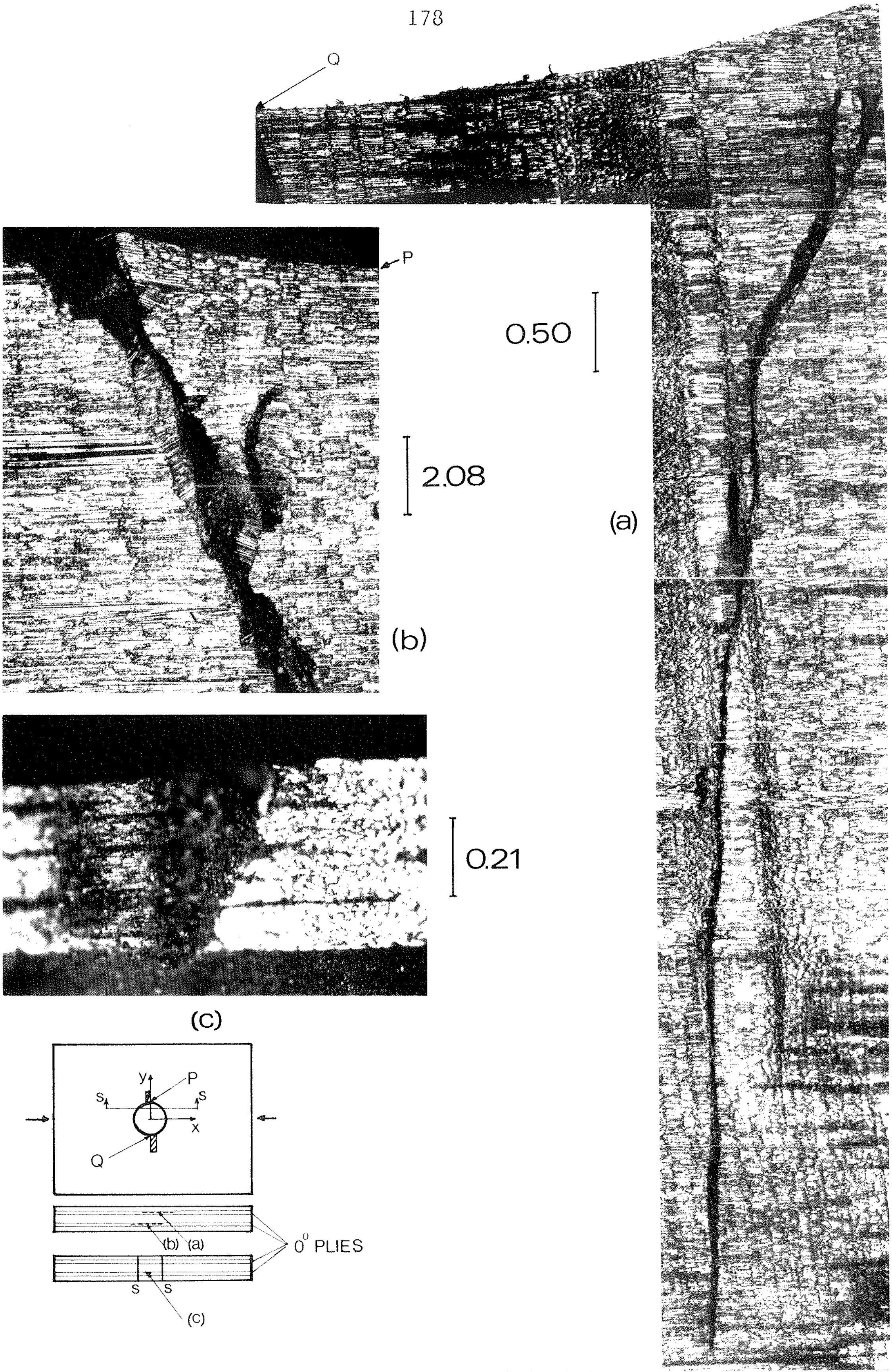

Figure 2.44 Internal damage at the vicinity of the hole (spec. IM15) a) Planform (x-y plane) view of damage in 0^0 layers extending outward from hole edge. b) Magnified view of fiber buckling near hole surface. c) Looking down on hole surface at section S-S showing fiber jut-out failure.

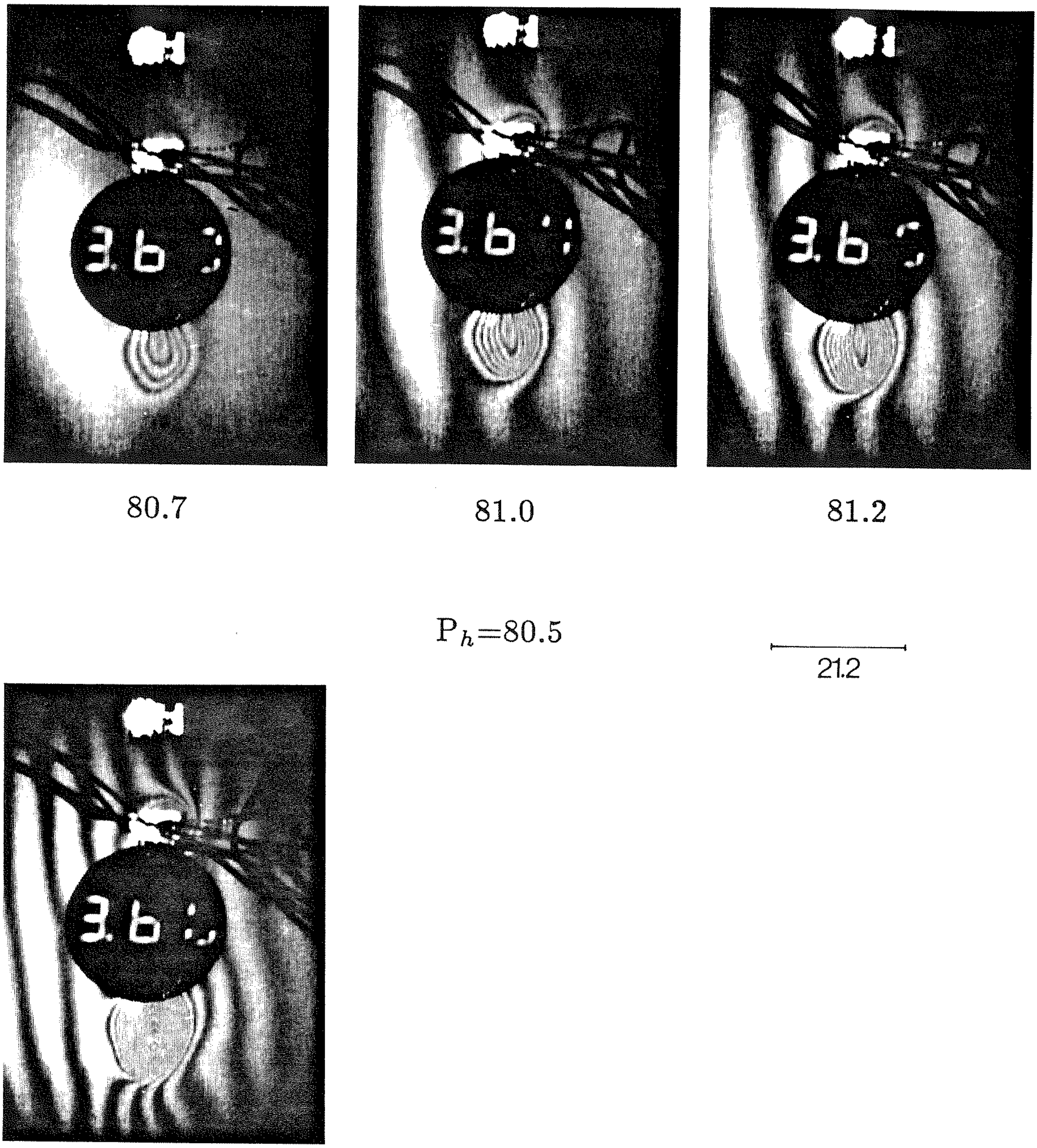

80.7

81.0

81.2

P$_h$=80.5

81.4

Figure 2.45 Local buckling of delaminated portions (spec. IM30).

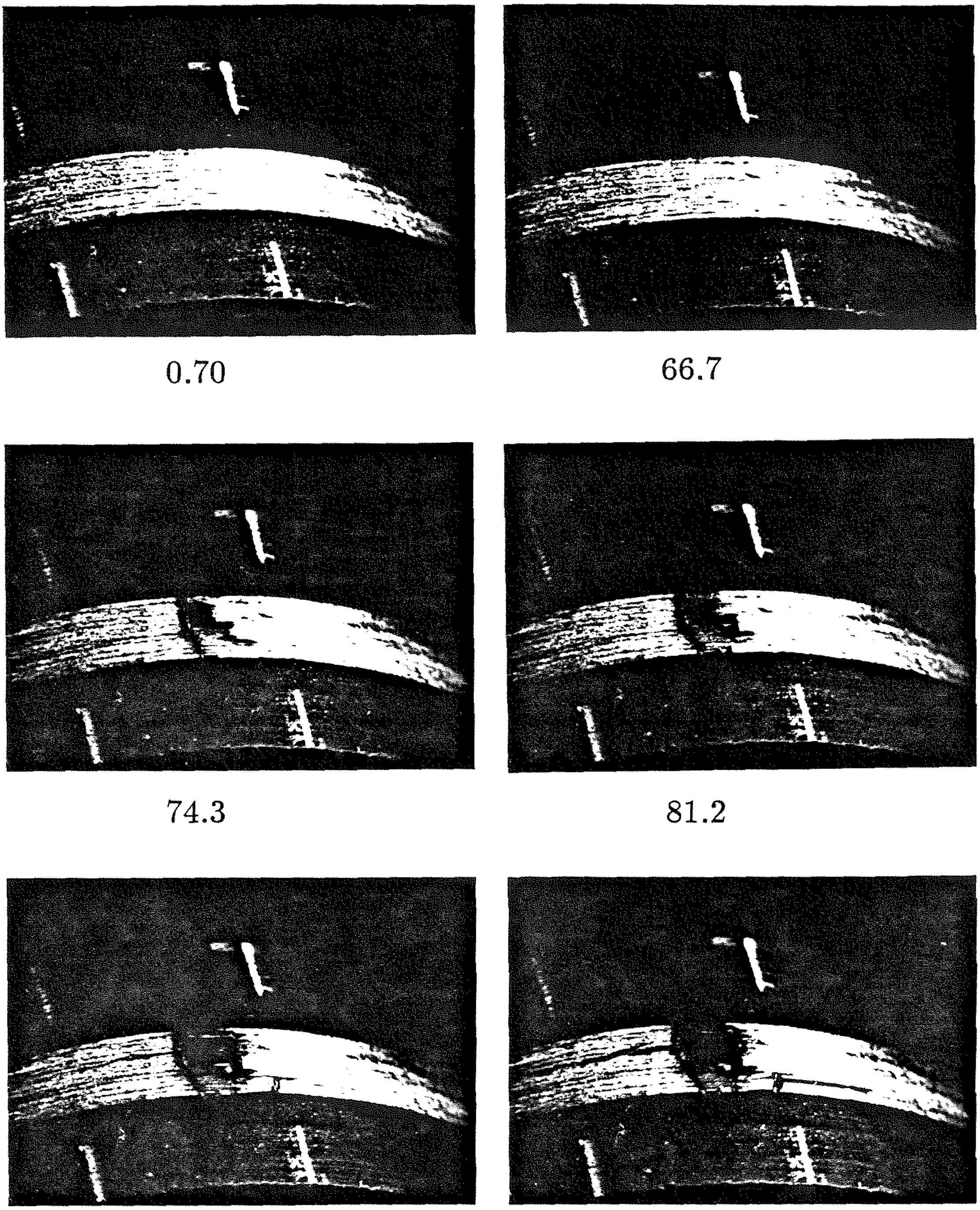

0.70

66.7

74.3

81.2

86.1

87.2

Specimen thickness = 7.38

Figure 2.46 Hole surface photomicrographs (spec. IM10).

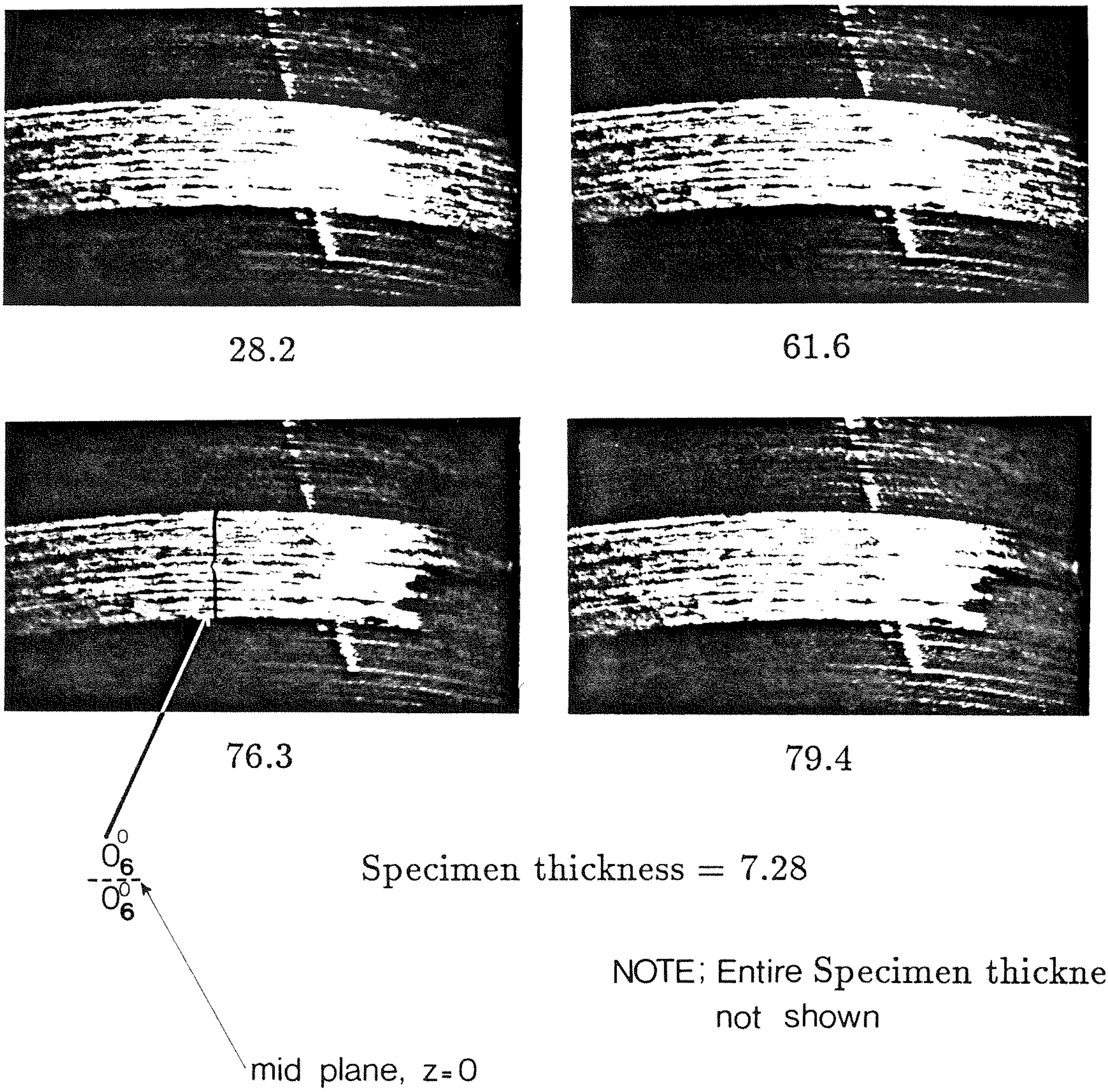

28.2 61.6

76.3 79.4

Specimen thickness = 7.28

NOTE; Entire Specimen thickness
not shown

Figure 2.47 Magnified views of hole surface showing progressive failure of 0^0 plies (spec. IM17).

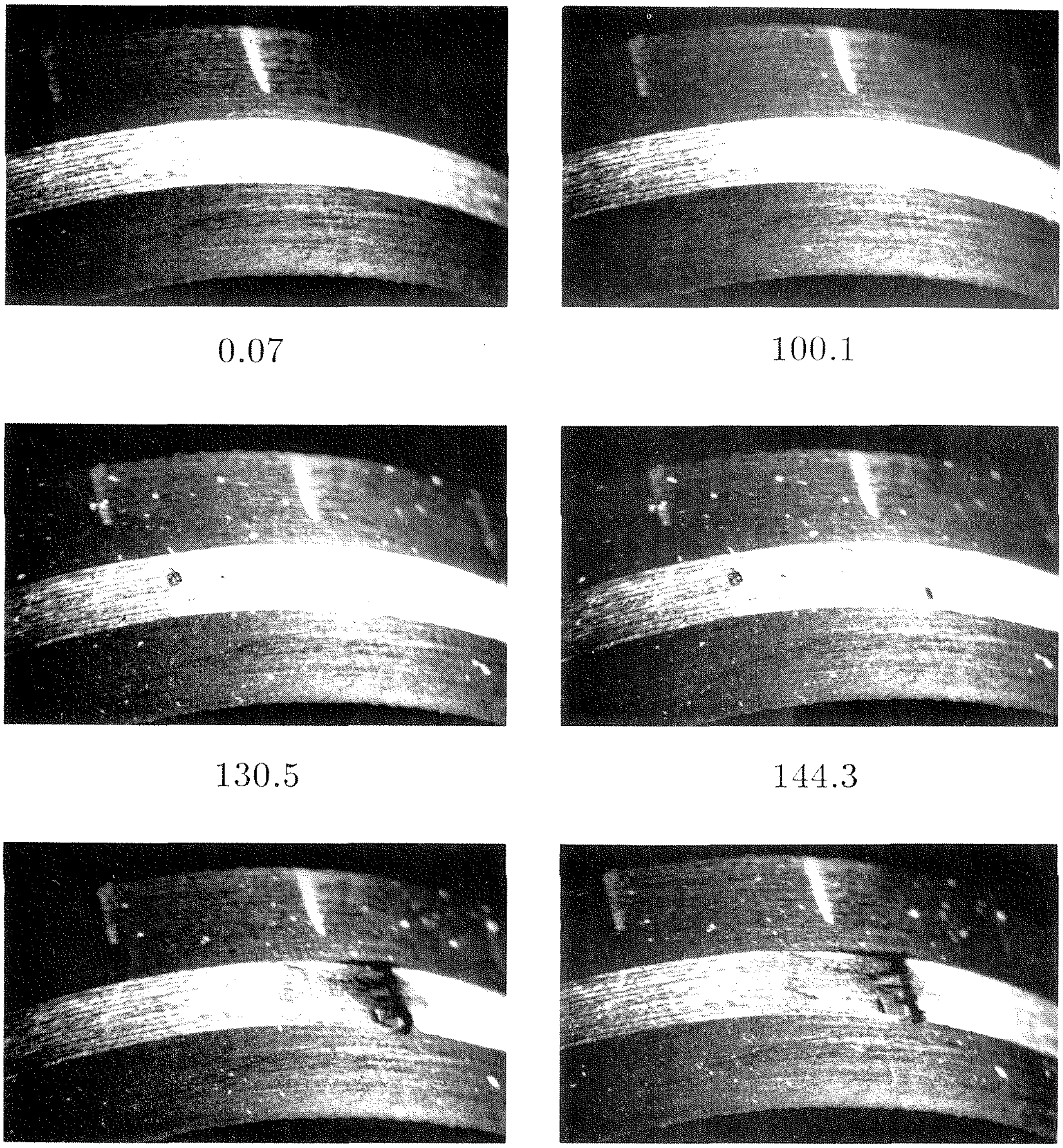

0.07

100.1

130.5

144.3

147.9

unloaded

Specimen thickness = 7.33

Figure 2.48 Hole surface photo-micrographs (spec. IM23).

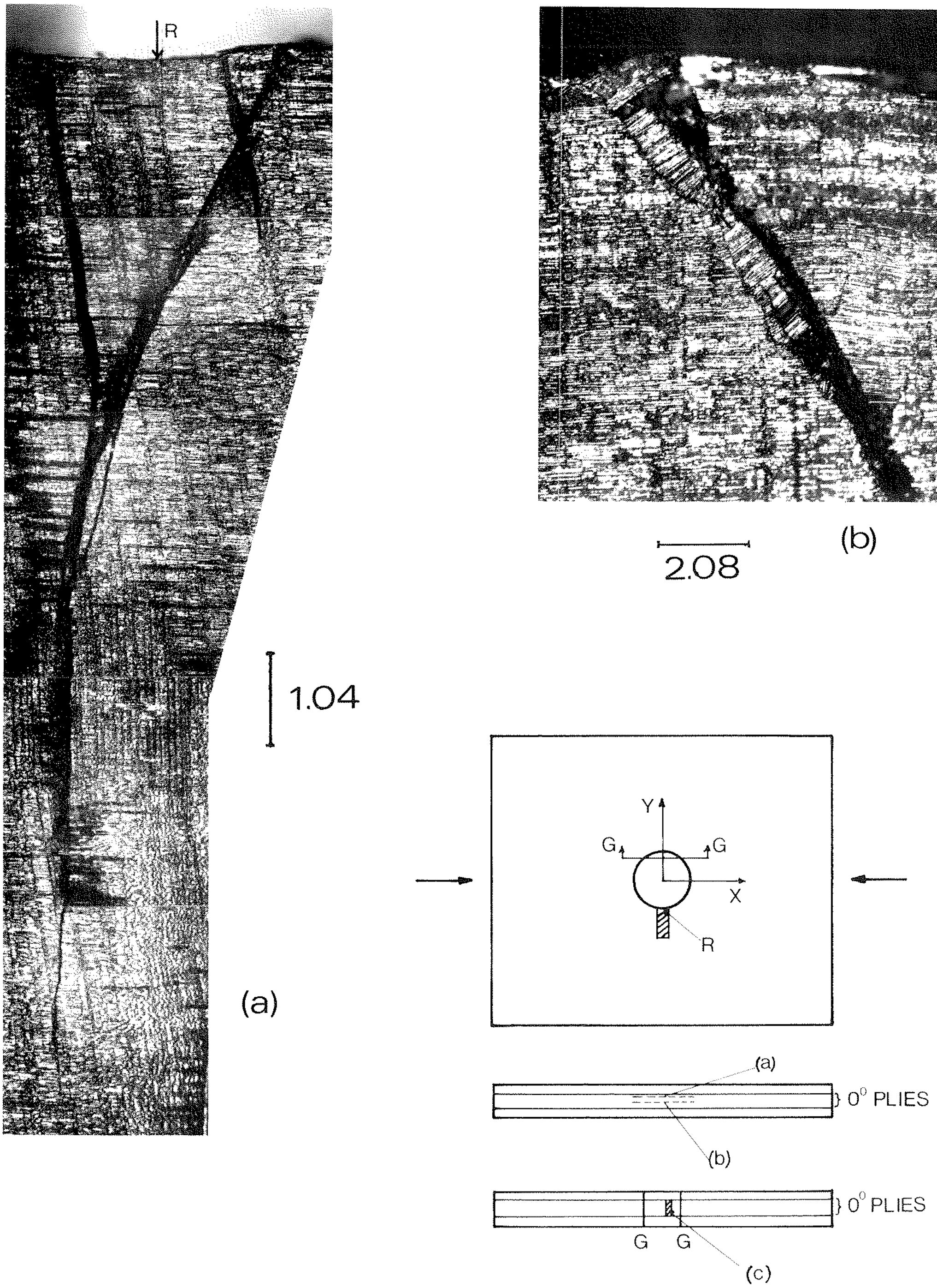

Figure 2.49 Internal damage at the vicinity of the hole (spec. IM23) a) Planform (x-y plane) view of damage in 0^0 layers extending outward from hole edge. b) Magnified view of fiber buckling near hole surface. c) Enlarged view of fiber jut-out failure on hole surface.

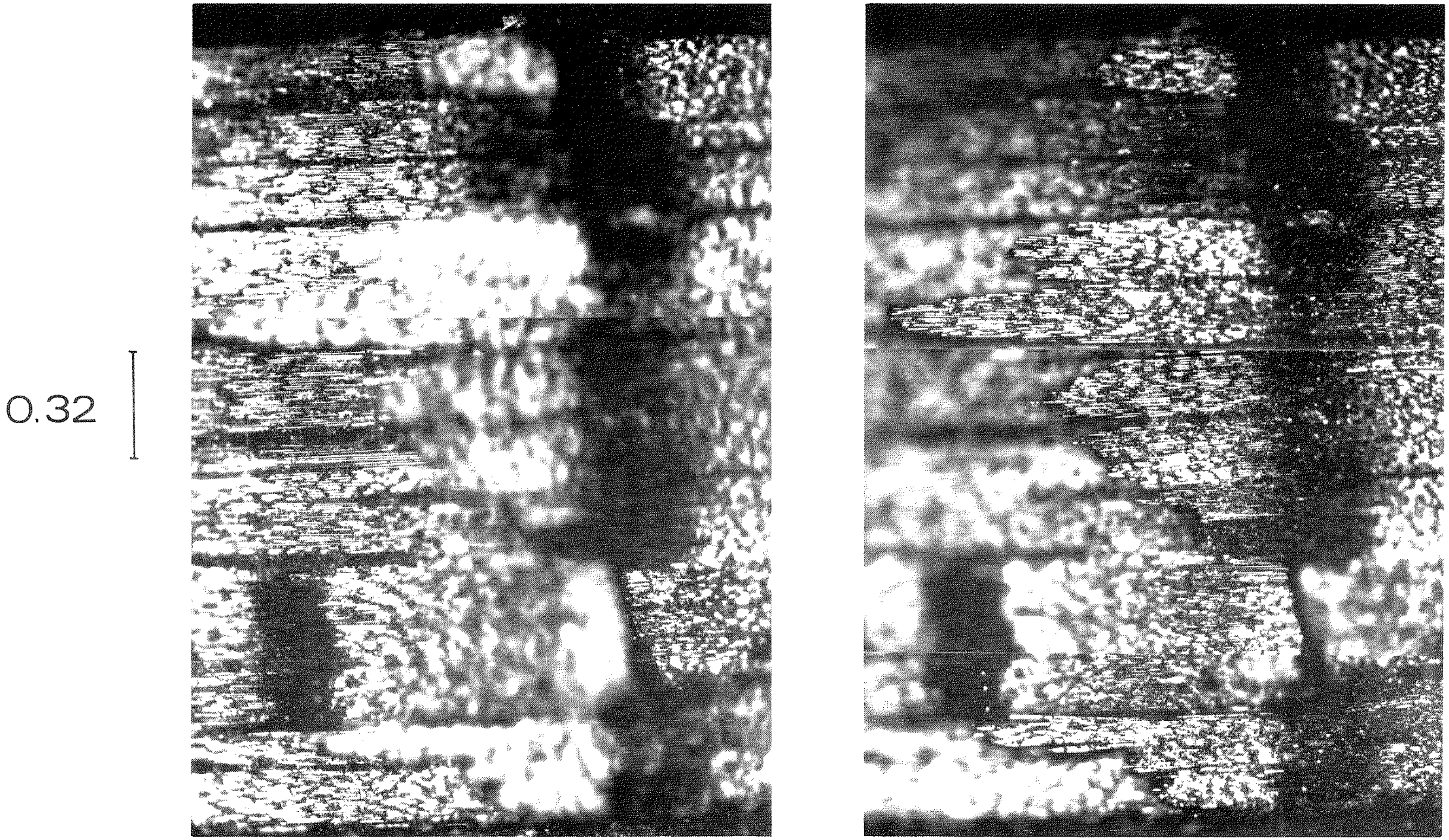

(c)

FIGURE 2.49 ....

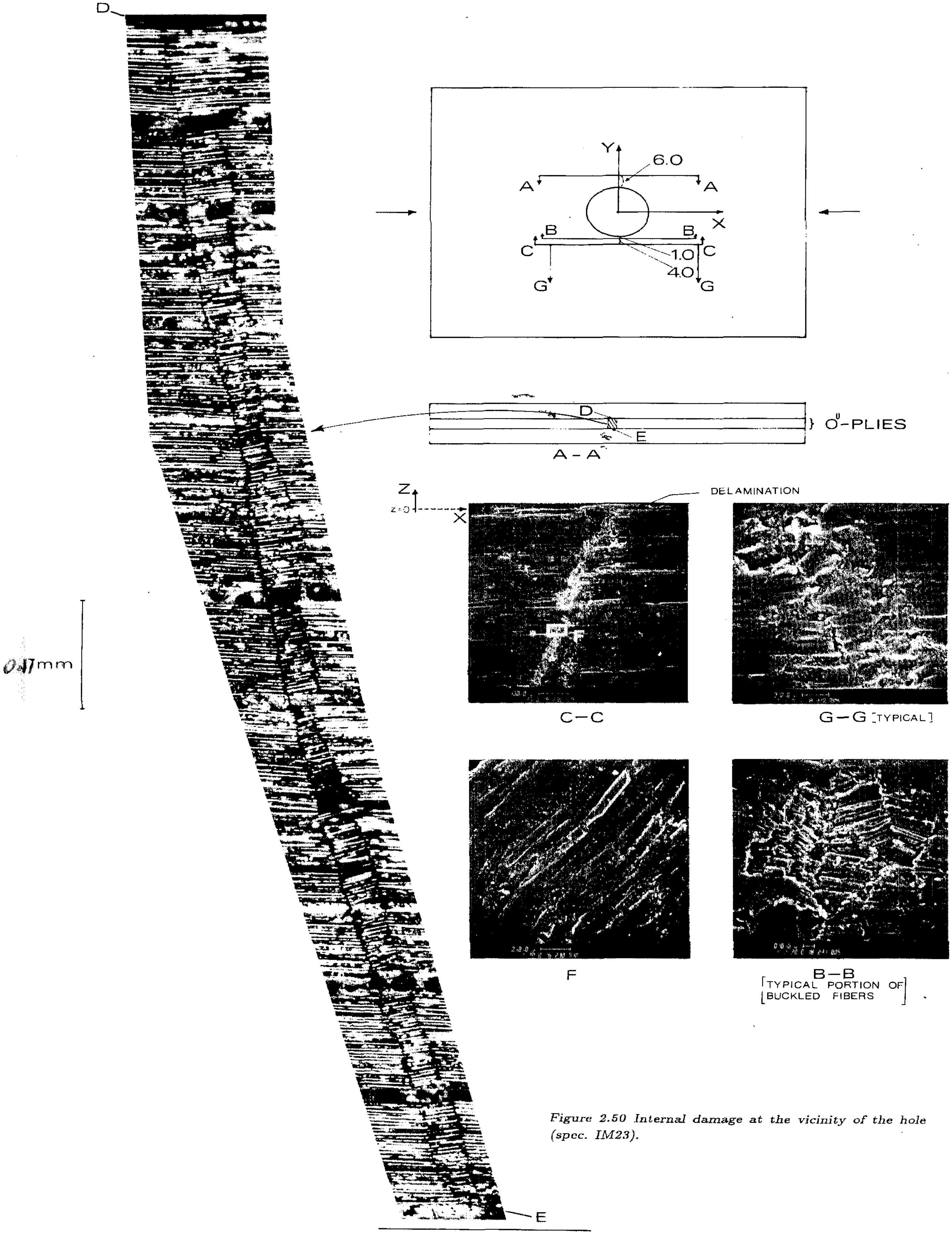

Figure 2.50 Internal damage at the vicinity of the hole (spec. IM23).

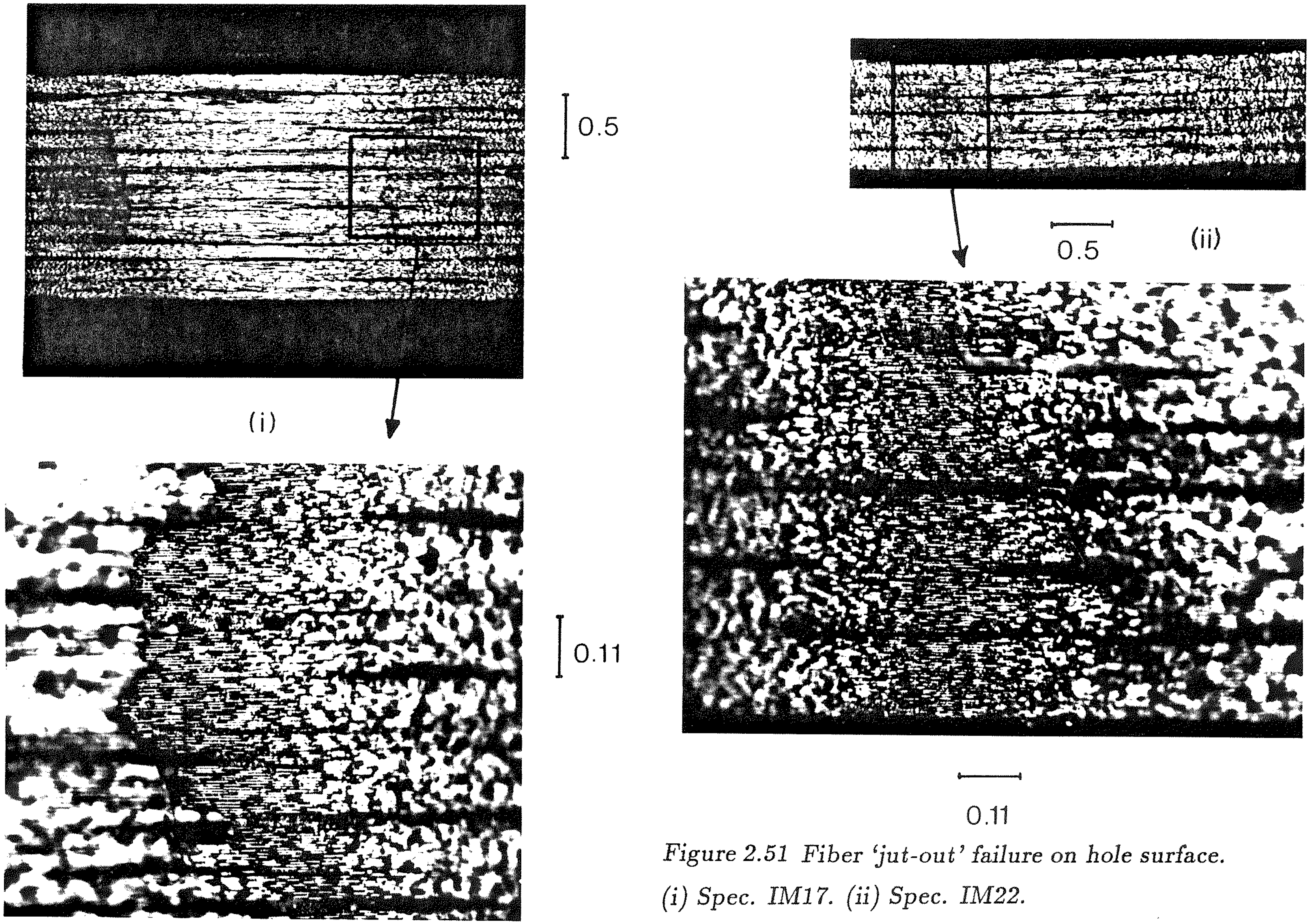

Figure 2.51 Fiber 'jut-out' failure on hole surface.
(i) Spec. IM17. (ii) Spec. IM22.

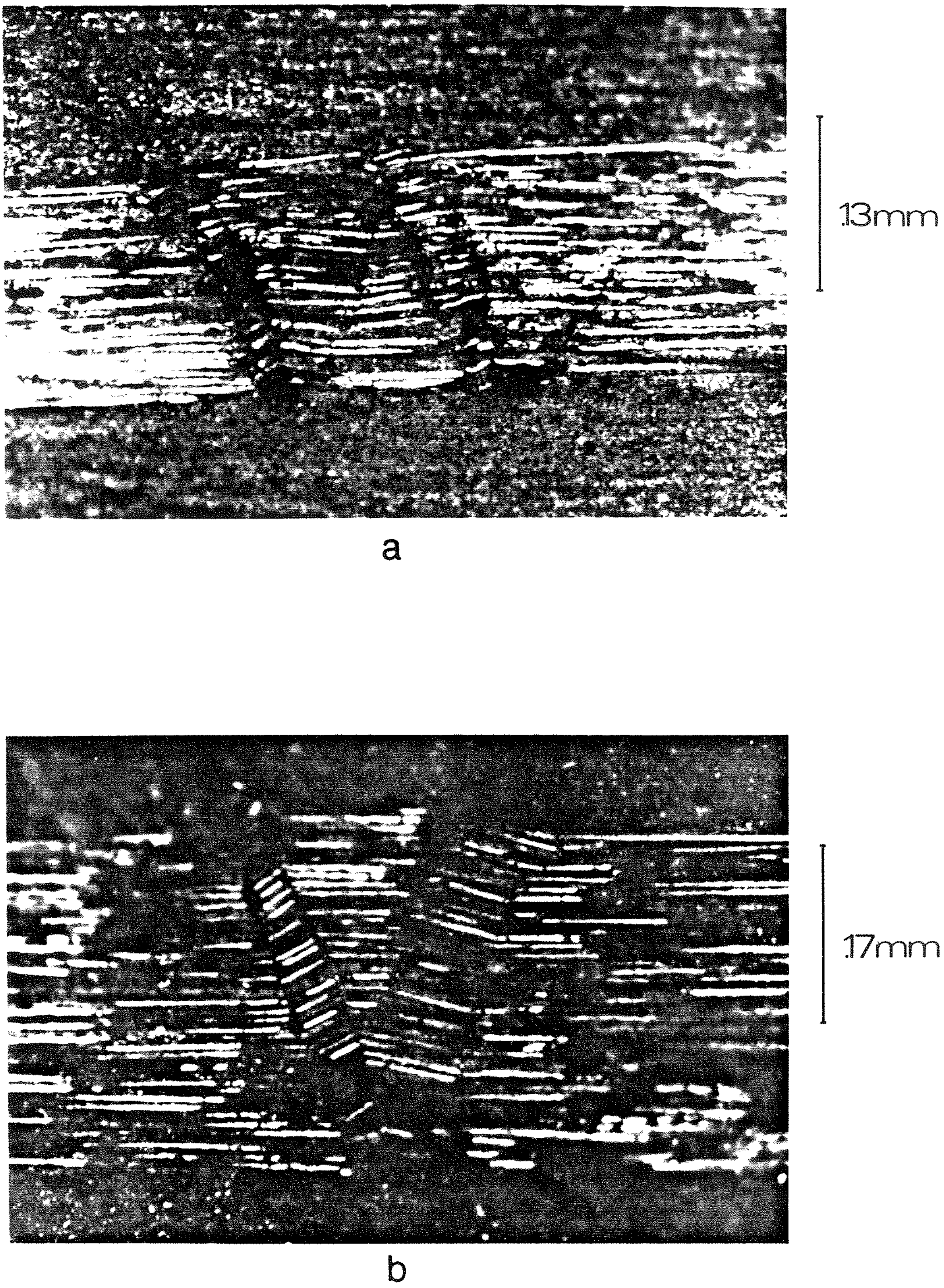

Figure 2.52 Forms of internal damage. (a) Microbuckling failure. (b) Appearence of Kink bands.

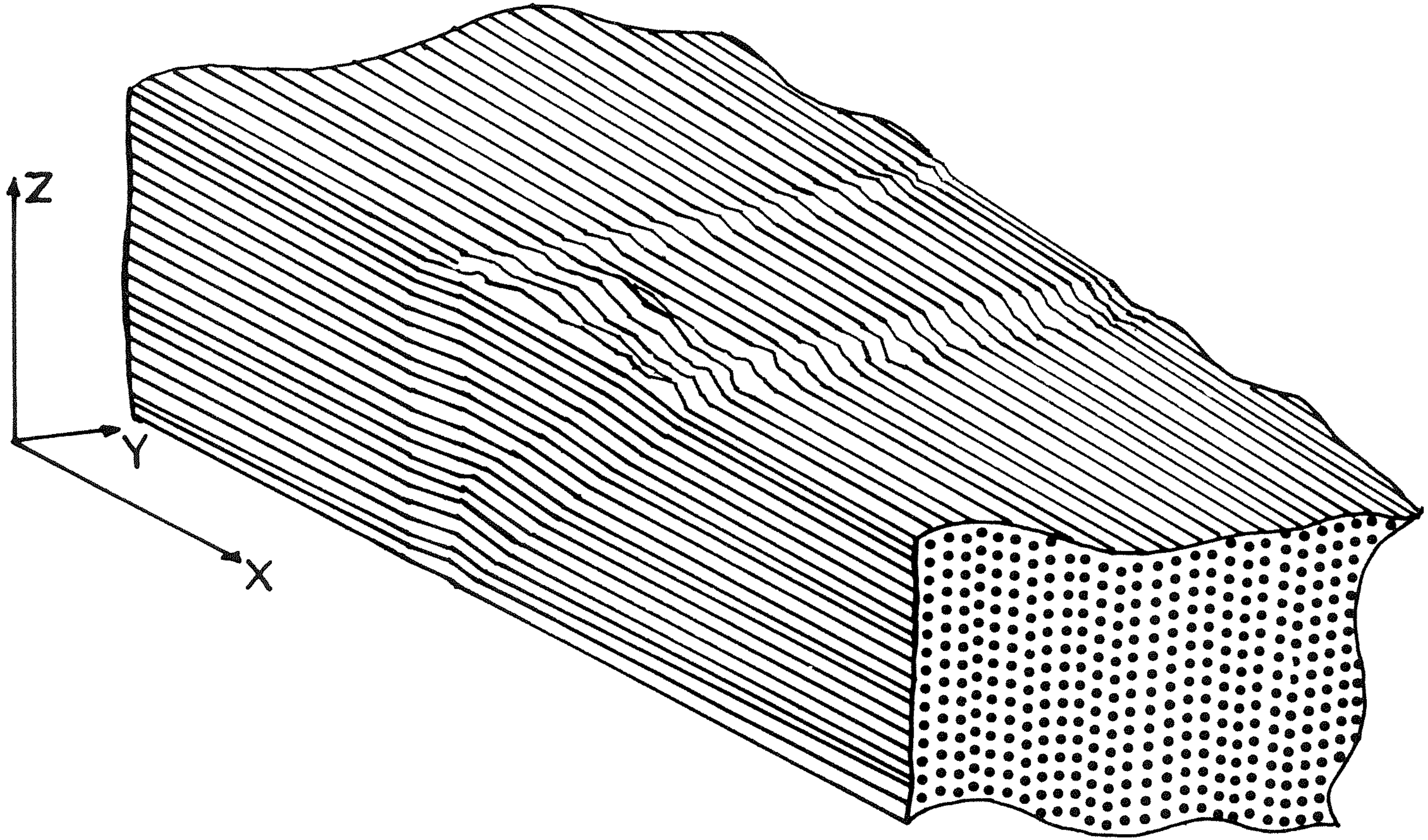

Figure 2.53 A three-dimensional view of the damage to a 0^0-ply in the close proximity of the hole.

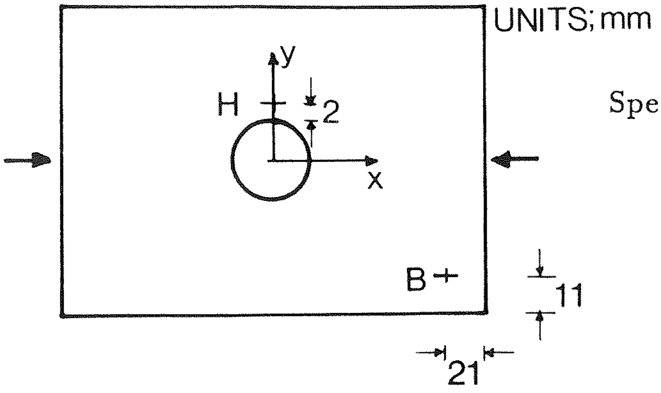

Specs. IM18[1], IM19, IM20

location	gage number
H	1,2
A	3,4
B	5
C	6,7

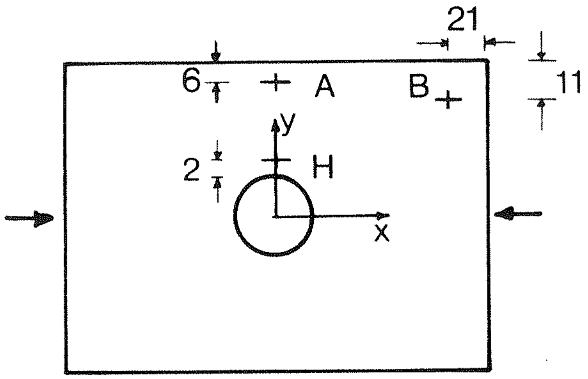

Specs. IM21,IM29-32

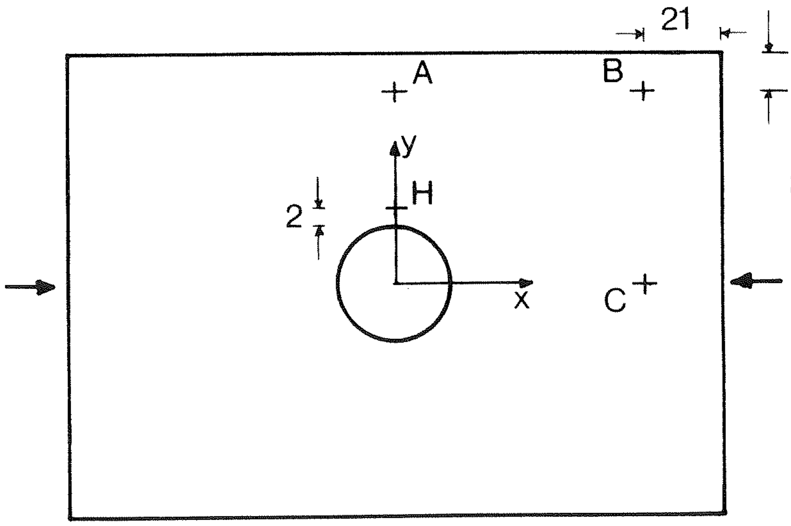

Specs. IM22[2], IM23-IM28

[1]-spec. IM18 mounted with gages at location 'H' only

[2]-gages mounted at location 'C' for spec. IM22 only

Figure 2.54 Strain gage locations for IM series specimens.

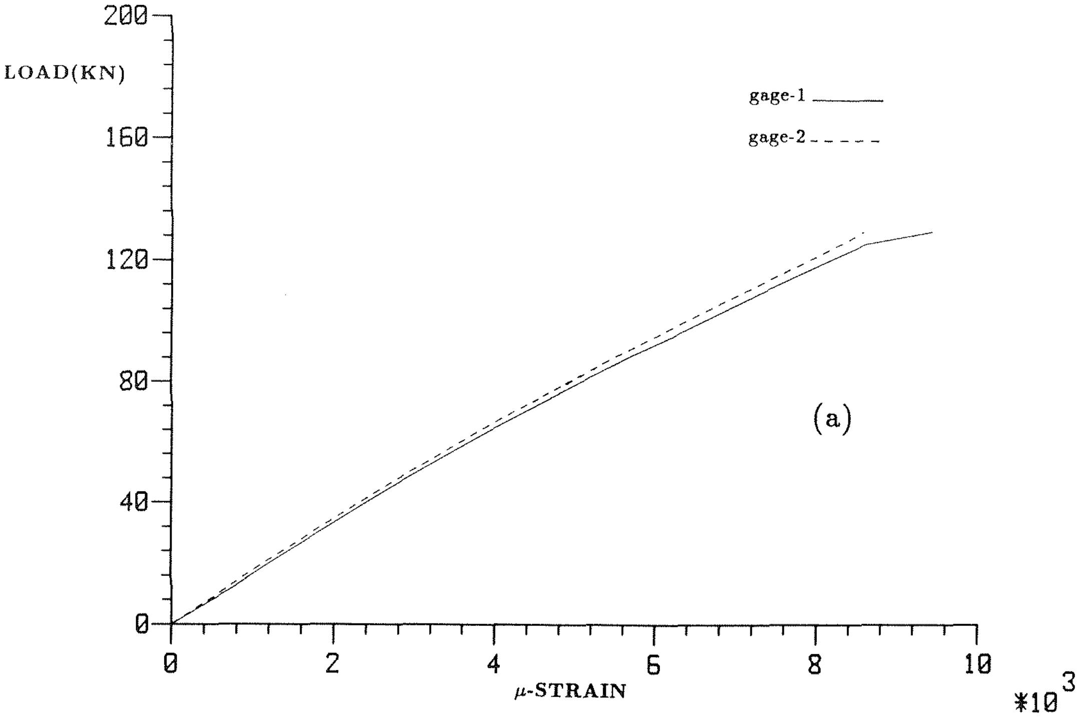

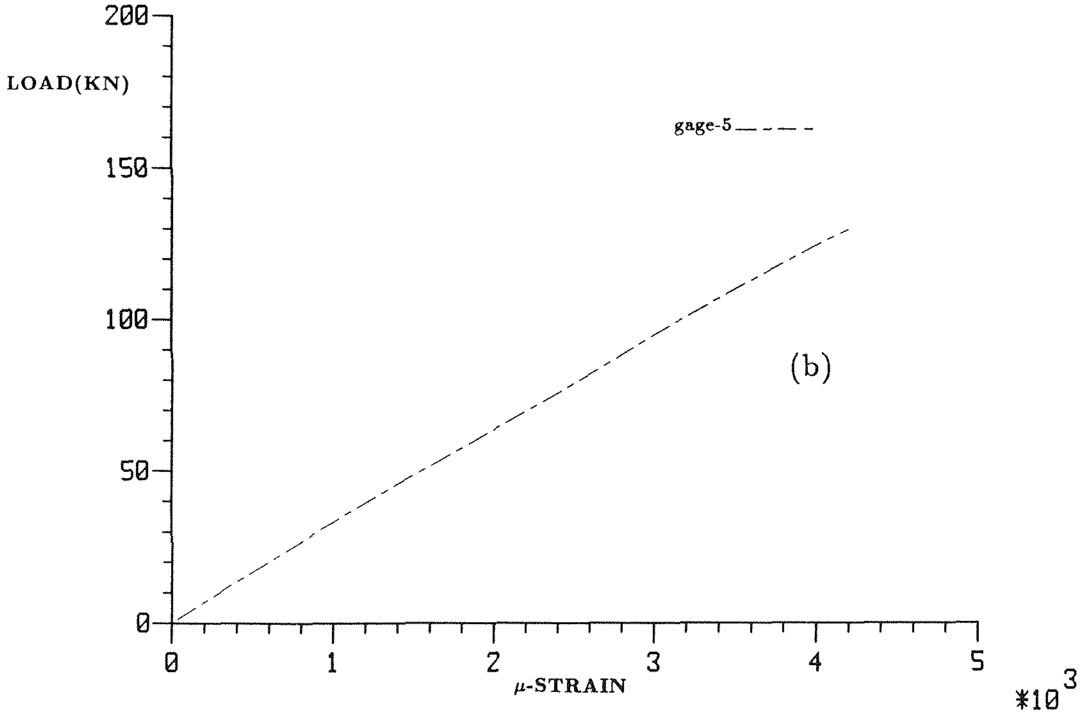

Figure 2.55 Strain gage response for spec. IM20. (a) location H (b) location B

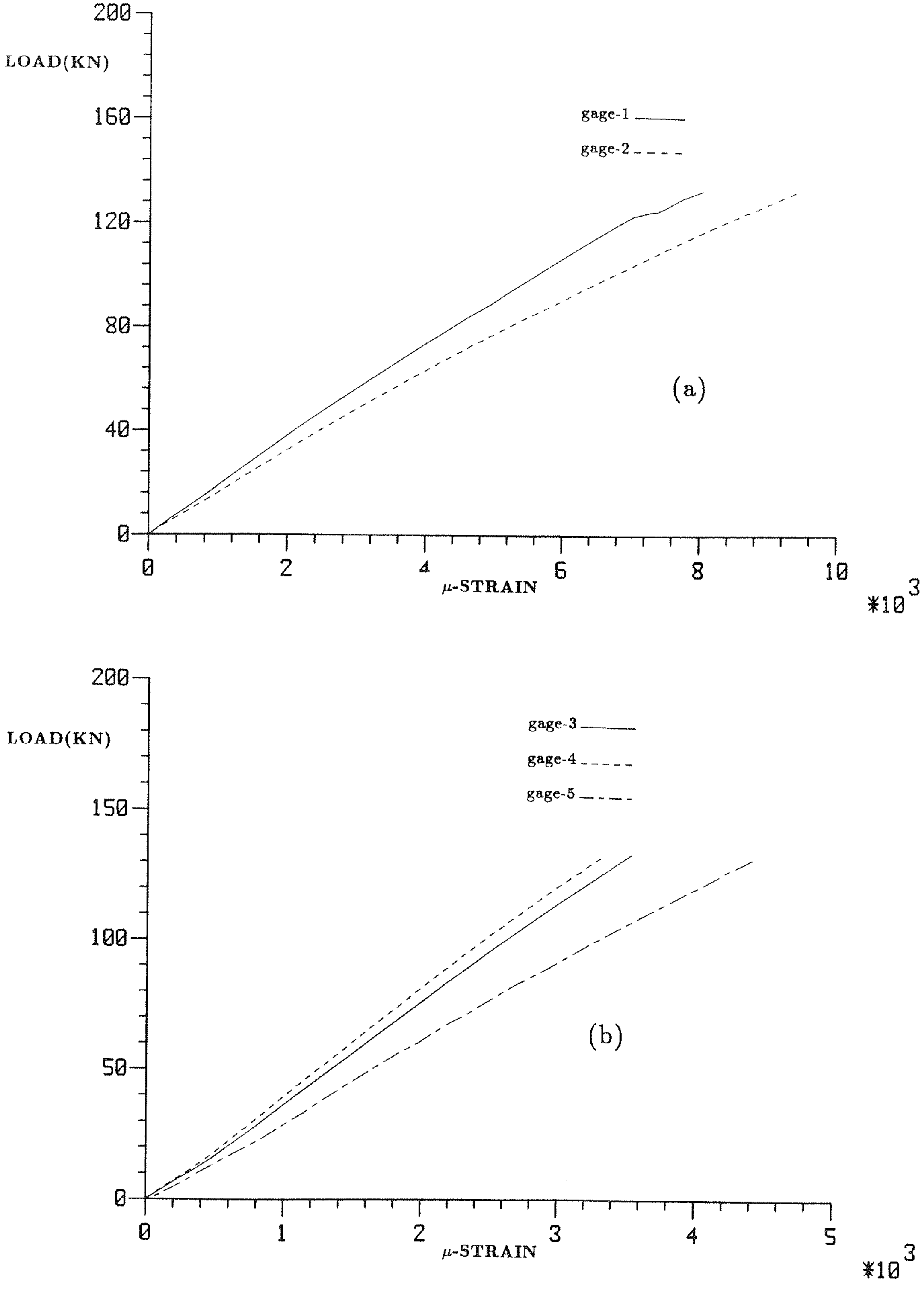

Figure 2.56 Strain gage response for spec. IM21. (a) location H (b) locations A and B.

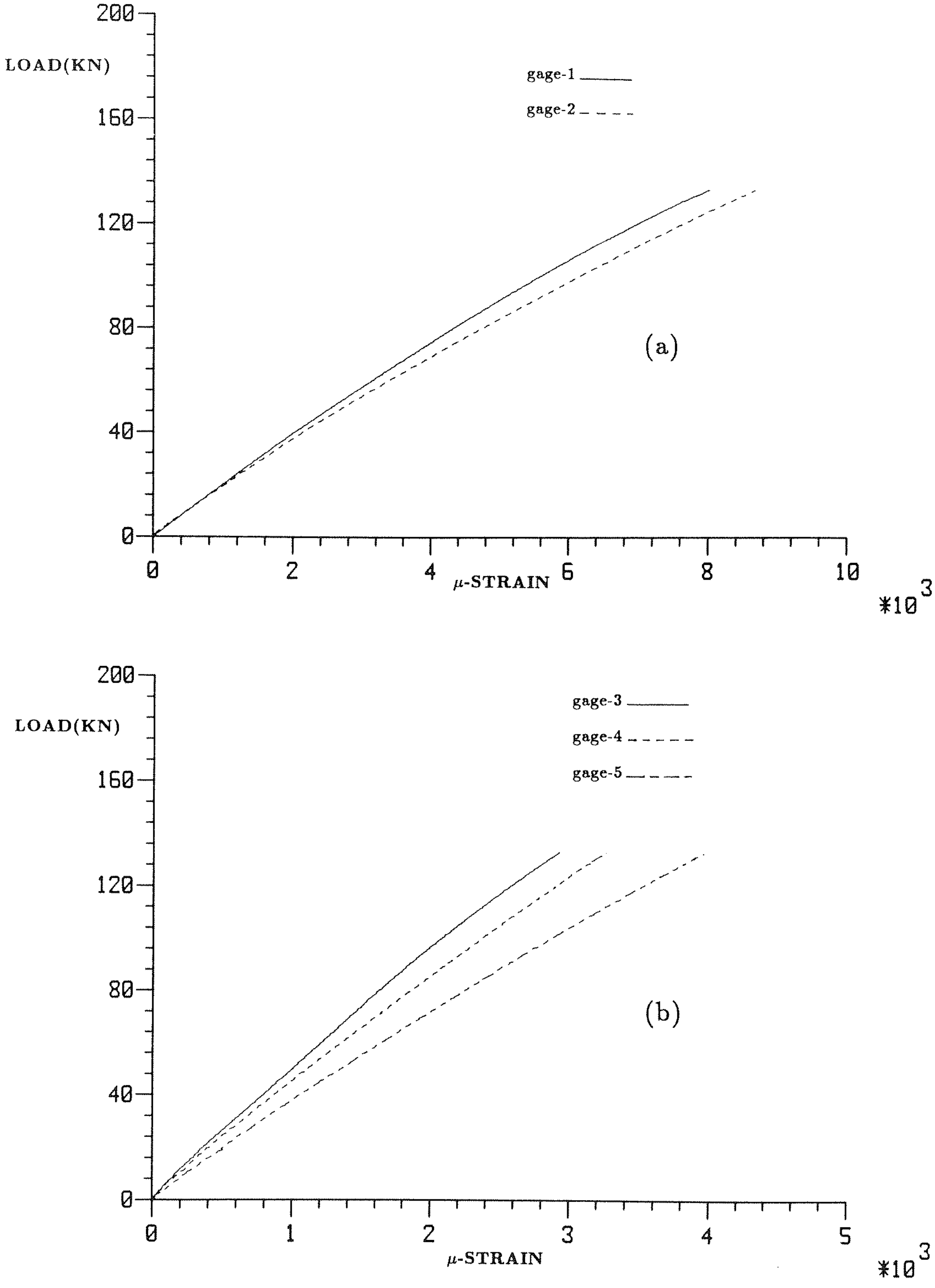

Figure 2.57 Strain gage response for spec. IM29. (a) location H (b) locations A and B.

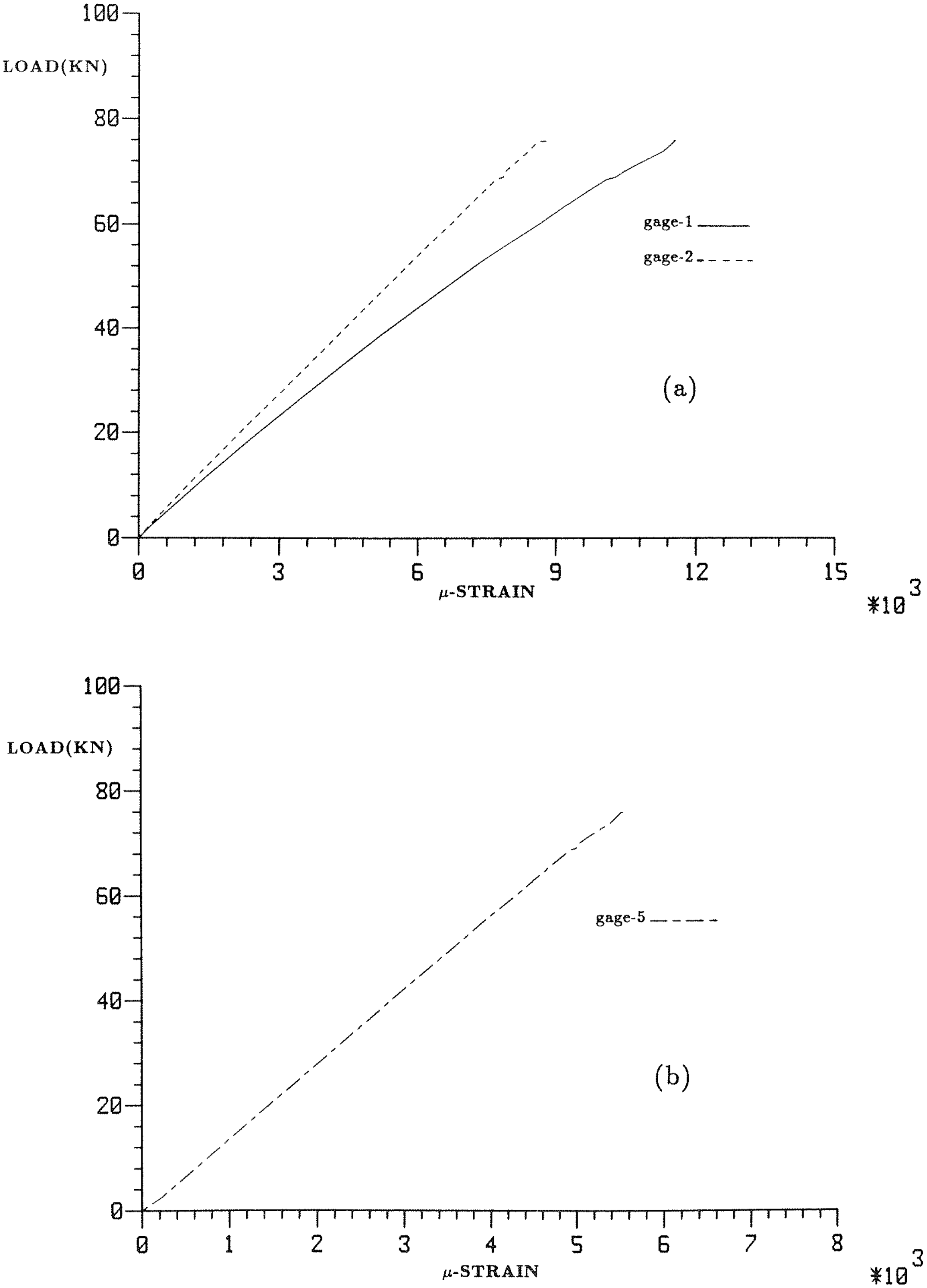

Figure 2.58 Strain gage response for spec. IM19. (a) location H (b) location B

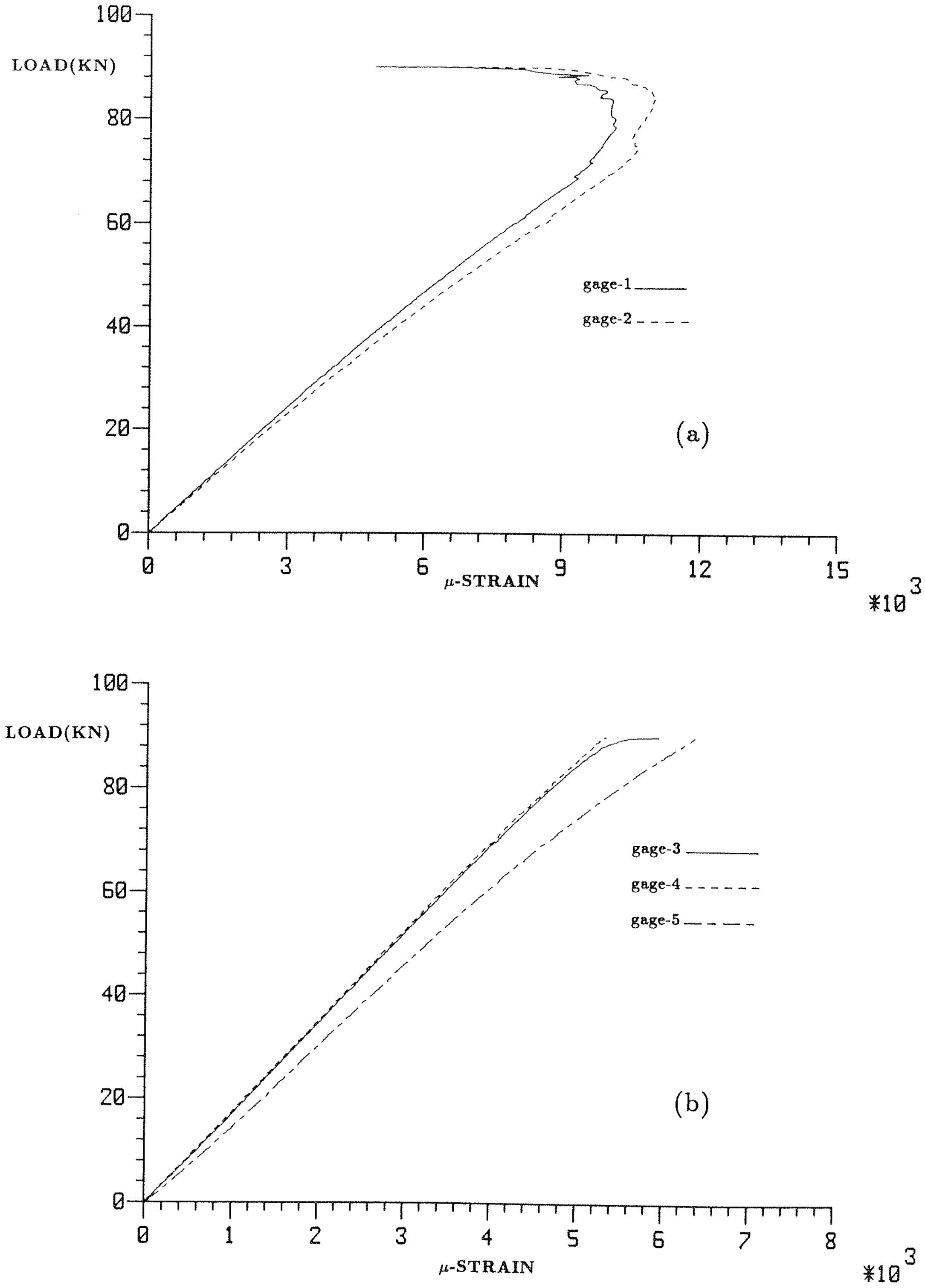

Figure 2.59 Strain gage response for spec. IM32. (a) location H (b) locations A and B.

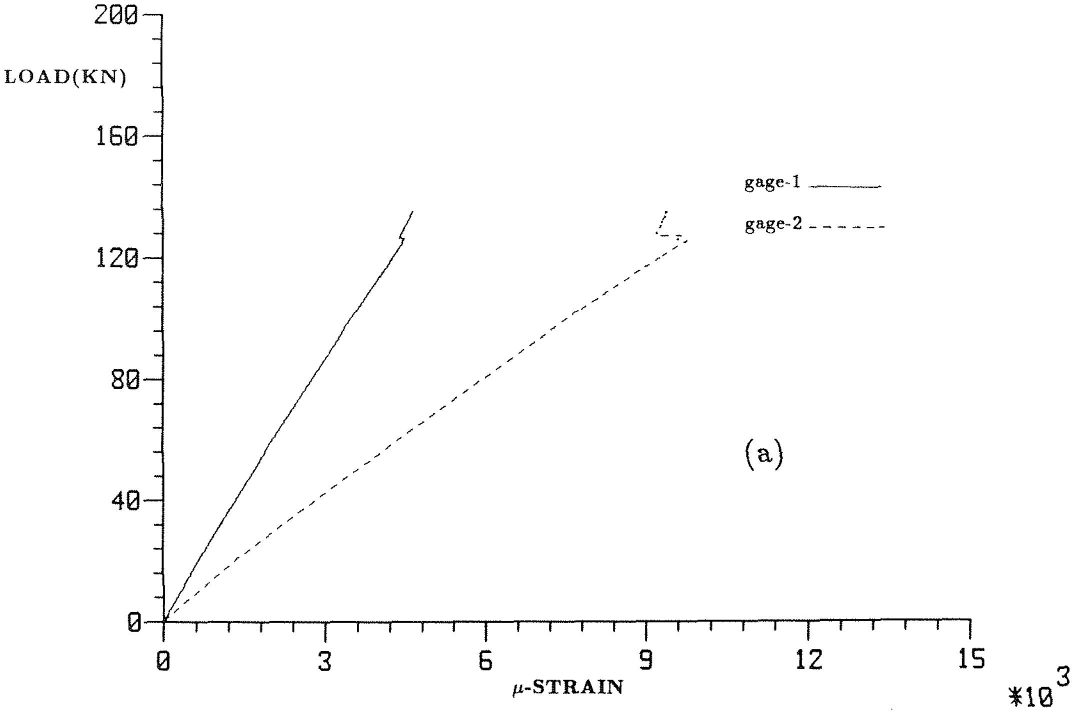

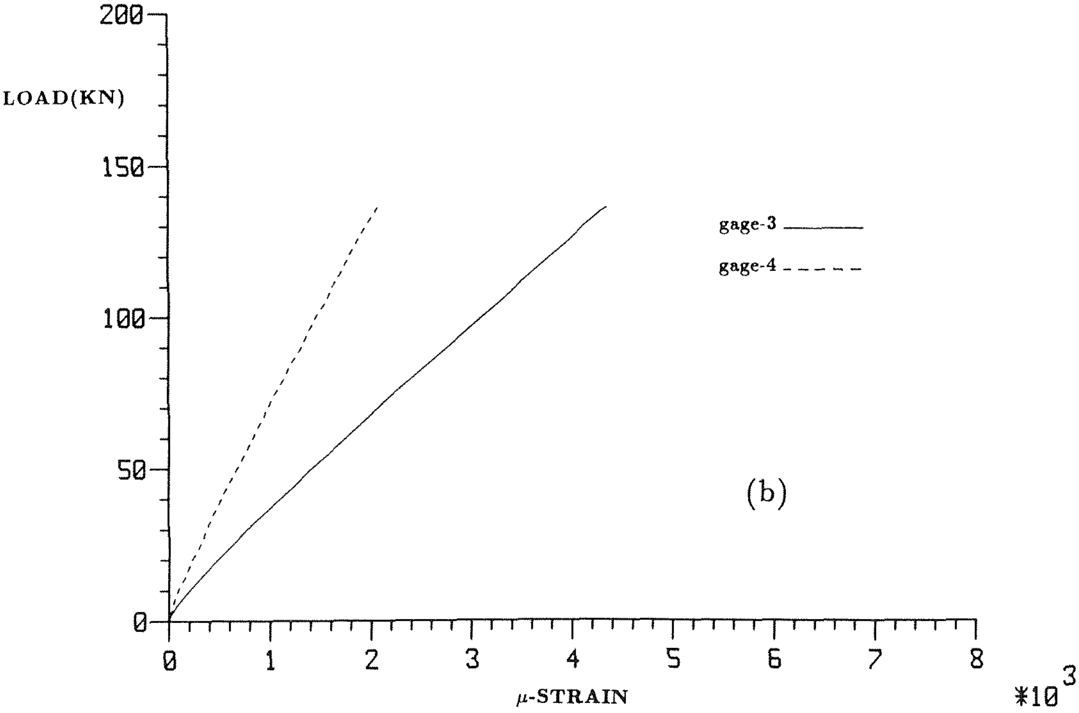

Figure 2.60 Strain gage response for spec. IM24. (a) location H (b) locations A and B. Note: gage 5 poorly bonded.

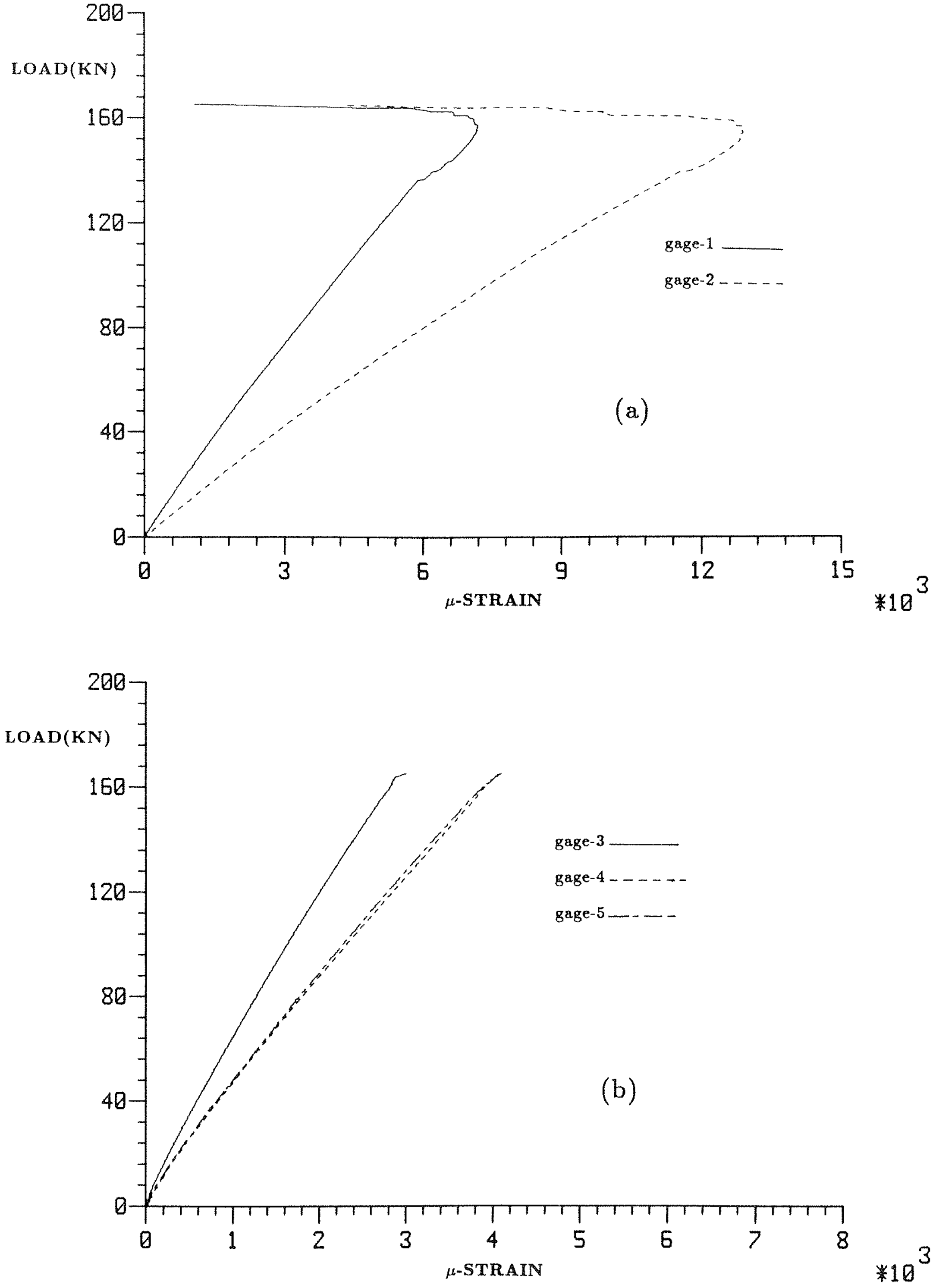

Figure 2.61 Strain gage response for spec. IM25. (a) location H (b) locations A and B.

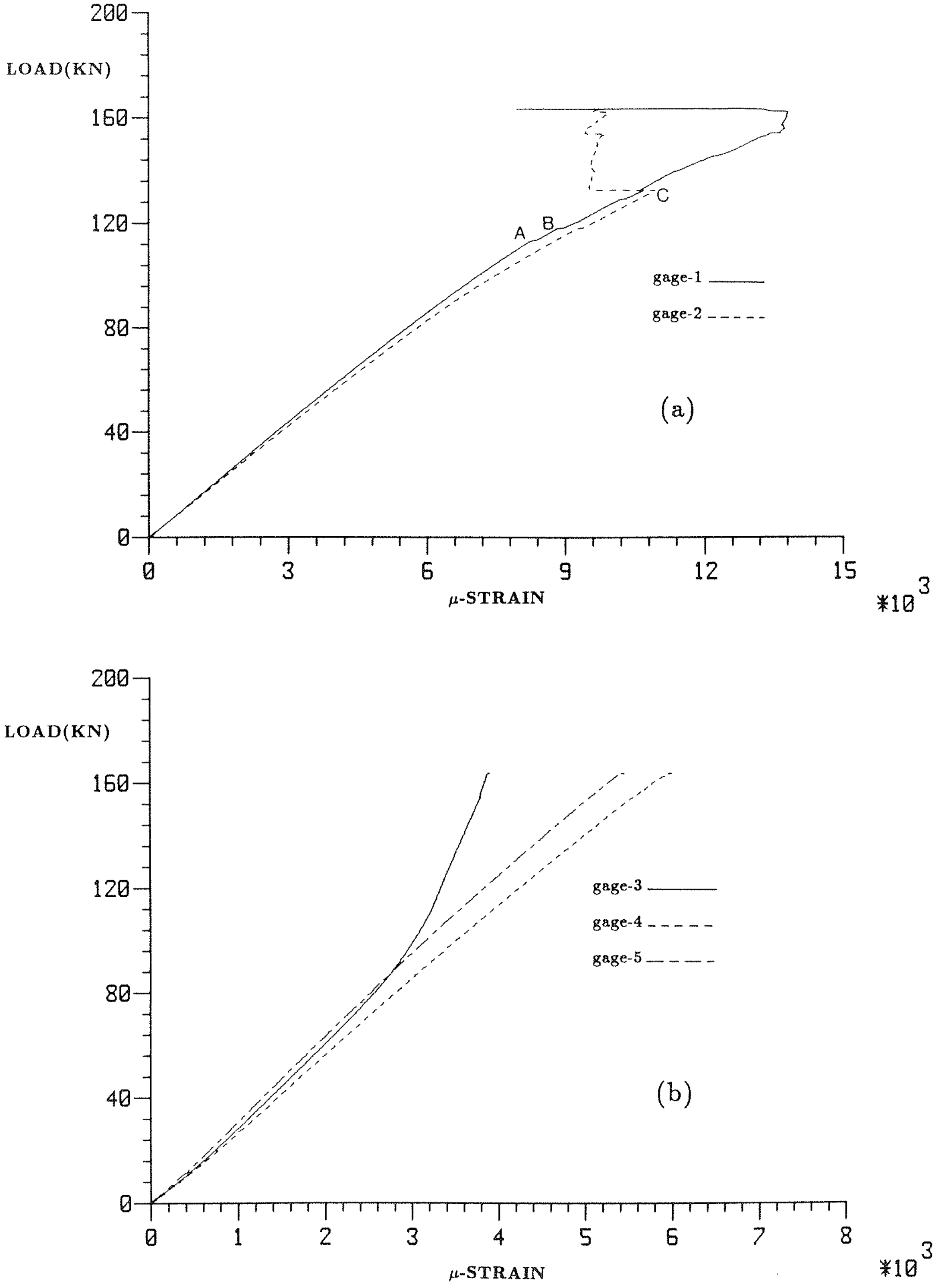

Figure 2.62 Strain gage response for spec. IM28. (a) location H (b) locations A and B. Note: gage 3 poorly bonded.

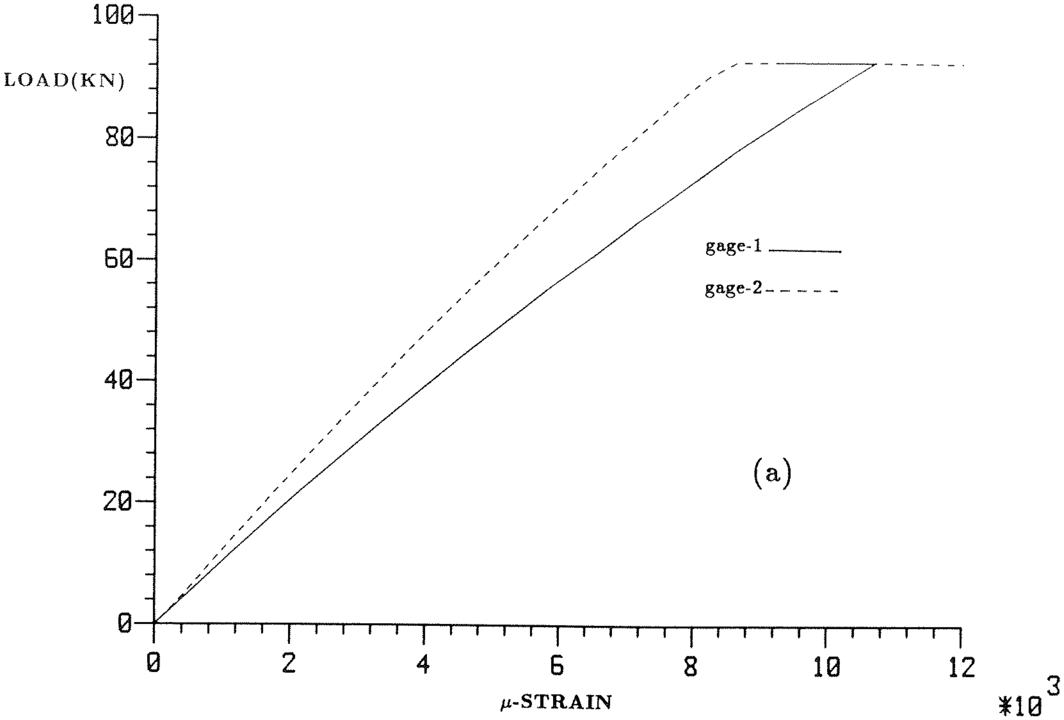

Figure 2.63 Strain gage response for spec. IM18. (a) location H only.

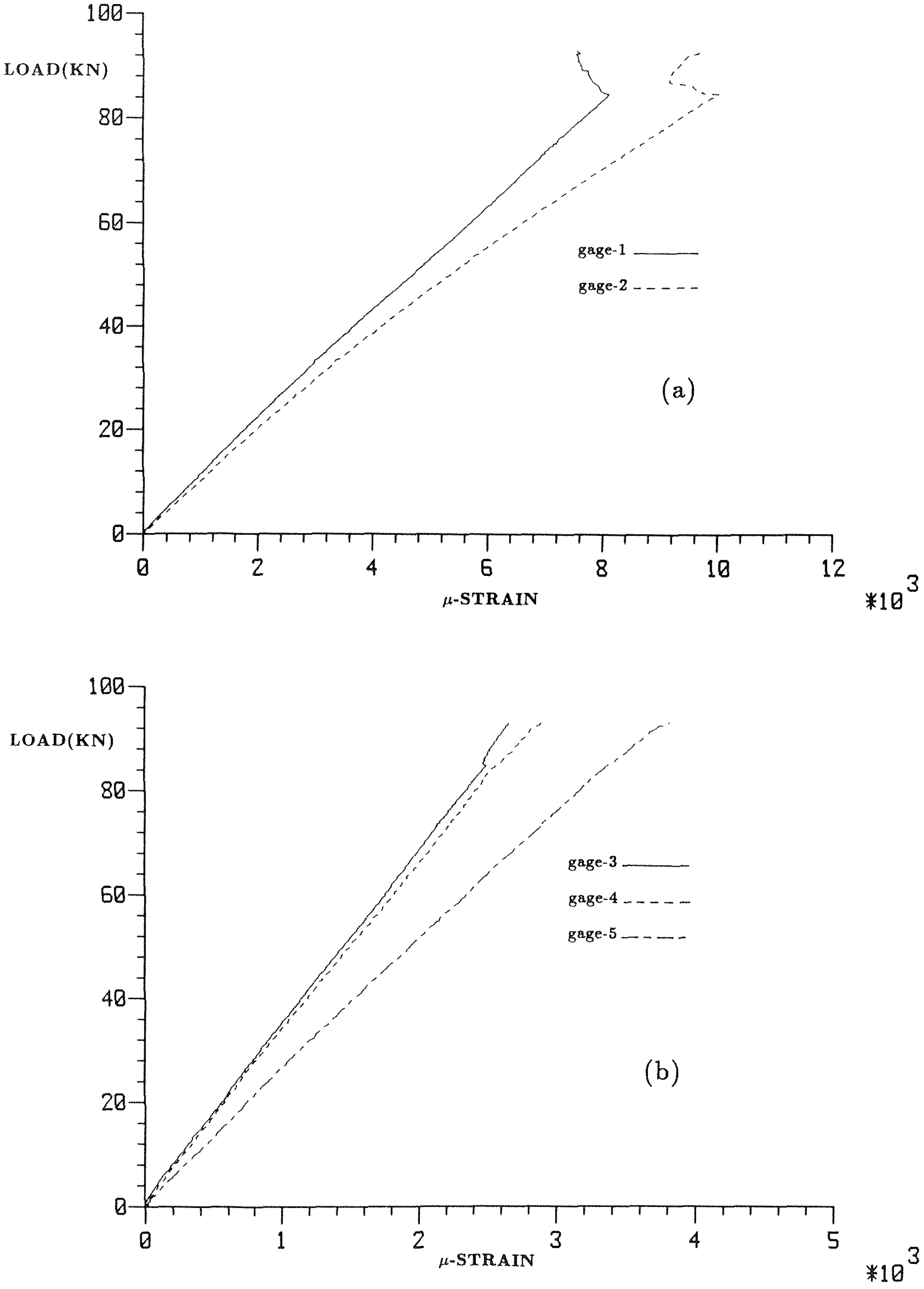

Figure 2.64 Strain gage response for spec. IM31. (a) location H (b) locations A and B.

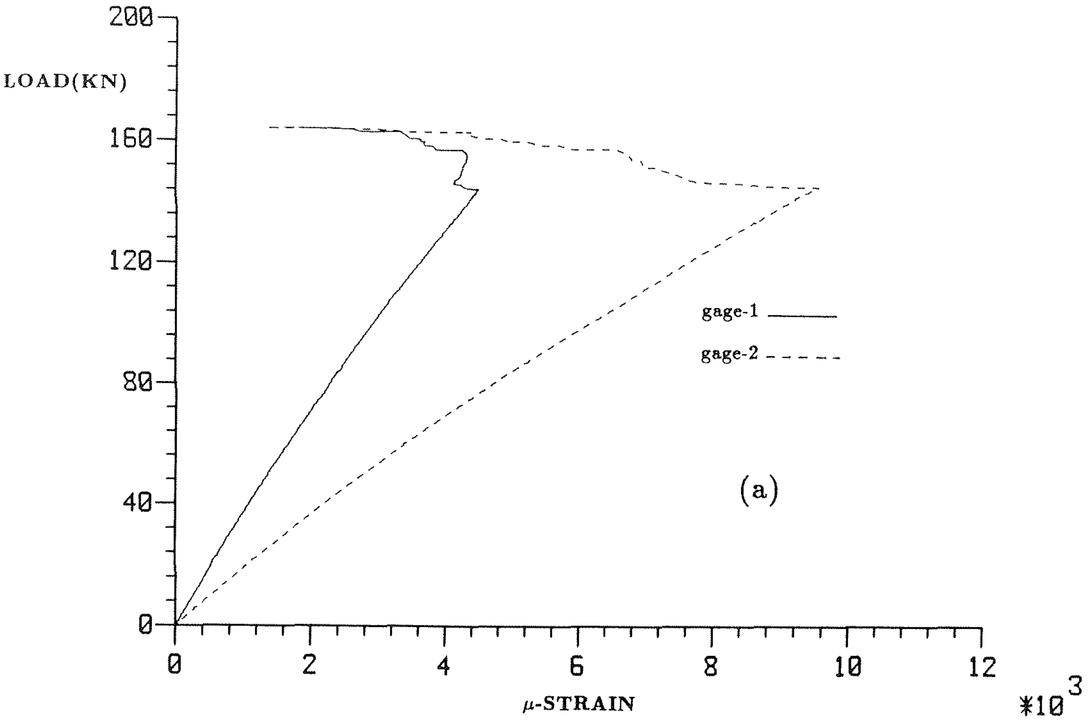

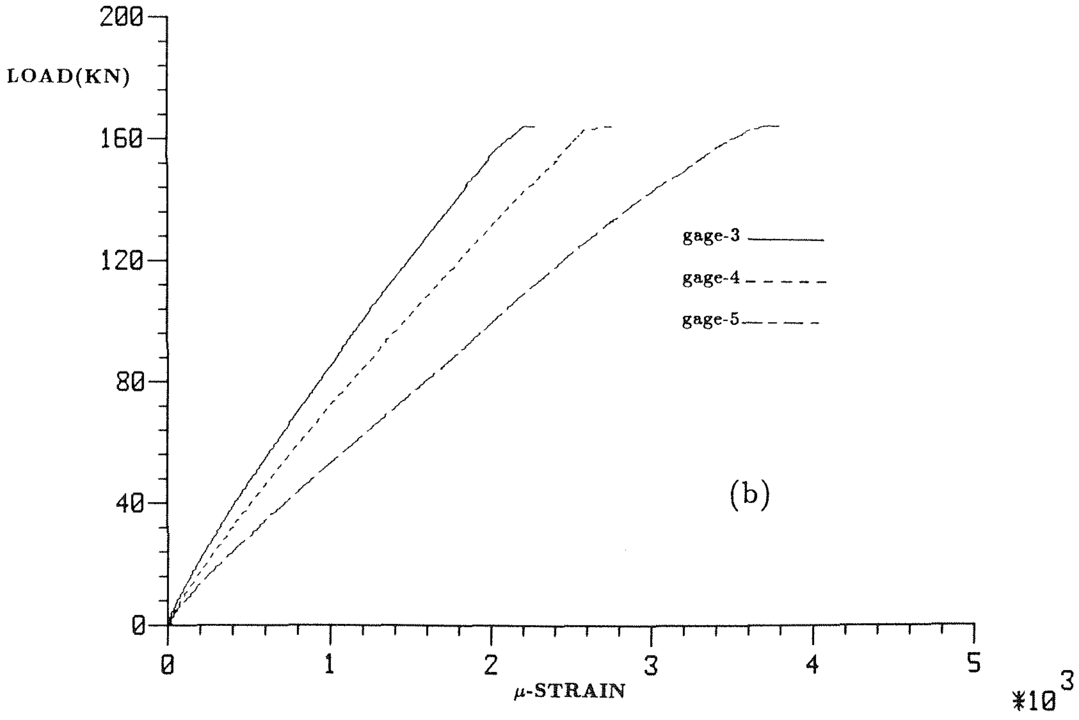

Figure 2.65 Strain gage response for spec. IM26. (a) location H (b) locations A and B.

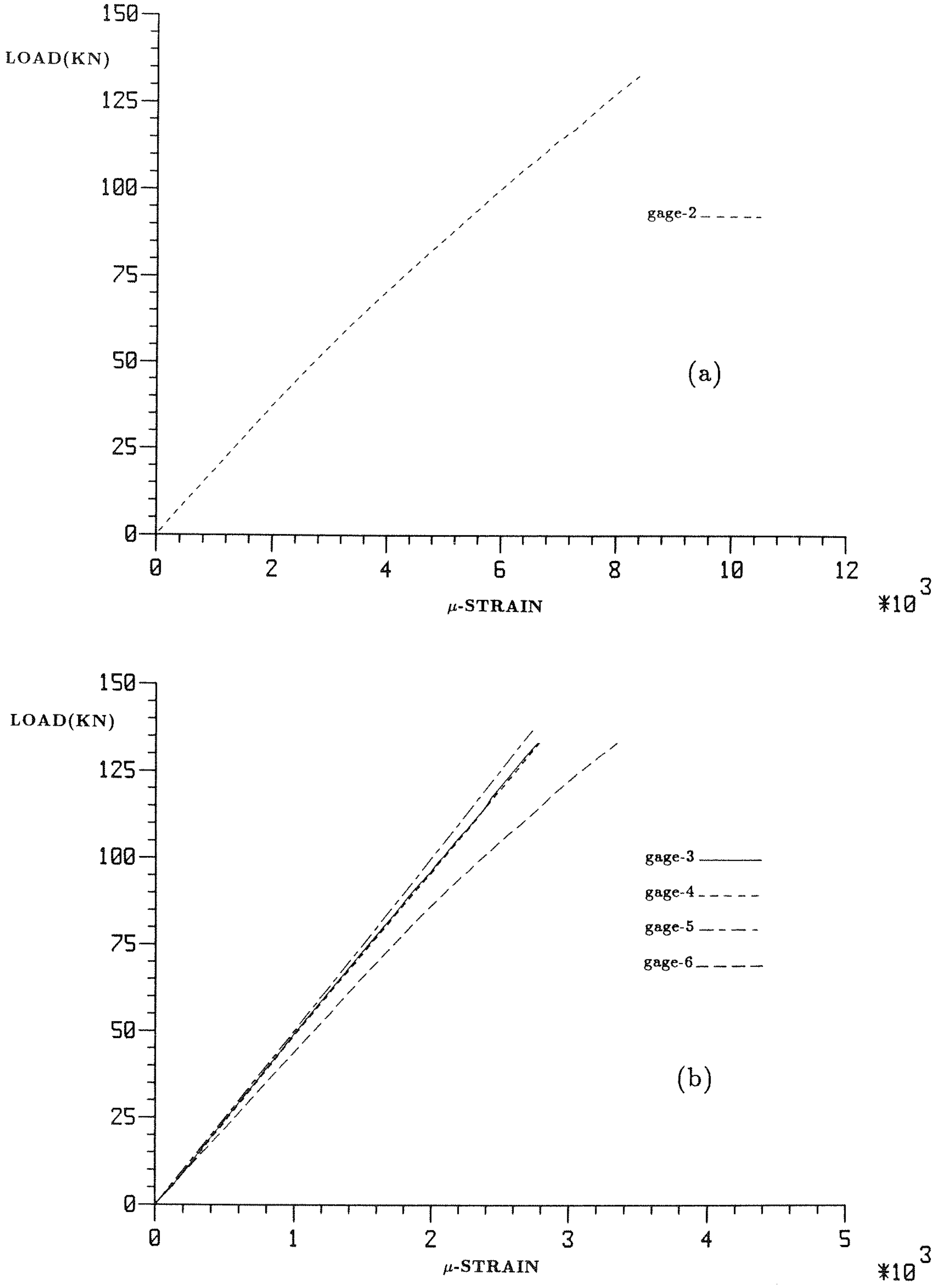

Figure 2.66 Strain gage response for spec. IM22. (a) location H, gage 1 poorly bonded. (b) locations A, B and C. Note: gage 7 poorly bonded.

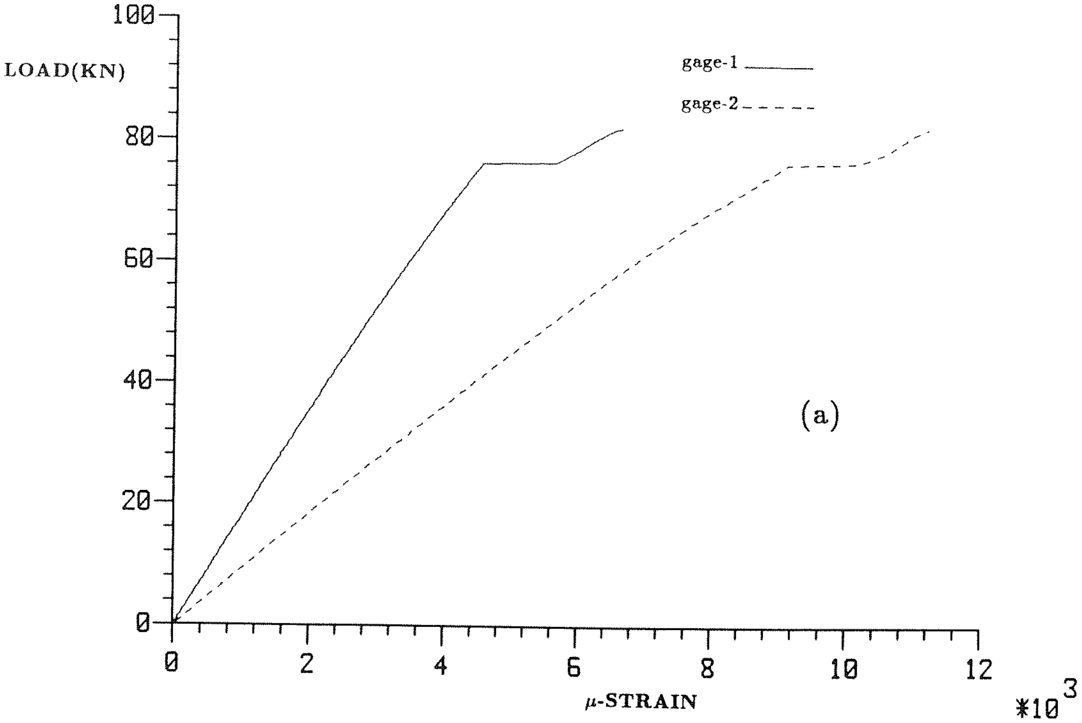

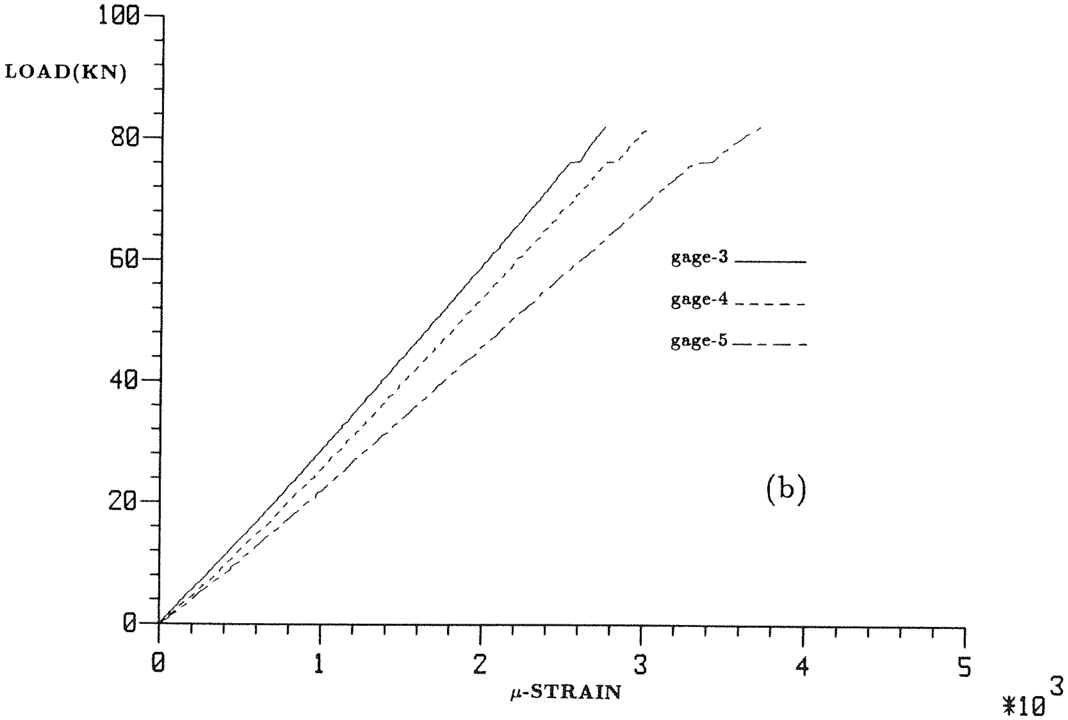

Figure 2.67 Strain gage response for spec. IM30. (a) location H (b) locations A and B.

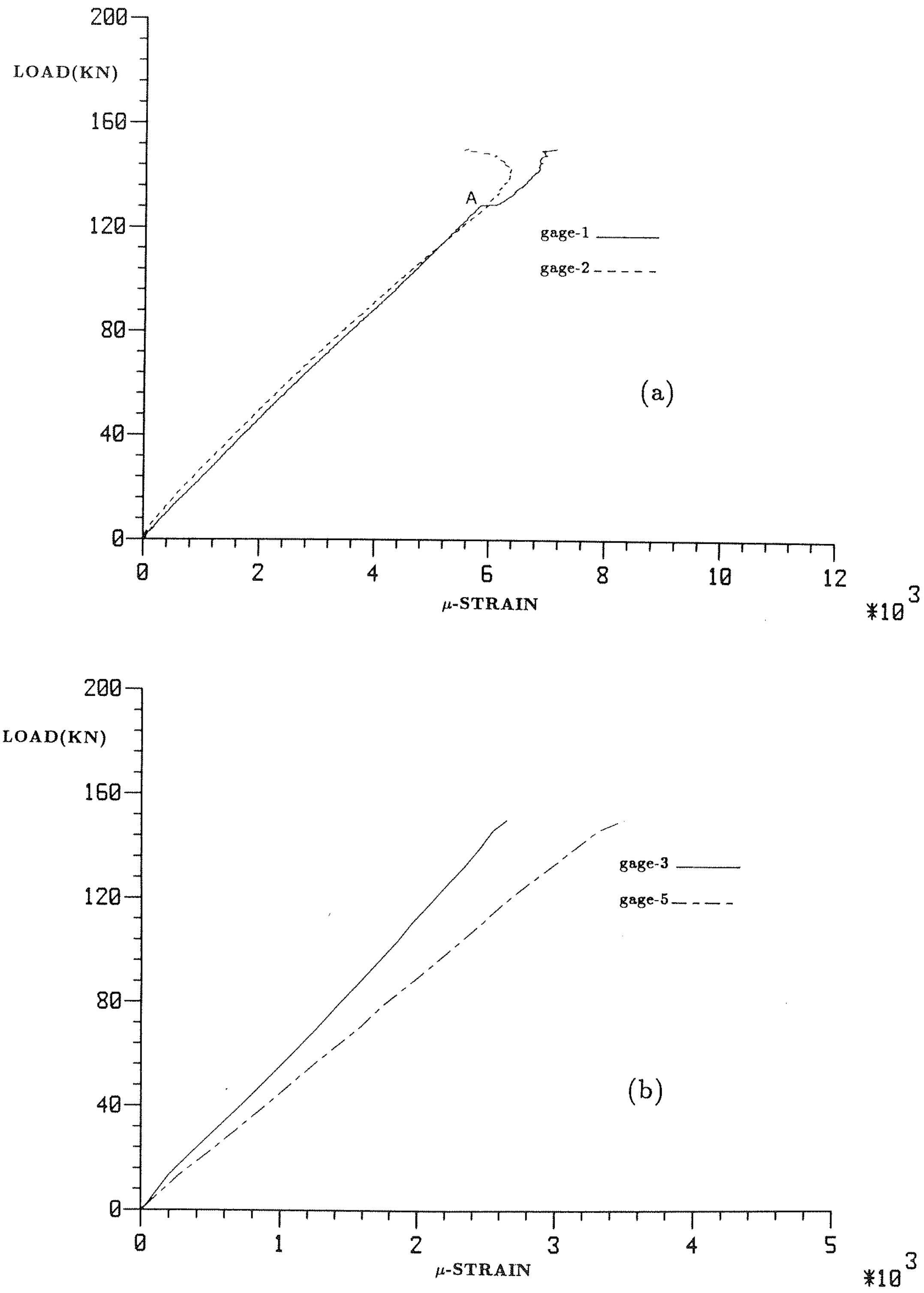

Figure 2.68 Strain gage response for spec. IM23. (a) location H (b) locations A and B. Note: gage 4 poorly bonded.

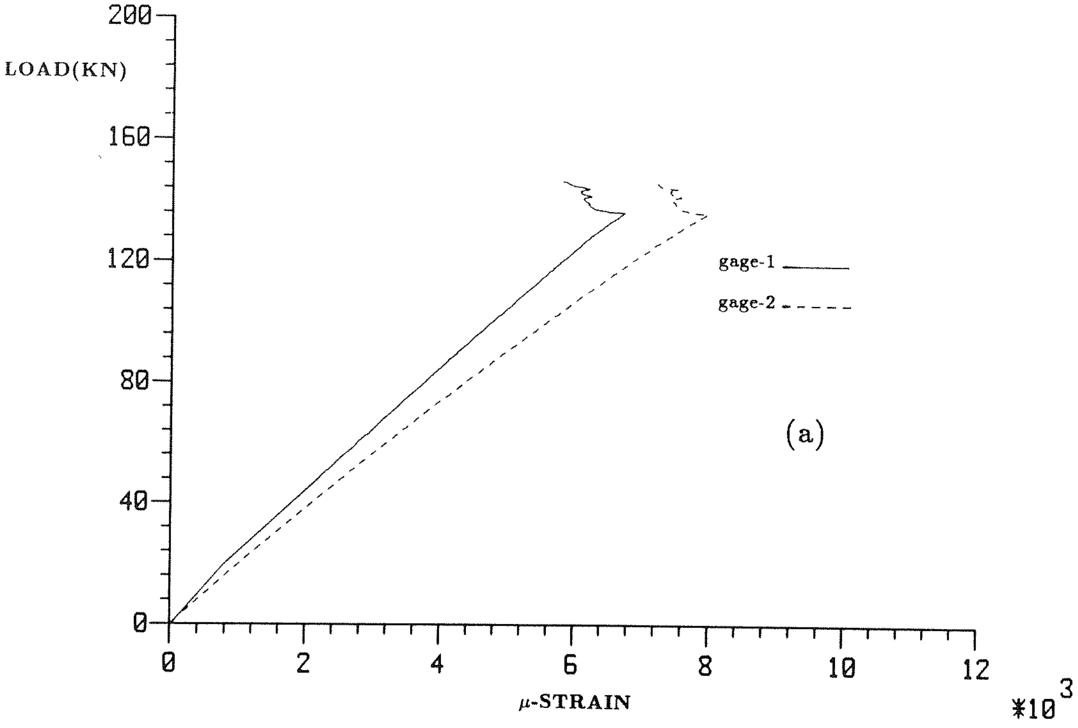

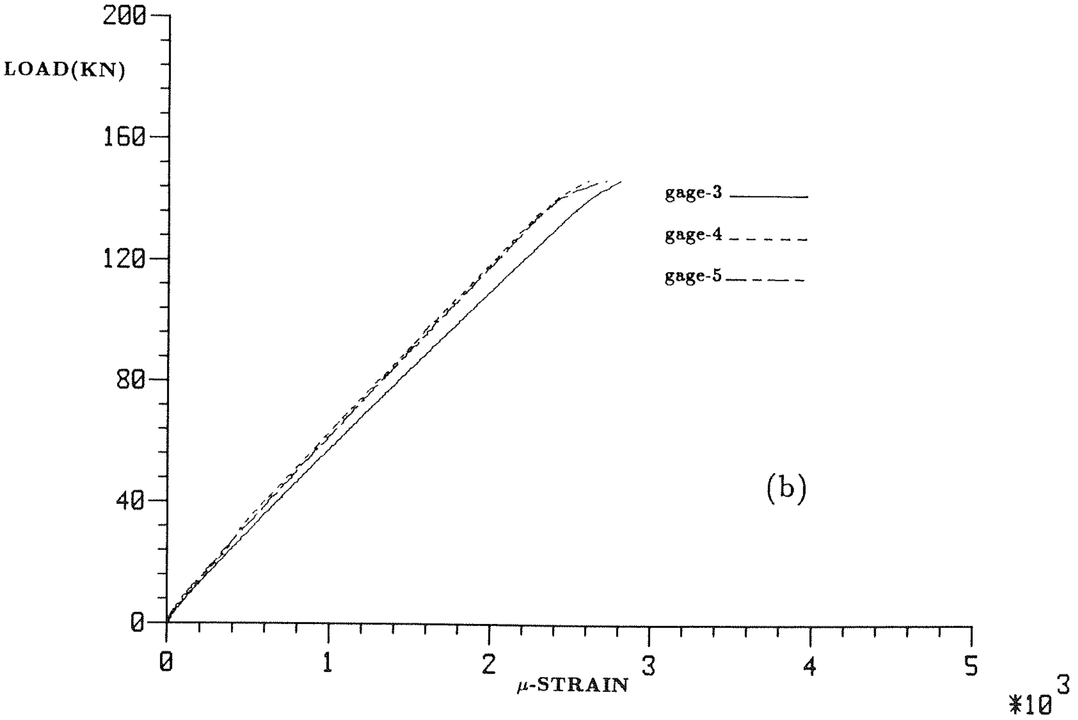

Figure 2.69 Strain gage response for spec. IM27. (a) location H (b) locations A and B.

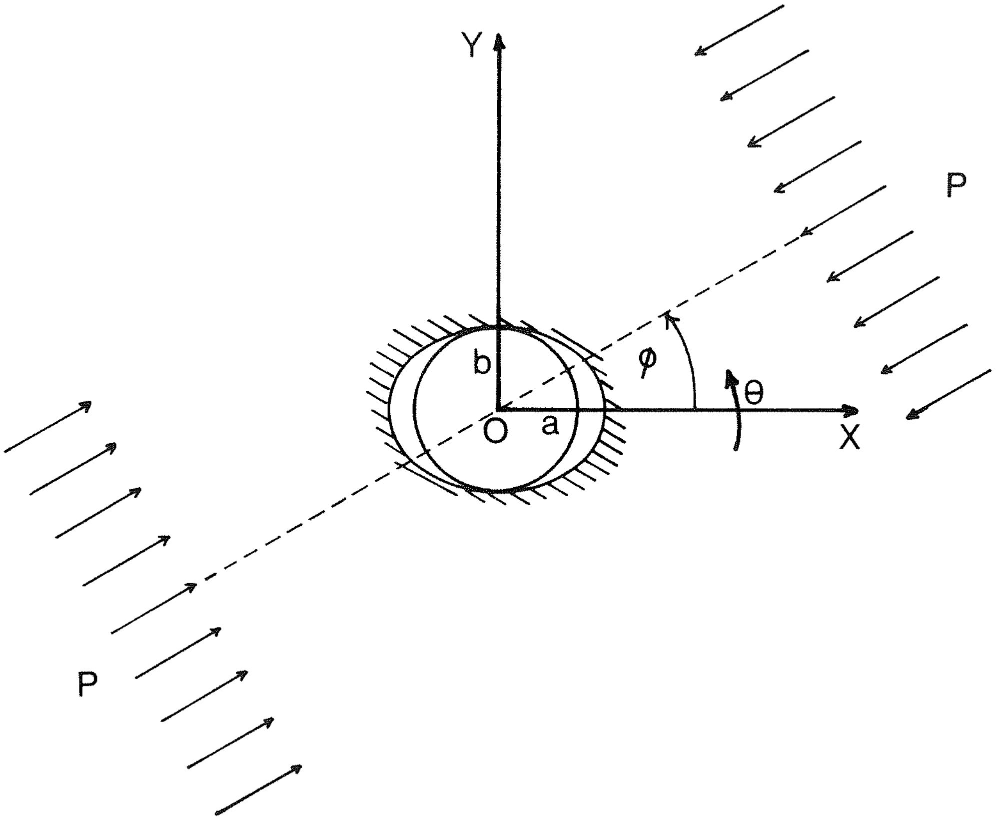

Figure 3.1 Configuration for stressed orthotropic plate.

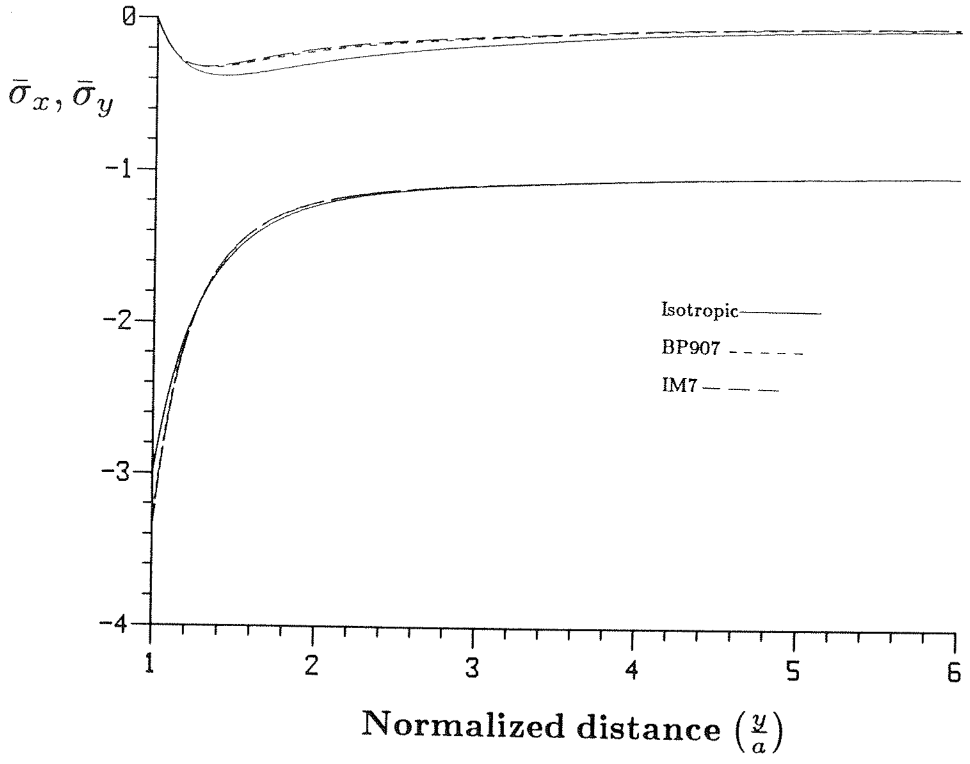

Figure 3.2a $\bar{\sigma}_x$ *and* $\bar{\sigma}_y$ *distribution along* $\bar{y}$*-axis at* $\bar{x}$*=0. (Type A laminate)*

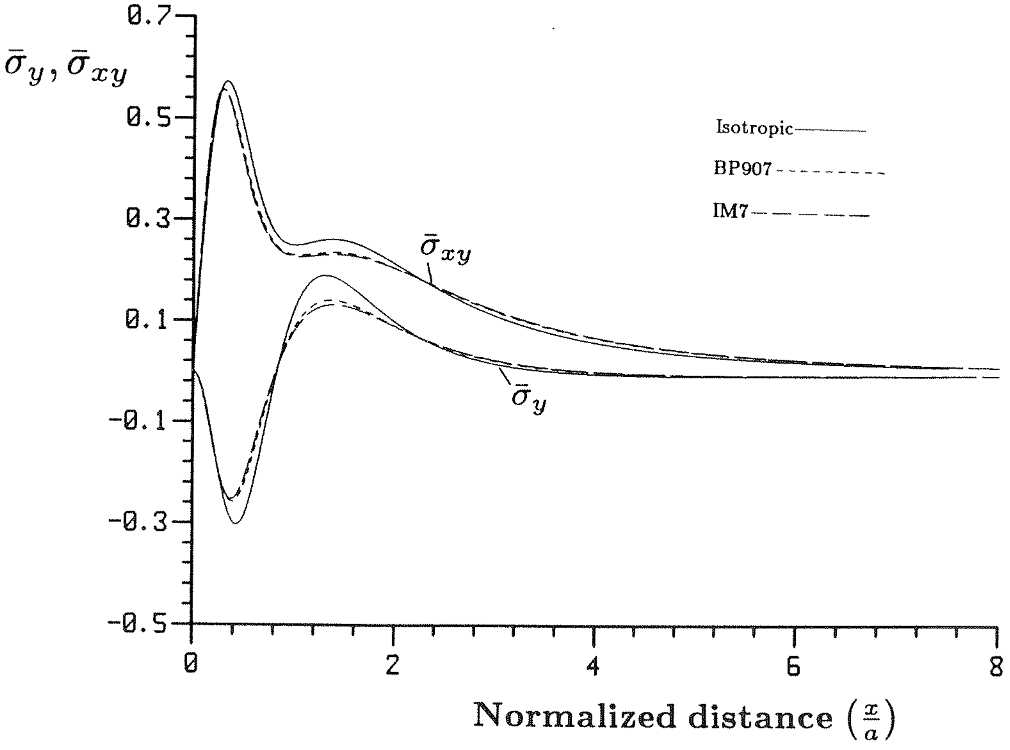

Figure 3.2b $\bar{\sigma}_y$ *and* $\bar{\sigma}_{xy}$ *distribution along* $\bar{x}$*-axis at* $\bar{y}$*=1. (Type A laminate)*

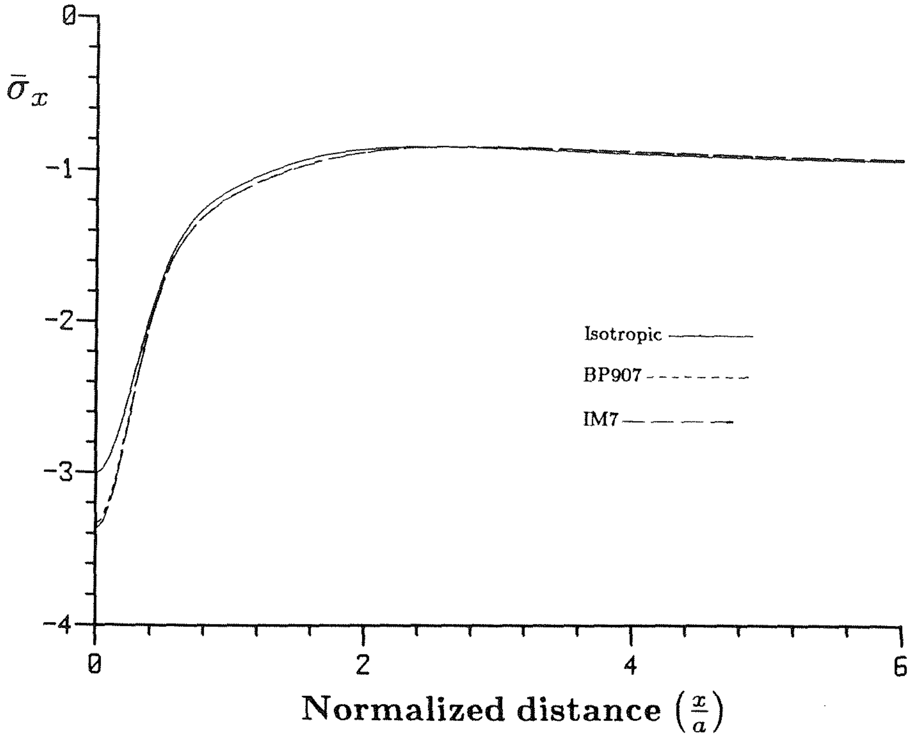

Figure 3.2c $\bar{\sigma}_x$ *distribution along* $\bar{x}$*-axis at* $\bar{y}=1$*. (Type A laminate)*

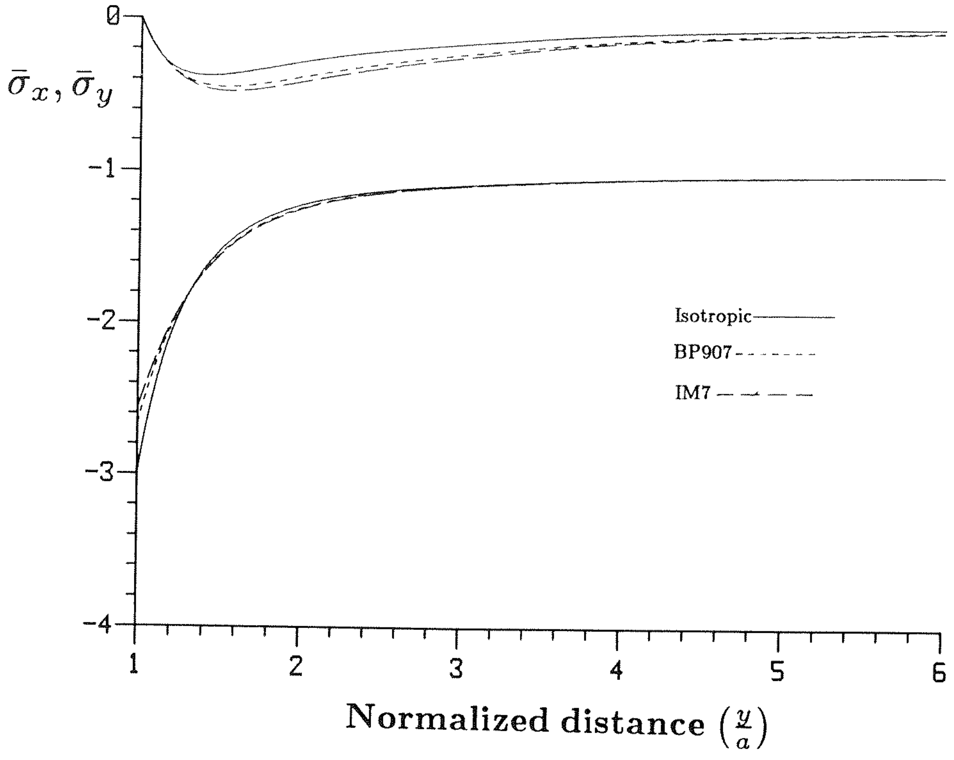

Figure 3.3a $\bar{\sigma}_x$ and $\bar{\sigma}_y$ distribution along $\bar{y}$-axis at $\bar{x}$=0. (Type B laminate)

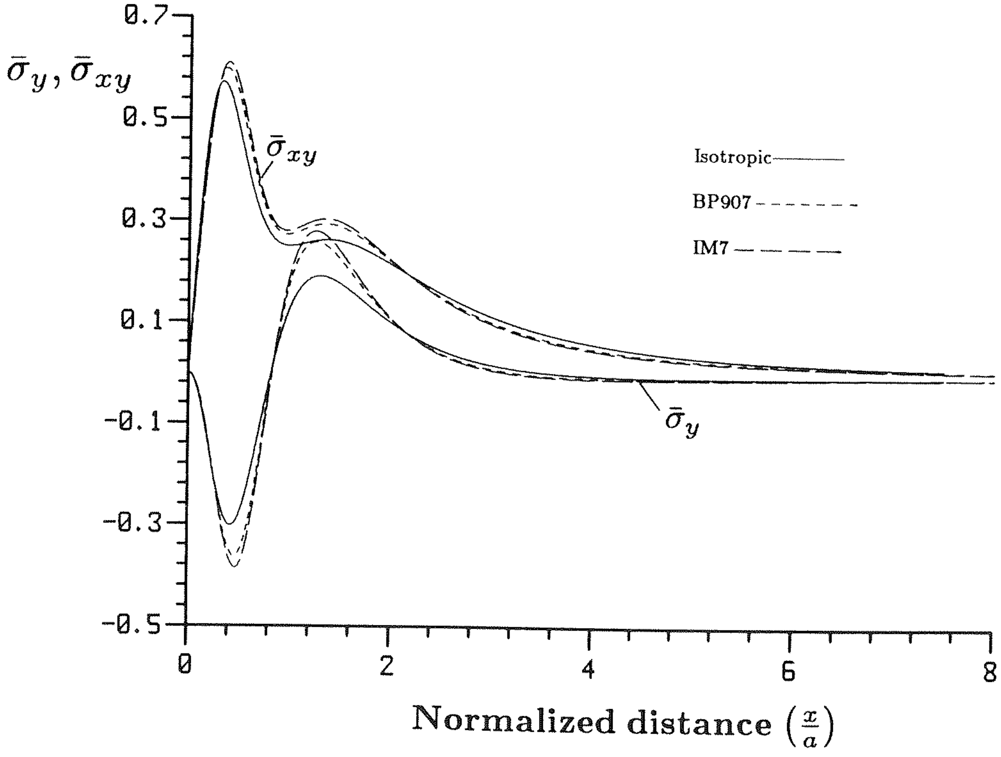

Figure 3.3b $\bar{\sigma}_y$ and $\bar{\sigma}_{xy}$ distribution along $\bar{x}$-axis at $\bar{y}$=1. (Type B laminate)

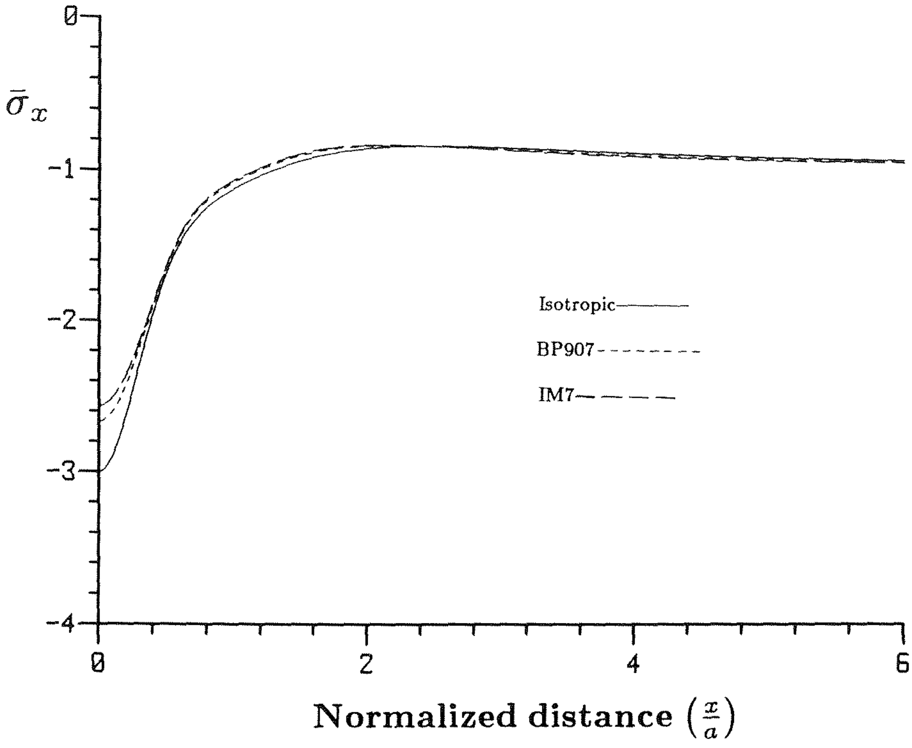

Figure 3.3c $\bar{\sigma}_x$ *distribution along* $\bar{x}$*-axis at* $\bar{y}=1$*. (Type B laminate)*

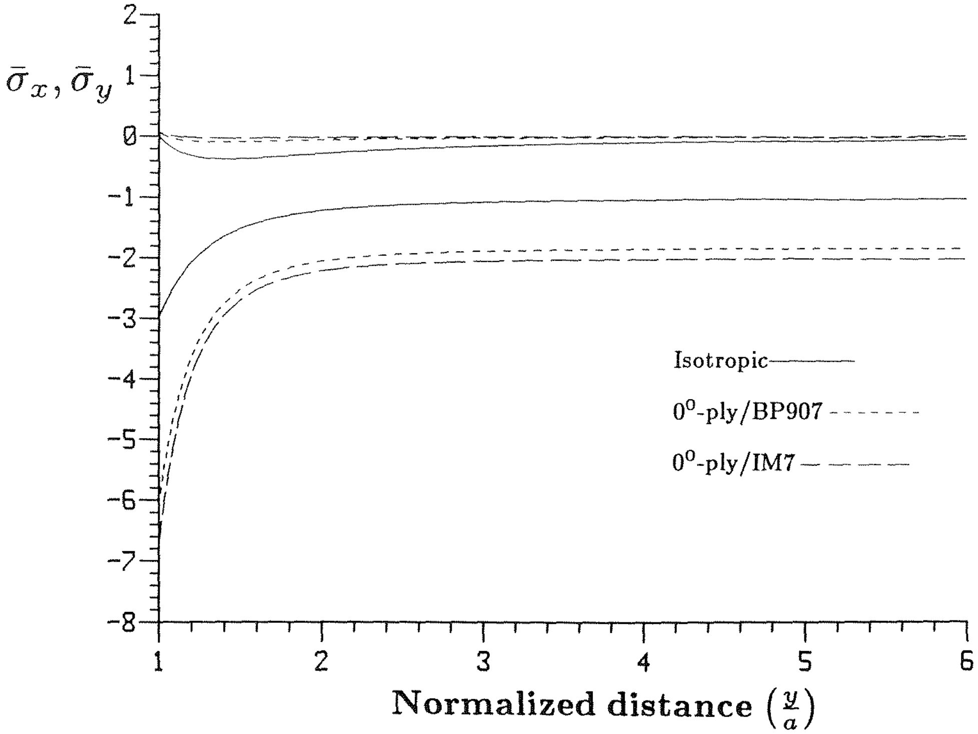

Figure 3.4a $\bar{\sigma}_x$ *and* $\bar{\sigma}_y$ *distribution in* 0^0 *plies along* $\bar{y}$*-axis at* $\bar{x}=0$*. (Type A laminate)*

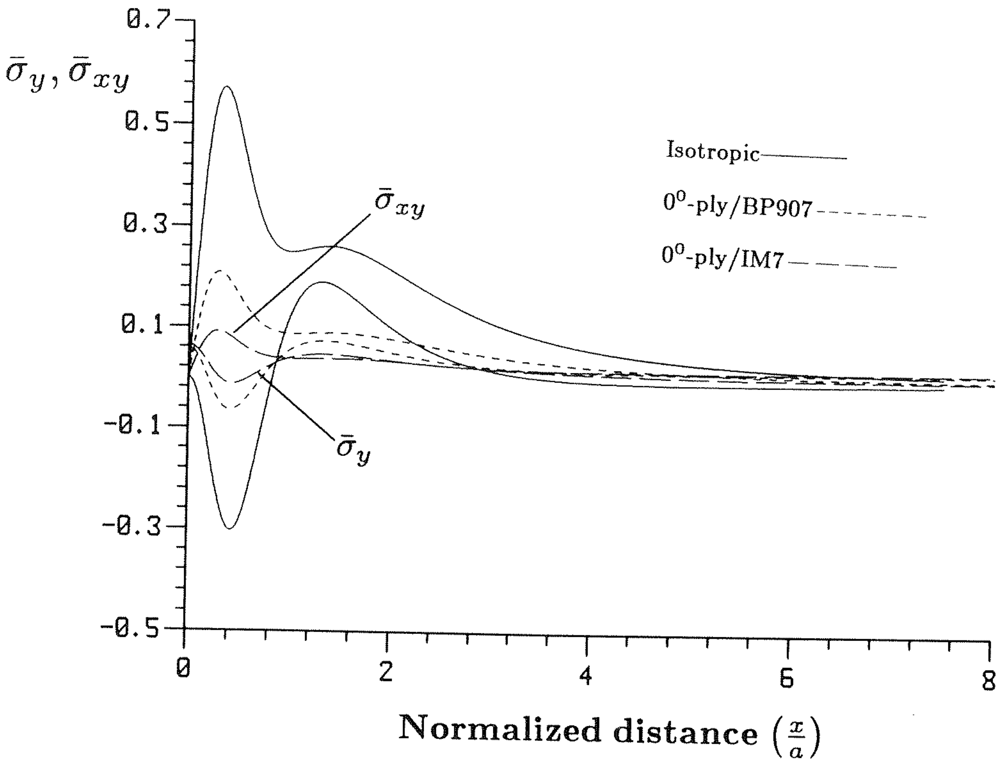

Figure 3.4b $\bar{\sigma}_y$ and $\bar{\sigma}_{xy}$ distribution in 0^0 plies along $\bar{x}$-axis at $\bar{y}$=1. (Type A laminate)

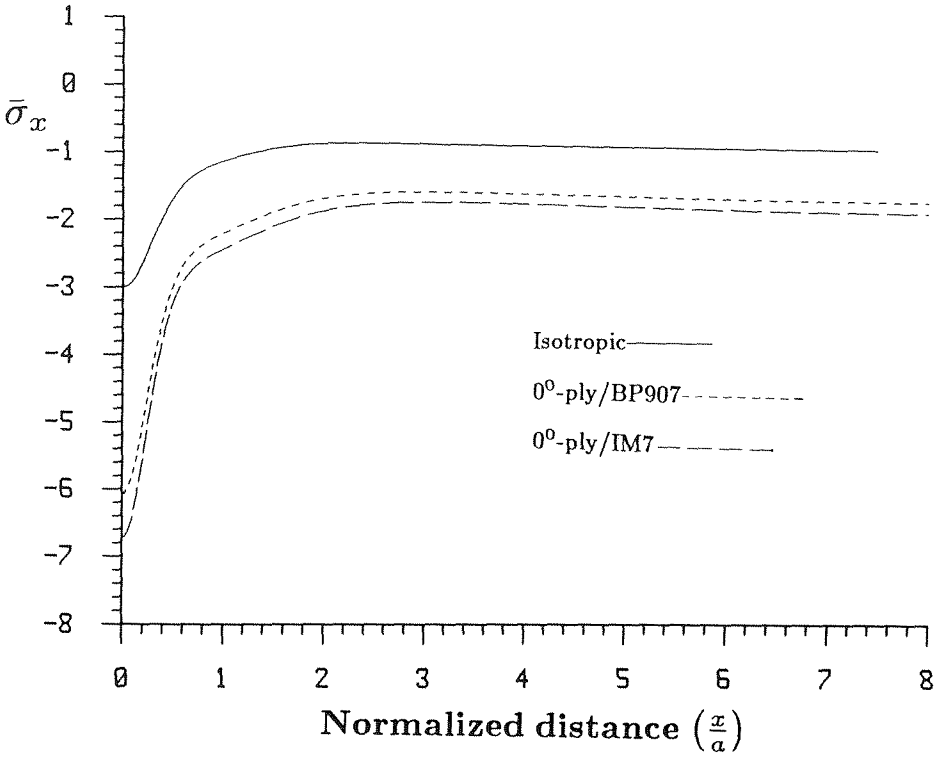

Figure 3.4c $\bar{\sigma}_x$ *distribution in* 0^0 *plies along* $\bar{x}$*-axis at* $\bar{y}=1$*. (Type A laminate)*

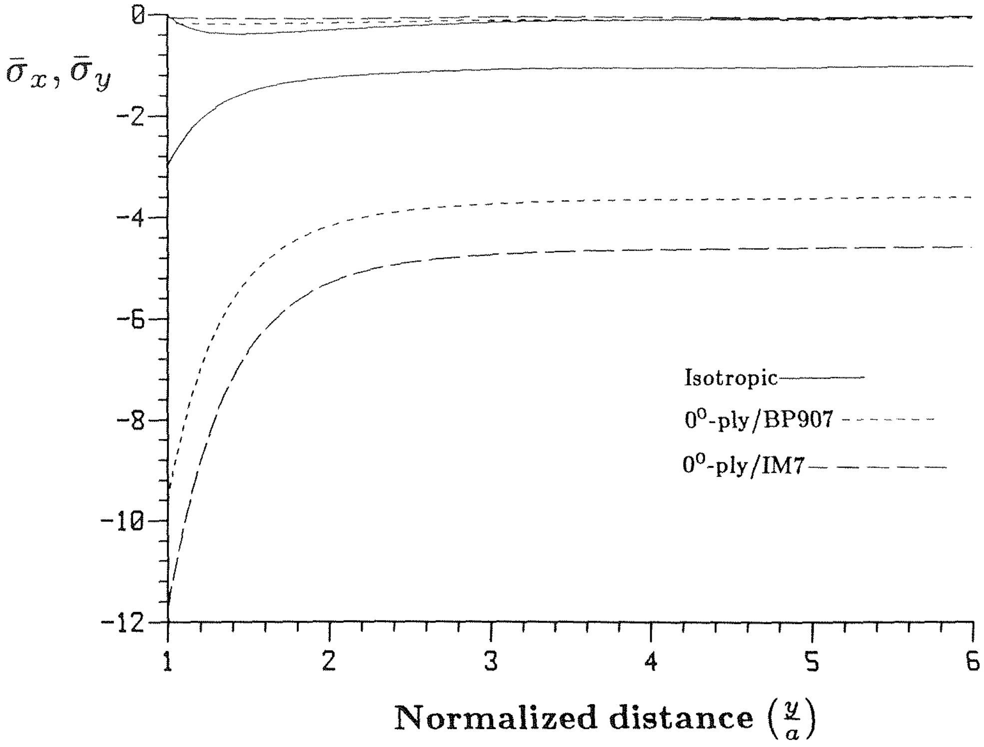

Figure 3.5a $\bar{\sigma}_x$ *and* $\bar{\sigma}_y$ *distribution in* 0^0 *plies along* $\bar{y}$*-axis at* $\bar{x}=0$. *(Type B laminate)*

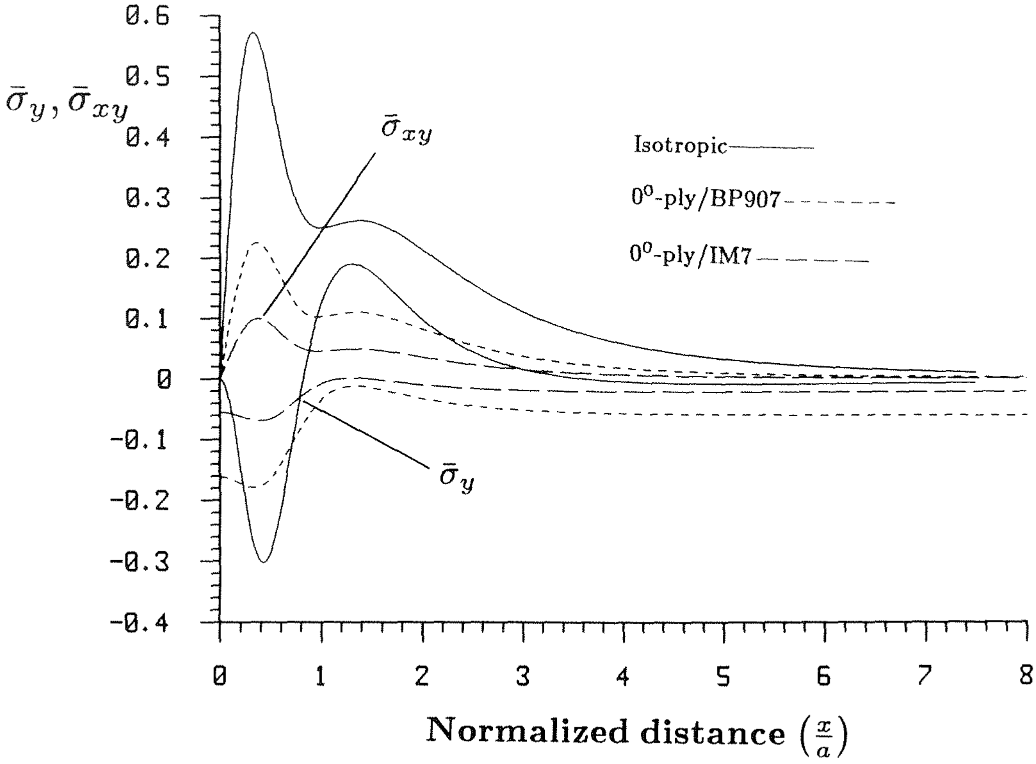

Figure 3.5b $\bar{\sigma}_y$ and $\bar{\sigma}_{xy}$ distribution in 0^0 plies along $\bar{x}$-axis at $\bar{y}$=1. (Type B laminate)

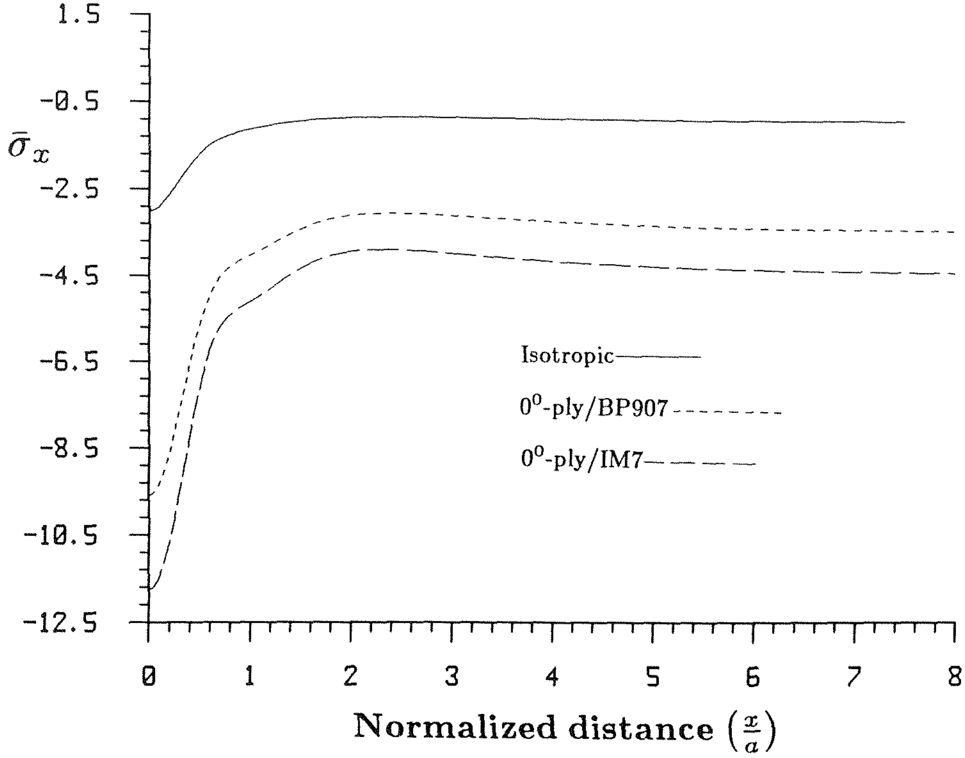

Figure 3.5c $\bar{\sigma}_x$ *distribution in* 0^0 *plies along* $\bar{x}$*-axis at* $\bar{y}$*=1. (Type B laminate)*

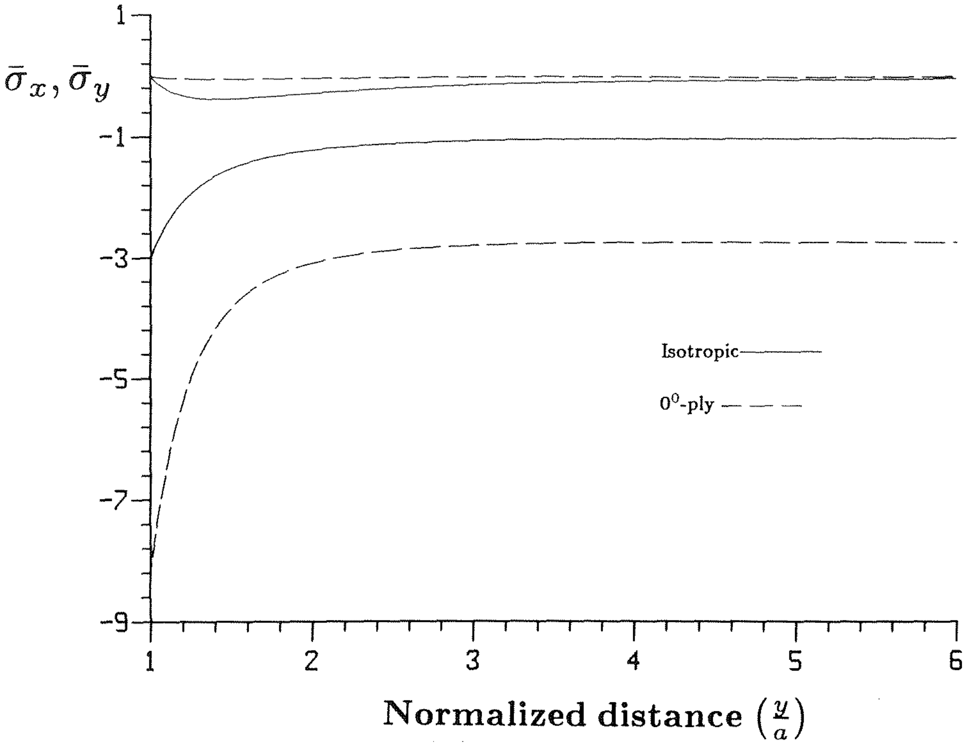

Figure 3.6a $\bar{\sigma}_x$ and $\bar{\sigma}_y$ distribution along $\bar{y}$-axis at $\bar{x}$=0. Solid line - Types C and D laminates, dashed line - 0^0 ply stresses.

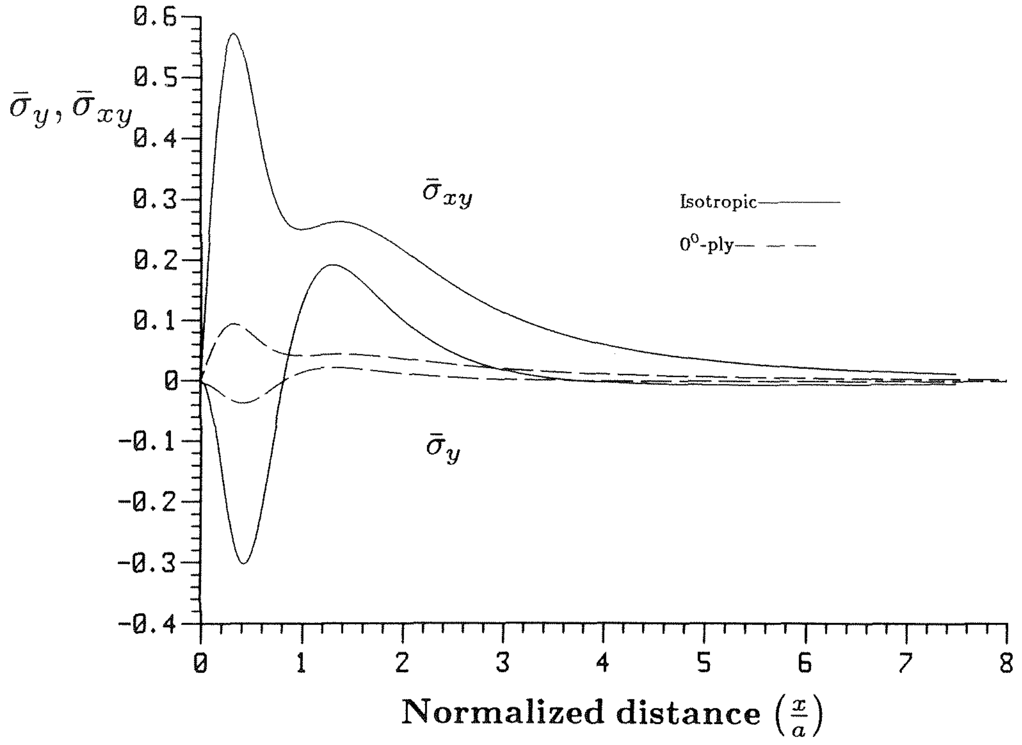

Figure 3.6b $\bar{\sigma}_y$ and $\bar{\sigma}_{xy}$ distribution along $\bar{x}$-axis at $\bar{y}$=1. *Solid line - Types* C and *D laminates, dashed line -* 0^0 *ply stresses.*

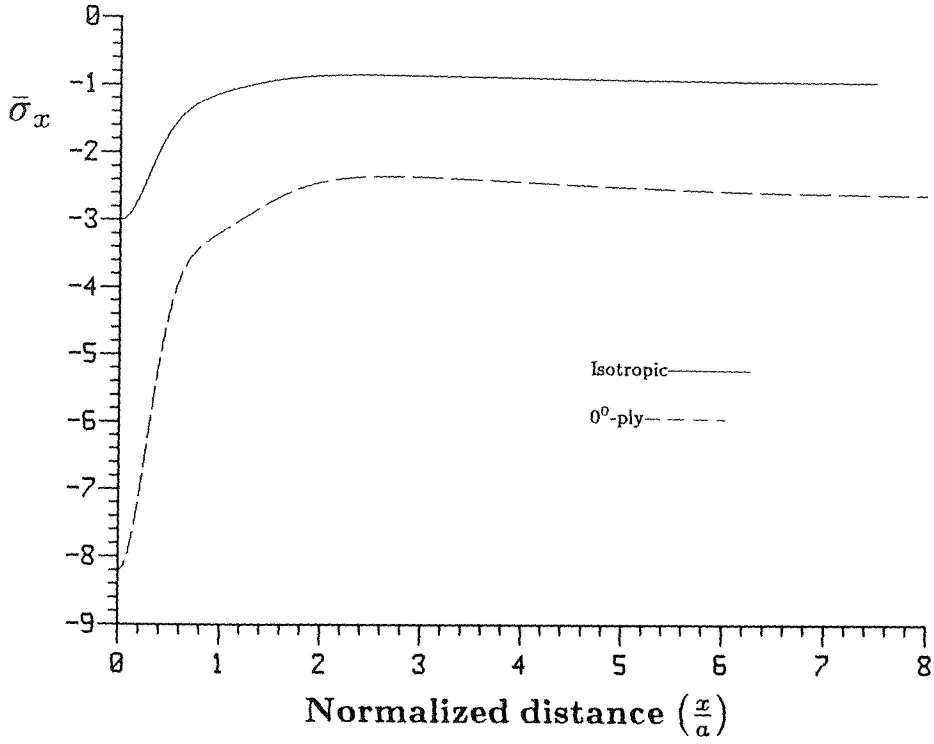

Figure 3.6c $\bar{\sigma}_x$ *distribution in along* $\bar{x}$*-axis at* $\bar{y}=1$*. Solid line - Types C and D laminates, dashed line -* 0^0 *ply stresses.*

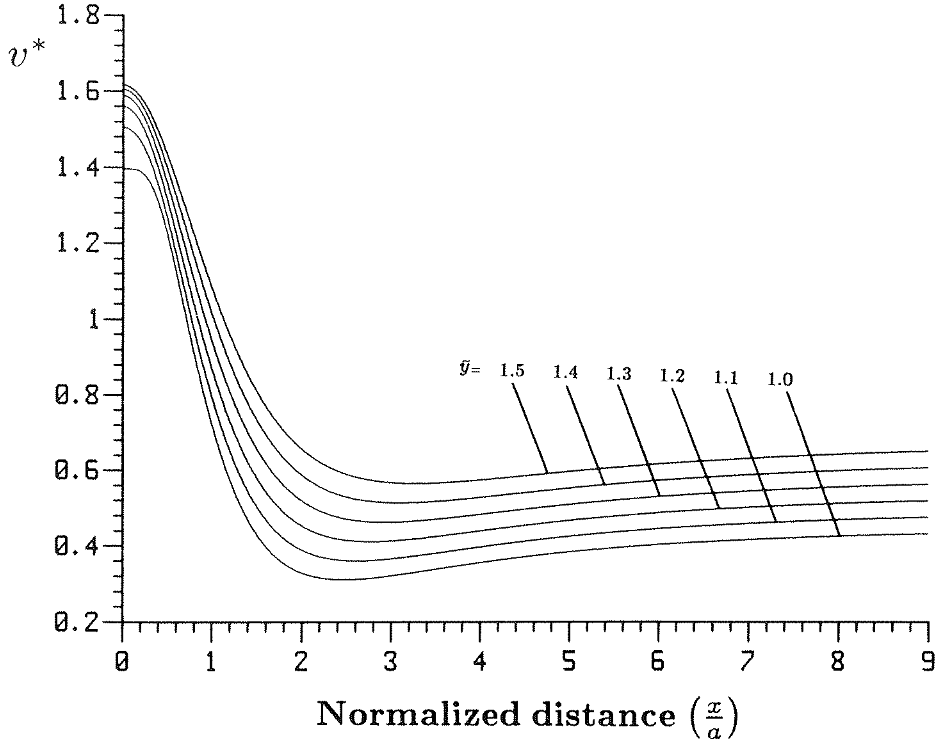

Figure 3.7a v^* *distribution along* $\bar{x}$ *at* $\bar{y}$*=1. (Laminate type A - T300/BP907)*

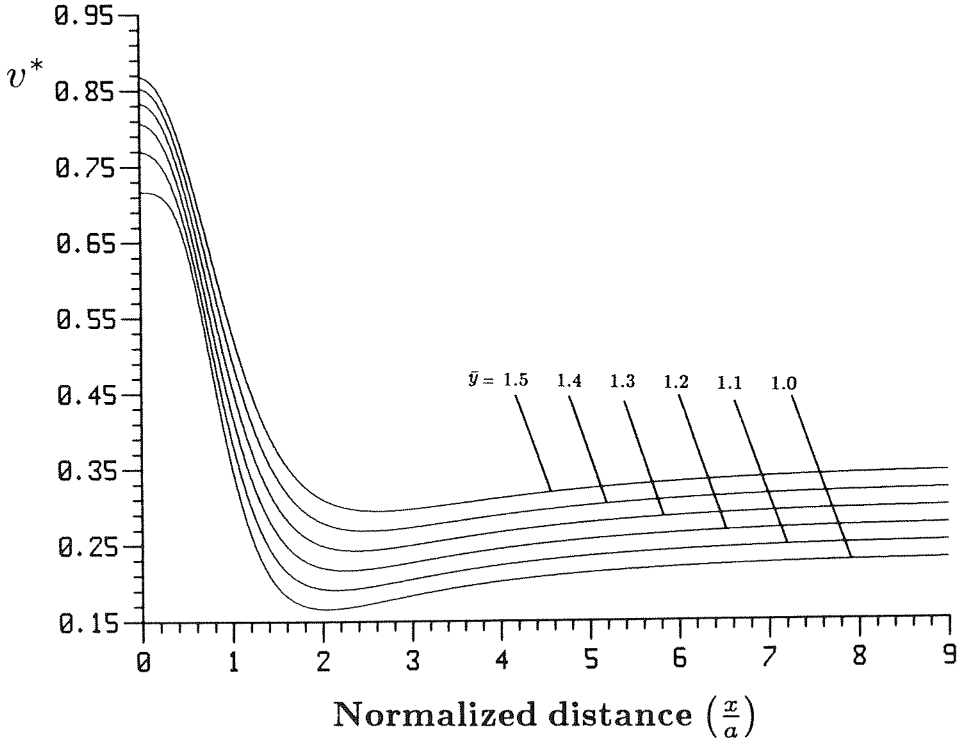

Figure 3.7b v^* *distribution along* $\bar{x}$ *at* $\bar{y}$*=1. (Laminate type B - T300/BP907)*

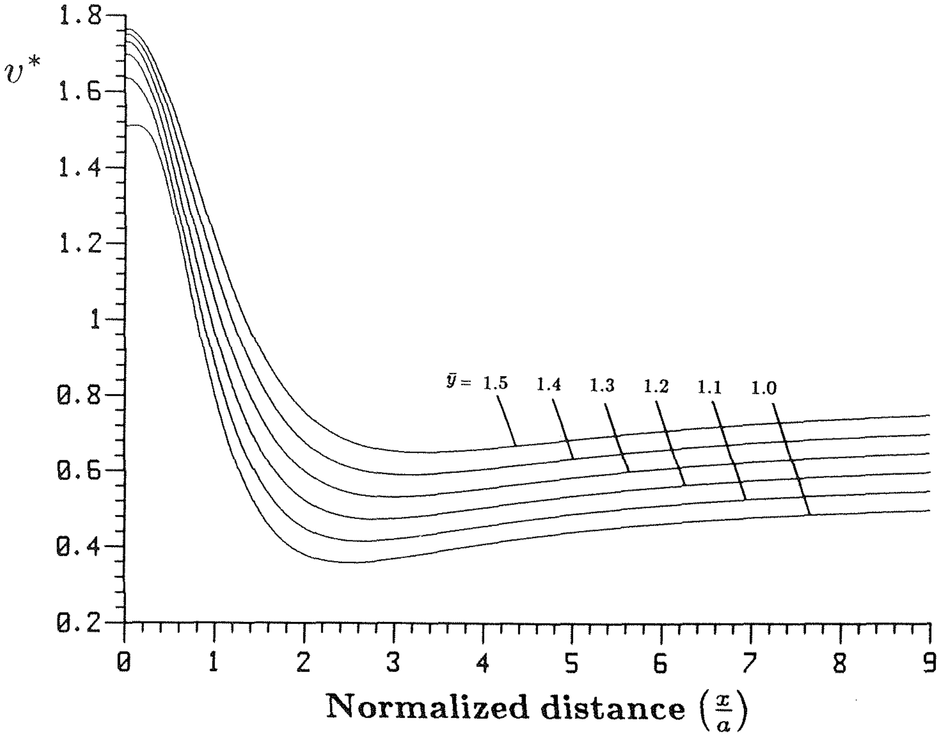

Figure 3.7c v^* *distribution along* $\bar{x}$ *at* $\bar{y}$*=1. (Laminate type A - IM7/8551-7)*

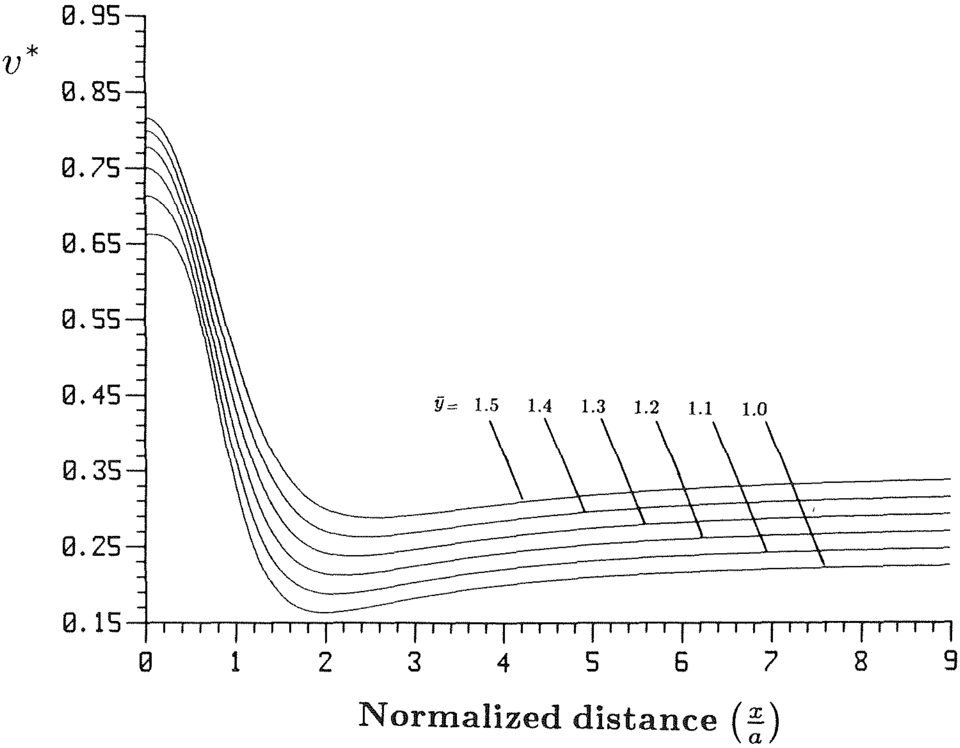

Figure 3.7d v^* *distribution along* $\bar{x}$ *at* $\bar{y}$*=1. (Laminate type B - IM7/8551-7)*

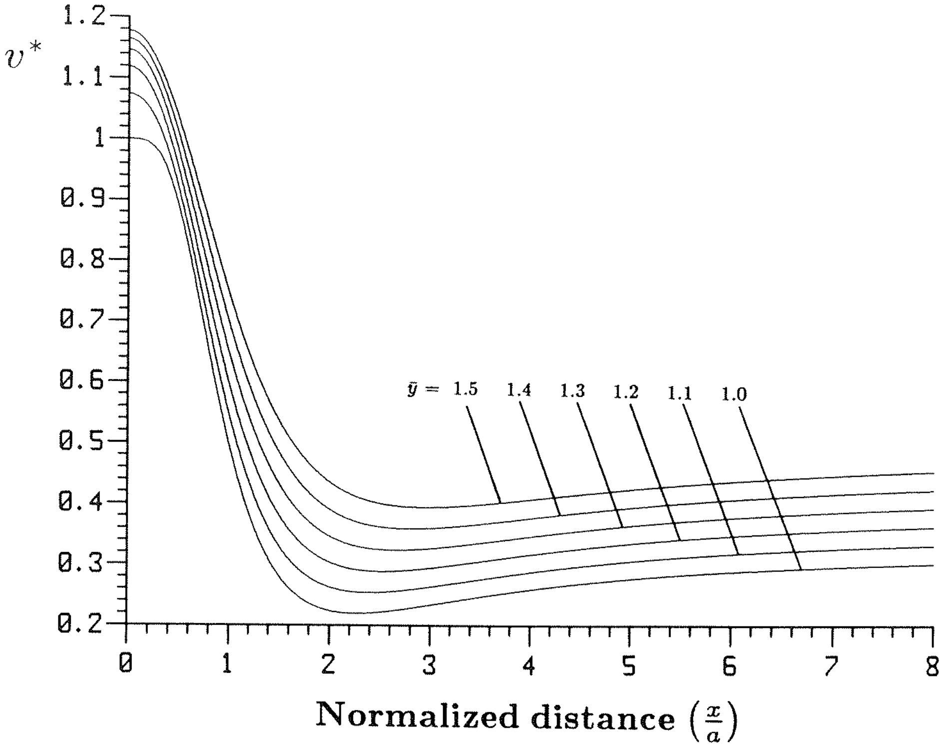

Figure 3.7e v^* *distribution along* $\bar{x}$ *at* $\bar{y}$*=1. (Laminate types C and D - IM7/8551-7, also Isotropic)*

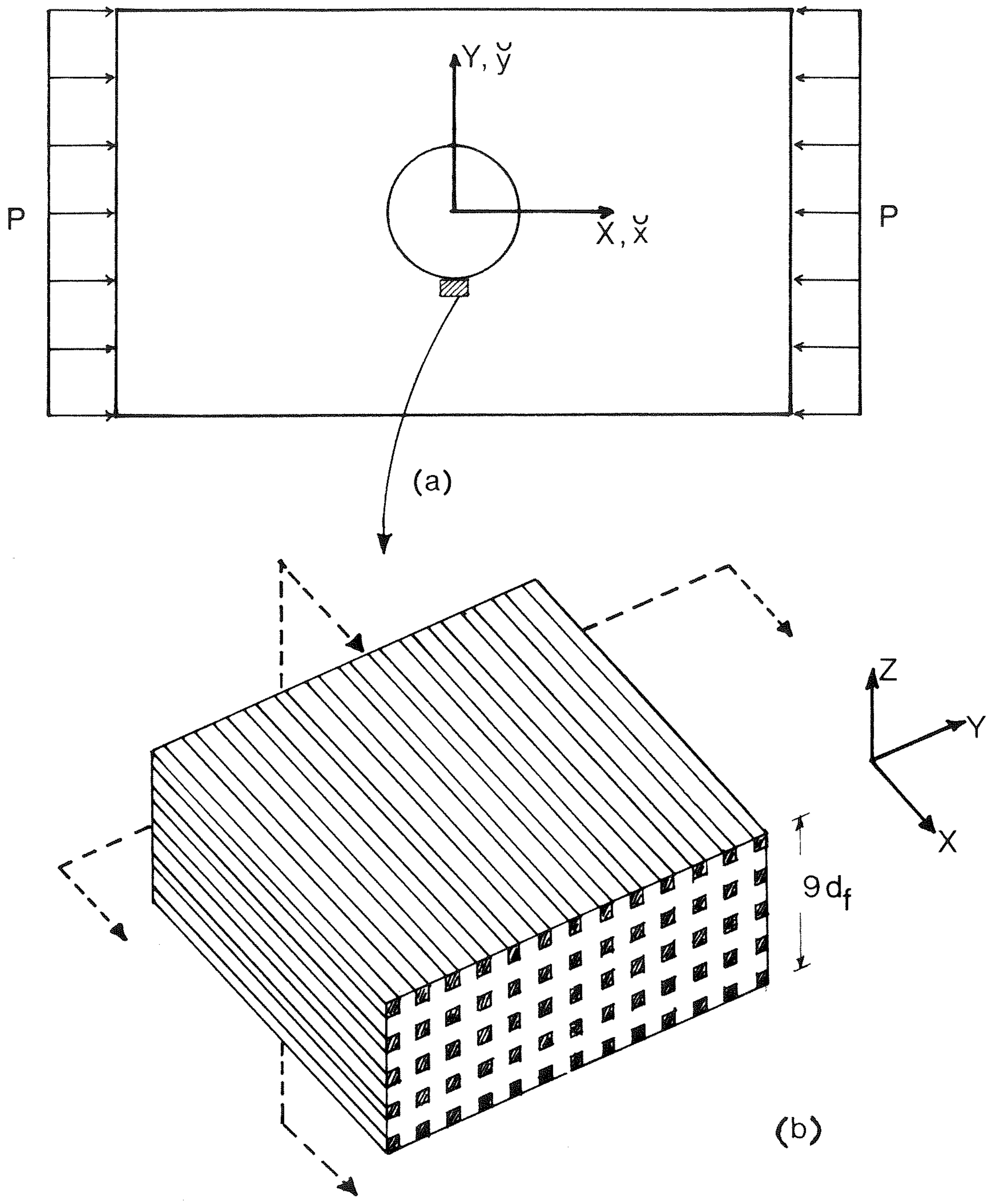

Figure 3.8 Isolated zero-ply portion. a) Adjacent to the hole. b) Exaggerated view of isolated portion.

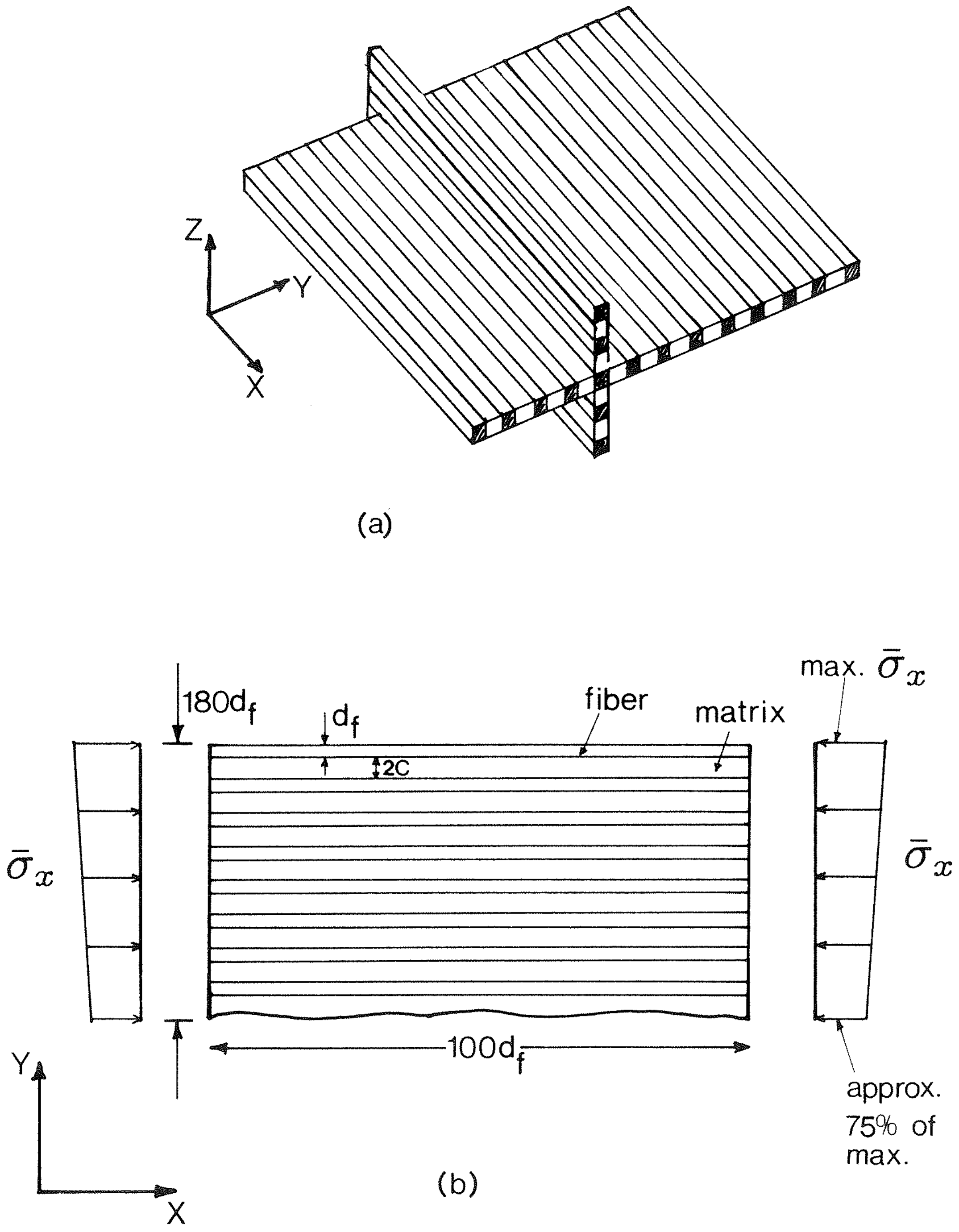

Figure 3.9 a) A typical idealized layer of a 0^0*-ply. b) Overall dimensions of idealized layer.*

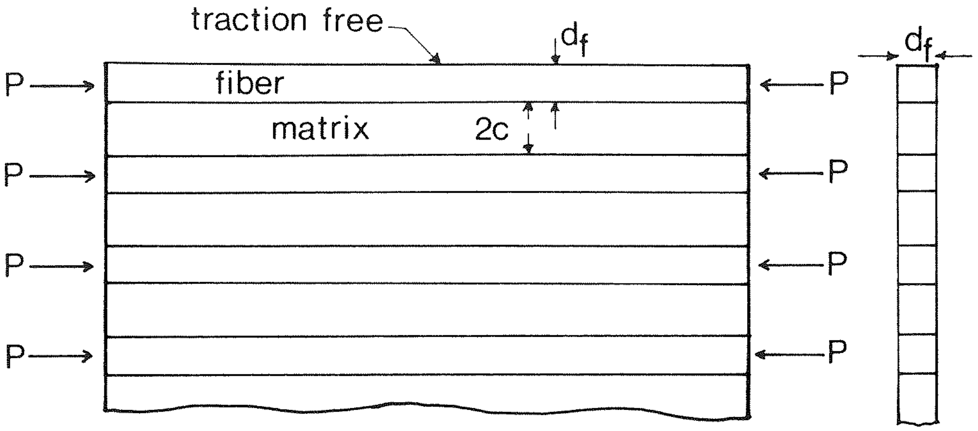

Figure 3.10 Model configuration to study micro-buckling of 0^0 *plies.*

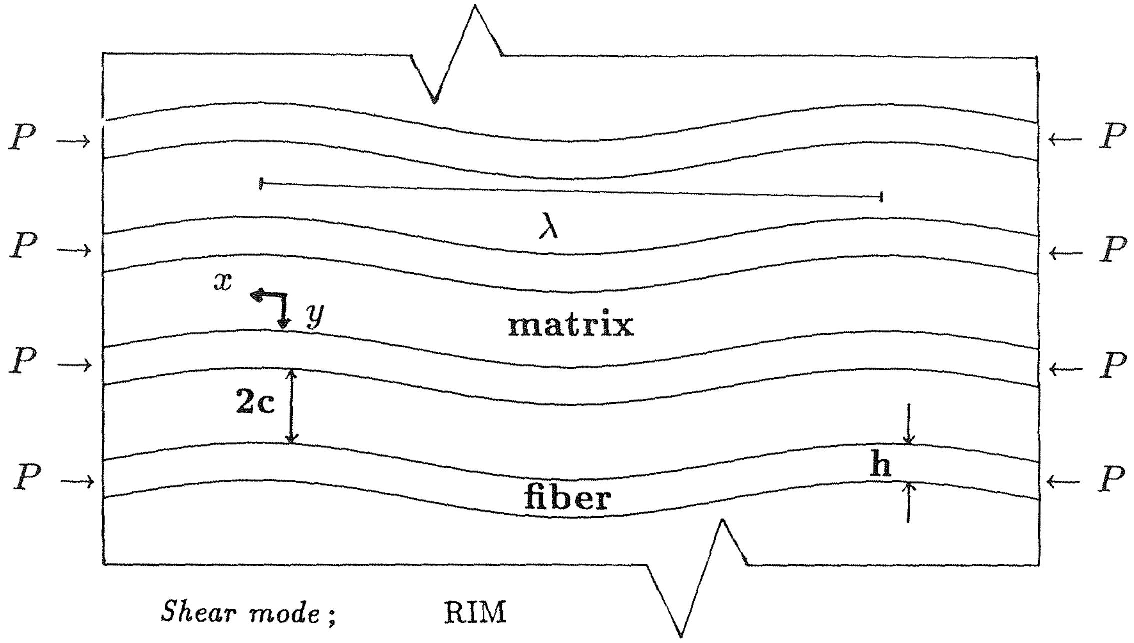

Shear mode ; RIM

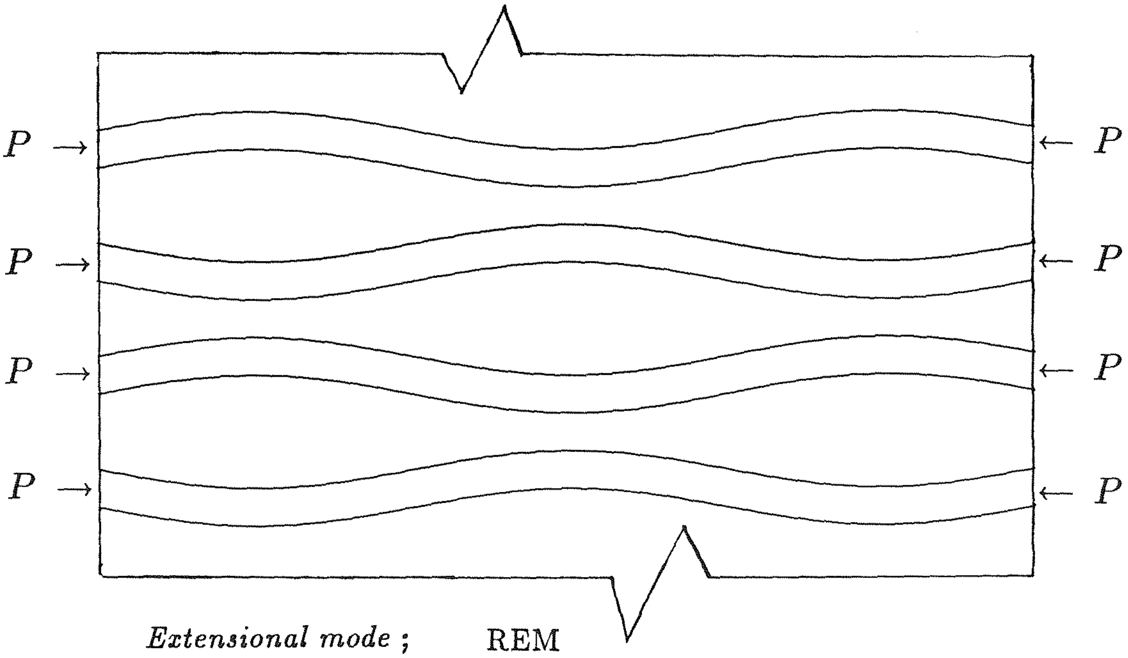

Extensional mode ; REM

Figure 4.1 The configuration studied by Rosen[4.4].

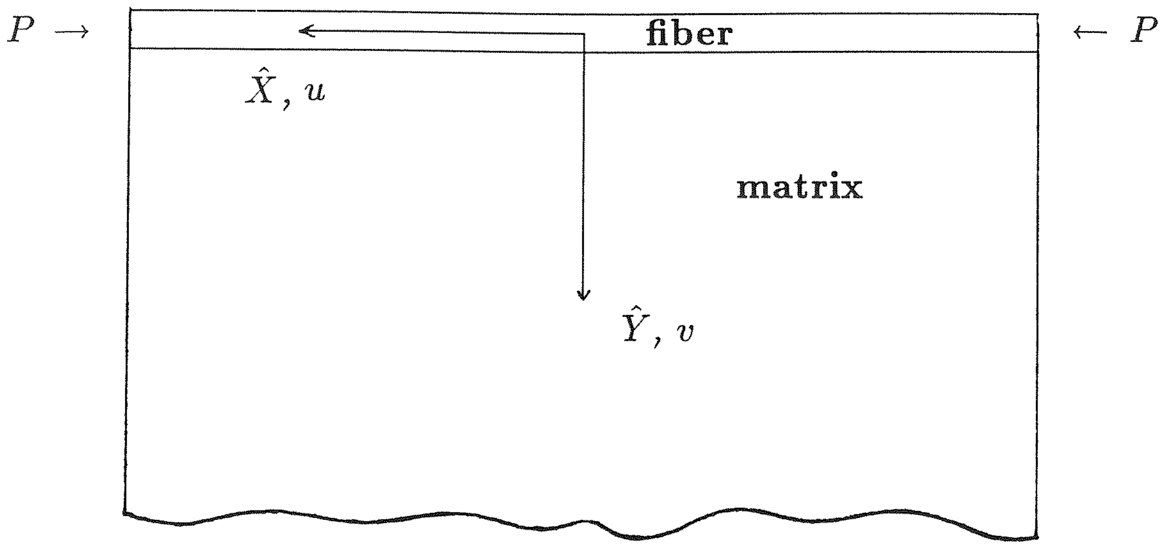

Figure 4.2 The single fiber composite.

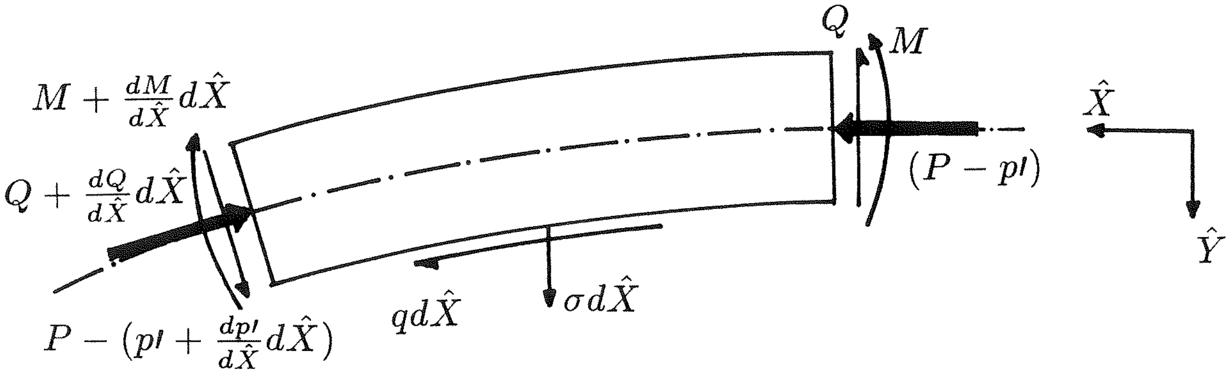

Figure 4.3 Isolated element of buckled fiber.

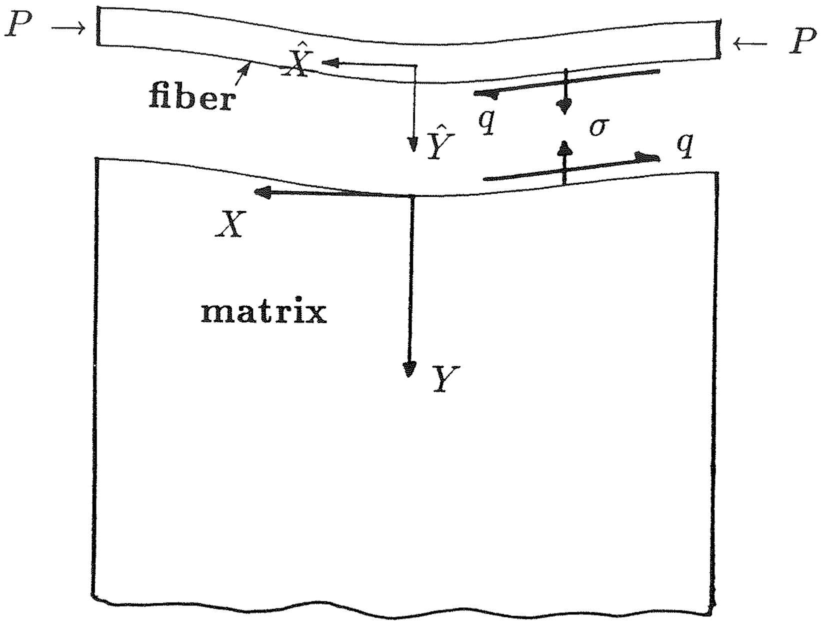

Figure 4.4 Matrix configuration at fiber buckling.

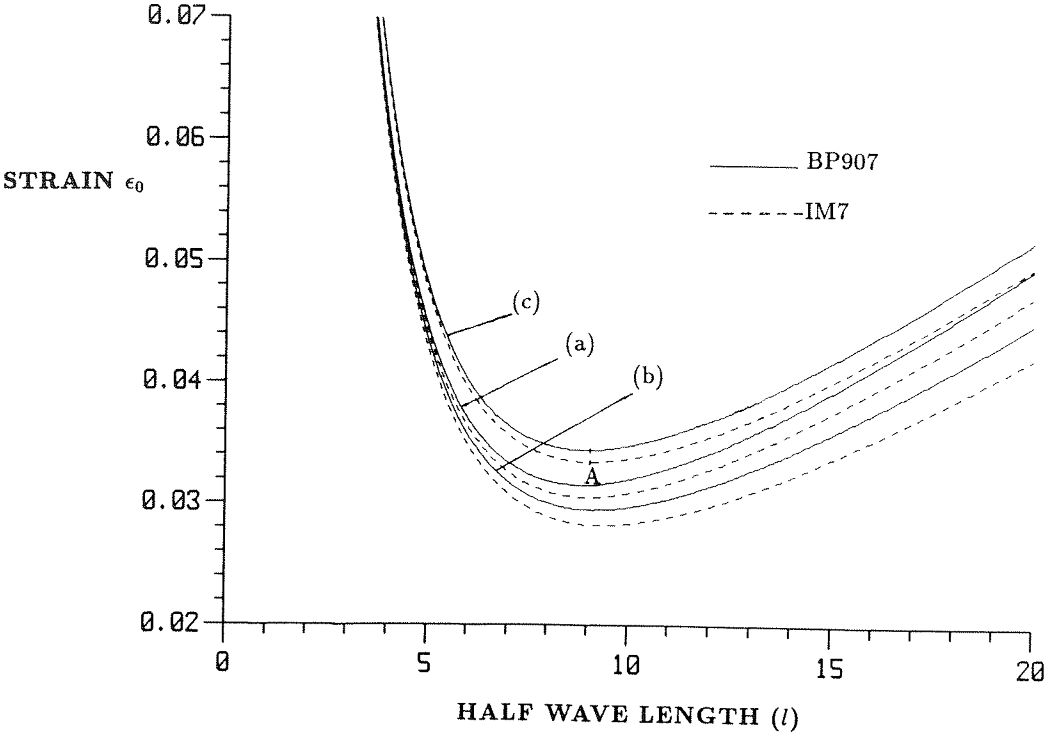

Figure 4.5 Variation of ϵ_0 with non-dimensional half wave length l. Comparison of predictive models; (a) Gough et al.[4.15] (b) Reissner [4.16] (c) present; dashed line-IM7, solid line-BP907.

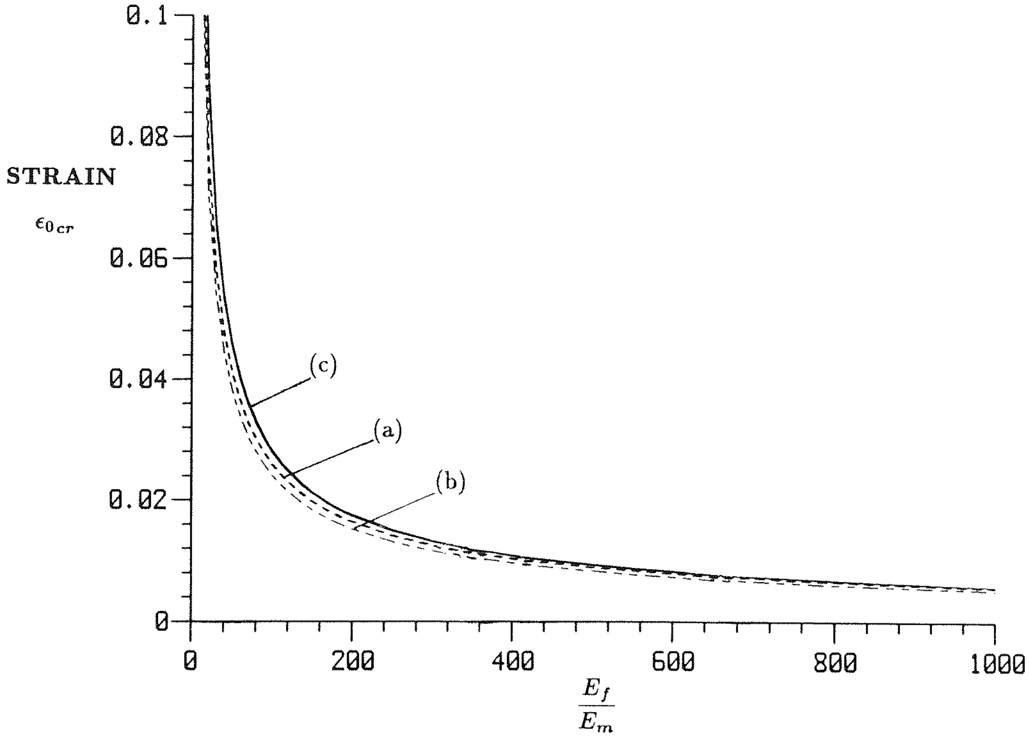

Figure 4.6 *Variation of critical ϵ_0 with ratio of Youngs moduli $\frac{E_f}{E_m}$. (a), (b), (c) as in Figure 4.5.*

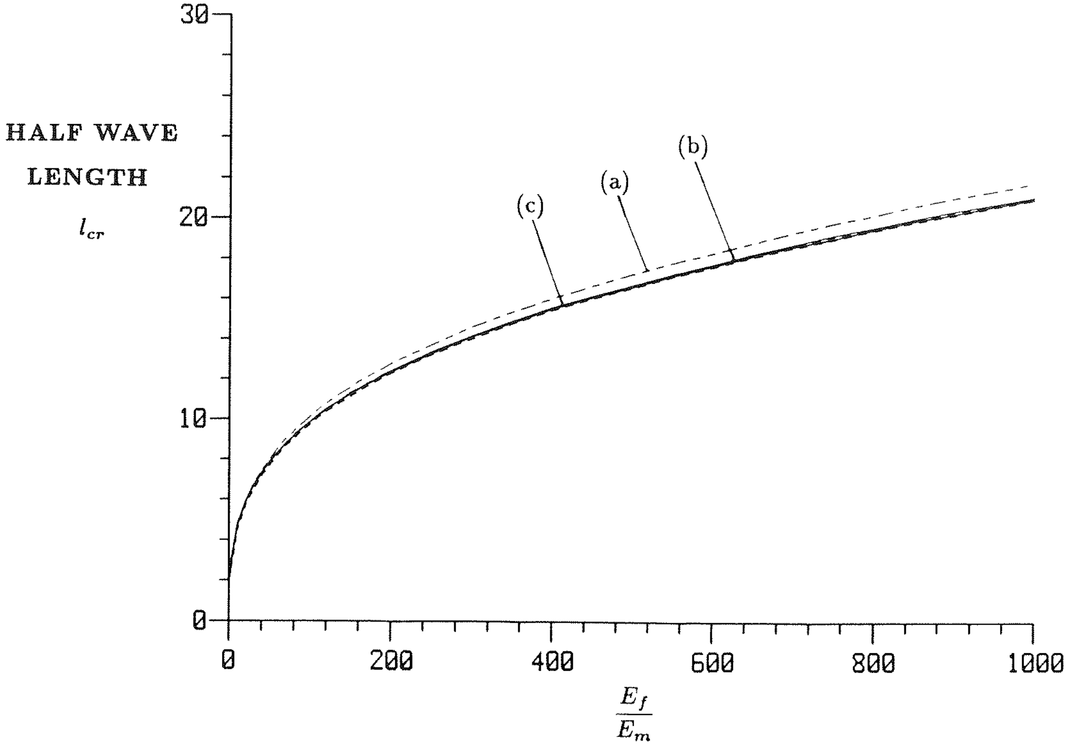

Figure 4.7 Variation of critical half wave length (l) with ratio of Youngs moduli $\frac{E_f}{E_m}$. (a), (b), (c) as in Figure 4.5.

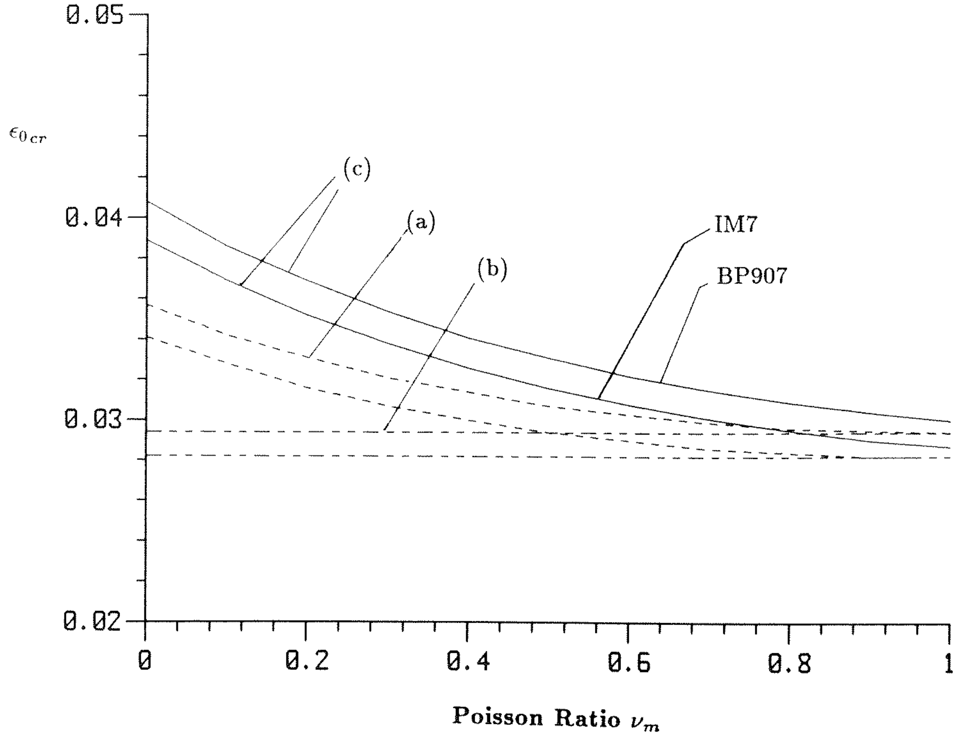

Figure 4.8a Effect of Poisson's ratio on critical strain ϵ_0. (a), (b), (c) as in Figure 4.5.

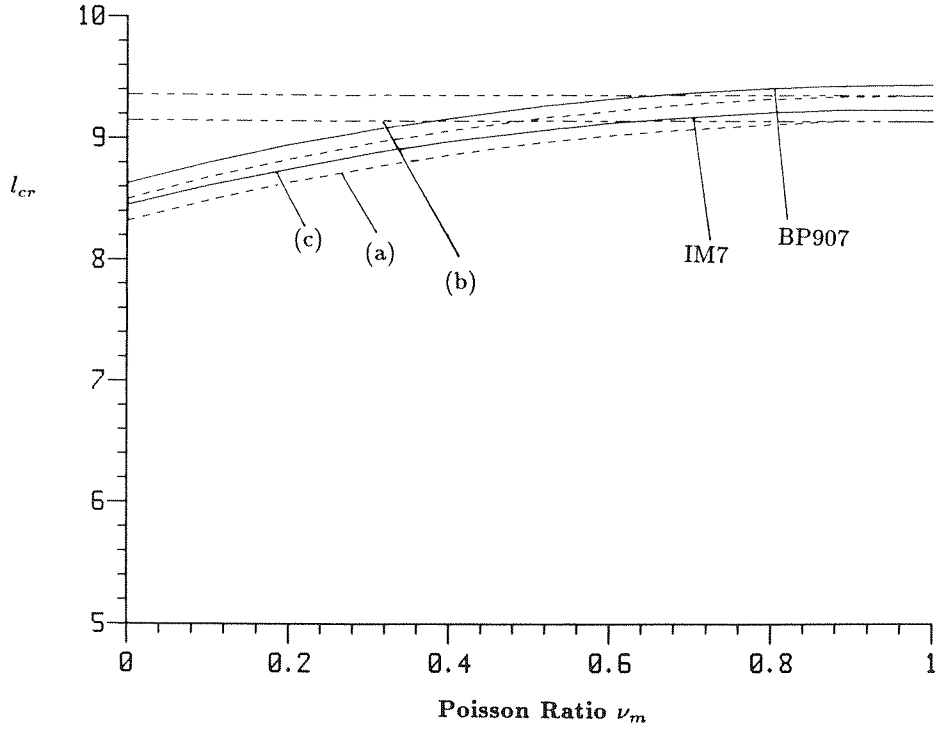

Figure 4.8b Effect of Poisson's ratio on critical half wave length l. (a), (b), (c) as in Figure 4.5.

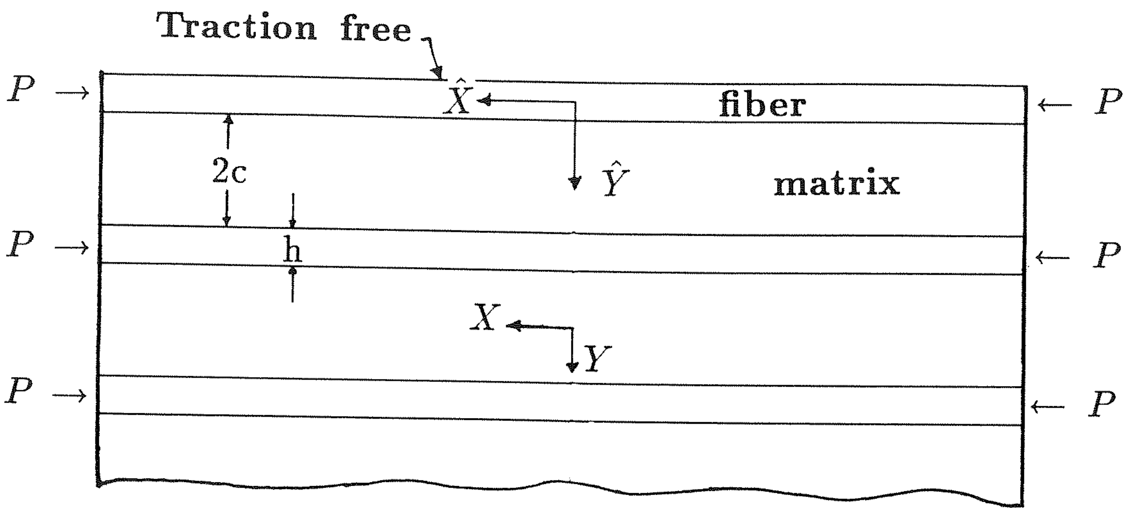

Figure 4.9 Configuration for unidirectional laminated composite.

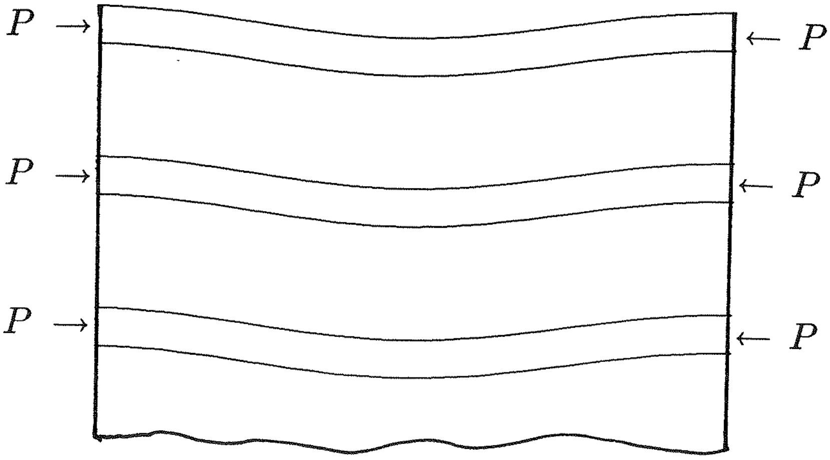

Figure 4.10 Buckled configuration of laminated composite.

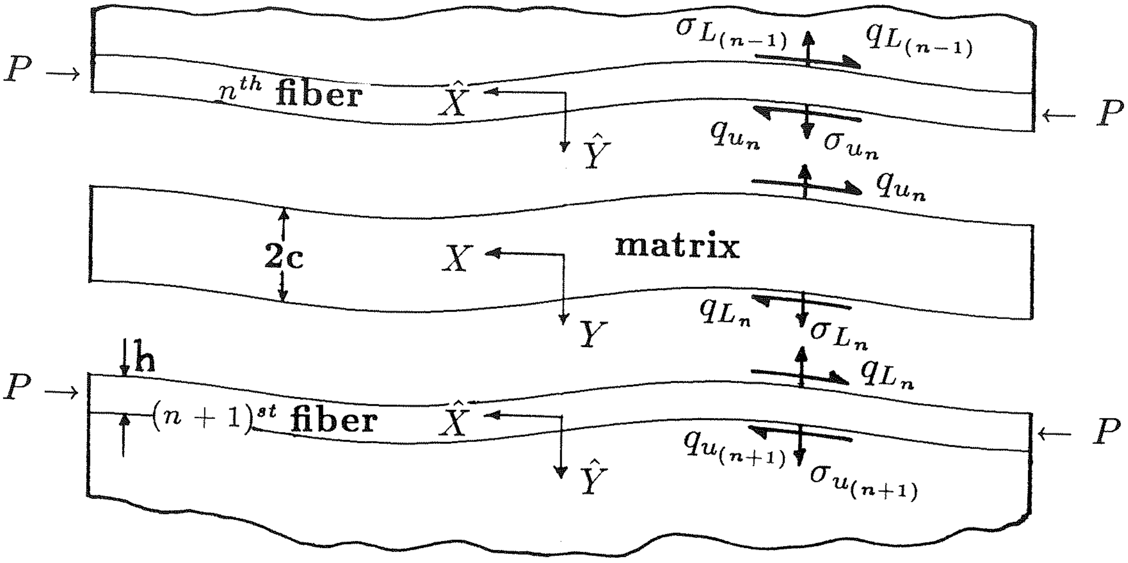

Figure 4.11 Isolated portion of buckled configuration. $n^{th}, (n+1)^{st}$ *fibers and sandwiched matrix.*

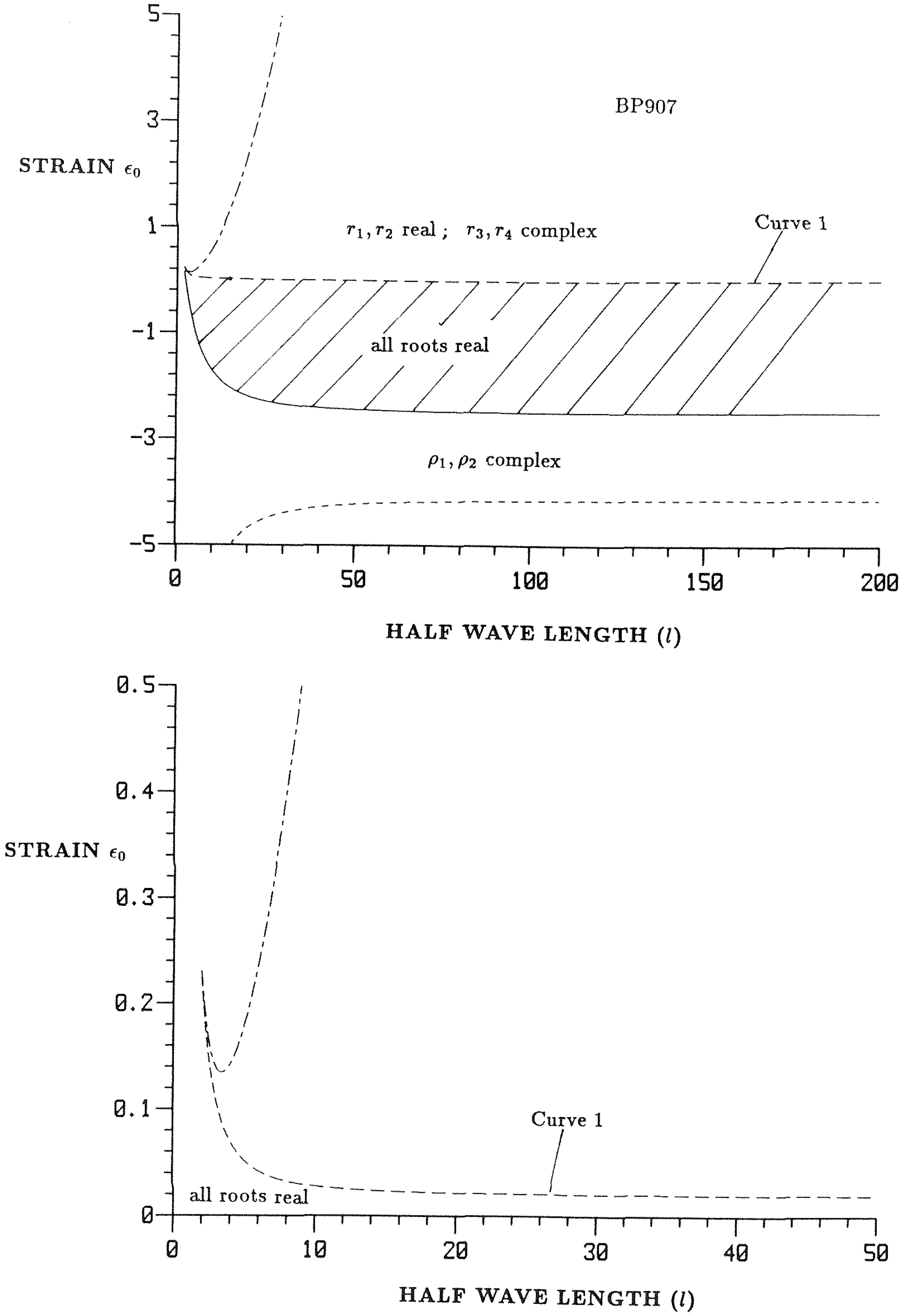

Figure 4.12a Behaviour of the discriminants associated with (4.46, 4.47) in the (ϵ_0, l) plane; T300/BP907.

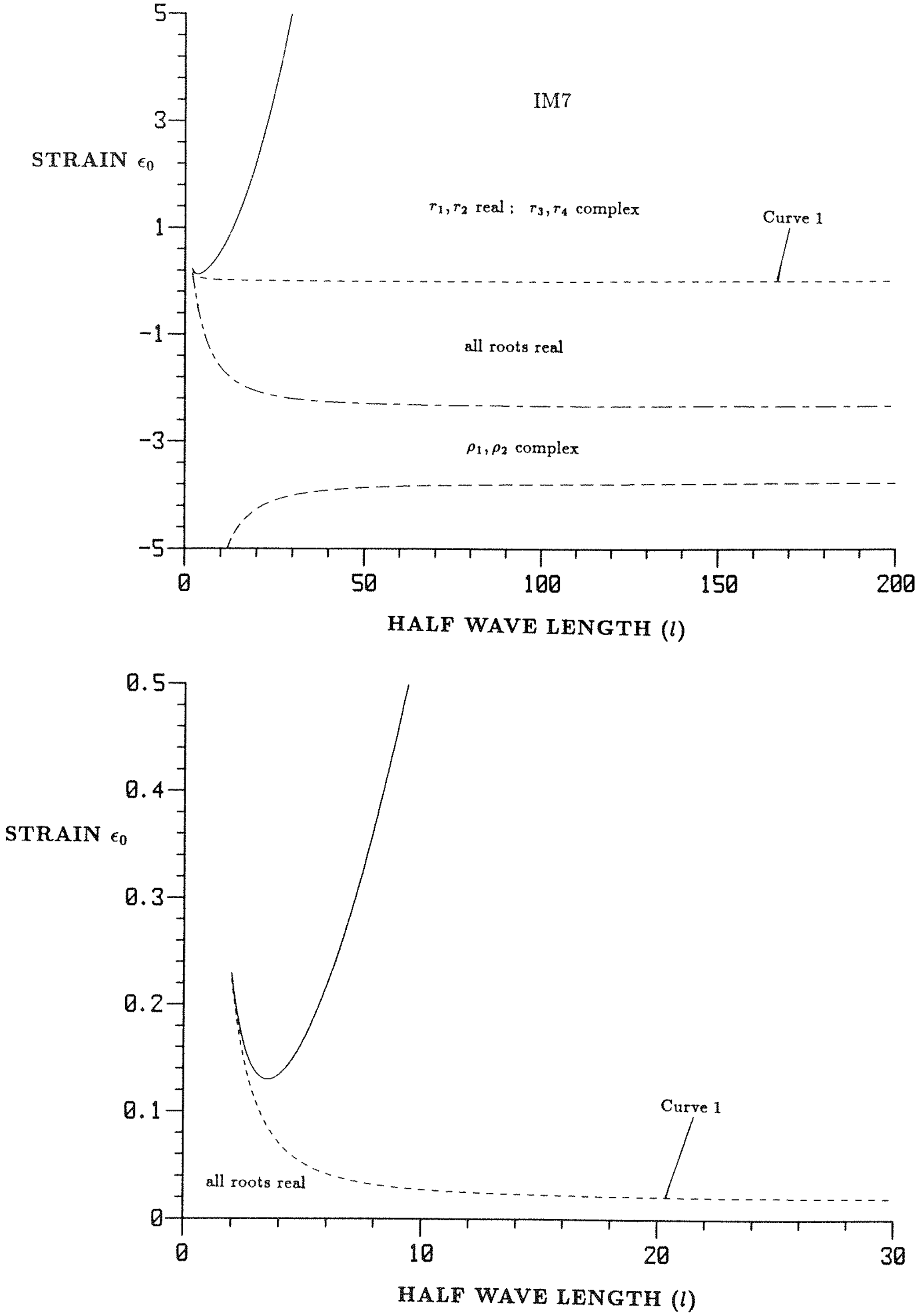

Figure 4.12b Behaviour of the discriminants associated with (4.46, 4.47) in the (ϵ_0, l) plane; IM7/8551-7.

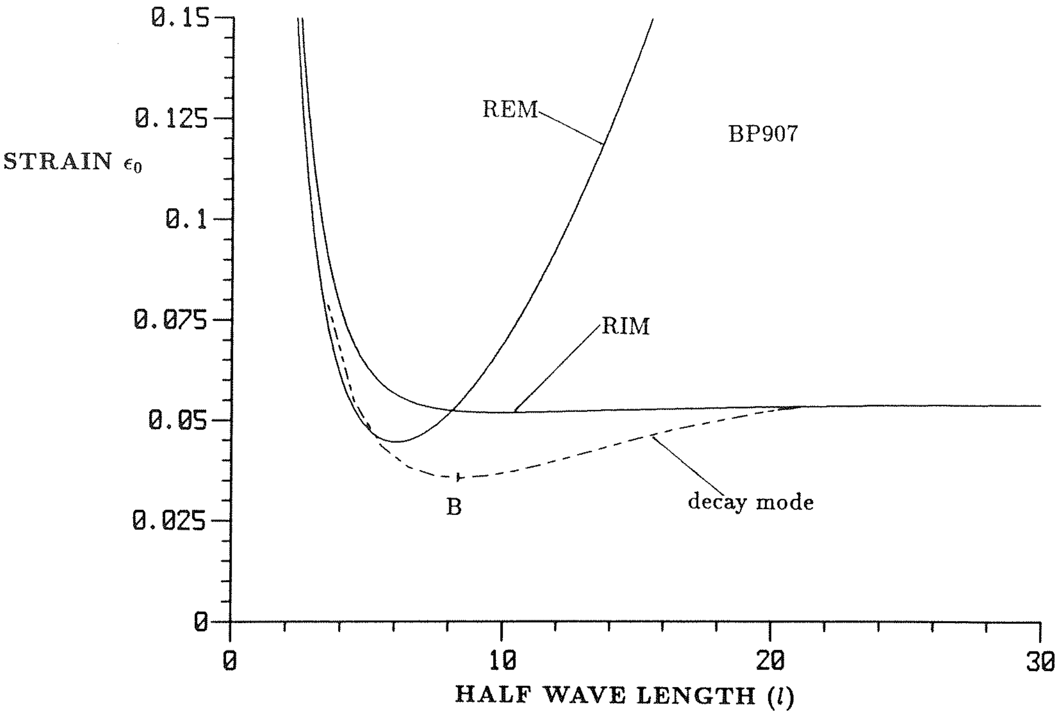

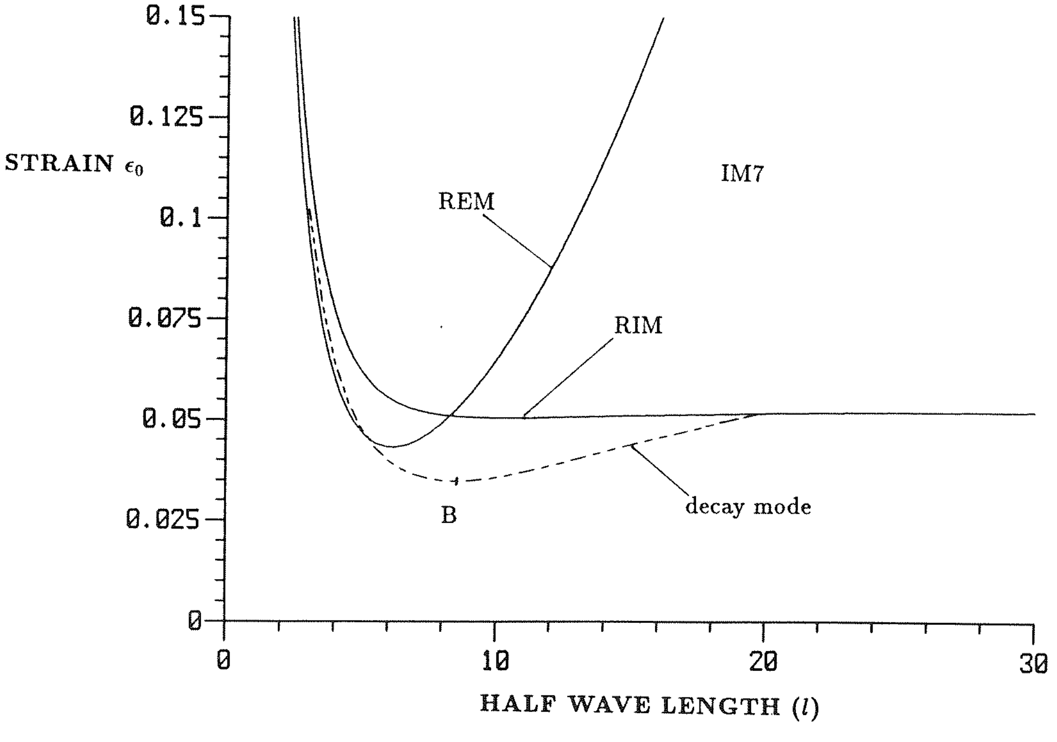

Figure 4.13 Variation of ϵ_0 with non-dimensional half wave length l. 'decay mode' denotes present results. (a) T300/BP907 (b) IM7/8551-7.

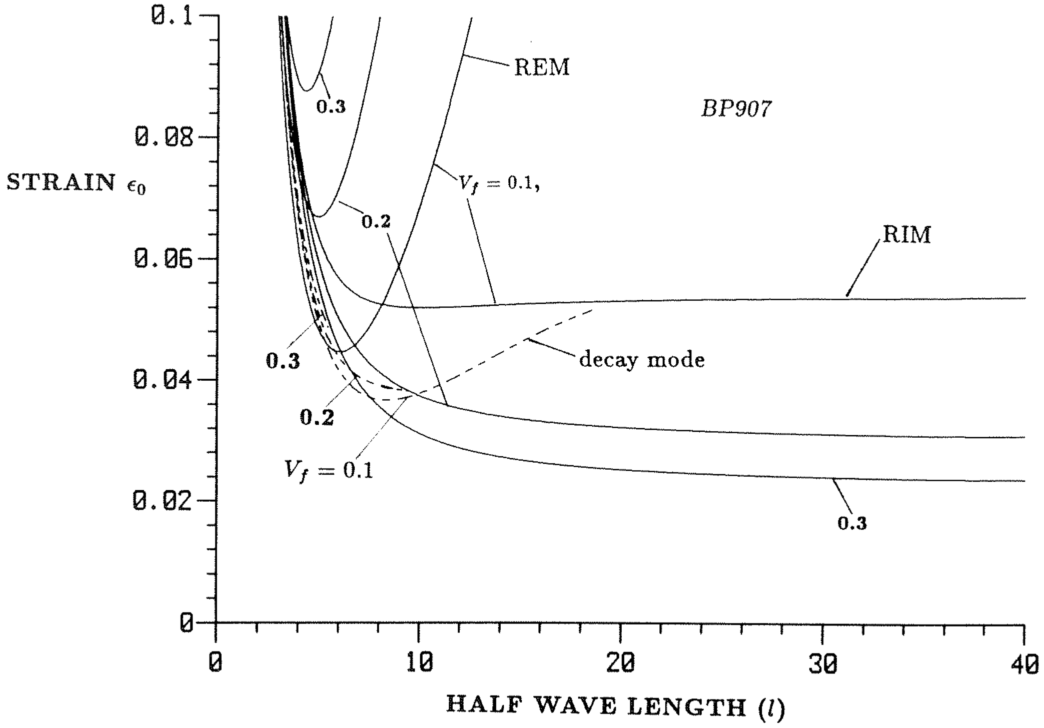

Figure 4.13c Variation of ϵ_0 *with non-dimensional half wave length* l*; T300/BP907,* V_f *as a parameter.*

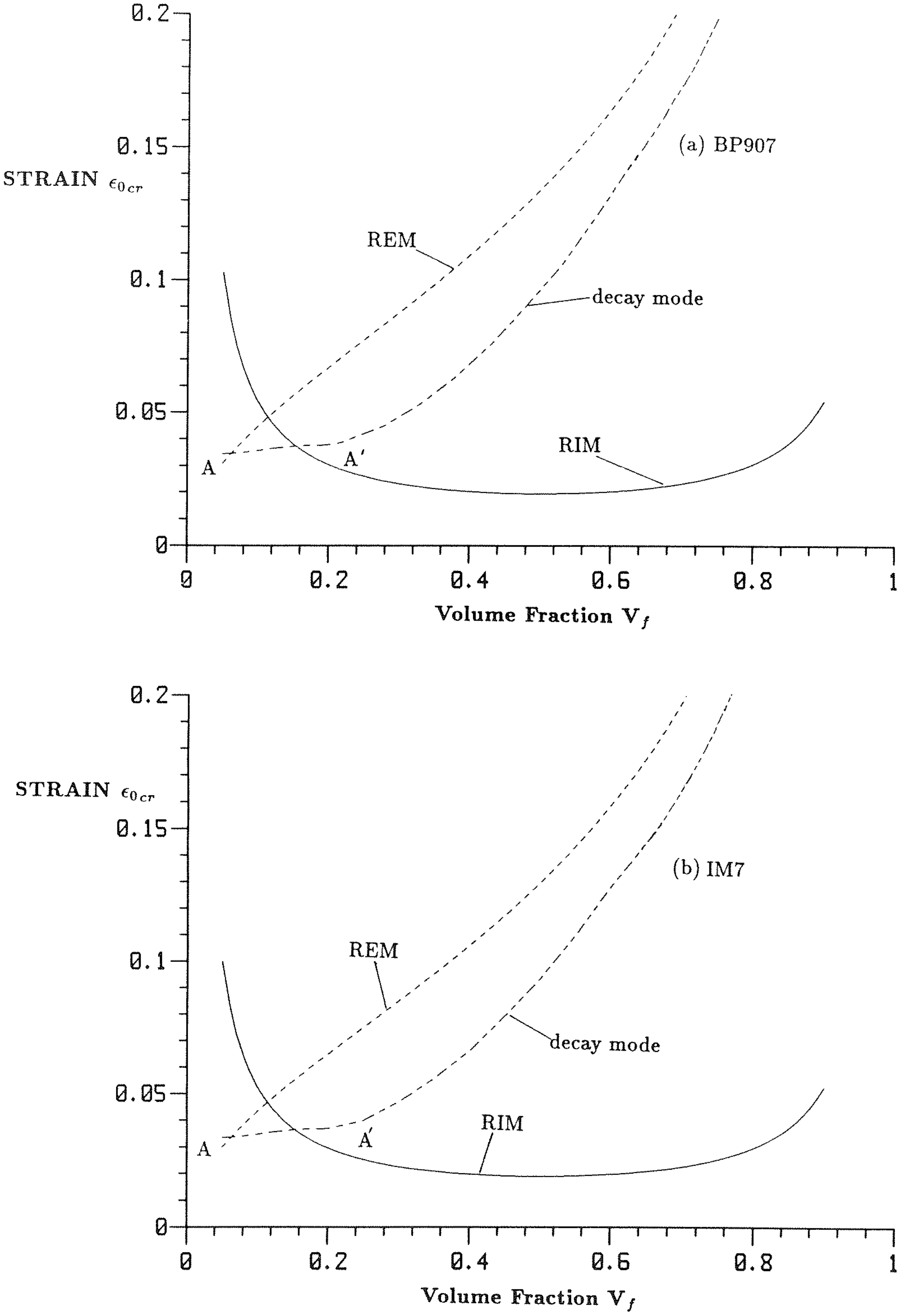

Figure 4.14 Variation of critical ϵ_0 with fiber volume fraction V_f; (a) T300/BP907 (b) IM7/8551-7.

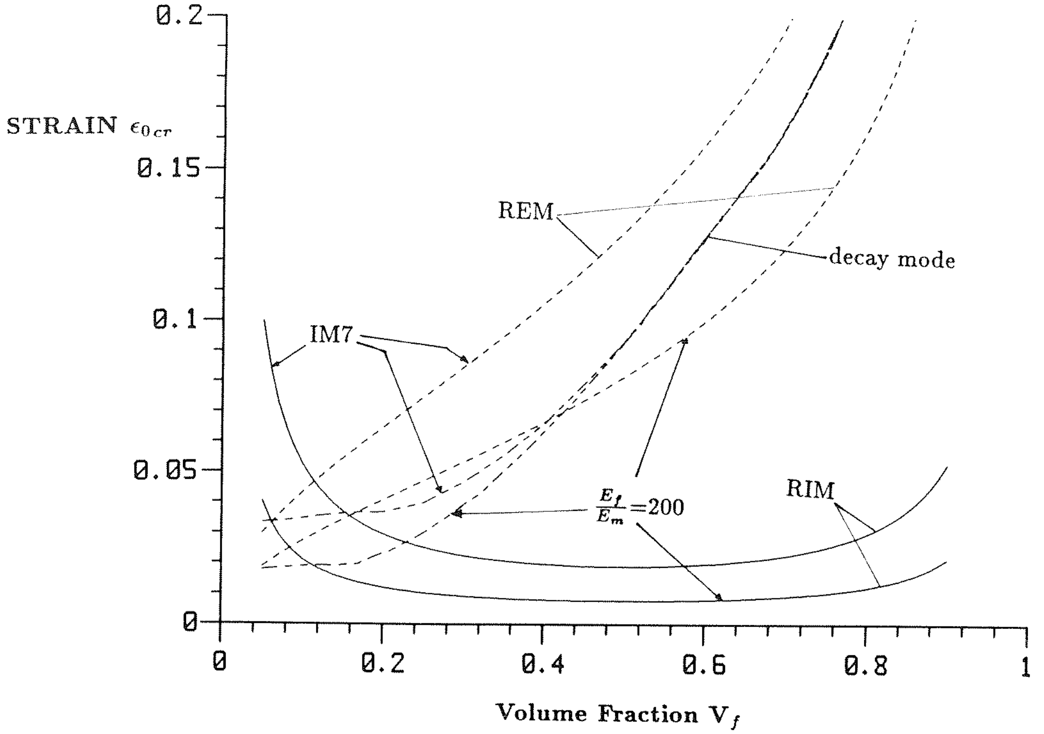

Figure 4.14c Variation of critical ϵ_0 with fiber volume fraction V_f; Comparison of IM7/8551-7 with composite of $\frac{E_f}{E_m} = 200$.

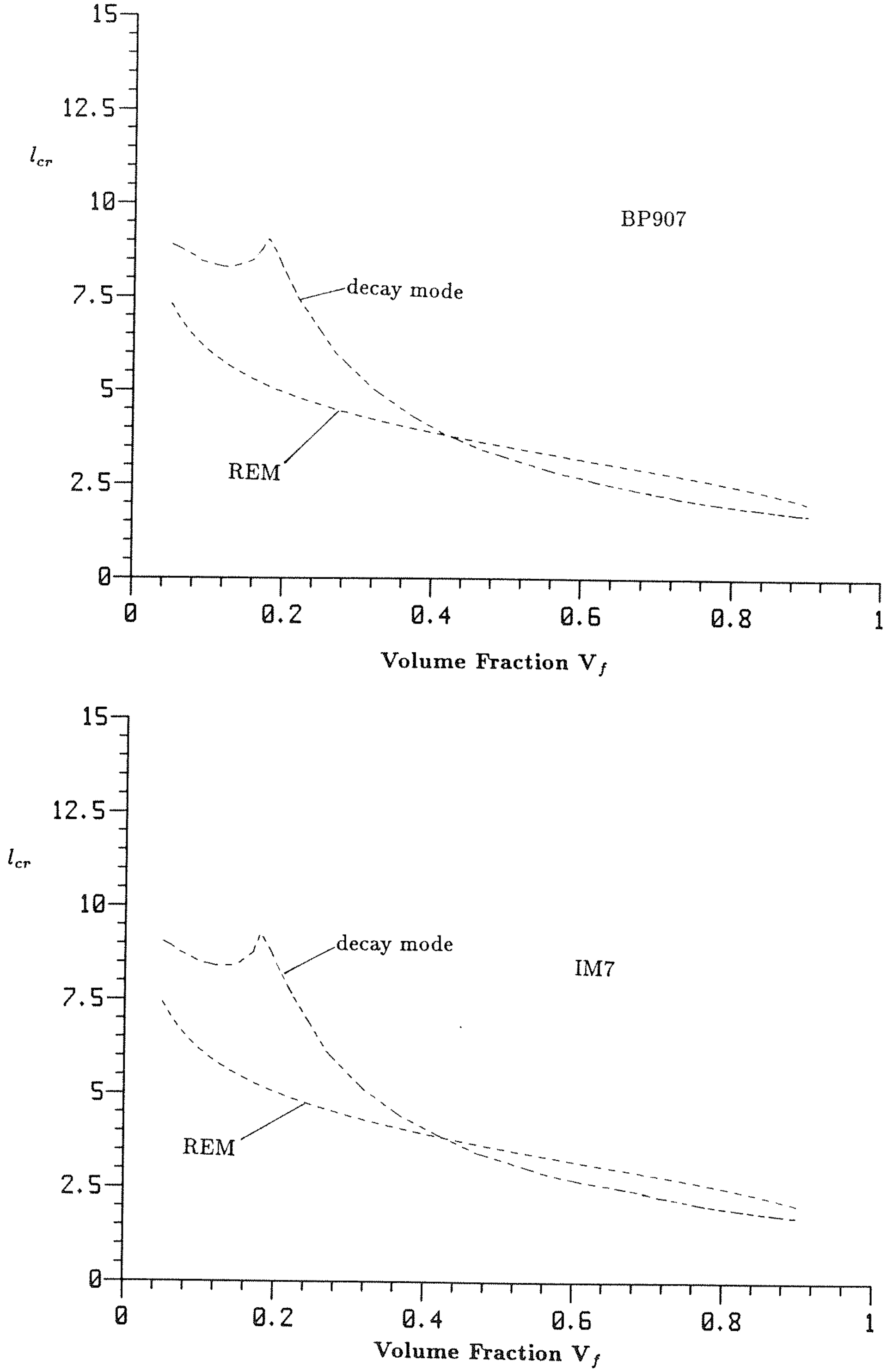

Figure 4.15 Variation of critical half wave length l with fiber volume fraction V_f; (a) T300/BP907 (b) IM7/8551-7.

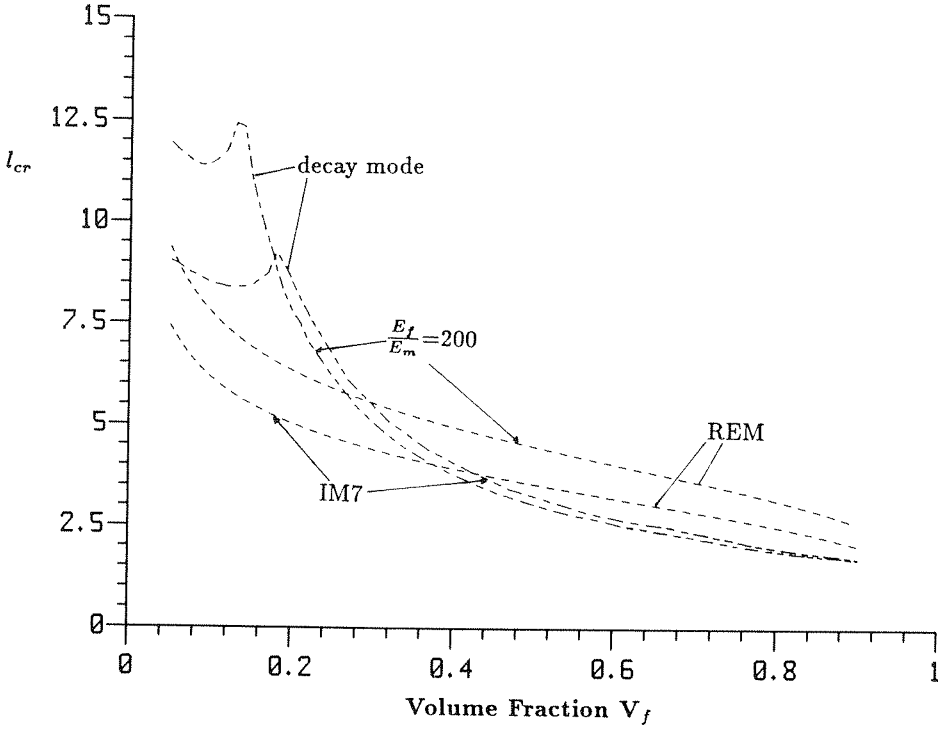

Figure 4.15c Variation of critical half wave length l with fiber volume fraction V_f; Comparison of IM7/8551-7 with composite of $\frac{E_f}{E_m} = 200$.

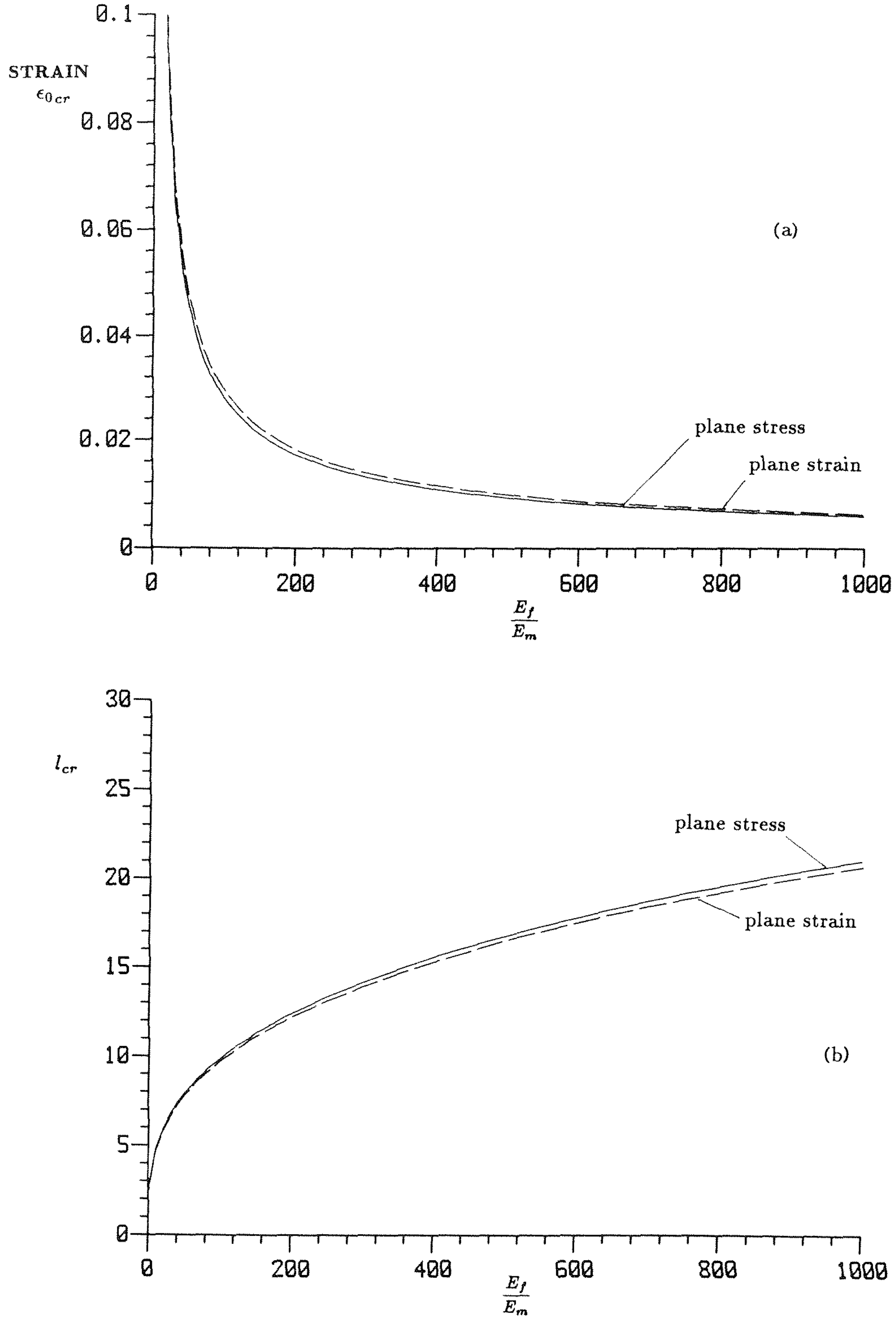

Figure 4.16 Comparison of plane stress and plane strain approximations for BP907 single fiber composite. a) ϵ_{cr} *variation. b)* l_{cr} *variation.*

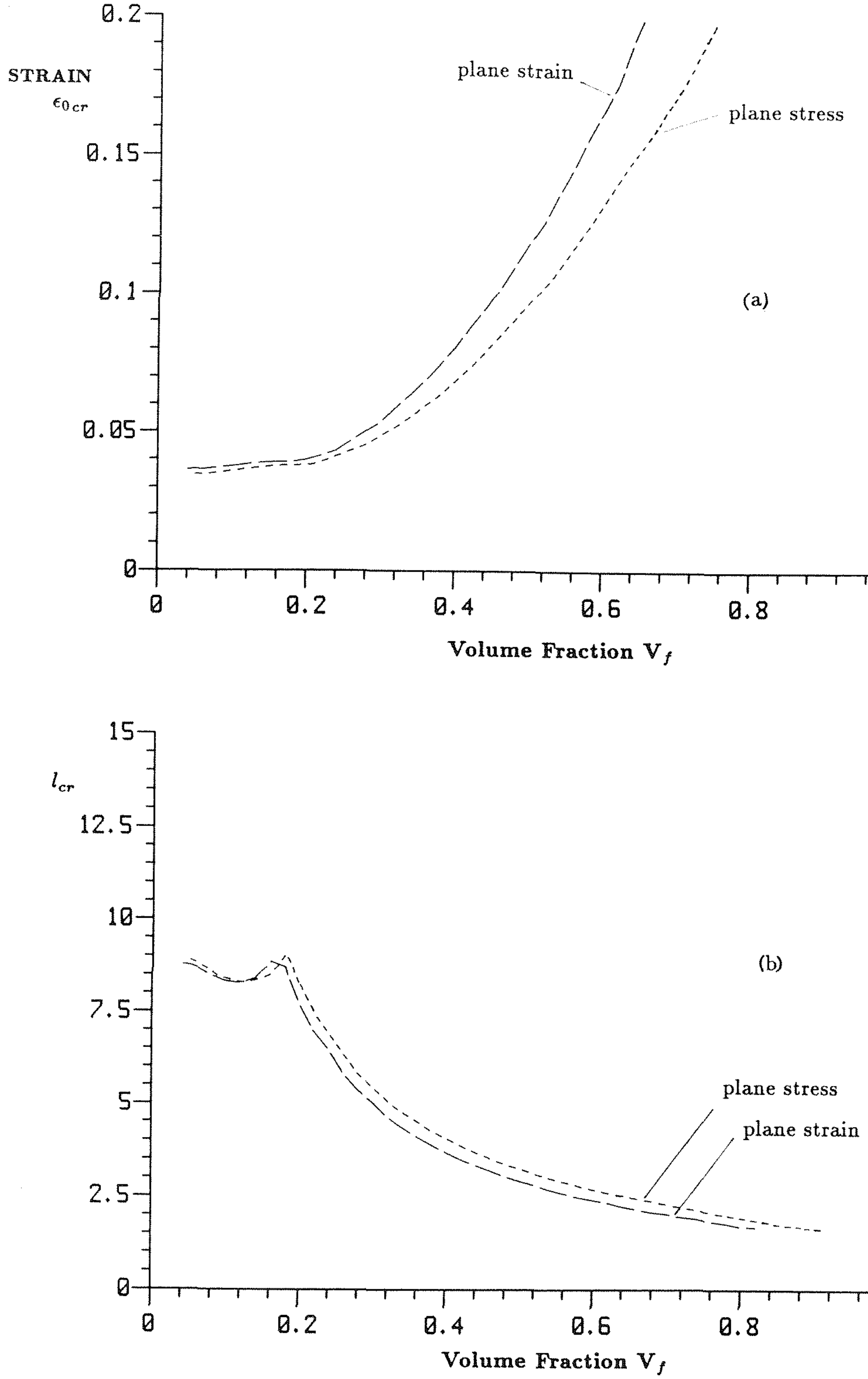

Figure 4.17 Comparison of plane stress and plane strain approximations for BP907 unidirectional composite. a) ϵ_{cr} variation. b) l_{cr} variation.

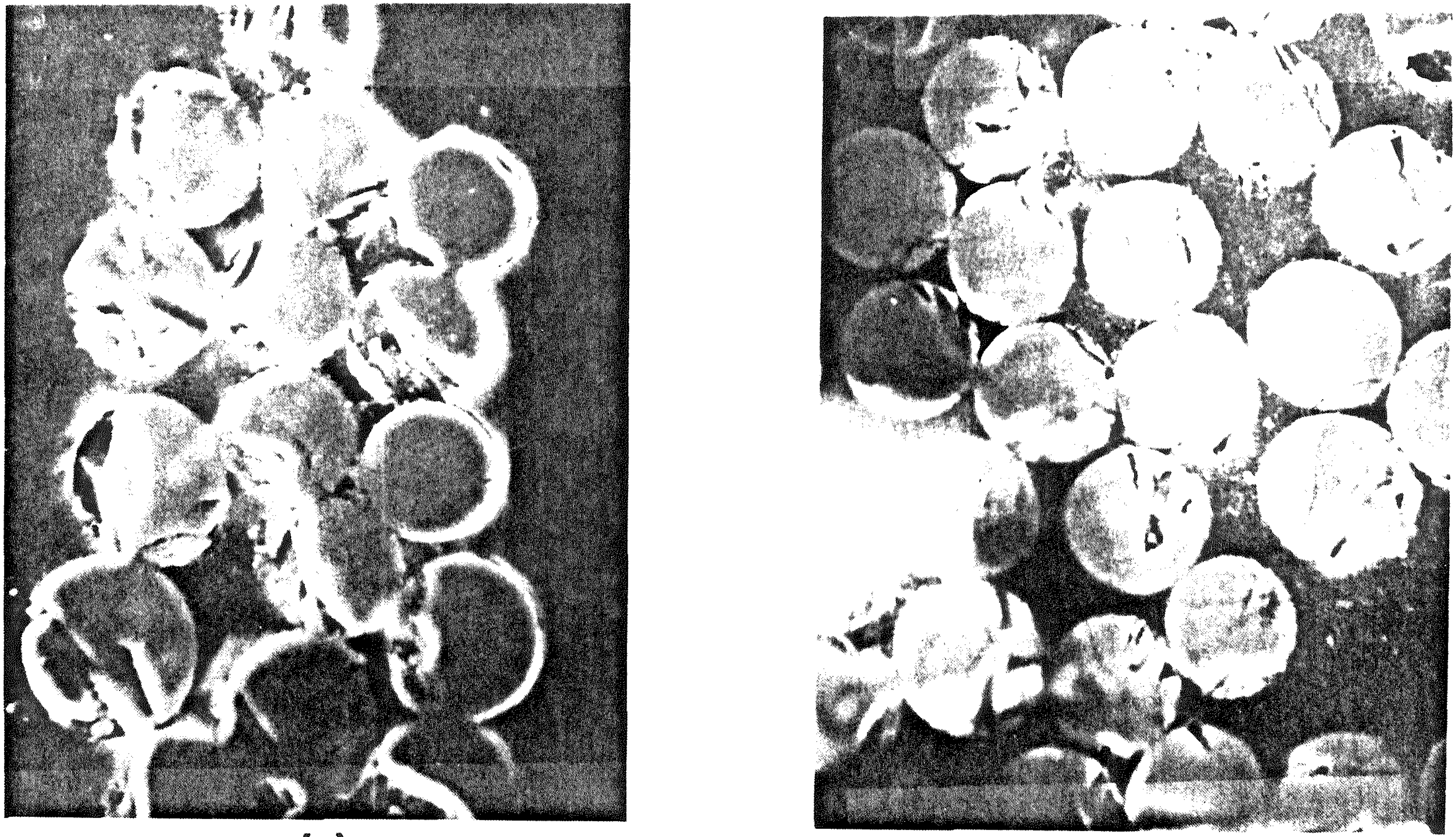

(a)
POOR BONDING

(b)
GOOD BONDING

Figure 4.18 SEM micrographs of typical ply cross-section contrasting 'good' and 'bad' interfacial bonding (from [4.22]).